Cranfield
UNIVERSITY

WILLIAM CHONG WOEI FONG

ADHESIVE AND MOLECULAR FRICTION IN TRIBOLOGICAL CONJUNCTIONS

SCHOOL OF ENGINEERING
DEPARTMENT OF AUTOMOTIVE ENGINEERING

PhD in the School of Engineering
Academic Year: 2011/12 (FULL TIME)

Supervisors:
DR MIRCEA TEODORESCU
PROF NICK VAUGHAN

JANUARY 2012

SCHOOL OF ENGINEERING
DEPARTMENT OF AUTOMOTIVE ENGINEERING

PhD in the School of Engineering

Academic Year: 2011/12 (FULL TIME)

WILLIAM CHONG WOEI FONG

ADHESIVE AND MOLECULAR FRICTION IN TRIBOLOGICAL CONJUNCTIONS

Supervisors:
DR MIRCEA TEODORESCU
PROF NICK VAUGHAN

JANUARY 2012

This thesis is submitted in partial fulfilment of the requirements for the degree of Doctor of Philosophy in the School of Engineering

Abstract

This thesis investigates the underlying causes of friction and inefficiency within an internal combustion engine, focusing on the ring-liner conjunction in the vicinity of the power-stroke top dead centre reversal. In such lubricated contacts, friction is the result of the interplay between numerous kinetics, with those at micro- and nano-scale interactions being significantly different than the ones at larger scales.

A modified Elrod's cavitation algorithm is developed to determine the microscopic tribological characteristics of the piston ring-liner contact. Predicting lubricant transient behaviour is critical when the inlet reversal leads to thin films and inherent metal-to-metal interaction. The model clearly shows that cavitation at the trailing edge of the ring-liner contact generated pre-reversal, persists after reversal and promotes starvation and depletion of the oil film. Hence, this will lead to boundary friction.

A fractal based boundary friction model is developed for lightly loaded asperity contacts, separated by diminishing small films, usually wetted by a layer of molecules adsorbed to the tips of the asperities. In nano-scale conjunctions, a lubricant layering effect often takes place due to the smoothness of surfaces, which is governed by the surface and lubricant properties. A molecularly thin layer of lubricant molecules can adhere to the asperities, being the last barrier against direct surface contact. As a result, boundary friction (prevailing in such diminishing gaps) is actually determined by a combination of shearing of a thin adsorbed film, adhesion of approaching asperities and their plastic deformation. A model for physio-chemical hydrodynamic mechanism is successfully established, describing the formation of thin adsorbed films between asperities. This model is effectively integrated with separately developed models that predict the adhesive and plastic contact of asperities.

Keywords: cavitation, adhesion, elastoplastic, solvation, boundary friction, adsorption, hard spheres, and fractal analysis

Acknowledgements

It is a pleasure to thank those who made this thesis possible. I owe my deepest gratitude to my supervisor, Dr Mircea Teodorescu who believed in my ability from the start till the end of the project duration. Without the break he provided me three years ago, I would never have achieved what I have today. His relentless encouragement, guidance and support be it work or life related made me into a better person in general. His words of wisdom will always remain to be the “take home message” from the time I spent working under him.

I would like to thank Professor Nick Vaughan for providing support in the work I did and also Professor Homer Rahnejat (Loughborough University) for his effort in assisting me to produce a number of good publications. I would also like to express my gratitude to Dr Sebastian Howell-Smith (Capricorn Automotive Ltd) who traveled down to Cranfield in the evenings to work on a few publications. It is also a pleasure to work with other researchers from Cranfield University, Loughborough University and Sheffield University throughout my PhD time. Finally, I am also thankful to the ENCYCLOPAEDIC project for giving me this opportunity to pursue my doctorate degree.

Contents

List of Figures

List of Tables

List of symbols

Chapter 2

α	Lubricant viscosity coefficient
α_o	Lubricant viscosity coefficient at $p = 0$
$\bar{\beta}$	Non-dimensional lubricant bulk modulus
$\bar{\eta}$	Non-dimensional lubricant viscosity
$\bar{\rho}$	Non-dimensional lubricant density
$\bar{t}$	Non-dimensional simulation time
β	Lubricant bulk modulus
β_a	Asperity curvature radius
δ	Ring deflection
ℓ	Connecting rod length
η	Lubricant viscosity
η_o	Lubricant viscosity at $p = 0$
η_R	Roeland's lubricant viscosity
Ω	Relaxation factor for fractional film content
ω	Engine speed in *rad/s*
ρ	Lubricant density
ρ_c	Lubricant density along cavitation region
ρ_o	Lubricant density at $p = 0$

σ	r.m.s. surface roughness
σ_r	Ring tension
τ	Total shear stress
τ_o	Eyring shear stress
θ	Fractional film content
ζ	Surface density at asperity peaks
A	Apparent contact area
a	Half of ring width
A_a	Asperity contact area
c	Ring crown height
D_{ij}	Influence coefficient for ring deflection
f_b	Boundary friction force
F_i	Residual term
f_n	Statistical functions for Greenwood and Tripp friction model, $n = 2, 5/2$
f_v	Viscous friction force
f_{tot}	Total friction force
g	Cavitation switch term
H	Non-dimensional lubricating film profile
h	Lubricating film profile
h_o	Undeformed central lubricating film thickness
h_s	Ring profile
h_{min}	Minimum lubricating film thickness
$J_{i,j}$	Jacobian matrix
L	Ring width

m	Pressure coefficient for boundary friction force
N	Engine speed in *rev/min*
n	Total grid points
P	Non-dimensional contact pressure
p	Contact pressure
p_1	External pressure acting on the ring
p_c	Cavitation pressure
R	Crank radius
R_x	Equivalent curvature radius of the ring
S	Squeeze rate
S_k	Distance of piston pin from TDC
t	Simulation time
u	Piston sliding velocity
U^*	Non-dimensional lubricant entrainment velocity
u_{av}	Lubricant entrainment velocity
W	Total ring load
W^*	Non-dimensional contact load
W_a	Total load carried by asperities
X	Non-dimensional coordinates along the ring width
x	Coordinates along the ring width
Z	Lubricant viscosity-pressure coefficient

Chapter 3

γ	Specific heat gas ratio
A_2	Top ring orifice cross section

A_3	Second ring orifice cross section
A_4	Third ring orifice cross section
C_d	Discharge coefficient
$m_{i,j}$	Mass of combustion gas
R_{gas}	Gas coefficient
T	Gas temperature
V	Inter ring crevice volume

Chapter 6

$\bar{\delta}$	Non-dimensional central deflection
$\bar{P}$	Non-dimensional asperity contact load
δ	Central deflection
$\Delta\gamma$	Surface energy
δ_c	Critical central deflection
δ_t	Deflection transition of elastic to elastoplastic deformation
$\delta_{pull\text{-}off}$	*Pull-off* central deflection
δ_{ep}	Elastoplastic central deflection
λ	Maugis-Dugdale's transition parameter
μ	Tabor's parameter
ν	Poisson's ratio
σ_o	Adhesive force intensity for the Dugdale potential
τ_a	Interfacial shear strength
A	Actual contact area
a	Contact radius
a_c	Critical contact radius

c	Contact radius based on Maugis-Dugdale contact model
$E*$	Reduced modulus of elasticity
h	Contact gap
h_a	Contact gap due to adhesion
P	Asperity contact load
P_f	Friction force due to asperity boundary adhesion
$P_{pull\text{-}off}$	*Pull-off* force
P_{ep}	Elastoplastic contact load
R	Contact curvature radius
S_y	Yield stress
z_o	Equilibrium spacing in the Lennard-Jones potential

Chapter 7

$\bar{P}$	Non-dimensional contact pressure
δ	Contact deformation
ϵ_θ	Convergence criterion for fractional film content
ν	Poisson's ratio
Ω_y	Pressure activation volume
ϕ_y	Shear activation volume
τ	Shear stress
τ_o	Eyring shear stress
A	Apparent contact area
A_h	Hamaker constant
$D_{i,j}^{k,l}$	Influence coefficient for contact deflection
E	Modulus of elasticity

E^*	Reduced modulus of elasticity
E_y	Barrier height for Eyring model
h	Contact gap profile
h_o	Undeformed central lubricating film thickness
h_s	Undeformed contact gap profile
k_B	Boltzmann constant
n	Iteration number
p_h	Hydrodynamic pressure
p_s	Solvation pressure
p_T	Total contact pressure
p_w	van der Waals pressure
Q	Activation energy
T	Lubricant temperature
U	Entraining velocity into the contact conjunction
V	Side leakage velocity

Chapter 8

$\bar{T}$	Dimensionless temperature
Δ	Grid step size
η^*	Packing fraction
$\phi_{\alpha\beta}$	Attraction potential
ρ^*	Number density
σ_α	Particle diameter of species α
σ_β	Particle diameter of species β
$c^*_{\alpha\beta}$	Direct correlation function between particles of species α and β

F^{p-p}	Interaction force between a pair of planar walls
F^{s-s}	Interaction force between a pair of large spheres
$g^*_{\alpha\beta}$	Pair correlation function between particles of species α and β
$h^*_{\alpha\beta}$	Indirect correlation function between particles of species α and β
m	Grid points
$M+1$	Total number of hard sphere species in a physical system
r^*	Core to core distance between particles
r_w	Concentration ratio of solvent in a fluid system
R_{eff}	Effective curvature radius of a pair of large spheres coming into contact
s	Core to core distance between particles
W^{s-s}	Interaction energy between a pair of large spheres

Chapter 9

δ	Central deflection of asperity
γ	Profile's density of frequencies
ϕ	Statistical distribution of asperities along a rough surface
ϕ_n	Random phase
σ	r.m.s surface roughness
A'	Truncated contact area
a'	Truncated contact radius
A'_L	Largest truncated contact area
A'_{tot}	Total truncated contact area
D	Fractal dimension
F	Total contact load
F_{frict}	Total friction force

G	Fractal roughness
L	Length of specimen
M	Number of ridges
$n(A')$	Truncated asperity size distribution
R	Asperity curvature radius
z	Asperity height distribution

Chapter 1

Introduction

1.1 Introduction

Tribology studies the interaction between surfaces in relative motion. The term was proposed in 1966 by a working group set up by the Minister of State for Education and Science of the British government (known as "Jost Committee") to investigate the unexpected increase in wear-linked machine failures. At that time, the cost associated with running factories and machinery was sharply increasing even though the technology was progressively improving. The new term was defined as *"the science and technology of interacting surfaces in relative motion and of related subjects and practices"* [1].

Like most natural phenomena, surface interactions are governed by competing kinetics operating at different length scales. At micro-scale, the bulk elastic properties of the material and lubricant dominate. Consequently, Amontons laws [2] established in the 17th century for nominally "dry" surfaces and validated by de Coulomb [3] in the 18th century, sufficed "dry-friction" modelling for over over 200 years. When Reynolds equation was initially proposed late 19th century [4], minimum films of $\approx 10^{-4}$m were expected. However, by the time the "Jost Committee" was established, the separation gaps dropped by almost two orders of magnitude. In 1993, Dowson [5] predicted (see figure 1.1) that separation gaps of 10^{-8} m will become common by the year 2000. He expected the value to drop down to even 10^{-9} m range in the following decade and this has been proven to be true with the increasing amount of nanotribology research in recent years.

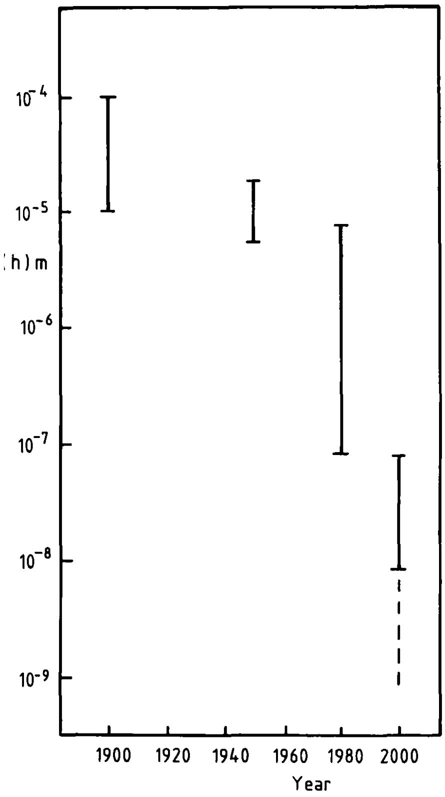

Figure 1.1: Thinning of fluid film [5]

Friction between two surfaces is defined as the tangential force resisting their relative motion. If an intervening fluid is present in the contact, the viscous shear is one of the dominant friction mechanisms. However, contacting surfaces are rarely smooth. If the separation gap is of the same order of magnitude as the surface roughness, the contact between opposing surfaces is dominated by kinetics between surface features on each side.

Therefore, to accurately predict surface interactions, aside from the obvious macro-scale kinematics between the approaching parts (e.g. relative velocity of the moving parts), one must also consider the less evident micro- and nano-scale kinetics between opposing surface features (see figure 1.2).The main goal of the study is to propose a model, which leads toward bridging the gap between these scales (from micro to nano).

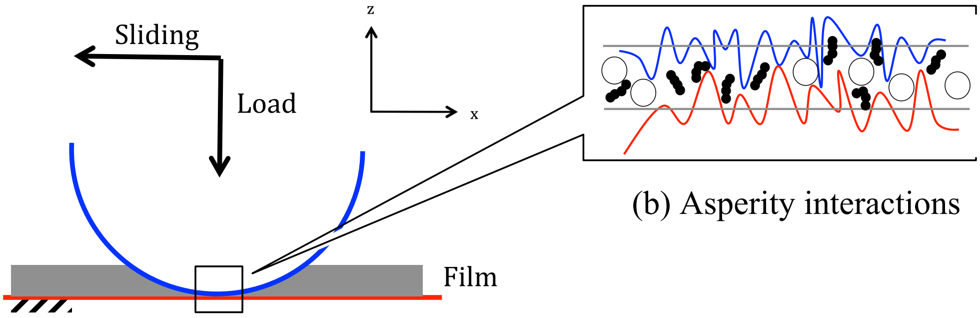

(a) Typical sliding roller contact

(b) Asperity interactions

Figure 1.2: Typical tribological conjunction

1.2 Motivation

Friction and wear causes machine elements to breakdown, reducing the overall efficiency and increasing operational costs. According to the report by the Jost committee, the approximated losses due to friction and wear of materials accounted for 2 to 3% of the UK's gross domestic product (GDP). In a typical internal combustion engine, the total energy from the fuel available at the driven wheels is about 12% [6, 7]. The thermal losses in the engine accounts for 60%, mechanical losses (15%) and losses in transmission and differential system (10%) [6, 7, 8]. The friction due to the piston ring assembly accounts for nearly 45% of the total mechanical losses of the engine [8]. Therefore, the top compression ring constitutes $\approx 2-4\%$ of the total expanded fuel energy. This is very significant given the size of the component. Figure 1.3 shows the power distribution of a typical automotive vehicle during an urban driving cycle.

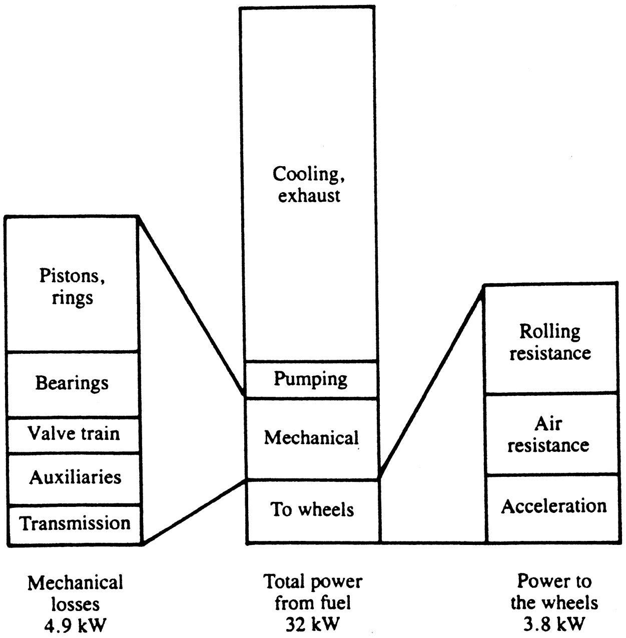

Figure 1.3: Power distribution in a typical automotive vehicle during an urban driving cycle [7]

Naturally, the substantial heat loss is the main concern for engine designers. However, recently, it has also been recognized that worthwhile efficiency gains can be obtained by paying more attention to the modest mechanical losses in the engine [7]. As an example, according to the statistics given by Society of Motor Manufacturers and Traders, UK, there are approximately 30 million vehicles on the British road in the year 2010. Considering the gasoline price at £1.30/litre, the total cost of power consumed in the UK through automotive sector is around £34.5 million/litre gasoline. Taking into account that the average total travel distance of a modern vehicle is about 10,000 miles/annum with an average fuel consumption of 12.5 miles/litre (from a recent survey by the European Union) during an urban driving cycle, the total cost of power consumed in the UK through vehicle use is approximately £43 billion/annum.

From these information, for example, a reduction of 10% in mechanical efficiency of the engine would lead to an improved fuel consumption of up to 1.5%. Apart from environmental gains due to reduced emission, this would accrue to a financial saving of £647 million/annum in the UK, which is substantial to the country's economy. Most of all, this shows the need for an improved fundamental understanding of the mechanisms underlying friction (e.g. piston ring/liner contact), in order to reduce the frictional losses with the tribological conjunction.

1.3 Aims

The aim of the study is to propose a mathematical model, which integrates macro scale kinematics (e.g. piston ring-liner relative motion) with the micro- and nano-scale kinetics governing the frictional losses in the tribological conjunction. The study attempts to build a friction model, which accounts for surface topography, asperity profile and lubricant physical-chemistry properties (e.g. the effect of thin adsorbed film sheared between sliding asperities on each side of the rough surface).

1.4 Objectives

The study is divided in two parts:

The first part proposes a model to predict the mechanisms of film formation in a piston ring-liner conjunction. A model is proposed, which predicts the cavitation extent, contact pressure and separation gap along the ring-liner conjunction. This model is used to predict film depletion and starvation during piston reversals.

The second part of the study investigates the nano-scale interaction between surface asperities on opposing sides of the contact. The objective is to develop an integrated multi-scale friction model for a rough surface. The model considers micro- and nano-scale kinetics (e.g. van der Waals and solvation) of thin adsorbed films together with asperity boundary adhesion for interacting surfaces operating under macro-scale kinematics (e.g. piston motion). The model predicts the friction force in the ring-liner conjunction along the power stroke top dead centre, where boundary friction plays a significant role.

It should be noted that due to the nature of the study, the literature review is embedded directly in the corresponding chapters.

1.5 Research Outline

Chapter 2 proposes a transient modified Elrod's cavitation model to predict the contact pressure, film thickness and the extend of the cavity formation during the entire engine cycle. The ring-liner friction is computed using a simplified analytical friction model. *Chapter 3* applies these models for new and worn top compression rings used in an Honda CRF450 engine. A simplified orifice-volume is applied to predict the blow-by and the inter-ring pressure. *Chapter 4* validates the film thickness with the measurements obtained using a Plint TE77 reciprocation test rig.

The second part investigates the asperity interactions in nano-scale tribological conjunctions. *Chapter 5* represents a brief overview of the kinetics governing friction force in micro- and nano- scale conjunctions. *Chapter 6* investigates the elastic and plastic deformation as well as the adhesion between two approaching asperities on opposite surfaces. *Chapter 7* proposes a model for shearing a molecularly-thin single-species of molecule lubricant film between approaching asperities. *Chapter 8* extends the model for a lubricant with multi-species of molecule. *Chapter 9* extends the single-asperity models developed in *Chapters 6* and *8* to a rough surface to predict boundary friction. The prediction is compared to the analytic friction model used in *Chapters 2* to *4*. *Chapter 10* concludes the study and highlights the future work.

Part I

Piston Ring Tribology

Chapter 2

Mechanisms of Film Formation

2.1 Introduction

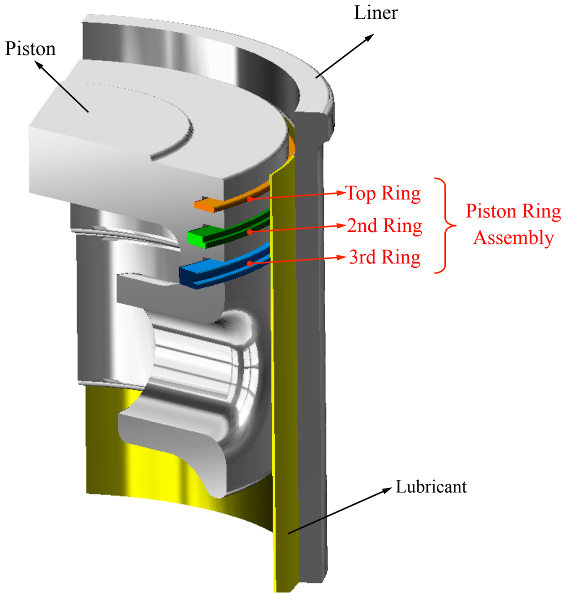

Figure 2.1: A simplified piston assembly showing the ring pack

The piston ring-liner conjunction represents a dynamic seal between the combustion chamber and the crankcase. Although vital for engine operation, the ring-liner conjunction is one of the most important source of engine frictional losses. Inadequate ring-liner lubrication leads to high fuel/oil consumption and increased engine emissions, causing a dramatic impact over the entire system's efficiency [9]. A significant part of the total friction loss in the IC engine happens between the piston ring and the cylinder liner contact [10]. This accounts for 40% – 60% of the total frictional losses produced in the IC engine [8].

The Reynolds equation [4] is commonly used to compute the contact pressure and film thickness of a tribological conjunction. The Swift-Steiber [11, 12] exit boundary conditions used along with the Reynolds equation predict the film pressure if cavitation is negligible. Therefore, as a first approximation, most piston ring-liner tribological models assumes a contact outlet pressure of either atmospheric or cavitation pressure. Although this may be an acceptable compromise between accuracy and model complexity, it can lead to erroneous conclusions. Cavitation in a fluid is the formation of pockets of gas due to the fluids' inability to sustain significant sub-ambient pressures [13]. This condition is often encountered when the machine elements in relative motion are separated by a layer of intervening film [14] (e.g. journal bearings, squeeze film dampers and piston ring-liner conjunctions). Dowson [15] used a submerged rotating drum on a flat surface to observe the cavitation phenomenon for both static and dynamic loading (see figure 2.2).

There are two phenomena, which are commonly referred to as cavitation. Gaseous cavitation (also known as aeration) represents the release of dissolved gases when lubricant pressure drops below saturation pressure [16]. Vapor cavitation represents lubricant boiling at the vapor pressure (usually lower than saturation pressure).

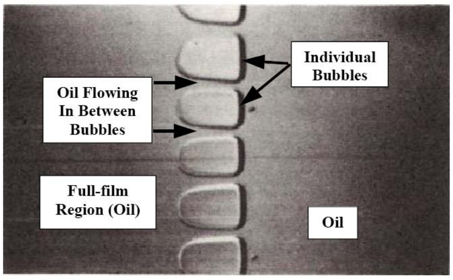

(a) Low entrainment

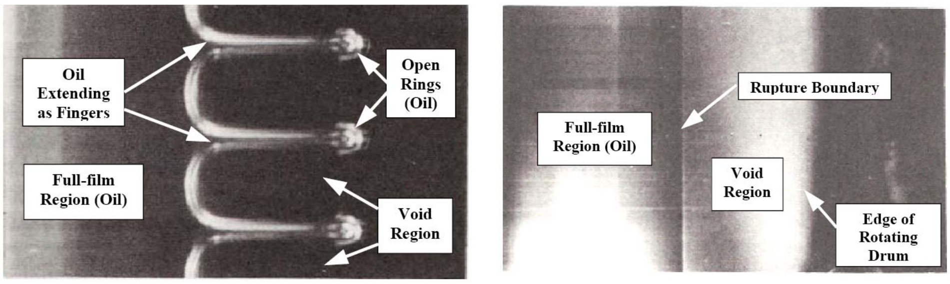

(b) Moderate entrainment (c) High entrainment

Figure 2.2: Cavitation pattern in a fluid flow operating under various entrainment velocities [15, 17]

In the piston ring-liner conjunction, cavitation is the consequence of sudden lubricant pressure drop in the diverging cross section of the ring [18]. This induces the transition of fluid from liquid form to gas-liquid mixture [19]. Etsion and Ludwig [20] measured the cavitation pressure as $\approx 50kPa$ above absolute zero. Stadler *et al* [21] proposed a simple experiment, which suggests that the cavitation pressure is lower than $0.02MPa$ (absolute pressure). Different aspects of the cavity formation and the advantages of various predictive techniques are well explained by Dowson [15], Floberg [22, 23] and most recently by Priest *et al* [13] for the ring-liner contact. Arcoumanis *et al* [24] and Dhunput *et al* [25] built an experimental test rig to investigate the transient behaviour of the cavitation streams as well as their development through the TDC.

Figure 2.3 shows a typical piston ring-liner conjunction. It must also be noted that each ring has specific operating conditions. Firstly, for each ring the contact geometry is unique. Secondly, the only lubricant available at the leading edge is the lubricant left over by the previous ring. Therefore, even if the first ring is fully flooded, the consequent rings are starved. Thirdly, the gas pressure at the leading and trailing edges of the contact as well as the pressure behind each ring are different.

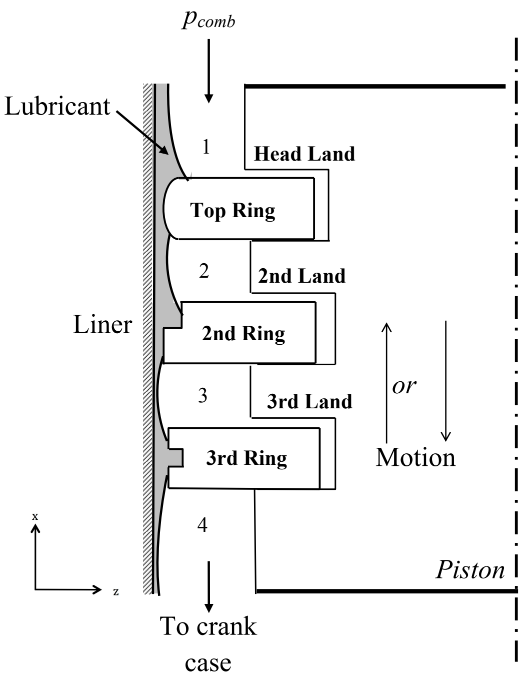

Figure 2.3: Schematic view of the piston ring-liner conjunction (p_{comb} is the combustion pressure)

2.2 Background

The main goal of the current chapter is to investigate the correlation between cavitation and starvation in the vicinity of the top dead centre (TDC) and bottom dead centre (BDC). The proposed model is generic. For the numerical example, the top (compression) ring was used. For most lubricants, the viscosity and cavitation pressure depend on the lubricant temperature. Therefore, these parameters will likely vary between the TDC and the BDC. However, implementing these requires detailed models for the transient heat flow and for the rheological parameters of the lubricant. Here an isothermal analysis is carried out for a $SAE5W30$ lubricant at 120^0C (as used by Akalin and Newaz [10]). Therefore, the viscosity is $\approx 0.00689Pa.s$ (*ASTM D341* [26] and [27]). The cavitation pressure used as a first approximation is $0.02MPa$, which is within the range measured by Stadler *et al* [21].

The classical formulation of the Reynolds equation does not account for the sub-ambient pressure in the diverging part of the contact [4]. One possible solution is limiting the outlet pressures to the atmospheric pressure [28] or to the cavitation pressure [29]. Although this is a very fast and convenient method, mass conservation of fluid flow in the cavitation region is not fulfilled. A solution for this problem is proposed by Jakobsson and Floberg [30] together with Olsson [31], known as the JFO theory. They used Reynolds equation with a new set of boundary conditions. They divided the contact in two separate regions: (i) full film and (ii) cavitation (see figure 2.4). In the full film region Reynolds equation describes the problem. However, in the cavitation region the film breaks down and lubricant behaviour is predicted using only the continuity of flow. This is an elegant approach, which for moderately and heavily loaded conditions represents a reasonable compromise between computational speed and accuracy [32]. However, it could be difficult to implement.

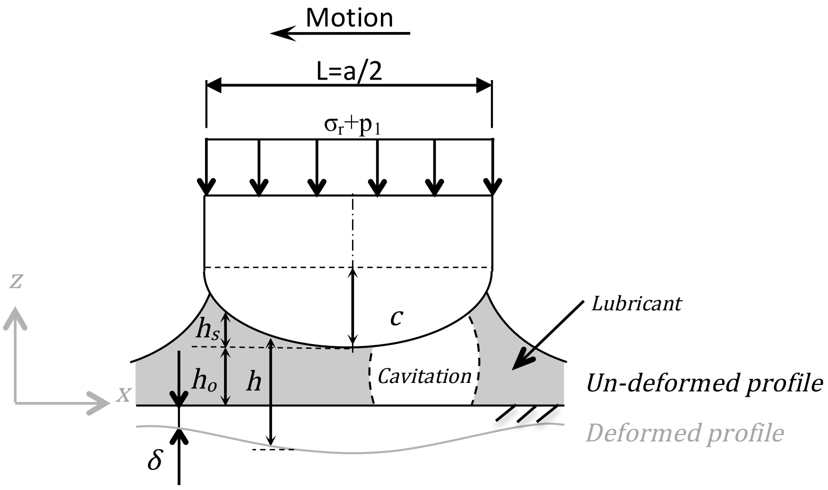

Figure 2.4: Piston ring-liner conjunction (c is the ring crown height)

Elrod [32] and Elrod and Adams [33] proposed an improved algorithm for the JFO approximation, which simplifies the prediction of the boundary between full film and cavitation regions. They introduced a non-dimensionalised parameter (θ), which represents the non-dimensional lubricant density in the full-film region ($\theta \geq 1$) and the fractional film content in the cavitation region ($0 < \theta < 1$).

$$\theta \rightarrow \begin{cases} \text{Full film } (\theta \geq 1) & \Rightarrow \theta = \rho/\rho_c \\ \text{Cavitation } (0 < \theta < 1) & \Rightarrow p = \beta(\theta - 1) + p_c \end{cases} \tag{2.1}$$

where p_c is the cavitation pressure and β is the lubricant bulk modulus.

Brewe [14] used the Elrod algorithm to predict vapor cavitation in a submerged journal bearing during steady state and transient conditions. Vijayaraghavan and Keith

[29] proposed a finite-differenceing scheme to predict the pressure distribution along the contact and validated the numerical results with Coyne and Elrod's experiments [34]. Yang and Keith [35] extended this approach for the piston ring lubrication, while Cioc and Keith [36] applied Elrod's algorithm using the Conservation Element (CE) and Solution Element (SE) method. Sawicky and Yu [37] proposed an analytical solution for the piston ring lubrication based solely on the JFO boundary condition. Bayada *et al* [38] maintained the core of the Elrod algorithm, redefined θ as "filling rate" and proposed an algorithm for EHL conditions. This is a function of the oil film thickness to the width of the gap. Damiens *et al* [39] investigated the starvation effect on an elliptical contact and Venner *et al* [40] used a modified version of the algorithm for starved point contact conditions.

An ideal ring would completely seal the combustion chamber. However, in reality combustion gases pass through several gaps or crevices (e.g. ring end gaps), leading to blow-by [41]. This affects engine performance and exhaust emissions [42, 43]. For a gasoline engine running at 2000 rev/min, the pressure behind the top ring was measured as $\approx 25\%$ of the combustion pressure [41], which (as a representative value) was also used in the current chapter as a first approximation.

The proposed numerical model uses as a base the solution proposed by Vijayaraghavan and Keith [29] for Elrod's algorithm. However, localised contact deflection (especially in the vicinity of the dead centers) could have significant consequences for the cavitation development (this will be discussed in figure 2.14). To account for it, the finite difference scheme suggested by Jalali *et al* [28] for an elastohydrodynamic contact was carefully adapted for the current conditions. The resulted integrated approach is referred to as Modified Elrod (Mod. Elrod) throughout the study.

2.3 Mathematical Model

2.3.1 Elrod equation

For the engine under investigation, the ring length to width ratio is over 100. Therefore, as a first approximation, the piston ring-liner conjunction is viewed as an infinitely long sliding bearing [27, 35, 44]. Although this assumes uniform radial loading and neglects piston secondary motion as well as ring dynamics, the final results could yet provide valuable information.

If the flow is laminar, the behaviour of most lubricated conjunctions can be predicted using a 1-dimensional Reynolds equation:

$$\frac{\partial}{\partial x}\left[\frac{\rho h^3}{\eta}\frac{\partial p}{\partial x}\right] = 12\left\{\frac{\partial}{\partial x}\left[\rho h\left(u_{av}\right)\right] + \frac{d}{dt}\left(\rho h\right)\right\} \tag{2.2}$$

Elrod's [32] modification provides an acceptable solution if the cavitation is to be present. In the full film section of the contact, both the Couette and Poiseuille terms are considered. In the cavitation region, only the Couette term plays an important role because the cavitation pressure is constant ($\partial p/\partial x = 0$). To account for this, the switch term, g is defined as:

$$g = \begin{cases} 1 \Rightarrow & \text{Full film, if } \theta \geq 1 \\ 0 \Rightarrow & \text{Cavitation, if } 0 < \theta < 1 \end{cases} \tag{2.3}$$

The contact pressure distribution in the contact can be expressed as:

$$p = g\beta \ln\theta + p_c \tag{2.4}$$

The equation obtained by substituting equation (2.4) into equation (2.2) predicts the transient behaviour for the full film and for the cavitation regions:

$$\frac{\partial}{\partial x}\left[\frac{\rho_c h^3}{\eta} g\beta \frac{d\theta}{\partial x}\right] = 12\left\{\frac{\partial}{\partial x}\left[\theta\rho_c h\left(u_{av}\right)\right] + \frac{d}{dt}\left(\theta\rho_c h\right)\right\} \tag{2.5}$$

Lubricant viscosity-pressure variation can be predicted using the Roelands [45] equation:

$$\eta_R = \eta_o e^{\alpha} \tag{2.6}$$

where $\alpha = (\ln\eta_o + 9.67)\{[1 + p/(1.98\times10^8)]^Z - 1\}/p$ and $Z = \alpha_o/[5.1\times10^{-9}(\ln\eta_o + 9.67)]$. Density variation with the contact pressure for mineral oils is given by Dowson and Higginson [46]:

$$\rho = \rho_o\left(1 + \frac{0.6\times10^{-9}p}{1 + 1.7\times10^{-9}p}\right) \tag{2.7}$$

The parabolic ring profile $h_s(x)$ used for the top compression ring is defined as (refer figure 2.4):

$$h_s(x) = \frac{cx^2}{(L/2)^2} \tag{2.8}$$

During most of the engine cycle the contact deflection is negligible and the ring-liner conjunction operates under hydrodynamic or mixed lubrication regimes [47]. However, in certain conditions, especially at the vicinity of the power stroke TDC where the combustion pressure is significant, limited local deformation can affect the lubrication regime. Therefore, for completeness, the current study includes the local elastic deflection in the overall solution. For a line contact the deflection at computation node i is [48]:

$$\delta(x)|_{x=idx} = \sum_{j=1}^{n} D_{ij}p_j - \frac{1}{4}\ln\left(R_x^2\frac{8W}{\pi}\right) \tag{2.9}$$

where p_j is the pressure applied at computation node j and D_{ij} is the influence coefficient. The elastic shape of the lubricant film profile, h (refer figure 2.4) for the top ring is [49]:

$$h(x) = h_o + h_s(x) + \delta(x) \tag{2.10}$$

where h_o is the undeformed central film thickness.

2.3.2 Friction force

Equation (2.10) predicts the elastic film shape for smooth profiles. However, both sides of the contact are microscopically rough. If the film is thick the effect of surface roughness can be neglected. However, when the lubricating film is thin, contact between individual asperities cannot be avoided. Consequently, the friction force has a viscous component (f_ν) due to lubricant shearing and a boundary component (f_b) due to direct surface asperity interaction. Therefore, for an element of area, dA the friction force is:

$$df_{tot} = df_b + df_\nu \tag{2.11}$$

The viscous friction force for a Newtonian fluid can be computed as:

$$\begin{aligned} df_{\nu} &= \tau \left(dA - dA_a\right) \\ \tau &= \eta u_{av}/h(x) \end{aligned} \tag{2.12}$$

where dA_a is the asperity contact area.

The boundary friction force is the result of shearing a very thin film (several layers of molecules), which prevails between interacting asperity tips. This non-Newtonian shear can be predicted using the classic Eyring model [50]. Therefore, the boundary friction force is:

$$df_b = dA_a(\tau_o + m\frac{dW_a}{dA_a}) \tag{2.13}$$

where τ_0 is the Eyring shear stress of the lubricant, m is the pressure coefficient of the boundary shear strength and dW_a is the load carried by the asperities.

Asperity contact area and the load carried by asperities can be predicted with good accuracy using the classical Greenwood and Tripp model [51]:

$$\begin{aligned} dA_a &= dA\pi^2 \left(\zeta\beta_a\sigma\right)^2 f_2\left(\lambda\right) \\ dW_a &= dA\frac{8\sqrt{2}}{15}\pi \left(\zeta\beta_a\sigma\right)^2 \sqrt{\frac{\sigma}{\beta_a}}E^* \times f_{5/2}(\lambda) \end{aligned} \tag{2.14}$$

where the statistical functions f_2 and $f_{5/2}$ are defined as:

$$f_n(\lambda) = \frac{1}{\sqrt{2\pi}}\int_{\lambda}^{\infty}(s-\lambda)^n e^{-s^2/2}ds$$

To speed up the calculation the polynomial approximation proposed by Teodorescu *et al* [52] was used. The polynomial approximations are:

$$\begin{aligned} f_2 &= -\frac{1}{10^4}(18\lambda^5 - 281\lambda^4 + 1728\lambda^3 - 5258\lambda^2 + 8043\lambda - 5003) \\ f_{5/2} &= -\frac{1}{10^4}(46\lambda^5 - 574\lambda^4 + 2958\lambda^3 - 7844\lambda^2 + 776\lambda - 6167) \end{aligned} \tag{2.15}$$

Therefore, the total friction force for the ring-liner contact is:

$$f_{tot} = \int_{inlet}^{outlet} df_{tot} dx \times L \tag{2.16}$$

2.3.3 Numerical solution

Vijayaraghavan and Keith [29] proposed a convenient transformation for the left hand side of equation (2.5):

$$g\frac{d\theta}{dx} = \frac{dg(\theta - 1)}{dx} \tag{2.17}$$

Using the derivations in *Appendix A*, equation (2.5) can be written in non-dimensional form as:

$$\frac{\partial}{\partial X}\left[\frac{\bar{\rho}_c H^3}{\bar{\eta}}\frac{\partial g(\theta - 1)}{\partial X}\right] = \psi\left\{\frac{\partial}{\partial X}\left[\theta\bar{\rho}_c H\right] + \frac{R_x}{b} S\left(\theta\bar{\rho}_c\right)\right\} \tag{2.18}$$

where $\psi = 12\left(R_x/b\right)^3/\bar{\beta}$ and $S = \left(dh/dt\right)/u_{av}$.

Equation (2.18) is solved numerically using the finite-difference technique proposed by Jalali *et al* [28] (see *Appendix A*). The Poiseuille term is discretized using central differences. This provides a second order accuracy, as the solution along the full film region must consider all the neighboring variables. For the Couette term, which is predominant in the the cavitation region, a backward differencing scheme with first order of accuracy is used. Backward differencing is used within the cavitation region to prevent instability due to the non-continuous solution of the cavitation algorithm. The residual term, F derived from the finite difference scheme mentioned is:

$$
\begin{aligned}
F_i = \quad & \frac{1}{2\Delta X^2}\left\{\begin{array}{l}
\left[\left(\frac{\bar{\rho}_c H^3}{\bar{\eta}}\right)_{i+1}+\left(\frac{\bar{\rho}_c H^3}{\bar{\eta}}\right)_{i}\right][g(\theta-1)]_{i+1} \\
-\left[\left(\frac{\bar{\rho}_c H^3}{\bar{\eta}}\right)_{i+1}+2\left(\frac{\bar{\rho}_c H^3}{\bar{\eta}}\right)_{i}+\left(\frac{\bar{\rho}_c H^3}{\bar{\eta}}\right)_{i-1}\right][g(\theta-1)]_{i} \\
+\left[\left(\frac{\bar{\rho}_c H^3}{\bar{\eta}}\right)_{i}+\left(\frac{\bar{\rho}_c H^3}{\bar{\eta}}\right)_{i-1}\right][g(\theta-1)]_{i-1}
\end{array}\right\} \\
& -\frac{\psi}{\Delta X}\left\{\begin{array}{l}
(1-\Phi)\left[(\theta\bar{\rho}_c H)_{i+1}-(\theta\bar{\rho}_c H)_{i}\right] \\
+(\Phi)\left[(\theta\bar{\rho}_c H)_{i}-(\theta\bar{\rho}_c H)_{i-1}\right]
\end{array}\right\} \\
& -\psi\frac{R_x(\theta\bar{\rho}_c)_i}{b}S^*
\end{aligned}
$$

The numerical algorithm operates in two consecutive loops (a pressure and a load loop). The pressure loop uses the iterative approach by Jalali *et al* [28] for integrating Reynolds equation as a starting point. However, the convergence for the proposed model is focused on θ and the lubricant pressure is computed after the convergence is achieved. The Jacobian matrix, J for this case can be expressed as:

$$J_{i,j} = \frac{\partial F_i}{\partial [g\theta]_j} \tag{2.19}$$

where F_i is the residual term (see equation (2.19)), and i, j are grid points along the piston ring width. The value of θ_i^k at iteration k can be computed as:

$$\theta_i^k = \theta_i^{k-1} + \Omega\Delta\theta_i^k \tag{2.20}$$

where Ω is the relaxation factor and $\Delta\theta_i^k = -(F_i + J_{i,i-1}\Delta\theta_{i-1}^k + J_{i,i+1}\Delta\theta_{i+1}^k)/J_{i,i}$.

The convergency criterion for θ is: $\sum\left(\theta_i^k - \theta_i^{k-1}\right)^{0.5}/n \leq 1.0 \times 10^{-7}$, where n is the number of mesh points ($n = 200$). In the load loop the contact load is compared with the reference load (see figure 2.6 in the following section). The convergence criterion is $|\int Pdx - W|/W \leq 0.01$.

The number of mesh points selected for the analysis is based on a simple convergence study tabulated in table 2.1 and 2.2. The percentage of deviation acceptable for the peak pressure and minimum fractional film content is at most 5%. The numerical model - Modified Elrod proposed here is summarised in a representative flow-chart (see figure 2.5). The chart describes briefly the procedure required to execute the numerical model.

Table 2.1: Grid size convergence based on peak pressure

No. of Grid Points	**Peak Pressure** (MPa)	**% Deviation**
100	5.4288	-
200	**5.6278**	**3.67**
300	5.7278	1.78
400	5.7846	0.99

Table 2.2: Grid size convergence based on minimum fractional film content

No. of Grid Points	**Minimum Fractional Film Content,** $\theta(-)$	**% Deviation**
100	0.9347	-
200	**0.9273**	**0.79**
300	0.9240	0.36
400	0.9232	0.08

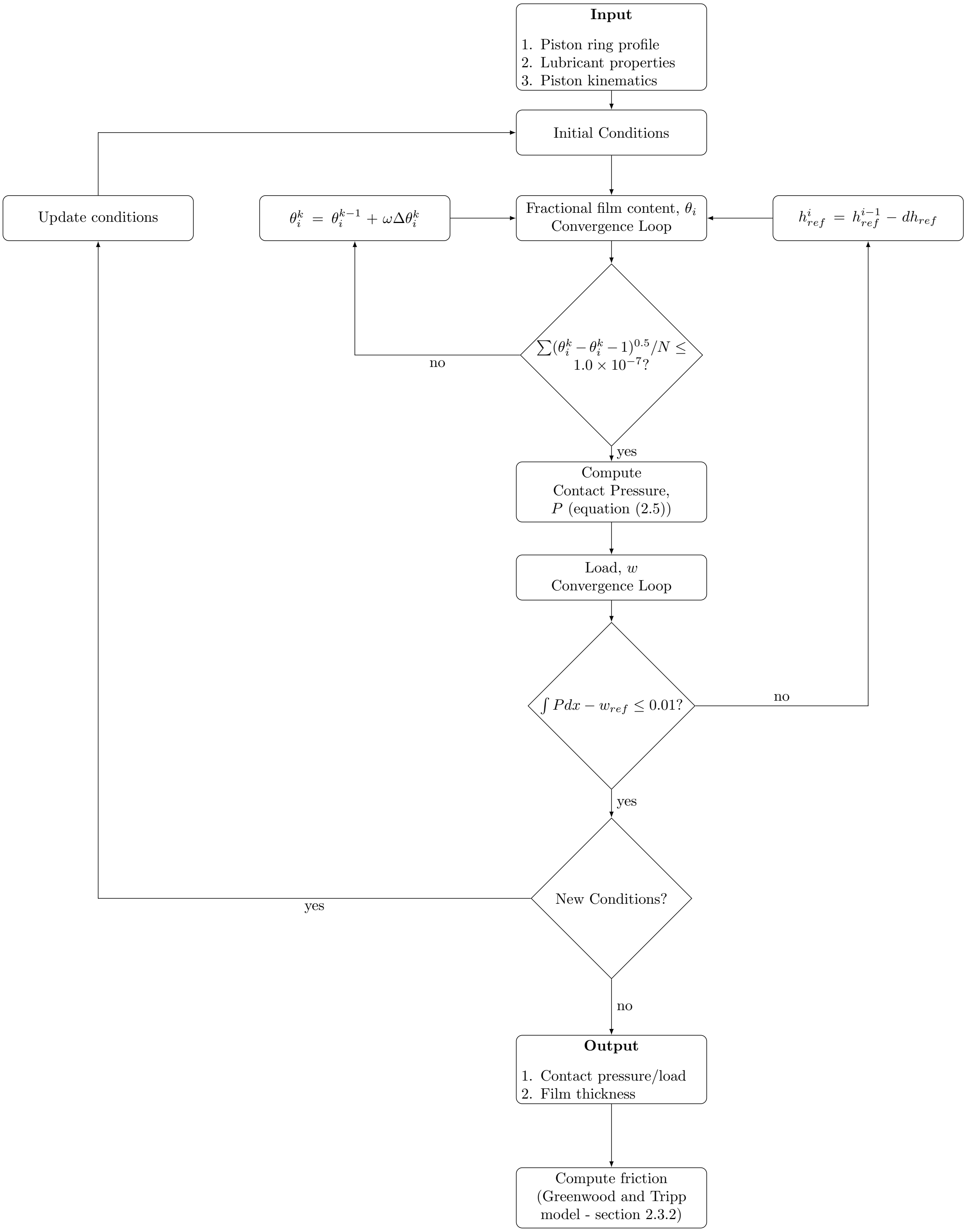

Figure 2.5: Flow chart - Modified Elrod for the piston ring lubrication analysis

2.4 Results and Discussion

The combustion pressure has a significant contribution to the contact load along the ring-liner conjunction. However, predicting the pressure distribution during engine cycle, requires a full analysis of all in-cylinder chemical phenomena. This is beyond the scope of the current investigation. Therefore, the combustion pressure measured by Mishra *et al* [47] at the engine speed simulated in the chapter was considered as an input.

During engine operation, the ring-liner contact pressure is assumed to be equal to the sum of the ring tension and the pressure acting behind the ring [47] (see figure 2.4). While the ring tension is an intrinsic characteristic of the ring, the pressure applied behind the ring is a function of the the combustion pressure and blow-by. Heywood [41] predicts that the pressure acting behind the top ring is roughly the same as the cylinder pressure.

Therefore, the forces per unit ring length acting on the top ring can be computed as:

$$W = (\sigma_r + p_1) \times L \tag{2.21}$$

Figure 2.6(a) and (b) show the measured combustion pressure [47] and the piston ring-liner contact load for one engine cycle at 2000 r*rev/min*.

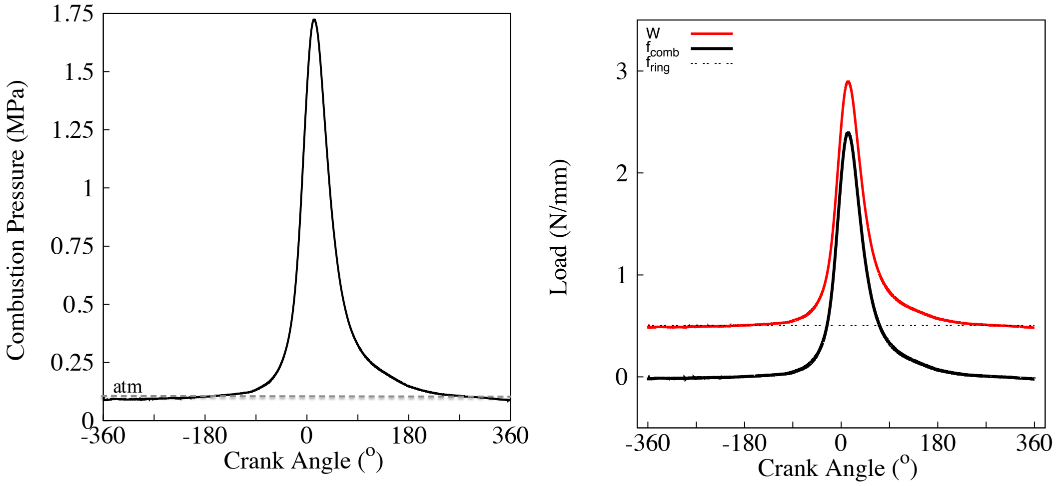

(a) Combustion pressure at 2000 rev/min [47] (b) Ring-liner contact load at 2000 rev/min

Figure 2.6: Combustion pressure and ring-liner loading conditions

The current analysis uses a generic set of values for piston-ring geometry and lubricant properties [27] (see Table 2.3-2.5). These input data are representative for modern gasoline IC engines. Therefore, the predictions could be easily verified with published results (e.g. Jeng [27], Yang and Keith [35] and Sawicky and Yu [37]).

Table 2.3: Lubricant properties (*SAE5W30*@120°C) [35]

Parameters	**Values**
η_0	0.00689 $Pa.s$
β	1.72 GPa
ρ_o	0.87 kg/m^3
α_o	$1.4 \times 10^{-8} Pa^{-1}$

Table 2.4: Piston ring geometrical parameters [27]

Parameters	**Values**
Crown Height, c	14.9 μm
Crank Radius, R	0.040 m
Connecting Rod Length, ℓ	0.1419 m
Bore Diameter	0.0889 m
Engine Speed, N	2000 rev/min
Ring Tension, σ_r	0.341 MPa
Blow-by	25 %
Cavitation Pressure, p_c	0.02 MPa (Absolute Pressure)

Table 2.5: Friction model parameters [27]

Parameters	**Values**
σ	0.37 μm
m	0.08
τ_o	2.0 MPa
γ	0.08
$\zeta\beta_a\sigma$	0.055
σ/β_a	0.001

Figure 2.7(b) shows piston sliding velocity assuming that the engine operates at 2000 *rev/min*. The sliding velocity of the piston is computed as:

$$u = R\omega\left[\sin\theta + \frac{R}{2\ell}\sin 2\theta\right] \tag{2.22}$$

Five representative operating conditions were selected: A, B, C, D and E. While A, B and C are in the mid-span of the stroke and have a significant entrainment velocity, D and E represents the vicinity of the power stroke TDC and suction stroke BDC respectively. At locations D and E, the entrainment velocity is small while the motion reverses its direction after reaching the dead centers.

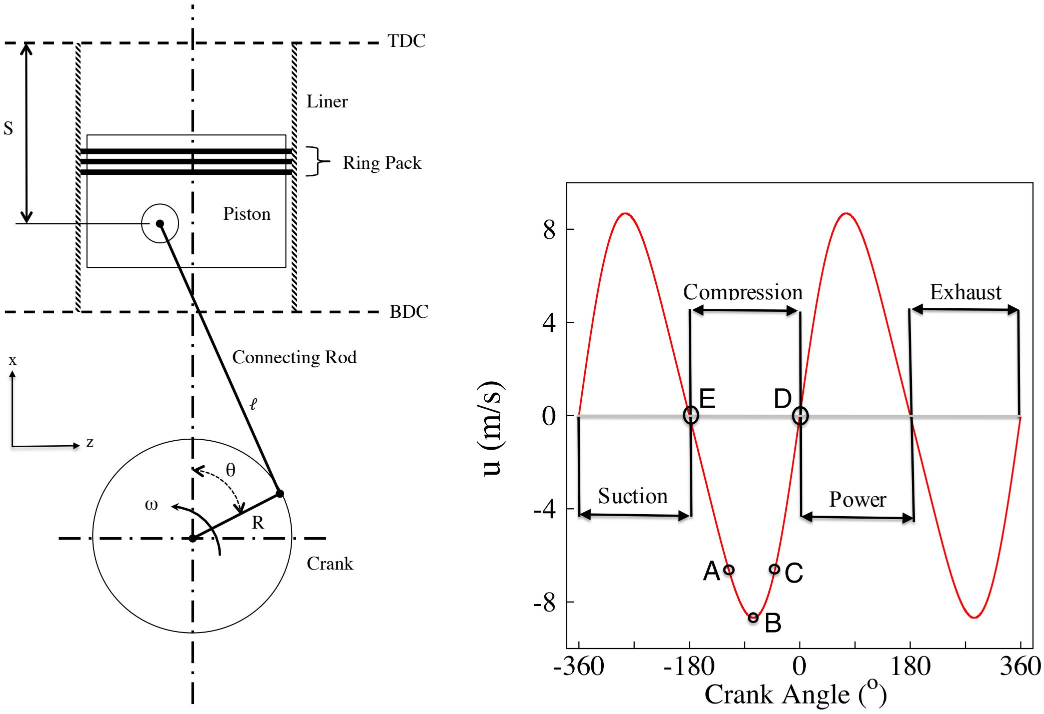

(a) Piston-crank schematics

(b) Sliding velocity

Figure 2.7: Kinematics of the piston ring relative to the bore at 2000 rev/min

Figure 2.8 shows the pressure distribution along the contact for operating conditions (A, B and C). Three algorithms are compared: (i) transient Reynolds, (ii) steady-state modified Elrod and (iii) transient modified Elrod. While, both versions of the modified Elrod predict significant cavitation regions, there are notable differences. Firstly, the location of the cavitation onset is different. Steady-state modified Elrod does not consider film history, and therefore, cavitation history. This underestimates the extent of the cavitation region. Additionally, the lubricant reformation is heavily dependent on the squeeze film effect. When this is significant, the lubricant reforms earlier (C).

Secondly, in all cases the lubricating film predicted is thinner for the transient modified Elrod. Initially this could seem an unexpected result. However, it is due to the extent of the cavitation region, which is underestimated by the steady-state algorithm. Using similar engine parameters, the minimum film thicknesses predicted by other authors are very close to the predictions of the current model: Jeng [27] (Transient Reynolds boundary conditions), Yang and Keith [35] (steady-state modified Elrod using Vijayaraghavan and Keith method [29]) and Sawicky and Yu [37] (steady-state modified Elrod using JFO boundary conditions).

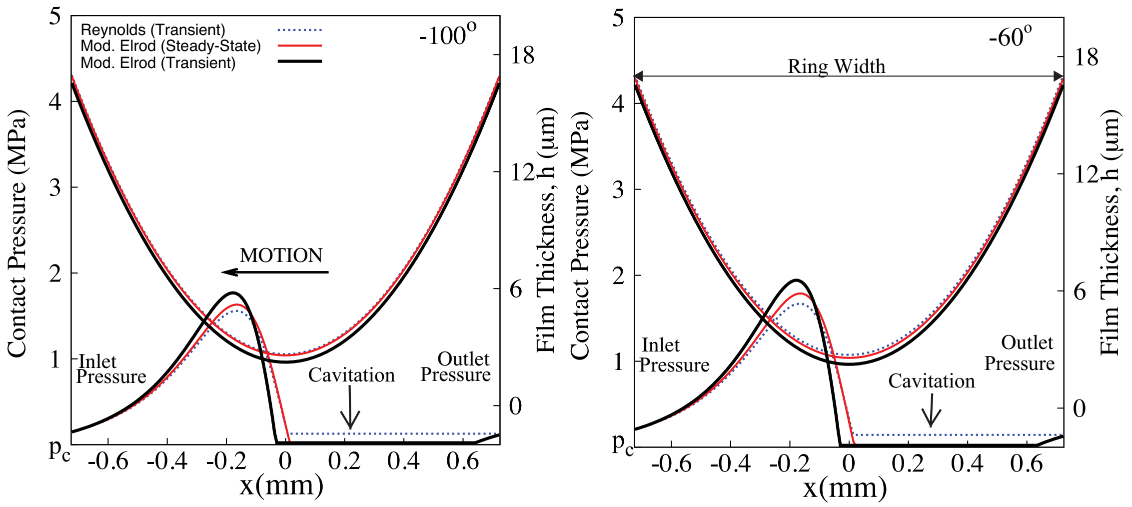

(a) Pressure distribution for *A* (b) Pressure distribution for *B*

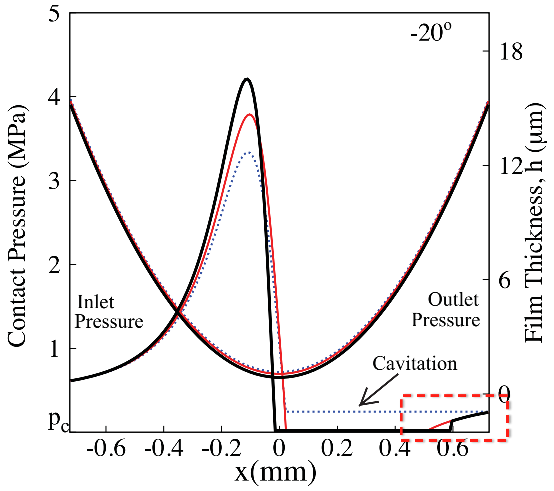

(c) Pressure distribution for *C*

Figure 2.8: Predicted top ring contact pressure at three crank angles comparing different solution method (see figure 2.7)

There is a direct correlation between film thickness and friction force magnitude. Therefore, it is particularly interesting to investigate the regions where the film is very thin. Figure 2.9 (b) and (c) expand the regions delimited in figure 2.9 (a). These correspond to the power stroke TDC and suction stroke BDC. The entrainment velocity is very small and the squeeze film is the only mechanism protecting the lubricant film. Consequently, while the steady-state algorithm inaccurately predicts a complete collapse of the film during reversal, for both transient algorithms there is a small delay between the inlet reversal and the minimum film thickness. Both transient algorithms predict a thinner film at the power TDC than at the suction

BDC, however, the difference is less significant for the transient modified Elrod. Higher contact loads at power TDC promote higher contact pressures, and therefore, smaller cavitation region.

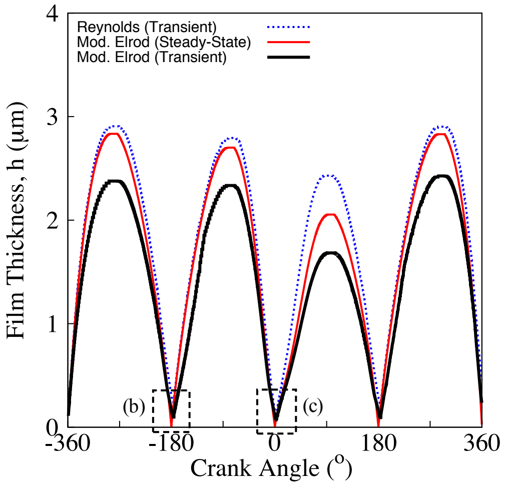

(a) Film thickness for onet engine cycle

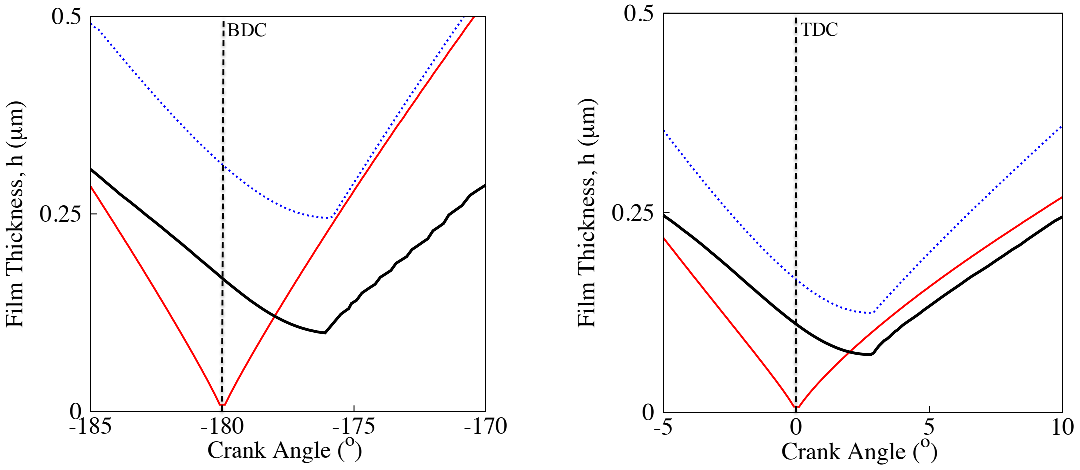

(b) Film thickness in the vicinity of the suction stroke BDC

(c) Film thickness in the vicinity of the power stroke TDC

Figure 2.9: Top ring - minimum film thickness comparison for three solution methods (2000 rev/min)

Figure 2.10 shows the lubricant film pressure distribution in the vicinity of the power stroke TDC (see figure 2.9 (c)). During piston slow down ($-10^{\circ} \rightarrow -0.1^{\circ}$) the pressure distribution for the steady-state prediction progressively deviates from the transient ones. Because this algorithm does not consider squeeze film, for vanishingly small films the pressure prediction is unrealistically high. Experimentally it was noted that for a ring-liner conjunction a limited cavitation region does survive through the dead centre inlet reversal [24, 25]. The current model predicts that immediately after inlet reversal, the “pre-reversal” cavitation region (suddenly located at the inlet) is sealed off by the lubricant film and forms a bubble (+0.1°). This bubble quickly implodes when the entrainment velocity picks up (e.g. +5° → +10°). However, while located at the inlet, it depletes the available lubricant and leads to starvation ($\theta < 1$). Consequently, the lubricant pressure increases and the film thickness decreases, with significant consequences over engine operation. Thinner films can lead to metal-to-metal interaction, which can lead to higher friction forces and increased wear. The pressure distribution and the film thickness predicted by the transient Reynolds and steady-state modified Elrod algorithms are similar with the predictions of Yang and Keith [35].

Figure 2.11. shows the fractional film content in the vicinity of the power stroke TDC. While both Elrod-based algorithms predict similar cavitation onset, the steady-state algorithm cannot predict the severity of the lubricant drainage. Figure 2.12 shows the lubricant pressure and figure 2.13 the fractional film content during BDC reversal. The pre-reversal cavitation survives through the reversal. However, due to lower contact pressure, the pre-reversal cavitation is larger. Therefore, the resulting bubble takes much longer to be fully absorbed into the oil film. It should be noted that although the full film region is smaller at the BDC reversal, lower contact pressures lead to thicker films.

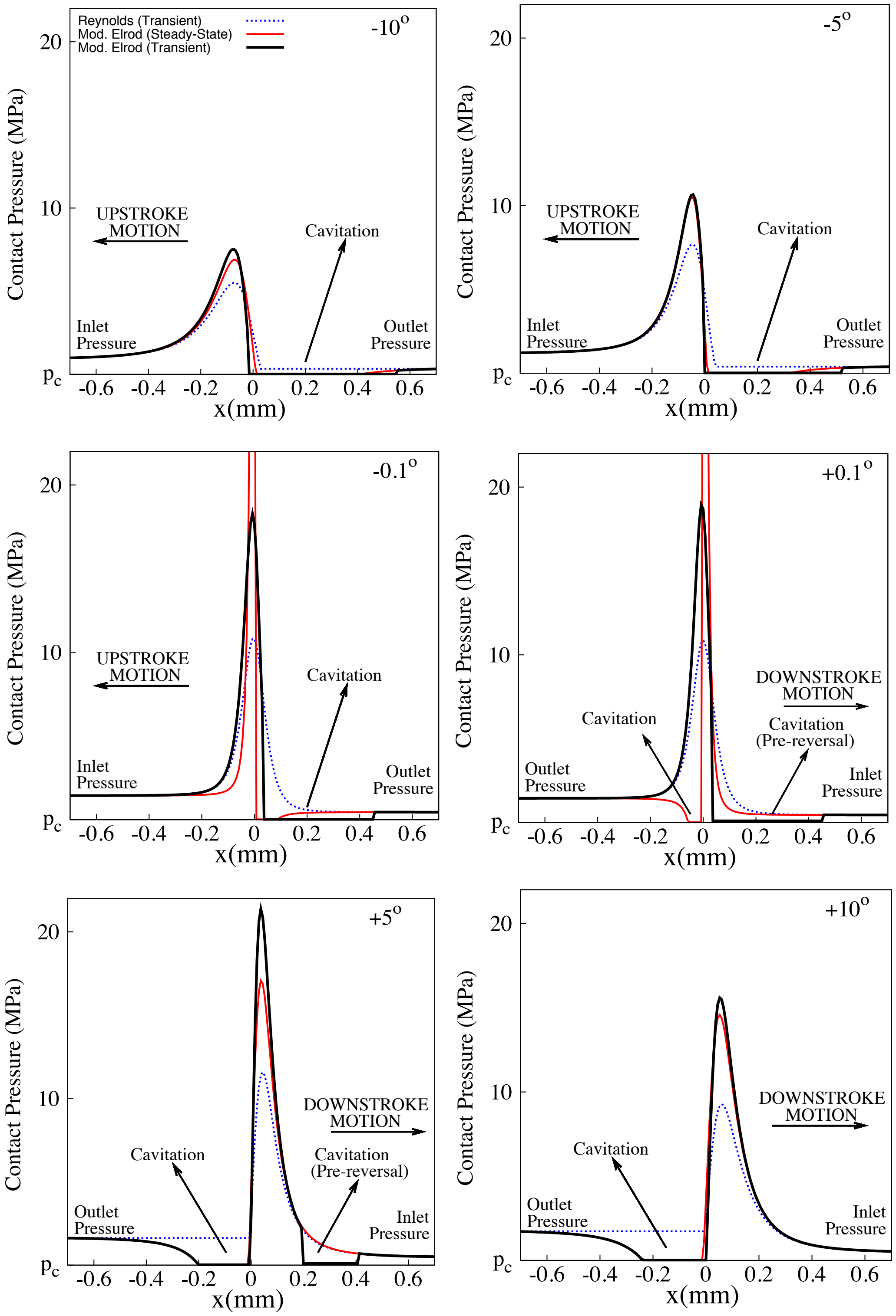

Figure 2.10: Top ring - pressure distribution in the vicinity of the power stroke TDC at different crank angles (2000 rev/min)

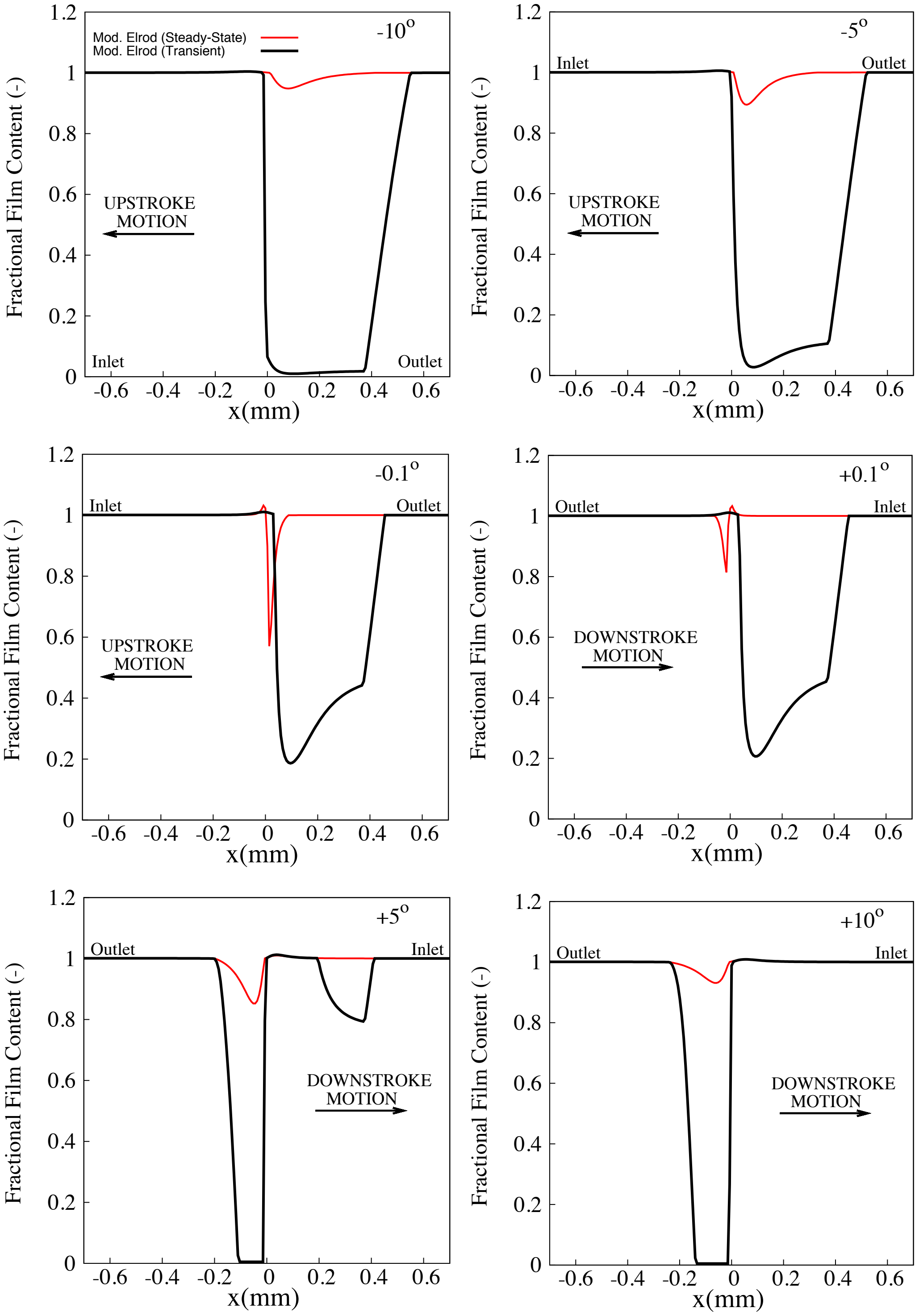

Figure 2.11: Top ring - fractional film content in the vicinity of the power stroke TDC at different crank angles (2000 rev/min)

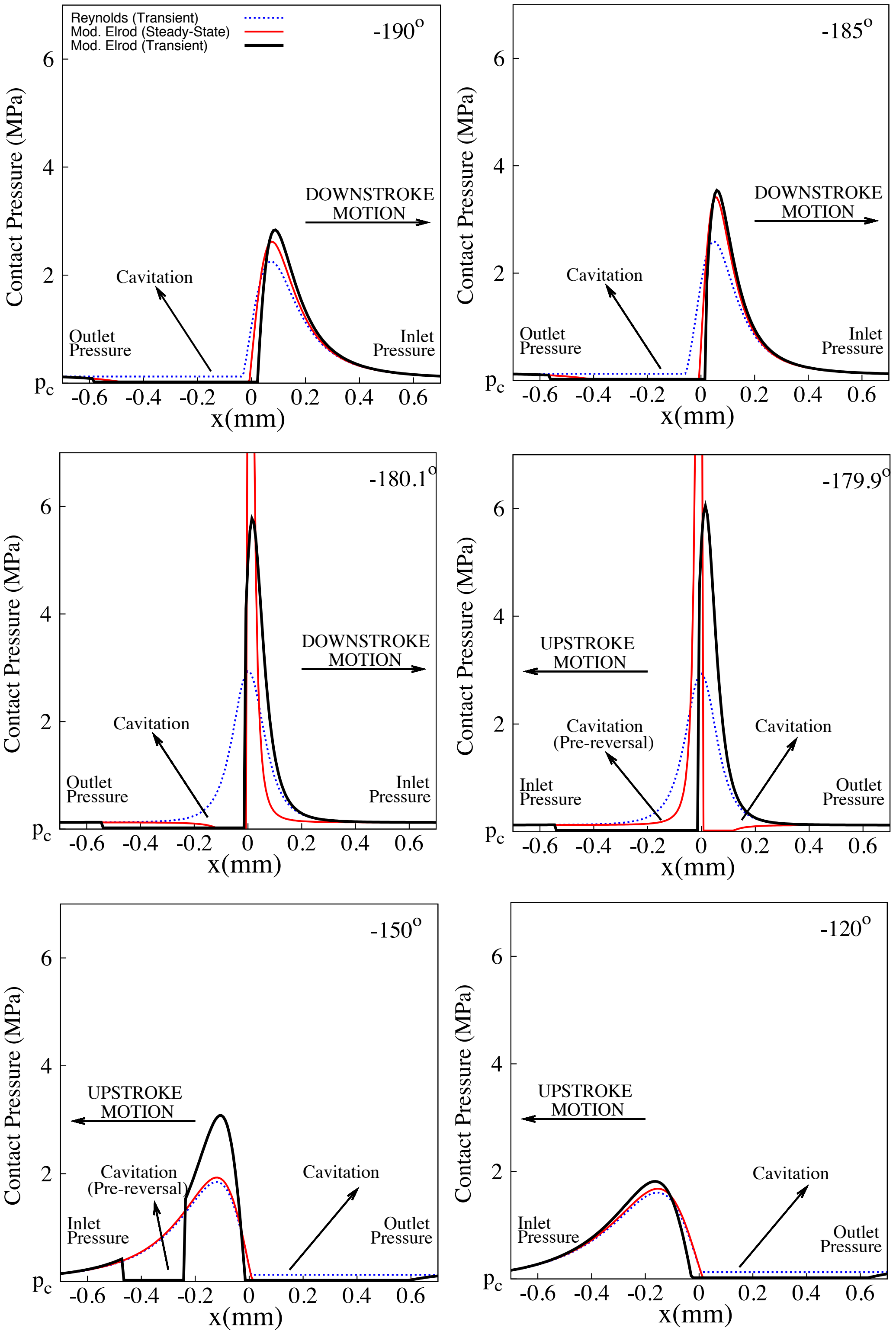

Figure 2.12: Top ring - pressure distribution in the vicinity of the suction stroke BDC at different crank angles (2000 rev/min)

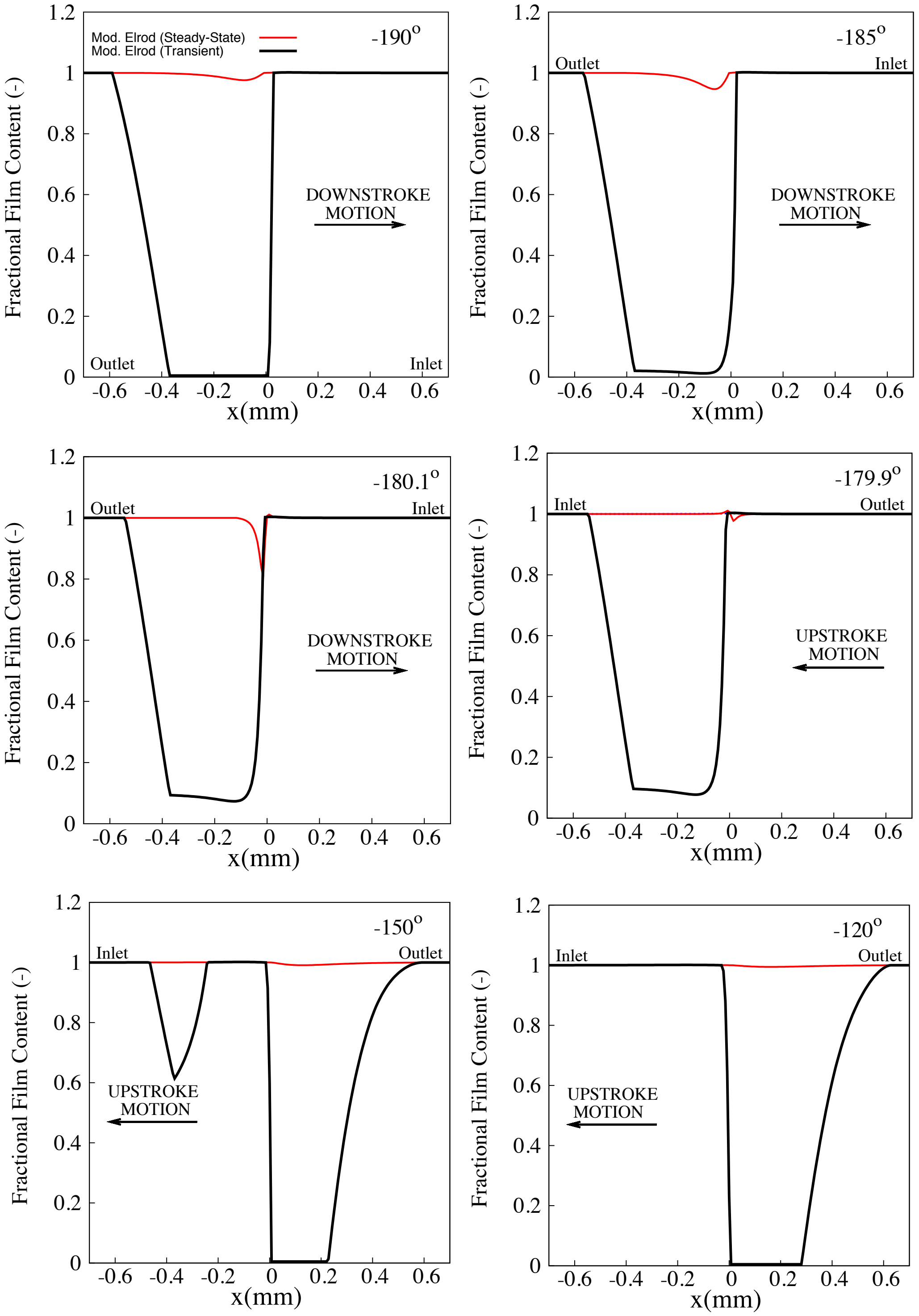

Figure 2.13: Top ring - fractional film content in the vicinity of the suction stroke BDC at different crank angles (2000 rev/min)

The pressure distribution (bold lines) and the squeeze film (thin line) in the vicinity of reversal points are shown in figure 2.14 . It was shown (see figure 2.9(b) and (c)) that due to an extensive cavitation region, the modified Elrod algorithm predicts a thinner oil film than Reynolds one does. Figure 2.14 shows that the absolute value of the squeeze term $|dh/dt|$ predicted by the transient Reynolds algorithm is larger than the one predicted by the modified Elrod algorithm. Therefore the thinner film predicted by the modified Elrod algorithm is attributed to the lack of support from the squeeze film term.

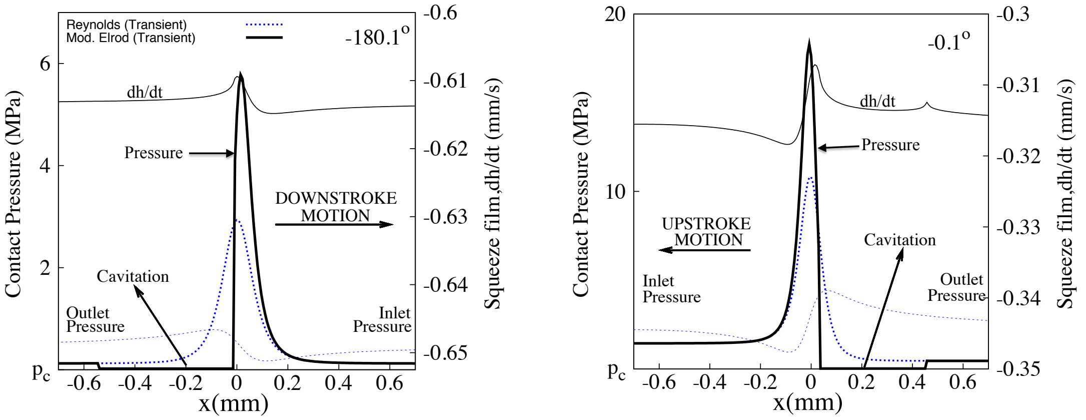

(a) Suction stroke BDC (−180.1°) (b) Power stroke TDC (−0.1°)

Figure 2.14: Top ring - pressure and squeeze film distribution at different crank angles (2000 rev/min)

One of the most important consequences of the decreased film thickness is an increased friction force. In the current analysis, the friction force is predicted using the model described in section (2.3.2). Figure 2.15 shows the viscous and boundary components of the friction force. The boundary friction force is very high in the vicinity of TDC and BDC where the distance between the ring and the liner is minimal and asperity interaction is very likely. The viscous friction force, however, is maximum in mid-span where the entrainment velocity is high and contact load is low. Additionally, transient Reynolds, which always predicts a full film, predicts a higher viscous friction than modified Elrod algorithms.

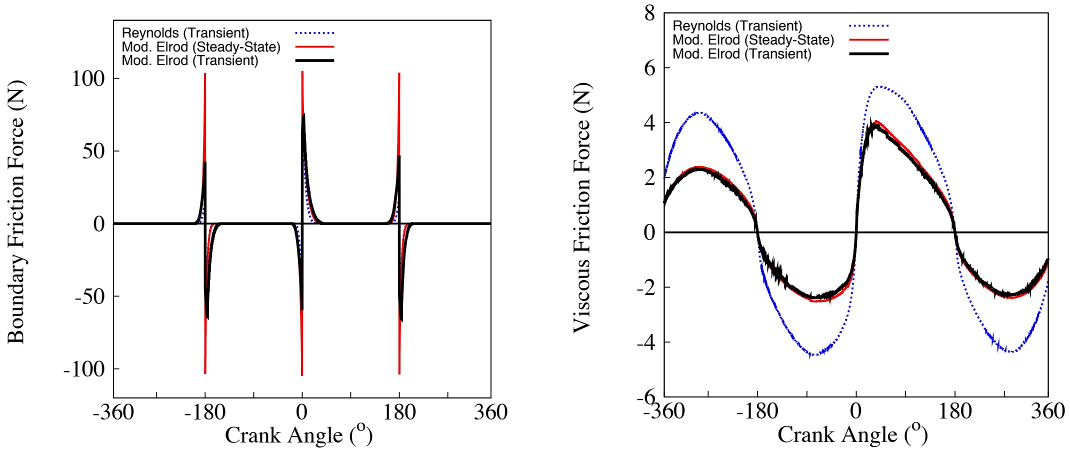

(a) Boundary friction force (b) Viscous friction force

Figure 2.15: Top ring - boundary and viscous friction forces for the engine running at 2000 rev/min

Figure 2.16 (a) shows the total friction force. As a direct result of an excessively thin film thickness around the dead centers the boundary friction force is overwhelmingly higher than the viscous friction force. This is expected for heavily loaded modern engines. Since the boundary component is the result of direct asperity interaction, very high values of the boundary friction force could lead to wear. Figure 2.16 (b) and (c) show details of the friction force at suction BDC and power TDC. In both cases due to thinner lubricant films, transient modified Elrod predicts highest friction force. The magnitude and trend of the friction force predicted by the transient Reynolds solution in the vicinity of the reversals is comparable with the predictions of Jeng's [27], which increases the level of confidence towards the numerical model.

Therefore, an effective method of decreasing total engine friction is reducing the boundary friction force near dead centres. These would be automatically achieved by increasing the film thickness. However, such a solution is not always possible and often not even desirable because a thicker oil trail can react with hot combustion gases much faster. One possible solution, which is beyond the scope of the current paper, is to locally modify the surface texture in the regions with high boundary friction. Such custom made topography (applied on the ring [53] or on the liner [54]) can decrease boundary friction without increasing oil consumption.

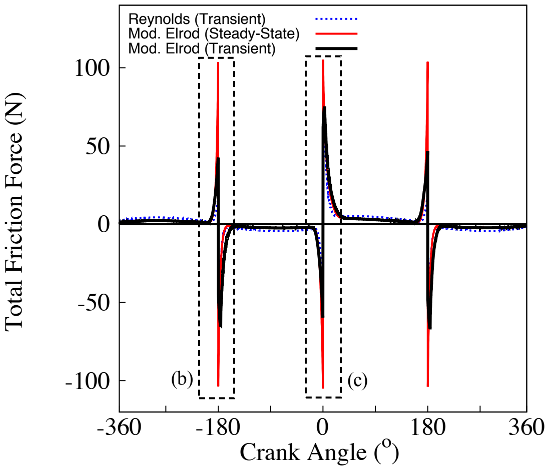

(a) Top ring - total friction force for the entire engine cycle

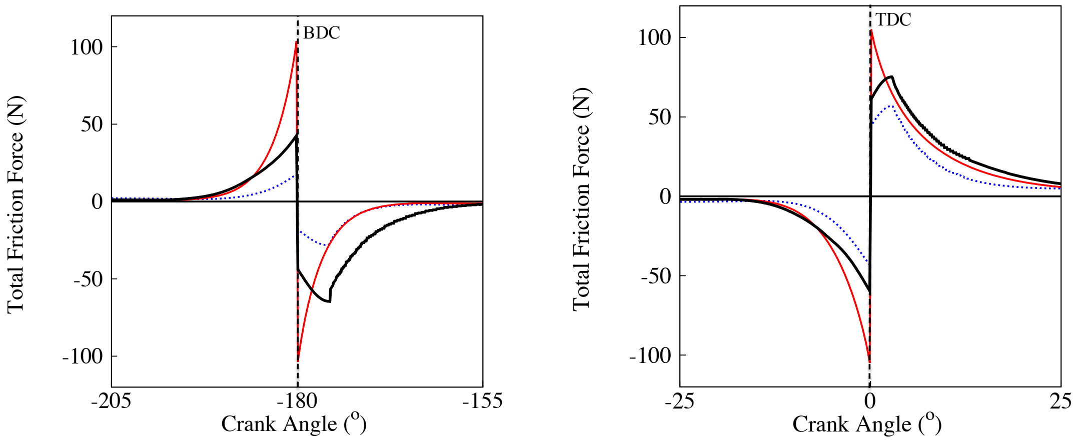

(b) Top ring - total friction force in the vicinity of the suction stroke BDC

(c) Top ring - total friction force in the vicinity of the power stroke TDC

Figure 2.16: Top ring - total friction force at 2000 rev/min

Figure 2.17 (a) shows the friction coefficient during engine operation ($\mu_f = f_f/W$). Although this is often used to characterize ring-liner friction, it could be deceiving (e.g. due to high contact forces, the friction coefficient is lower in the vicinity of the power TDC).

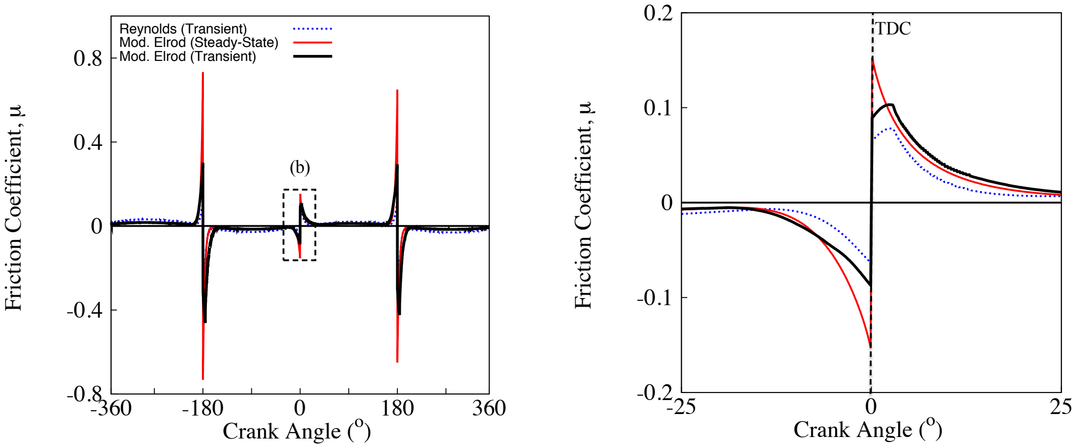

(a) Top ring - friction coefficient for the entire engine cycle

(b) Top ring - friction coefficient in the vicinity of the power stroke TDC

Figure 2.17: Top ring - friction coefficient at 2000 rev/min

Figure 2.18 shows the lubricant thickness for three engine speeds. This increases with engine speed during the entire engine cycle, including in the vicinity of the dead centers where the the boundary component of the friction force is very high. Consequently, the total friction force drops (see figure 2.19).

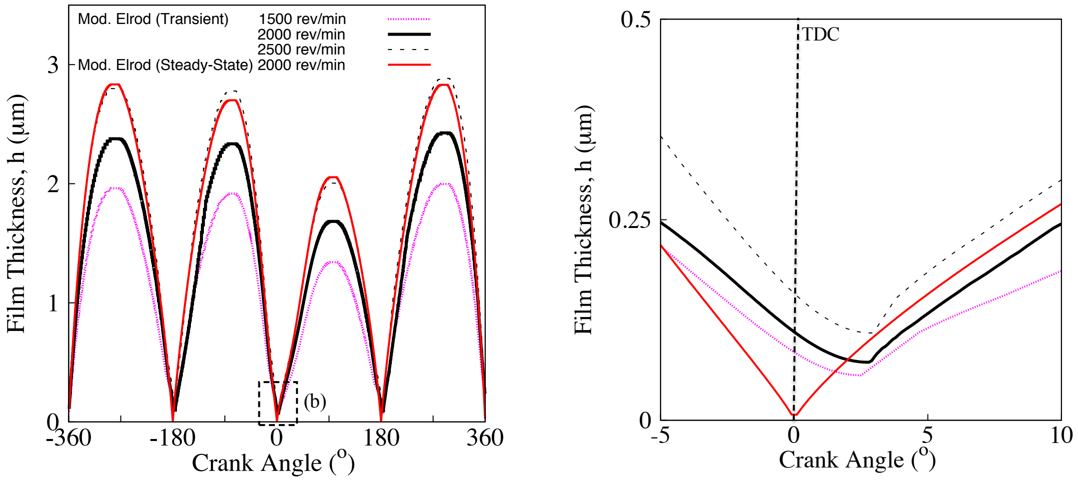

(a) Top ring - minimum film thickness for the entire engine cycle

(b) Top ring - minimum film thickness in the vicinity of the power stroke TDC

Figure 2.18: Top ring - minimum film thickness for three engine speeds

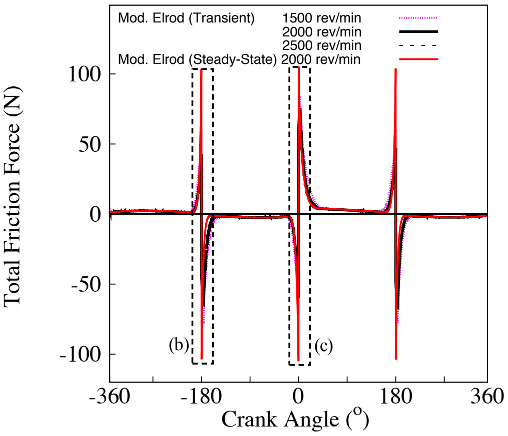

(a) Top ring - total friction force for the entire engine cycle

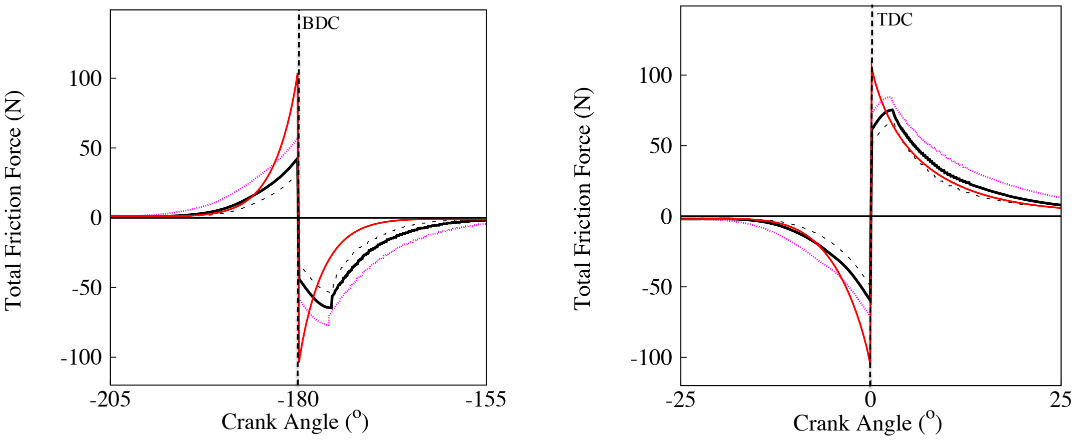

(b) Top ring -total friction force in the vicinity of the suction stroke BDC

(c) Top ring - total friction force in the vicinity of the power stroke TDC

Figure 2.19: Top ring - total friction force for three engine speeds

Figure 2.20 (a) shows the length of the cavitation region for one engine cycle. While the piston approaches the dead centre, the cavitation progressively shrinks, however, it does not fully vanish (see figure 2.20 (b)). The “pre-reversal” cavitation is sealed off by the lubricant and forms a bubble at the inlet. Although this is gradually absorbed by the lubricant film (see figure 2.21), before it fully vanishes, the inlet is starved ($\theta < 1$ and $g = 0$ in equation (2.5)). This leads to thinner films of lubricant, and consequently, higher boundary friction. However, it should also be noted that steady state modified Elrod does not predict a cavitation region in vicinity of the dead centres (see figures 2.10 and 2.12). Therefore, the predicted film is thicker, and consequently, the friction force is seriously underestimated (see figure 2.19).

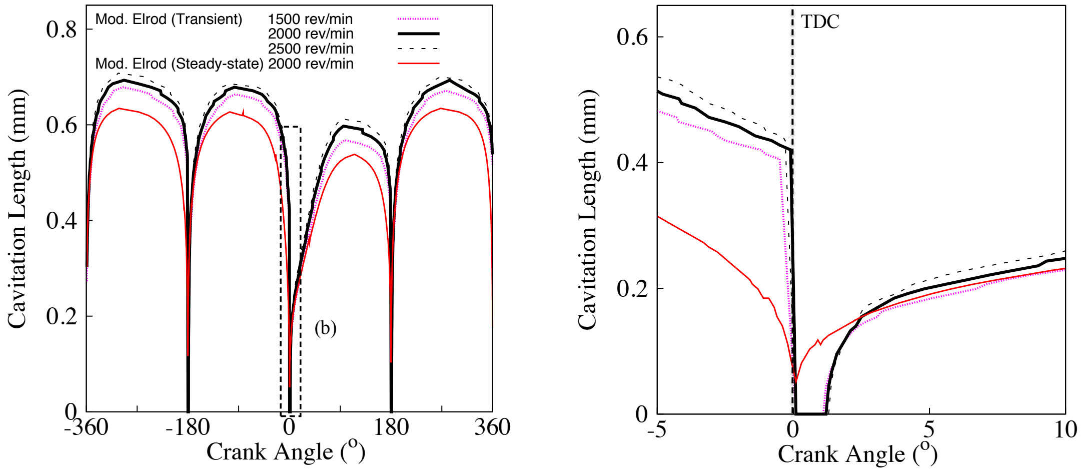

(a) Top ring - cavitation length for one engine cycle

(b) Top ring - cavitation length in the vicinity of the power stroke TDC

Figure 2.20: Top ring - cavitation length at different engine speeds

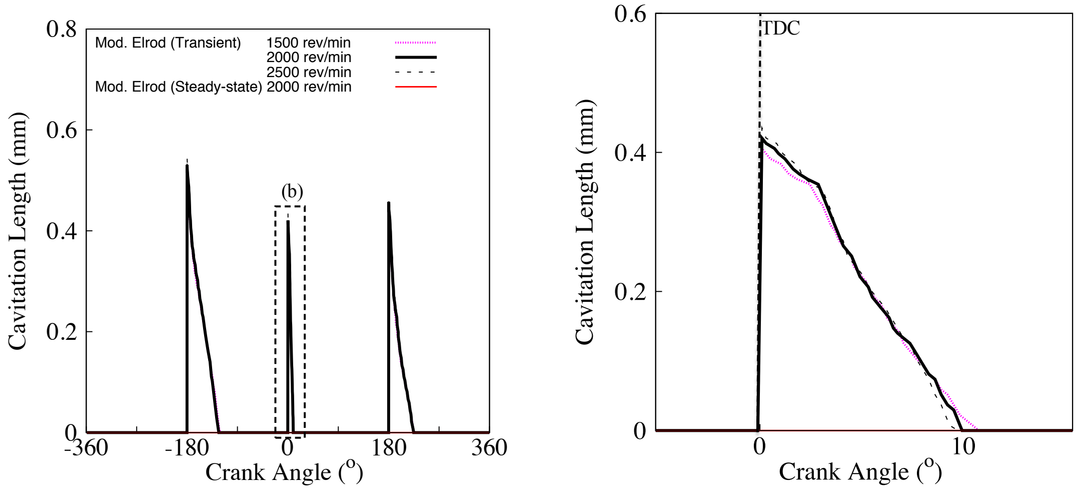

(a) Top ring - length of the inlet bubble for one engine cycle

(b) Top ring - length of the cavitation in the vicinity of the power stroke TDC

Figure 2.21: Top ring - length of the inlet bubble formed by the pre-reversal cavitation

2.5 Summary

This chapter proposes a numerical model to predict the film formation for the piston ring-liner. The model has at the base the approach proposed by Vijayaraghavan and Keith [29] for Elrod's cavitation algorithm. The transient nature of the piston ring lubrication is being investigated. The model predicted a "pre-reversal" cavitation, which was shown to deplete the lubrication film, increasing the friction along the reversal region.

Chapter 3

Effect of Combustion Chamber Blow-by on Piston Ring-Liner Tribology

3.1 Introduction

During the power stroke, the combustion pressure is significantly higher than the crankcase pressure, while during the suction stroke, the pressure in the combustion chamber drops below the crankcase pressure. The piston rings do not provide a perfect sealing between the two chambers, allowing gas exchange through a series of micro-scale crevices [41]. This affects engine performance and exhaust emissions [42, 43]. Heywood [41] described that the largest crevice in an engine is between the piston, piston rings and cylinder liner. The upper section of the top compression ring and the head land of the piston are exposed to the combustion chamber. It is invariably being assumed in lubrication analysis that the pressure on the upper surface and head land is equal to the combustion chamber pressure [8, 41]. The pressure within the top and second ring region is heavily influenced by the sealing efficiency of the the top ring. This produces a pressure difference between the upper section and the lower section of the top ring, which plays a significant role in the piston ring-liner lubrication. The sealing capability of the ring depends not only on the ring tension, but also on the engine speed and load [55]. Higher engine speeds combined with lower engine load often produce a higher blow-by (lower sealing efficiency) due to the top ring's tendency to flutter [55].

Blow-by can be predicted once the pressure difference between the upper section and the lower section of the top ring is known. The gas flow along the piston ring pack is similar to the labyrinth seal [8, 56]. Therefore, Eweis [56] proposed an orifice and volume method to predict the inter-ring pressures which was being further improved by Ting *et al.* [57, 58]. The method assumes that gas can only flow through the ring end gaps. Ruddy *et al* [59] extended the model by considering cyclic variation of temperature in the combustion chamber, gas volume trapped within the ring grooves and also the ring pack dynamics. Kuo *et al.* [60], Yang [44], Mufti *et al* [61] and most recently Aghdam *et al.* [43] applied the orifice and volume method to predict the inter-ring pressures for the entire piston ring pack.

3.2 Inter ring pressure

A simple blow-by model is used to predict the effect of blow-by on the lubrication conditions of the ring-liner conjunction. The model is based on the volume and orifice theory [8, 43, 44]. Figure 3.1 shows the gas flow direction and notation used in the model. The gas in the crevice volumes is assumed to obey the ideal gas law.

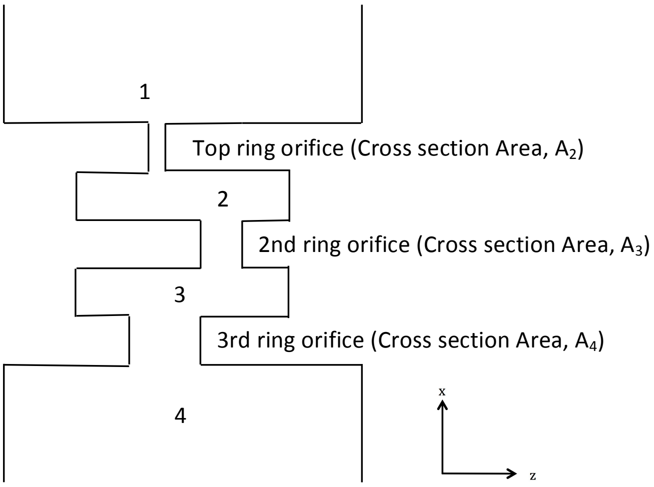

Figure 3.1: Orifice-Volume model with orifice cross section and inter ring crevice volumes in Table 3.1

Therefore, the mass flow rate for the combustion gas flowing through the ring end gaps can be expressed as:

$$\frac{dm_{i,i+1}}{dt} = C_d A \left[\frac{2\gamma_i}{(\gamma_i - 1)R_{gas}T_i}\right]^{\frac{1}{2}} p_i \times \left(\frac{p_{i+1}}{p_i}\right)^{\frac{1}{\gamma_i}} \left[1 - \left(\frac{p_{i+1}}{p_i}\right)^{\frac{\gamma_i - 1}{\gamma_i}}\right] \quad (3.1)$$

where

$(i, i+1)$ = Flow from location i to $i+1$
c_d = Discharge coefficient ($c_d = 0.65$) [43]
γ = Specific heat gas ratio ($\gamma = 1.3$)

The rate of pressure change for the combustion gas flowing through the orifices formed by ring end gaps can be obtained using:

$$\frac{dp_{i+1}}{dt} = \frac{R_{gas}T_{i+1}}{V_{i+1}}.\left(\frac{dm_{i,i+1}}{dt} - \frac{dm_{i+1,i+2}}{dt}\right) \quad (3.2)$$

Therefore, the inter-ring pressure at each crank angle, n for the whole engine cycle can be computed as [44]:

$$(p_i)_{n+dn} = (p_i)_n + \frac{dt}{2}\left[\left(\frac{dp_i}{dt}\right)_n + \left(\frac{dp_i}{dt}\right)_{n+dn}\right] \quad (3.3)$$

where dn is the crank angle increment. Figure 3.2 shows the inter ring pressures predicted for the Honda 450 CRF engine running at 7500 *rev/min*. The pressures are computed using the crevice geometries included in table 3.1. It can be observed that due to the flow of the blow-by gas, the inter ring pressure between the top and the second ring is higher than the top ring land pressure after about 75^o crank angle (see figure 3.2(b)). Rather than using a scaled down actual pressure ($\approx 25\%$ of the combustion pressure), the predicted inter ring pressure between the top and second ring (2nd land) is used as the outlet pressure for the top ring in this chapter unless being stated otherwise.

Table 3.1: Blow-by model geometric parameters

Parameters	**Values**
Orifice cross section area, A_2	0.025 mm^2
Orifice cross section area, A_3	0.042 mm^2
Orifice cross section area, A_4	0.065 mm^2
Inter ring crevice volumes, V	108.69 mm^3
Temperature, T	120 ^oC

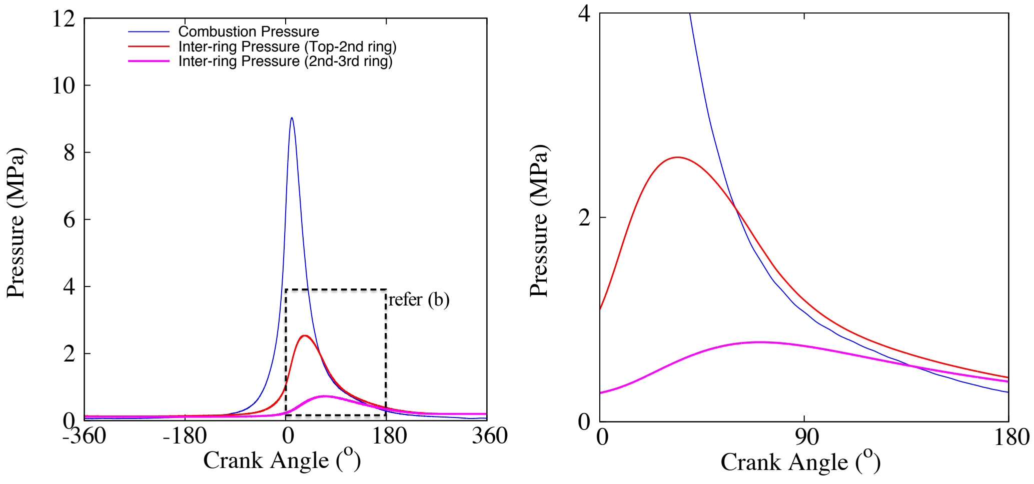

(a) Entire cycle

(b) Combustion stroke

Figure 3.2: Combustion and inter-ring pressures at 7500 rev/min - Wide Open Throttle

3.3 Numerical Analysis

Assuming an isothermal analysis, the current study focuses on the effect of blow-by on the cavitation formation at motion reversal points especially during the power stroke is investigated. The study also looks at the role played by the new and worn top ring profile in the piston ring-liner lubrication. Firstly, the piston sliding velocity is computed using the investigated engine's geometrical data (see table 4.1). For 7500 *rev/min*, the sliding velocity for the piston is shown in figure 3.3.

Table 3.2: Piston Ring Lubrication Reference Parameters [47]

Parameters	**Values**
Crank Radius, R	0.031 m
Connecting Rod Length, ℓ	0.1056 m
Bore Diameter	0.096 m
Engine Speed, N	7500 rev/min

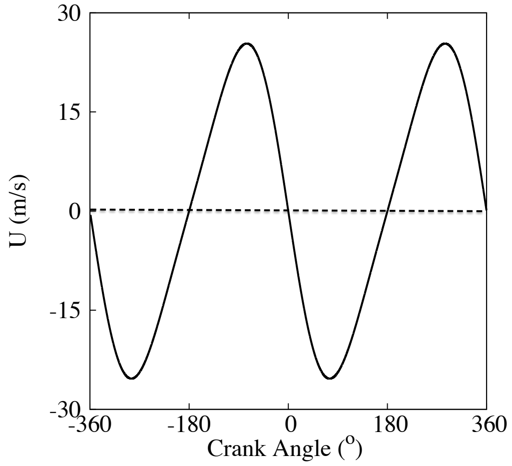

Figure 3.3: Piston sliding velocity at 7500 rev/min

The contact load for the top ring is computed in figure 3.4(a) using the combustion pressure measured at 7500 *rev/min*. The current approach uses measured profiles and predicted inter-ring pressures as the input to analyse the piston ring lubrication. The measured profiles for a new and worn top ring are curve-fitted as shown in figure 3.4(b). The approach is believed to be able to take the analysis a step closer to the actual physical problem.

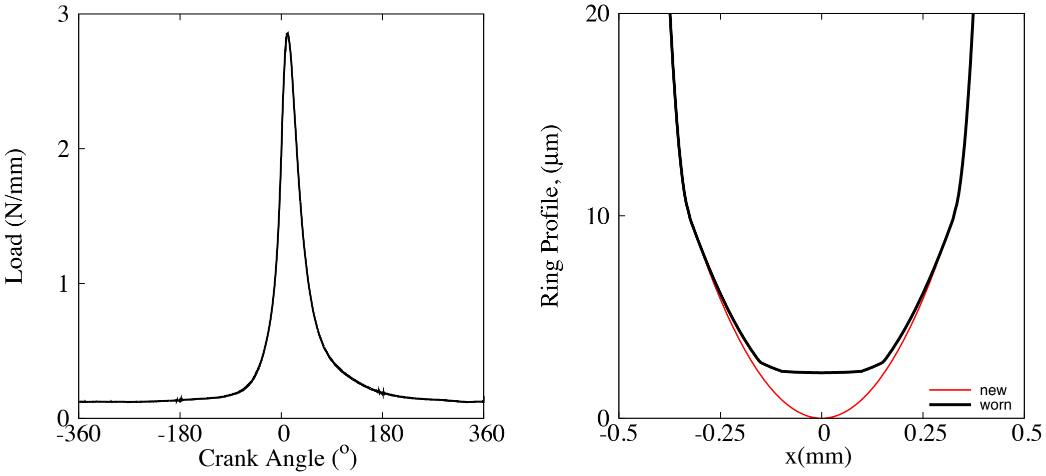

(a) Top ring load

(b) New and worn top ring profile

Figure 3.4: Top ring contact condition

The analysis of this chapter builds on from the modified Elrod model discussed earlier by implementing the engine data for the Honda 450 CRF engine. The lubricant properties used for the current numerical analysis are shown in table 3.3.

Table 3.3: Constants for Lubricant Properties

Parameters	**Values**
η_0	0.00828 $Pa.s$ at 120^o (Castrol SAE 10W-40)
β	1.72 GPa
ρ_o	0.87 kg/m^3
α_o	$1.4 \times 10^{-8} Pa^{-1}$
Cavitation Pressure, p_c	0.02 MPa (Absolute Pressure)

Using the modified Elrod's cavitation model, the pressure distributions for the new and worn top ring along the power stroke TDC are shown in figure 3.5. The pressure distribution of the top ring shows that a worn ring produces a lower pressure due to a more flattened profile. The worn ring's peak pressure seems to be more consistent as compared to the more dramatic change in pressure for the new ring. Figure 3.6 shows the fractional film content predicted using the modified Elrod's cavitation algorithm. Due to the flatter nature of the profile, the cavitation region ($\theta < 1.0$) for the worn ring seems to be less significant as compared to the new ring profile. A smaller pre-reversal cavitation region produced for the worn ring increases the recovery rate of the cavitation region.

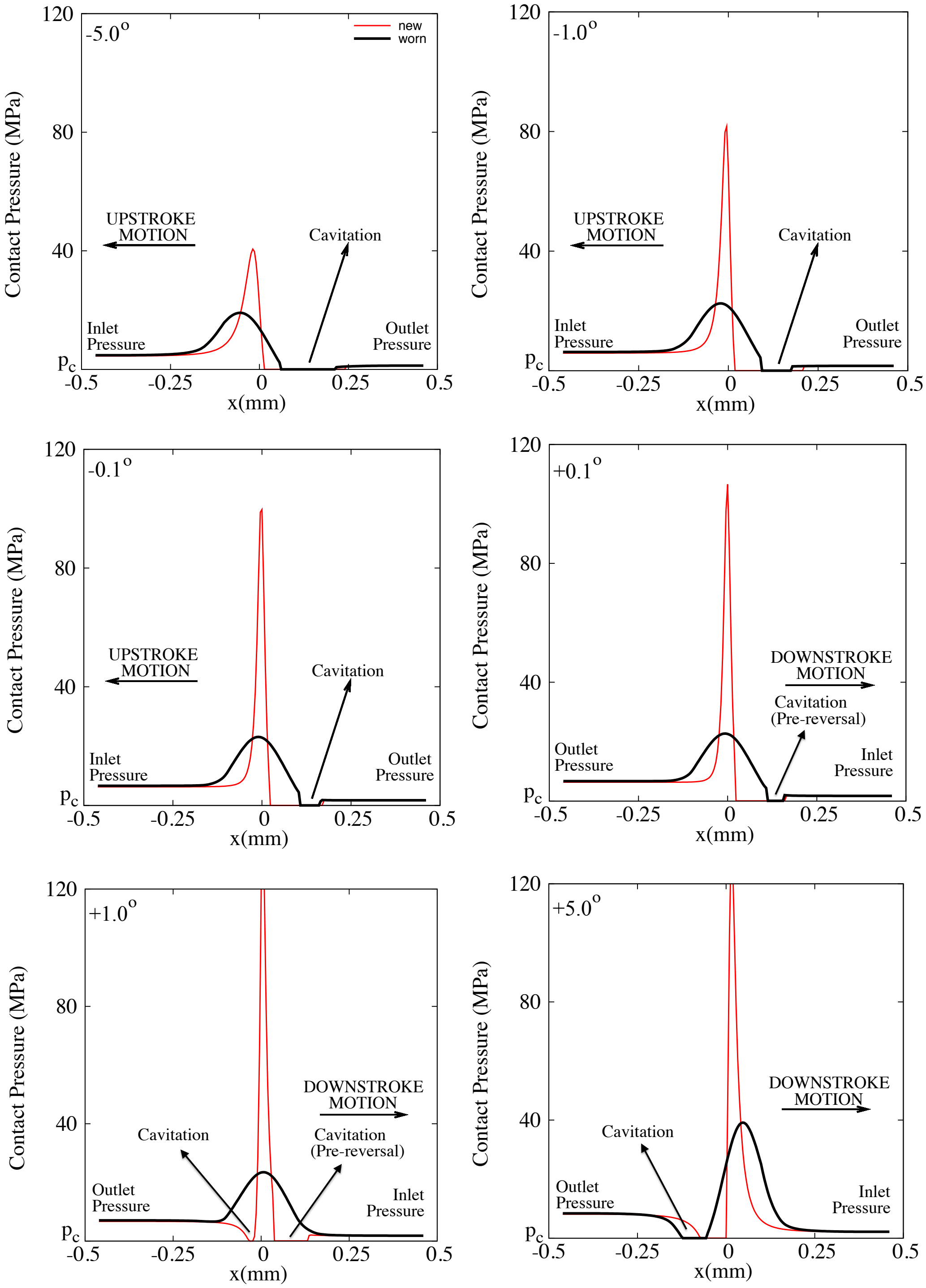

Figure 3.5: Top ring - transient analysis comparison around TDC firing event - Contact pressure at 7500 rev/min (Wide Open Throttle)

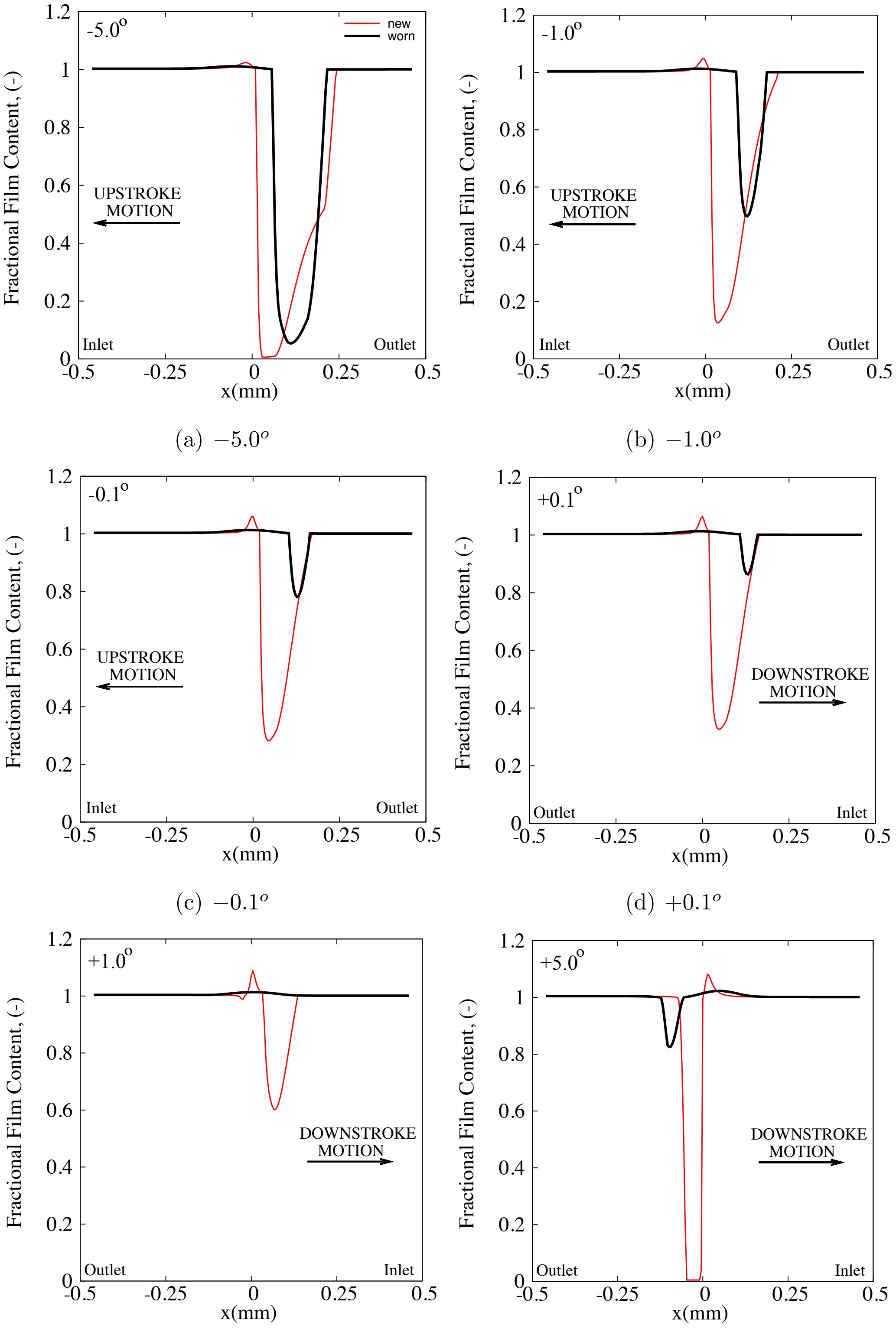

(a) -5.0^o

(b) -1.0^o

(c) -0.1^o

(d) $+0.1^o$

(e) $+1.0^o$

(f) $+5.0^o$

Figure 3.6: Top ring - transient analysis comparison around TDC firing event - Fractional film content at 7500 rev/min (Wide Open Throttle)

The minimum film thickness along the whole engine cycle for the new and worn top ring is shown in figure 3.7. The predicted minimum film thickness for the worn ring is larger than the new ring. A thicker lubricating film between the ring-liner conjunction will reduce the probability of asperity interactions which in turn will decrease the friction along the ring-liner contact.

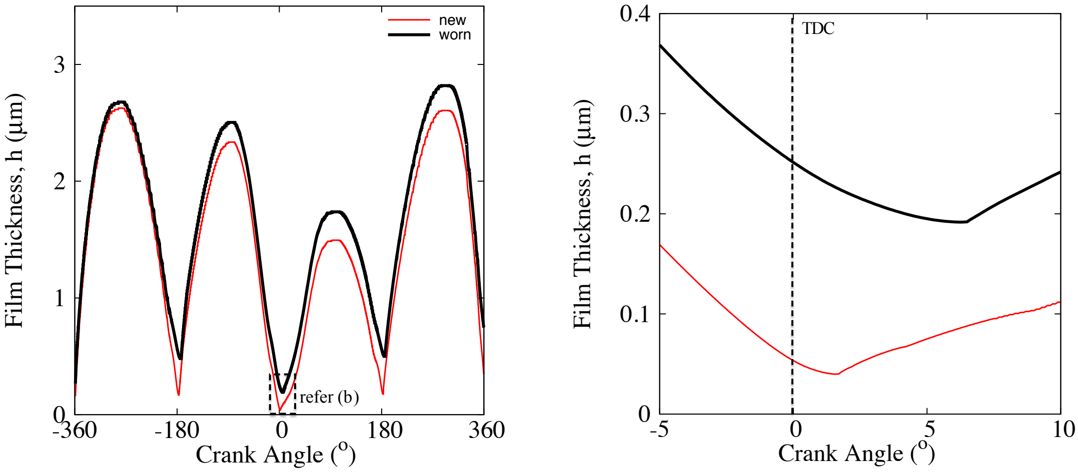

(a) Single engine cycle

(b) Power stroke TDC

Figure 3.7: New and worn top ring comparison - Minimum film thickness at 7500 rev/min (Wide Open Throttle)

Assuming a surface roughness, $\sigma = 0.37\mu m$ [27], the friction force along the whole engine cycle for both the new and worn rings are predicted using the friction model discussed in the previous chapter. Figure 3.8 shows the boundary and viscous friction for the simulated ring profiles. The new ring exhibits a more significant boundary friction while the worn ring produces a higher viscous friction. The approach of assuming the new and worn ring having similar r.m.s. surface roughness might be counter intuitive. However, this comparison proved that a less dramatic curvature for the ring profile encourages the boundary friction reduction along the contact along most regions of the engine cycle.

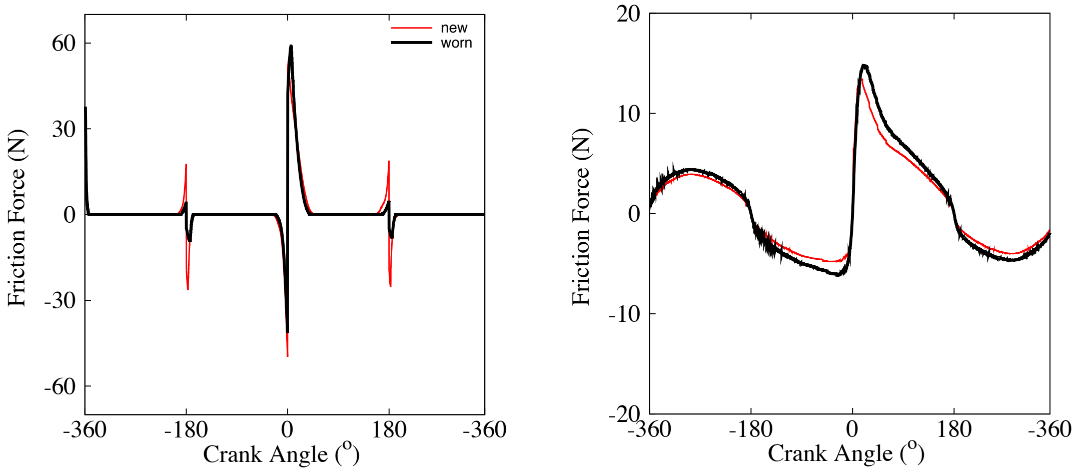

(a) Boundary friction (b) Viscous friction

Figure 3.8: New and worn top ring frictional comparison for $\sigma = 0.37\mu m$ - Boundary and viscous friction force at 7500 rev/min (Wide Open Throttle)

Figure 3.9 presents the total friction force for the new and worn rings. It can be observed that at piston motion reversal points, the new ring produces a higher friction. However, along the power stroke TDC, due to the increasing combustion pressure, the friction of the worn ring is higher after piston motion reversal (see figure 3.9). Another observation is that in the mid-stroke span, the worn ring produces higher friction, mainly dominated by the viscous action.

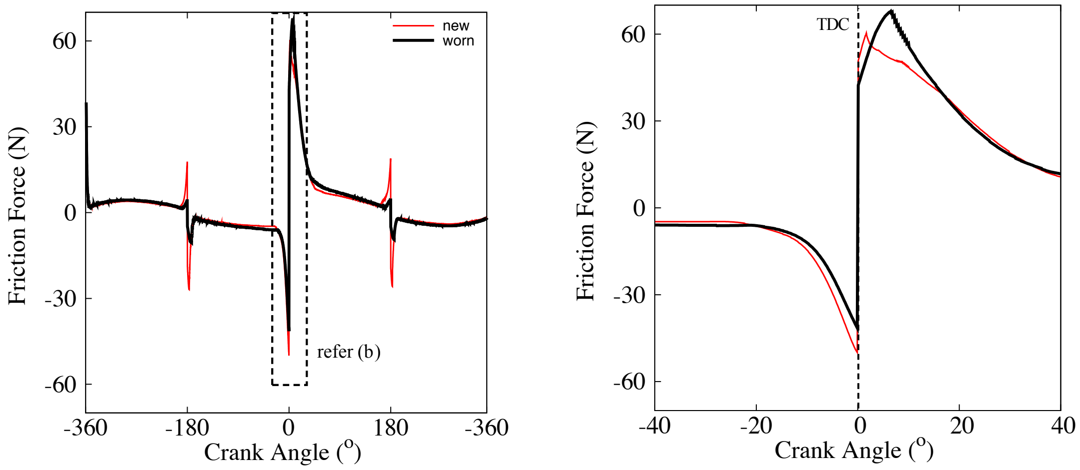

(a) Single engine cycle (b) Power stroke TDC

Figure 3.9: New and worn top ring frictional comparison for $\sigma = 0.37\mu m$ - Total friction force at 7500 rev/min (Wide Open Throttle)

Using a different surface roughness of $0.22\mu m$ [47], the friction components and total friction for both the simulated ring profiles are shown in figure 3.10 and 3.11. Due to less rough surface, the boundary friction for both the rings is reduced significantly. At some reversal regions along the engine cycle, the worn ring shows no boundary lubrication at all.

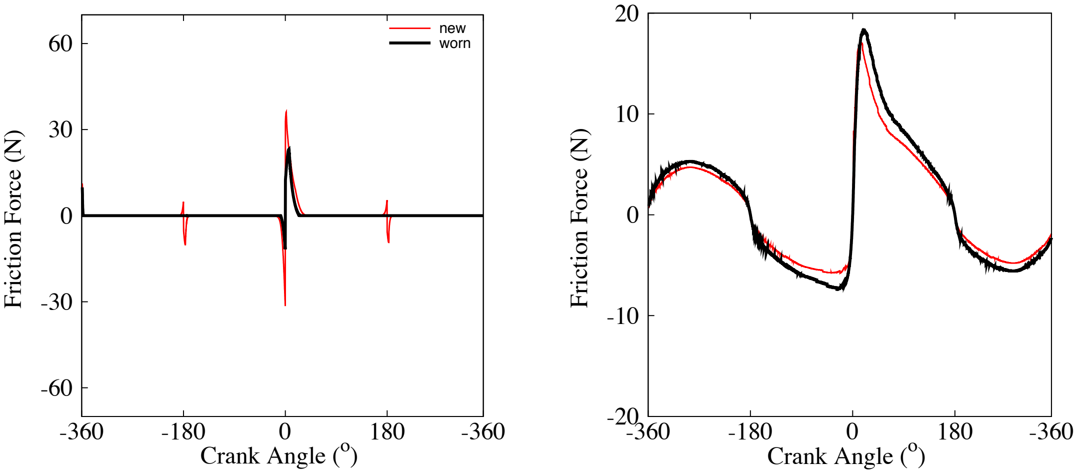

(a) Boundary friction

(b) Viscous friction

Figure 3.10: New and worn top ring frictional comparison for $\sigma = 0.22\mu m$ - Boundary and viscous friction force at 7500 rev/min (Wide Open Throttle)

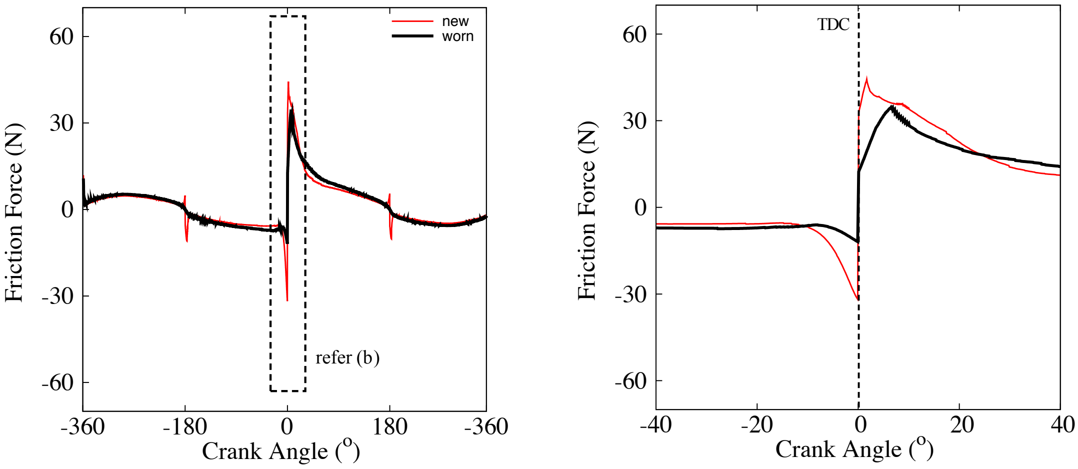

(a) Single engine cycle

(b) Power stroke TDC

Figure 3.11: New and worn top ring frictional comparison for $\sigma = 0.22\mu m$ - Total friction force at 7500 rev/min (Wide Open Throttle)

3.4 Comparison between scaled and predicted inter-ring pressure for a new top ring

The previous chapter assumes that the pressure between the top and second ring to be a percentage of the head land pressure. However, it is shown using the blow-by model discussed earlier in the study, the inter-ring pressure between the top and second ring (2nd land) shows a deviation from the characteristics of the scaled-down pressure curve (see figure 3.12(a)). Figure 3.12 (b) shows the comparison between the contact pressure distribution predicted using the scaled and predicted inter-ring pressure. For a downstroke motion, the leading edge of the top ring is exposed to the inter-ring pressure. It can be observed that due to the higher inlet pressure, the peak pressure for the top ring is reduced. The reduced peak pressure helps to decrease the friction of the contact.

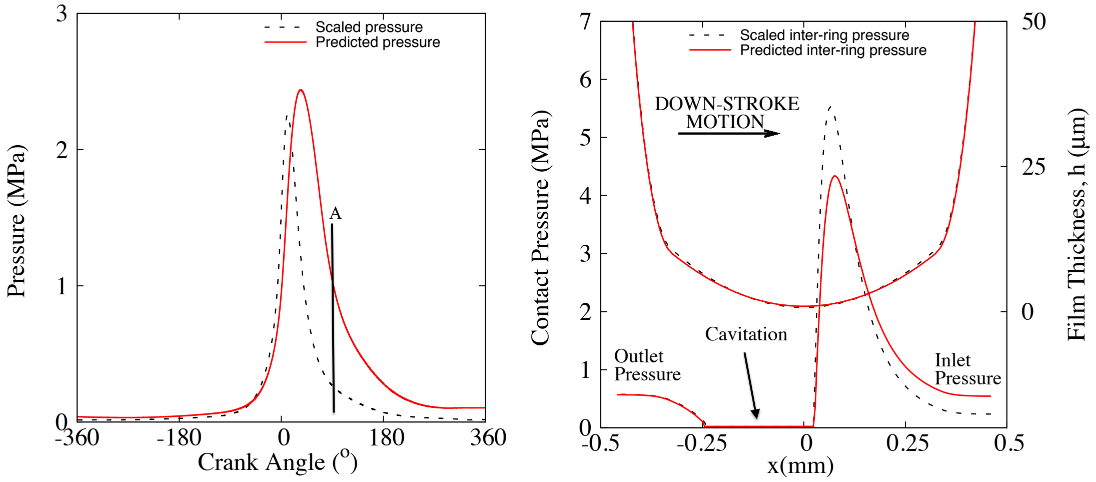

(a) Inter-ring pressure

(b) Contact pressure and film profile at A

Figure 3.12: Predicted and "scaled" [4] second land inter-ring pressure at 7500 rev/min (Wide Open Throttle)

Figure 3.13(a) shows the minimum film thickness for a single engine cycle using the scaled and predicted inter-ring pressure. The minimum film thickness along the vicinity of the power stroke TDC does not differ a lot between both assumptions (see figure 3.13(b)). This characteristic is expected based on the inter-ring pressure difference shown in figure 3.12(a). An interesting thing to note is that the significant difference between both the methods can only be seen after the power stroke TDC. The minimum film thickness assuming the predicted inter-ring pressure is smaller than the scaled approach after the power stroke TDC ($0 - 180°$). The smaller film between the ring and liner increases the contact's friction force. This is reflected through figure 3.14 assuming the r.m.s surface roughness to be $0.37\mu m$ for crank angles $0 - 180^o$.

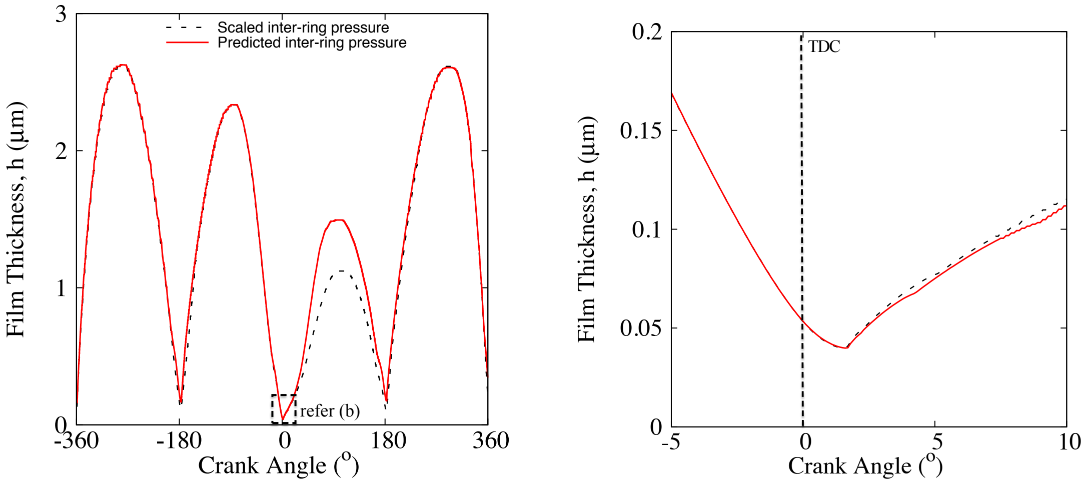

(a) Single engine cycle (b) Power stroke TDC

Figure 3.13: Minimum film thickness based on the predicted and "scaled" Inter-ring pressure (top-2nd ring) at 7500 rev/min (Wide Open Throttle)

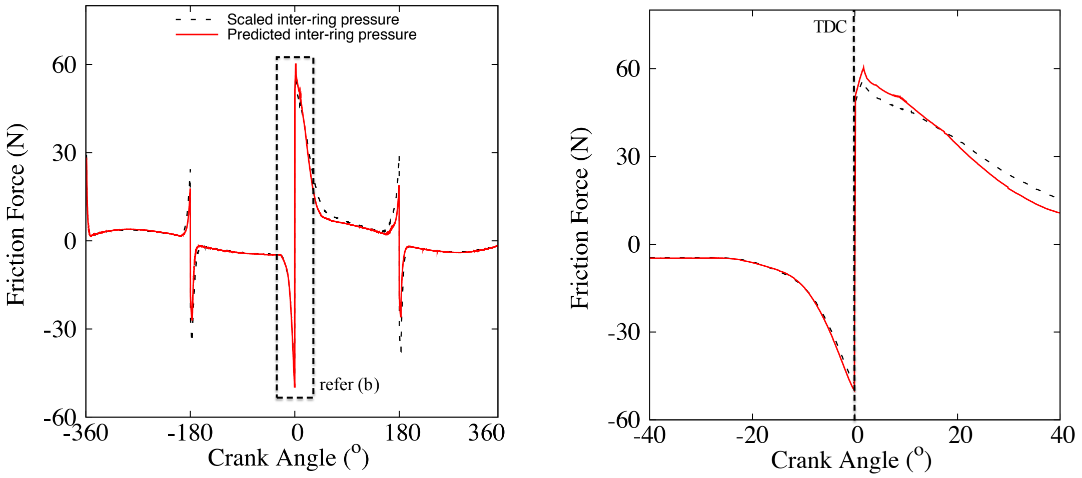

(a) Single engine cycle (b) Power stroke TDC

Figure 3.14: Friction force based on the predicted and "scaled" Inter-ring pressure (top-2nd ring) at 7500 rev/min (Wide Open Throttle)

3.5 Summary

This chapter includes the effect of combustion gas blow-by in the piston ring lubrication analysis. The measured new and worn ring profiles are used to simulate the tribological characteristics along the contact conjunction. The influence of the added considerations into the modified Elrod's model are being discussed. It was shown that the effect of inter-ring pressure are significant especially during the power-stroke of the engine cycle.

Chapter 4

Validation of the Modified Elrod's Cavitation Algorithm

4.1 Introduction

Friction induced by the piston ring-liner contact comprises a considerable amount of the total parasitic loss in an IC engine. It has been reported that this constitutes up to 40-60 % of the total engine friction loss. To improve and optimise the friction performance of an engine, the numerical analysis coupled with experimental validations for the piston ring lubrication proves to be a key player. A numerical analysis alone might be able to show only the trend or characteristics of a tribological contact. The results of a numerical analysis still requires experimental validations before being able to be used for a practical application. The modified Elrod's cavitation model developed in the study has been shown its tribological capabilities in the previous two chapters. Numerical results show reasonable characteristics of the piston ring lubrication. In this chapter, an experimental validation of the model is included to increase the level of confidence of the numerical model's application on a piston ring lubrication problem.

4.2 Plint TE77 Reciprocator

In this validation study, the piston ring-liner contact is simulated using a Plint high frequency reciprocating test rig (see figure 4.1(a)). The experimental validation was conducted by Avan *et al* [62] at Sheffield University for a tapered ring profile shown in figure 4.1(b). The average minimum film thickness was measured at mid-span location only. The lubricant film thickness was measured using an ultrasonic technique where a sound wave is propagated and reflected from the ring-liner contact[62]. The sliding velocity of the reciprocator is shown in figure 4.1(c).

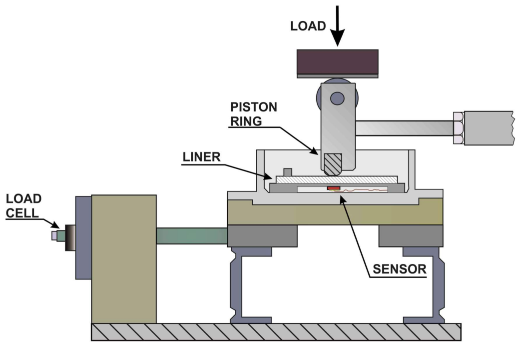

(a) *Plint TE77* at Sheffield University [62]

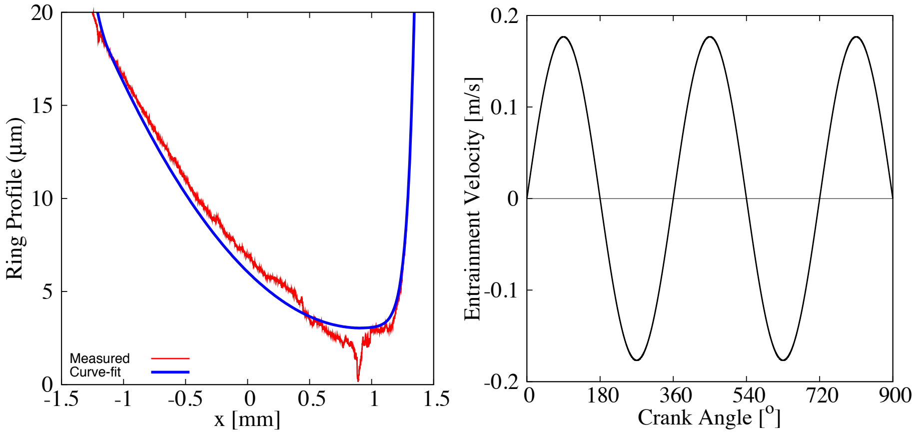

(b) Ring Profile

(c) Kinematics of Plint 77 operating at 7.5 Hz

Figure 4.1: Simulated piston ring-liner contact

During the experiment, a conventional cast-iron liner and a tapered ring section are fixed on the reciprocator [62]. A 10 MHz piezoelectric sensor is glued to the back face of the liner in order to measure the film thickness at mid stroke. Experimental tests are carried out for several loading and reciprocating speeds using the base oil and $SAE10W40$. The lubricating film thickness are measured using the ultrasonic technique. For validation purposes, the numerical model proposed *Chapter 2* is used to predict the pressure profile and film thickness by applying the contact conditions of the experiment. The measured lubricant dynamic viscosity at room temperature for the base oil and $SAE10W40$ are $0.168 Pa.s$ and $0.253 Pa.s$.

Table 4.1: Plint TE77 experimental data

Parameters	**Values**
Crank Radius, R	0.0075 m
Stroke Length, ℓ	0.015 m
Temperature, T	20 °C

4.3 Numerical Analysis

The experiment conducted is aimed at validating the minimum film thickness predicted using the modified Elrod's model proposed in *Chapter 2*. The minimum film thickness predicted at various crank angles is shown in figure 4.2 for both the base oil and $SAE10W40$. The numerical analysis simulated the rig operating at $7.5Hz$ with a constant ring loading of $75N$. The analysis using the base oil predicted a thinner film throughout the simulated domain as compared to $10W40$ at constant load. A thinner film induces higher friction and the possibility of metal-metal contact depending on the contact conditions. The thicker film predicted by using the $SAE10W40$ is due to the increased viscosity caused by the additives.

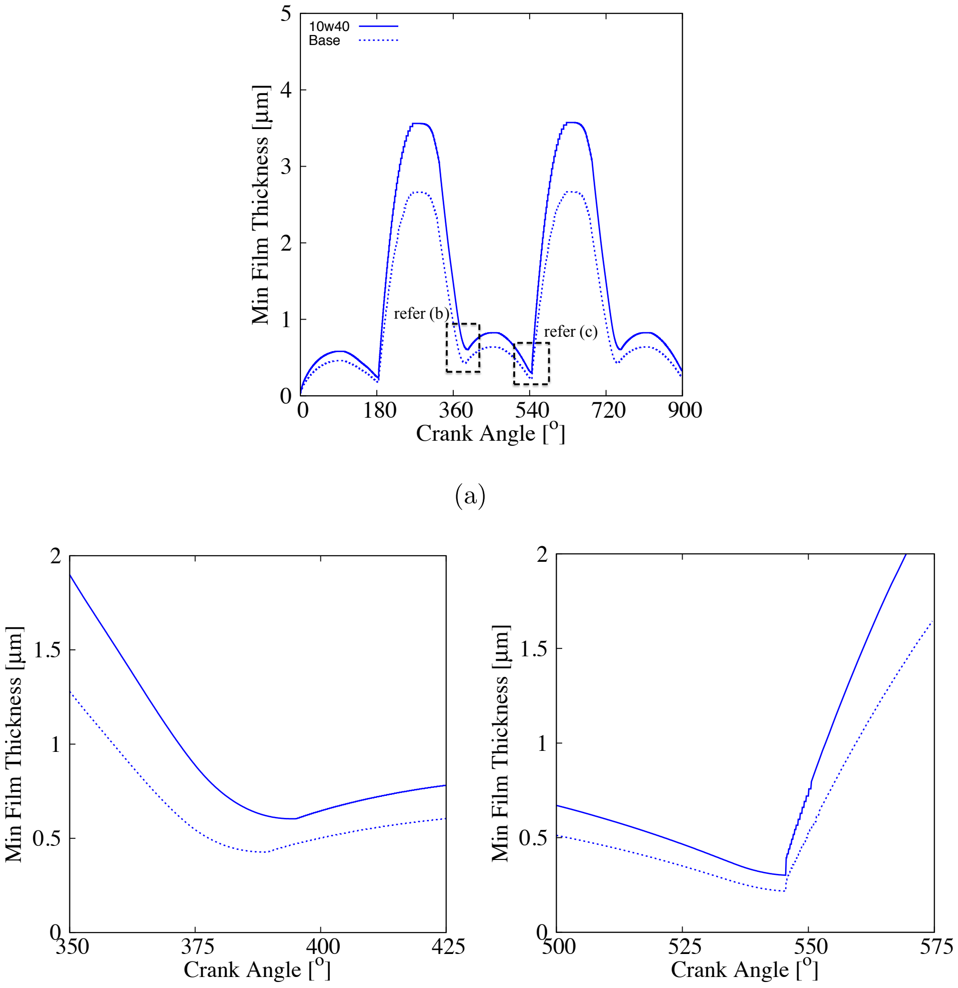

(a)

(b)

(c)

Figure 4.2: Minimum film thickness comparison between base oil and $10W40$ for *Plint TE77* operating at $7.5Hz$ with a constant load of $75N$

Assuming the tapered side of the ring as the leading edge, figure 4.3 shows the tribological characteristics of the ring-liner contact at 270°, which is the mid-span stroke of the liner. The contact pressure distribution (see figure 4.3(b)) along the ring shows two distinct cavitation regions: cavitation at the outlet (cav) and pre-reversal cavitation at the inlet (p-cav). The latter cavitation region was the initial cavitation created at the trailing edge of the ring before motion reversal which occurs at 180°. It can be observed that the pre-reversal cavitation has yet to fully implode. The two cavitation regions discussed can also be clearly seen through the fractional film content of the lubricants as shown in figure 4.3(c).

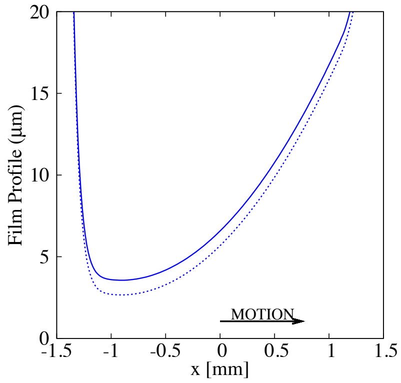

(a) Film Profile

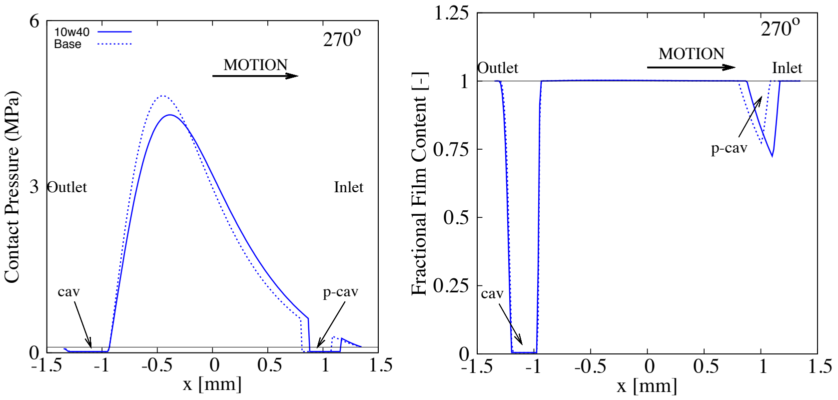

(b) Contact Presusre

(c) Fractional Film Content

Figure 4.3: Tribological characteristics comparison at 270° for *Plint TE77* operating at $7.5Hz$ with a constant load of $75N$

The contact pressure distributions for the ring along the vicinity of 360° before and after motion reversal are shown in figure 4.4. Before motion reversal, a cavitation region is formed at the trailing edge of the ring. This region then turned into the pre-reversal cavitation after motion reversal at 360.2°. As the ring starts to accelerate, the pre-reversal cavitation begins to implode and in the process creates a cavitation at the trailing edge of the contact as can be seen at 370° and 380°. However, the pre-reversal cavitation at 380° for the base oil still exist while the lubricant $SAE10W40$ shows a full implosion of this cavitation region at this angle.

Figure 4.5 shows the fractional film content variation along the reversal region at 360°. The pre-reversal cavitation created after motion reversal (360.2° onwards) can be seen to implode. At the same time, a cavitation forms at the trailing edge of the contact. The fractional film content distribution shows clearly the transition of the cavitation regions either at the leading or the trailing edge of the contact.

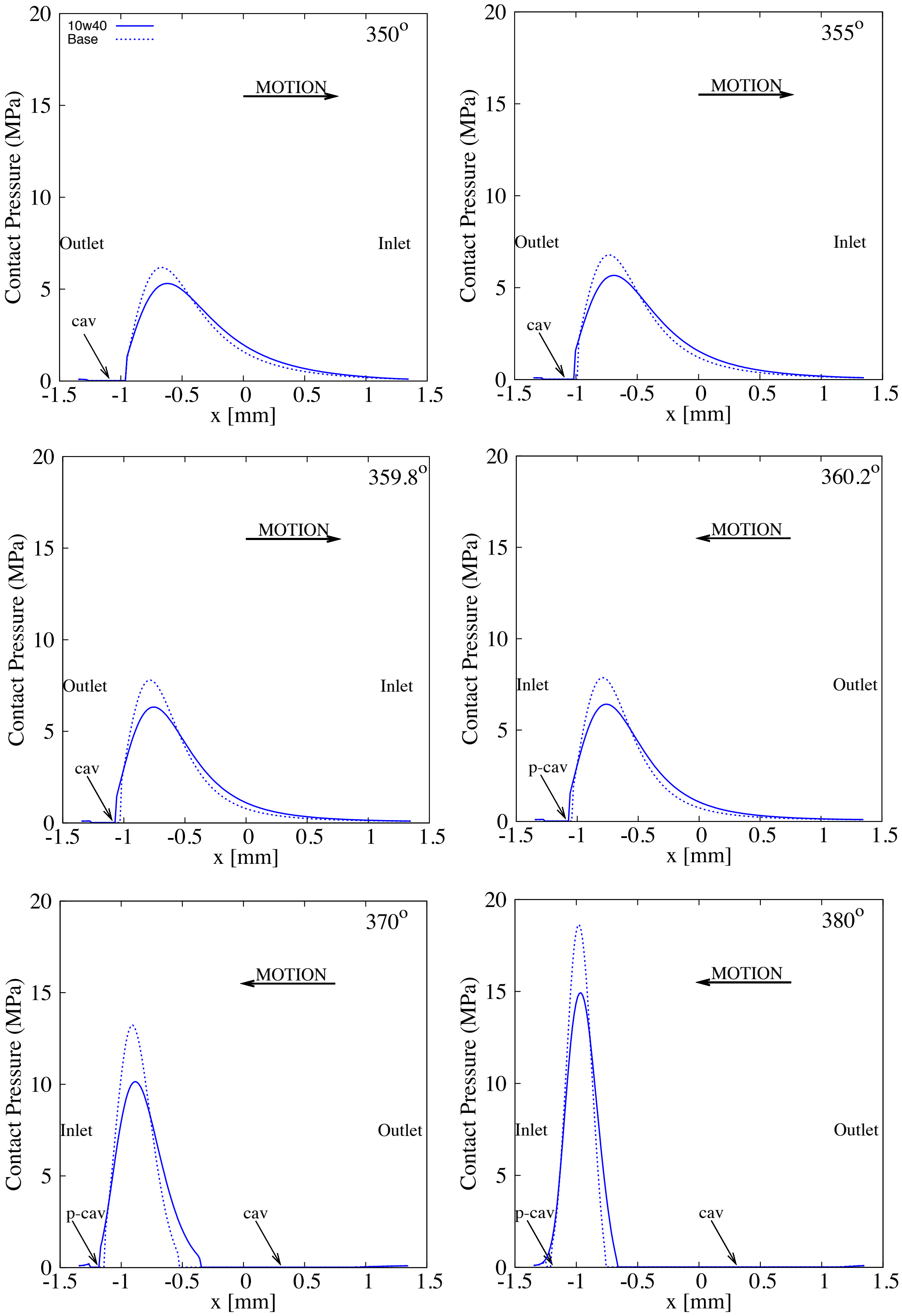

Figure 4.4: Contact pressure comparison along the vicinity of 360° for *Plint TE77* operating at $7.5Hz$ with a constant load of $75N$

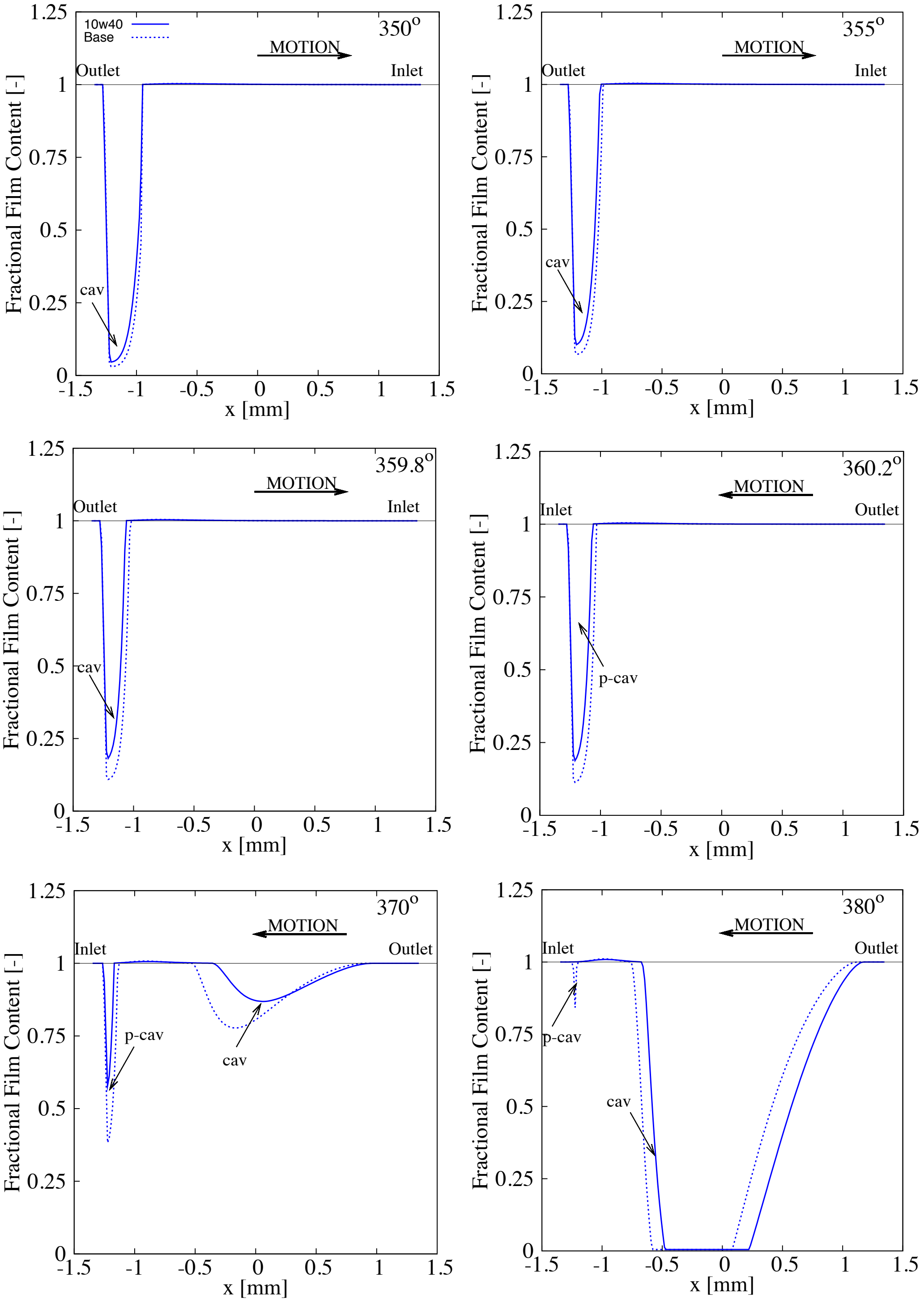

Figure 4.5: Fractional film content comparison along the vicinity of 360° for *Plint TE77* operating at $7.5 Hz$ with a constant load of $75 N$

Figure 4.6 shows (a) the film thickness, (b) contact pressure and (c) fractional film content of the ring-liner contact at 450°. It should be noted that after the reversal, the tapered edge of the ring the trailing edge of the contact. Due to the nonsymmetrical profile of the ring, all three parameters are significantly different from their counterparts before reversal 4.3. Figure 4.6(b) shows a higher and concentrated pressurised region as compared to the pressure profile in figure 4.3(b). The cavitation formed at the trailing edge is also larger (see figure 4.6(b)).

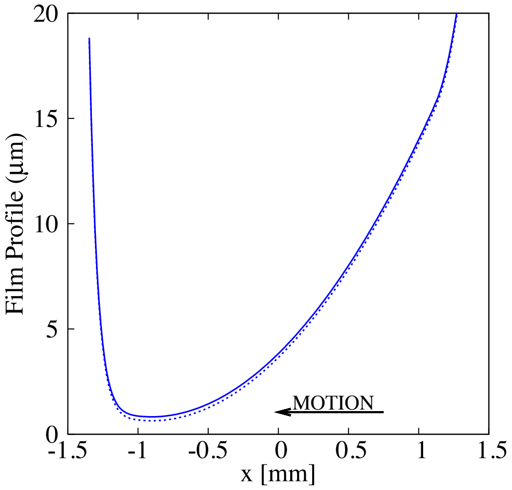

(a) Film Profile

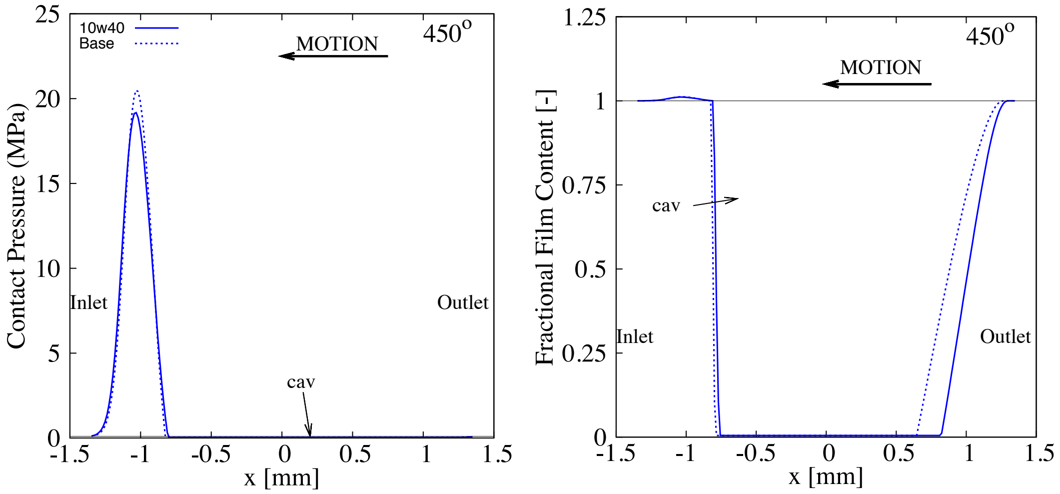

(b) Contact Presusre

(c) Fractional Film Content

Figure 4.6: Tribological characteristics comparison at 450° for *Plint TE77* operating at $7.5Hz$ with a constant load of $75N$

The contact pressure and fractional film content along the reversal region at 540° are shown in figure 4.7 and 4.8. From both sets of figures along 540°, the pre-reversal cavitation implodes at a slower rate (full implosion 125° after reversal at 540°) as compared to the reversal point at 360°. This is due to the larger cavitation region formed at the trailing edge of the tapered ring before the piston motion reversal.

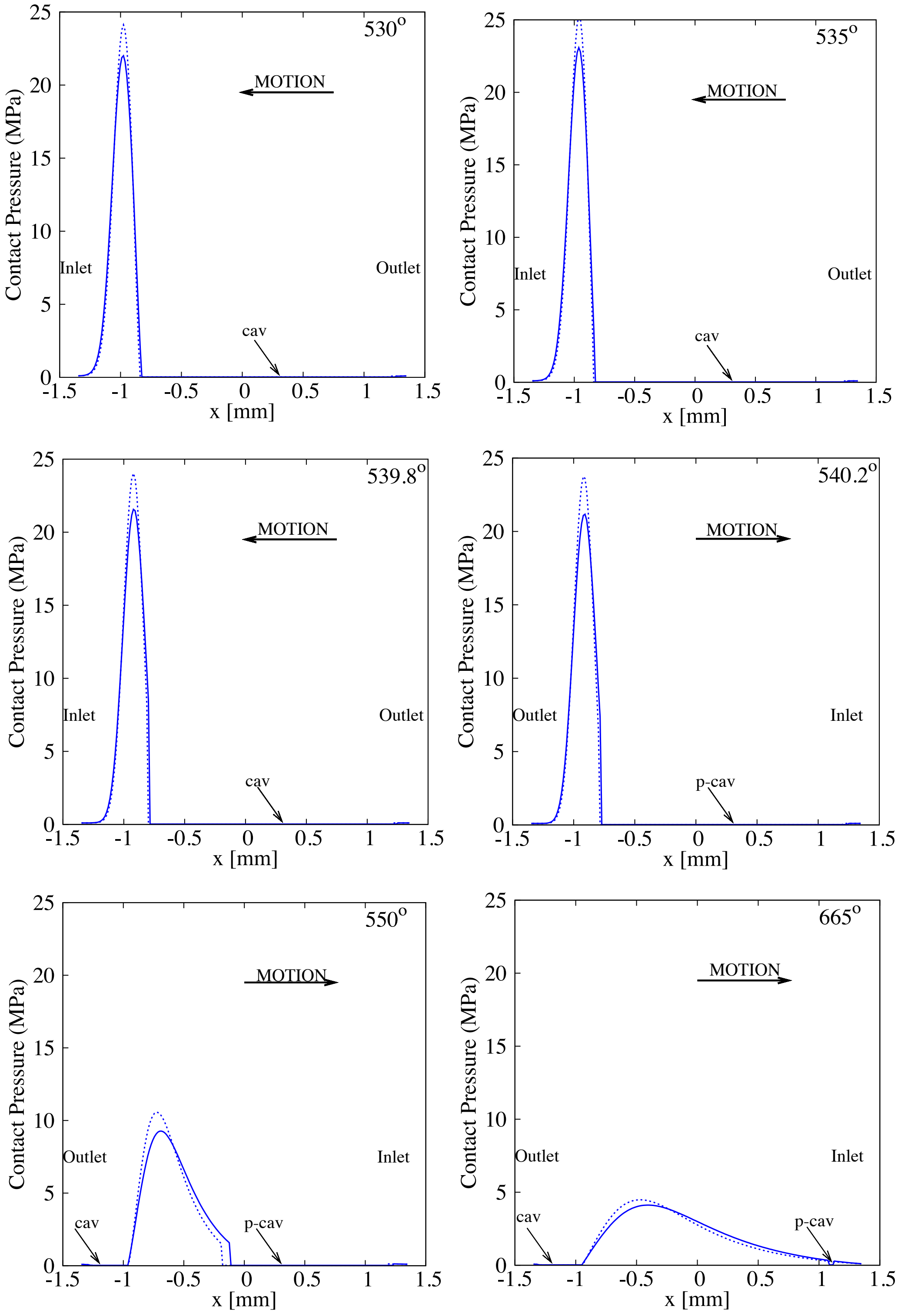

Figure 4.7: Contact pressure comparison along the vicinity of 540° for *Plint TE77* operating at $7.5Hz$ with a constant load of $75N$

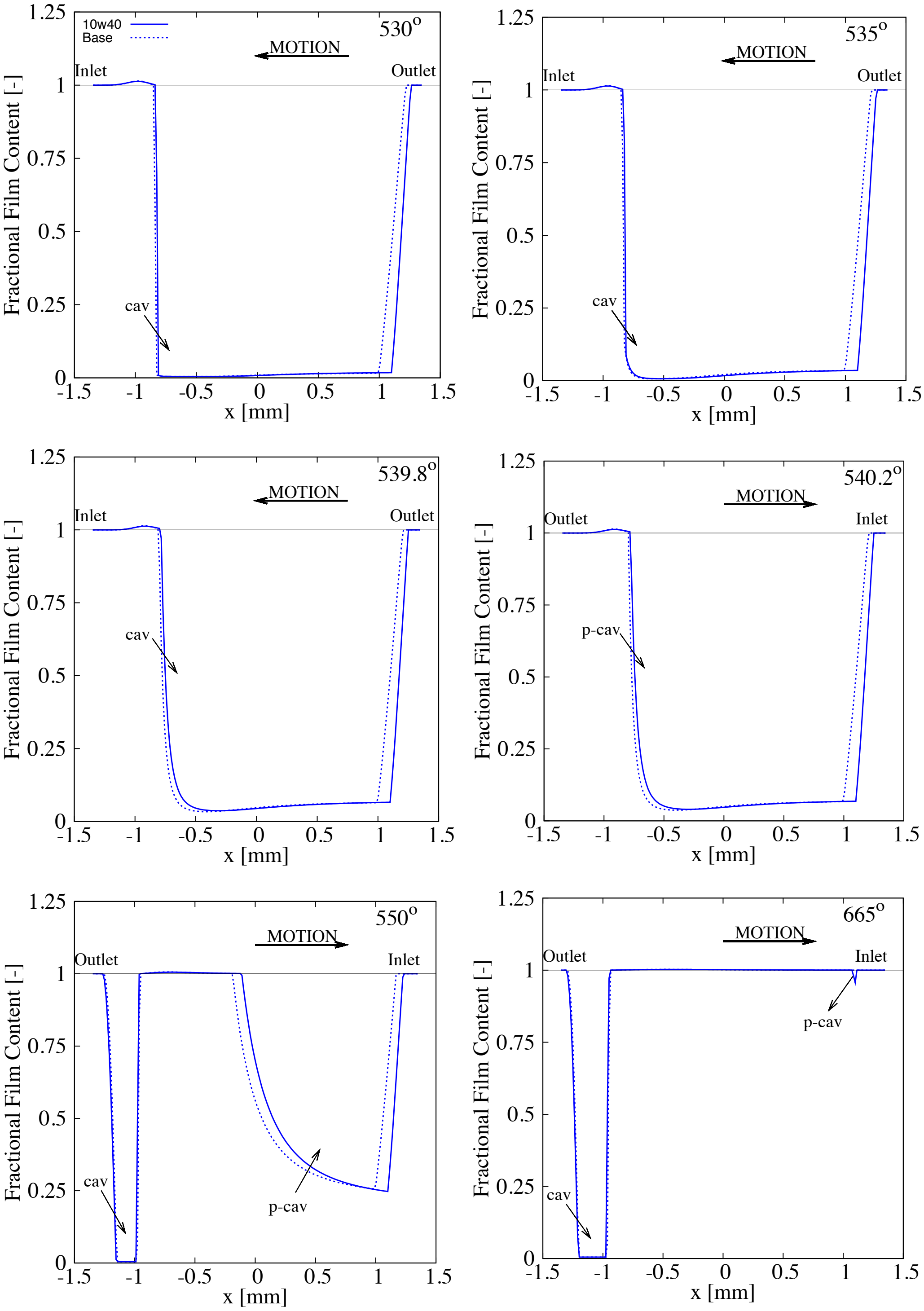

Figure 4.8: Fractional film content comparison along the vicinity of 540° for *Plint TE77* operating at $7.5Hz$ with a constant load of $75N$

Figure 4.10 shows the minimum film thickness variation for different operating frequencies of the reciprocating rig *Plint TE77* at a constant loading of $75N$. As the operating frequency is being increased, the entrainment velocity along the ring-liner contact is also being increased (see figure 4.9). Therefore, an increase in the film thickness can be seen for both the base oil and $SAE10W40$. The minimum film thickness along the simulated domain is shown for different loading conditions for the *Plint TE77* operating at a constant frequency of $7.5Hz$.

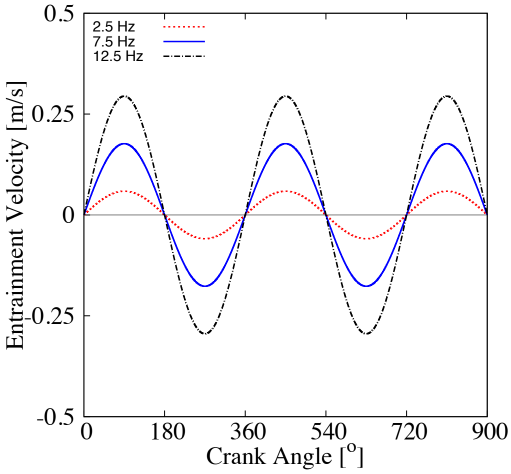

Figure 4.9: Entrainment velocity of the ring-liner contact for various operating frequencies at a constant load of $75N$

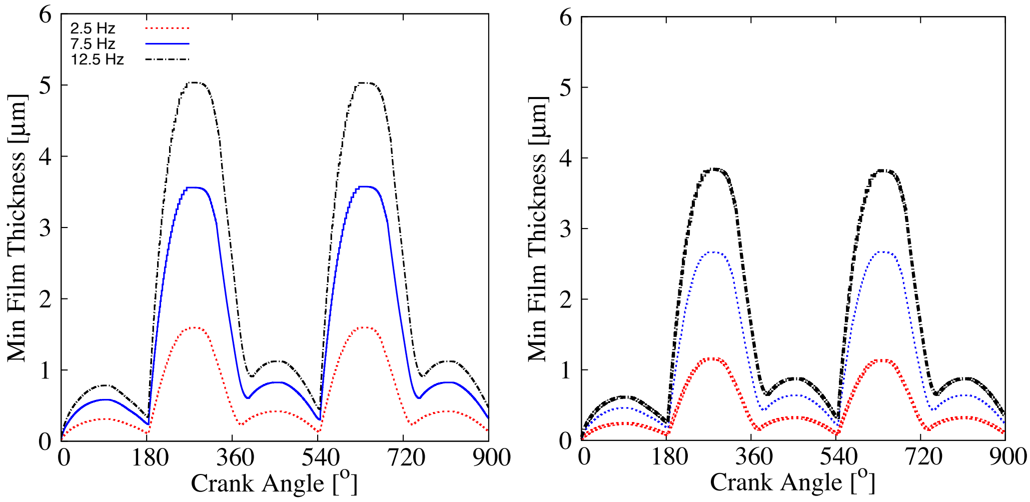

(a) $SAE10W40$ (b) Base

Figure 4.10: Minimum film thickness comparison for *Plint TE77* operating at various frequencies with a constant load of $75N$

The reciprocator is also being run at a constant frequency of $7.5Hz$ with an increasing ring loading. The effect of increasing the ring load is shown in figure 4.11. The increased load reduces the minimum film thickness predicted for both the lubricant used. It can also be noticed that the drop in film thickness for the base oil is more significant than $SAE10W40$. The better load carrying capacity of the $SAE10W40$ is due to the effect of additives included to improve the performance of the lubricant.

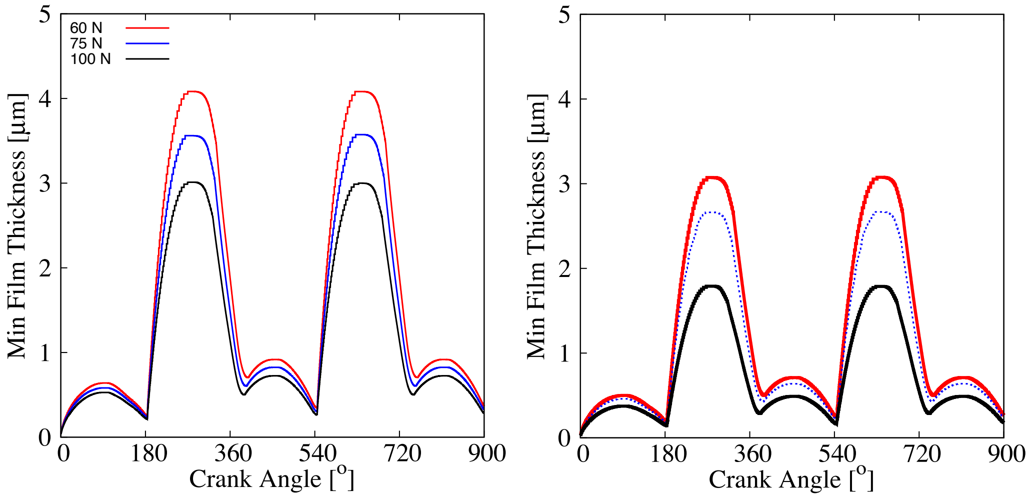

(a) $SAE10W40$ (b) Base

Figure 4.11: Minimum film thickness comparison for *Plint TE77* operating at various loading conditions with a constant operating frequency of $7.5Hz$

With the measured r.m.s surface roughness of $0.38\mu m$, the boundary and viscous friction component for the base oil and $SAE10W40$ are shown in figure 4.12. It can be seen that due to the thinner film thickness produced by using the base oil, the boundary friction for the base oil is higher as compared to $SAE10W40$. As a result of this, the total friction force produced by the base oil is higher than the $SAE10W40$ as can be observed in figure 4.13(a). The friction coefficient comparison between both the lubricants is included in figure 4.13(b).

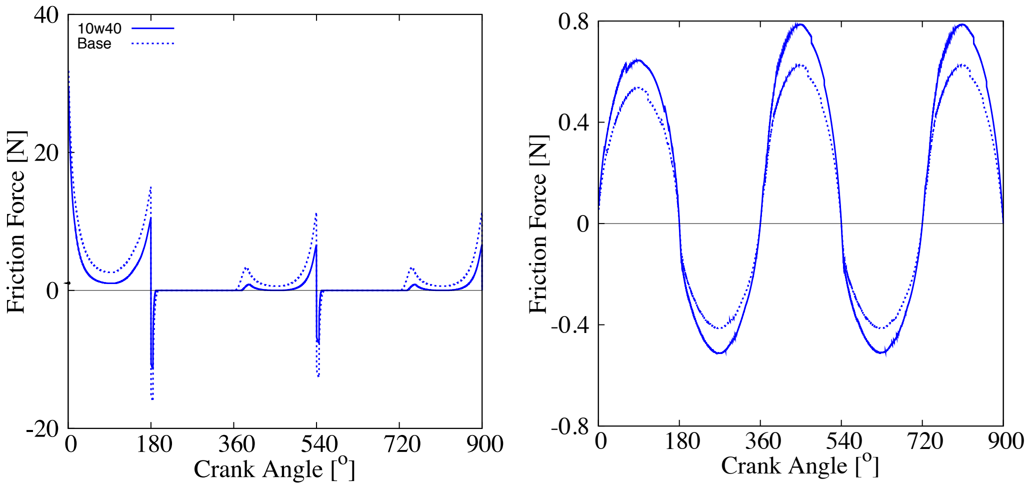

(a) Boundary friction (b) Viscous friction

Figure 4.12: Friction components comparison between base oil and $10W40$ for *Plint TE77* operating at 7.5 Hz with a constant load of $75N$

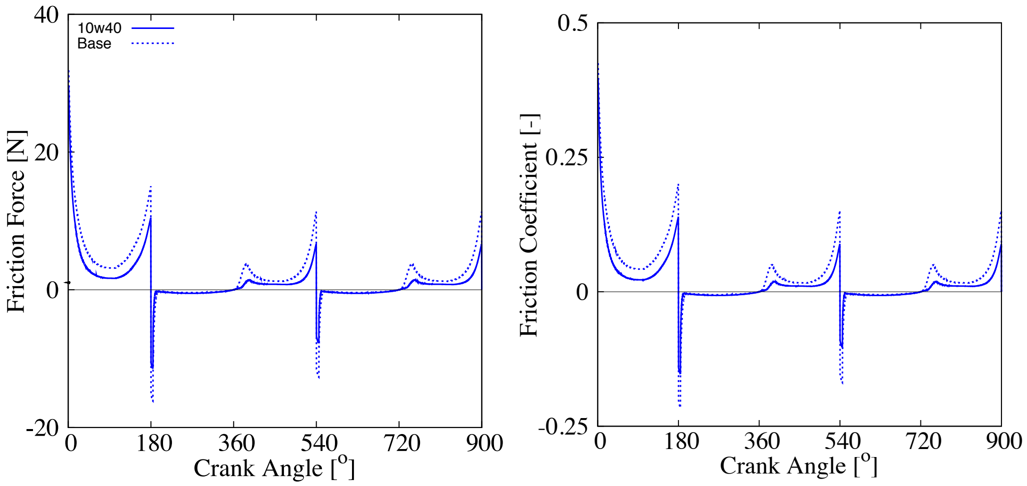

(a) Total friction (b) Friction Coefficient

Figure 4.13: Frictional characteristics comparison between base oil and $10W40$ for *Plint TE77* operating at $7.5Hz$ with a constant load of $75N$

The shear stress distribution along the ring at 270° and 450° is shown in figure 4.14. It is assumed that shearing of the lubricant does not occur along cavitation regions. From figure 4.12, there are no boundary friction along the ring at this angle and the shear is purely viscous. Figure 4.15 shows the shear stress distribution in the vicinity of the 360° reversal. The magnitude of the shear stress fluctuates significantly. When boundary shear dominates (370° and 380°), the shear stress along the ring-liner contact increases significantly. Figure 4.16 shows the shear stress in the vicinity of the 540° reversal. It should be noted that immediately following the reversal the shear stress drops significantly. This is mainly due to the increasing entrainment velocity and also the larger contact area of the ring after motion reversal.

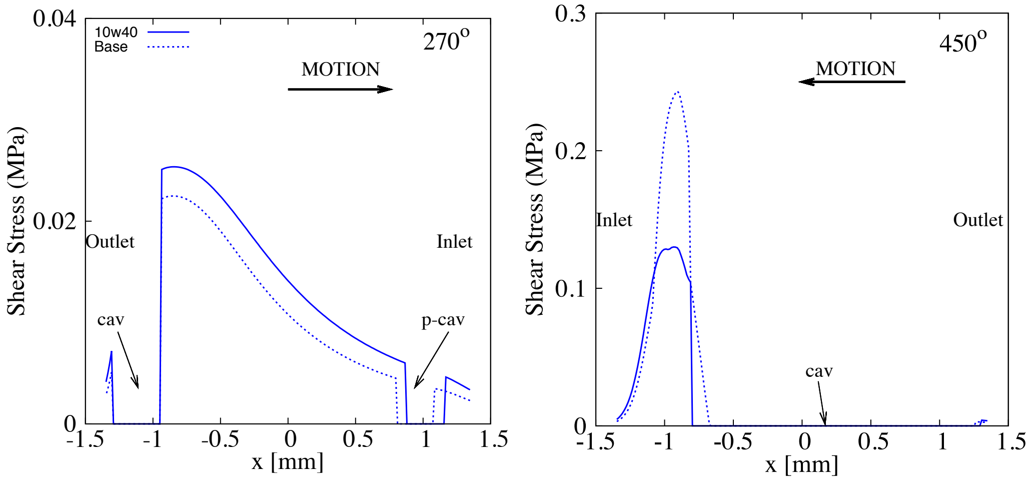

(a) 270°　　(b) 450°

Figure 4.14: Total shear stress comparison for *Plint TE77* operating at $7.5Hz$ with a constant load of $75N$

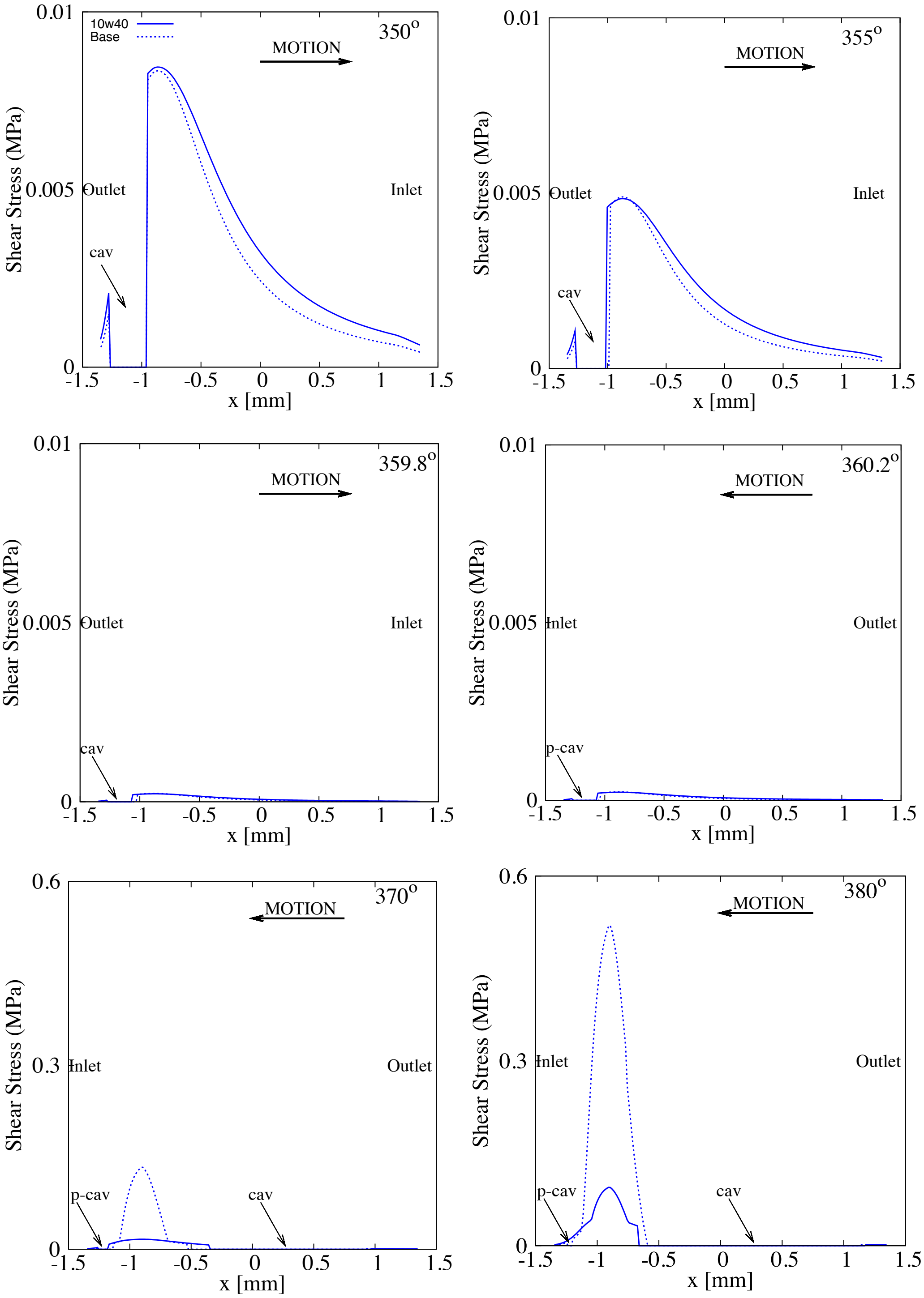

Figure 4.15: Total shear stress comparison along the vicinity of 360° for *Plint TE77* operating at $7.5Hz$ with a constant load of $75N$

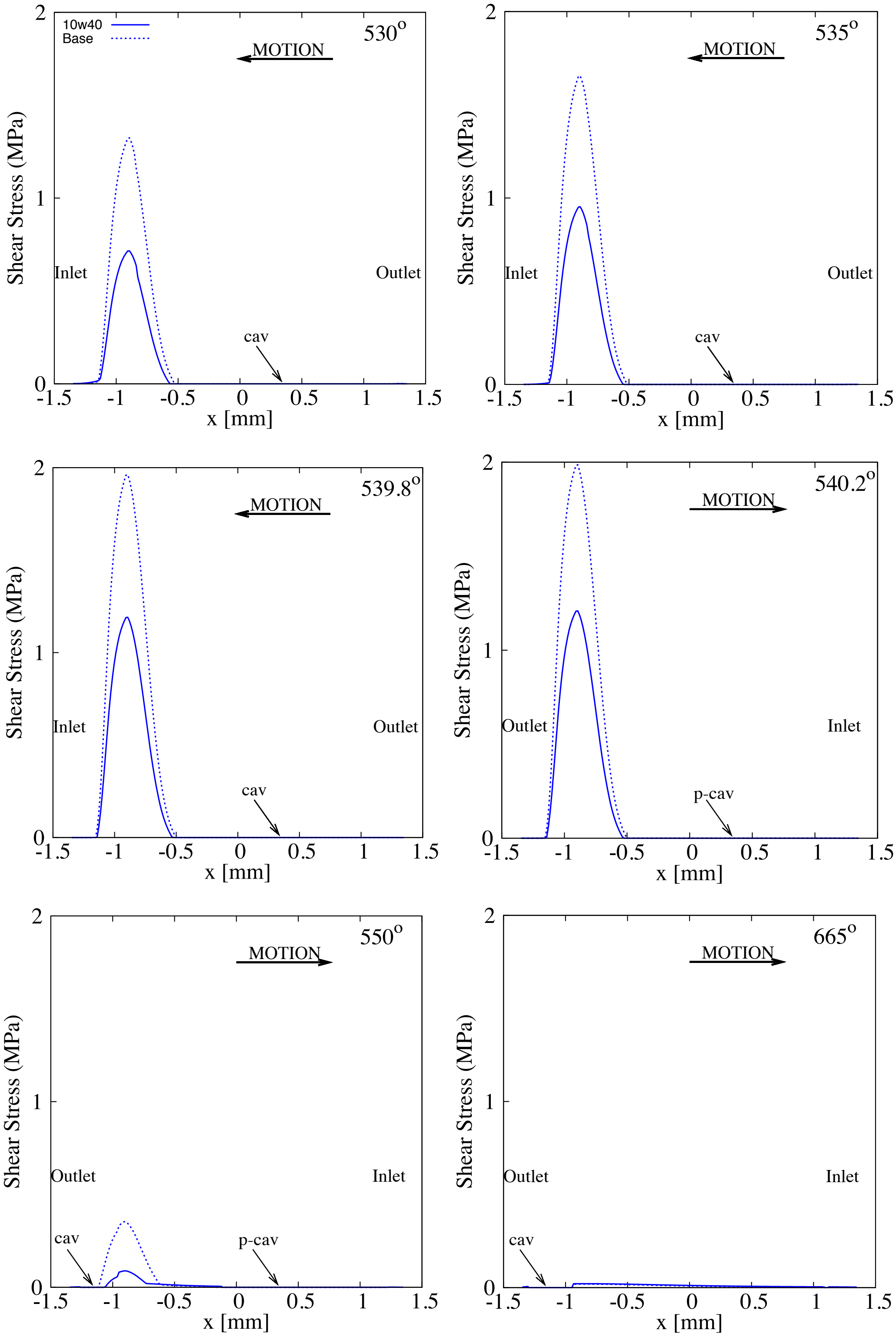

Figure 4.16: Total shear stress comparison along the vicinity of 540° for *Plint TE77* operating at 7.5 Hz with a constant load of $75N$

The total friction force along the simulated domain is plotted in figure 4.17 for different operating frequencies of the *Plint TE77* at $75N$. It can be seen that the friction force decreases with the increase in the operating frequency. For the load variation under a constant operating frequency (see figure 4.18), the friction force variation is less significant for $SAE10W40$. However, for the base oil, under the load of $100N$, the friction force is significantly higher than the other two loading conditions. This is affected by the increasing influence of the boundary friction where more asperity interactions are expected.

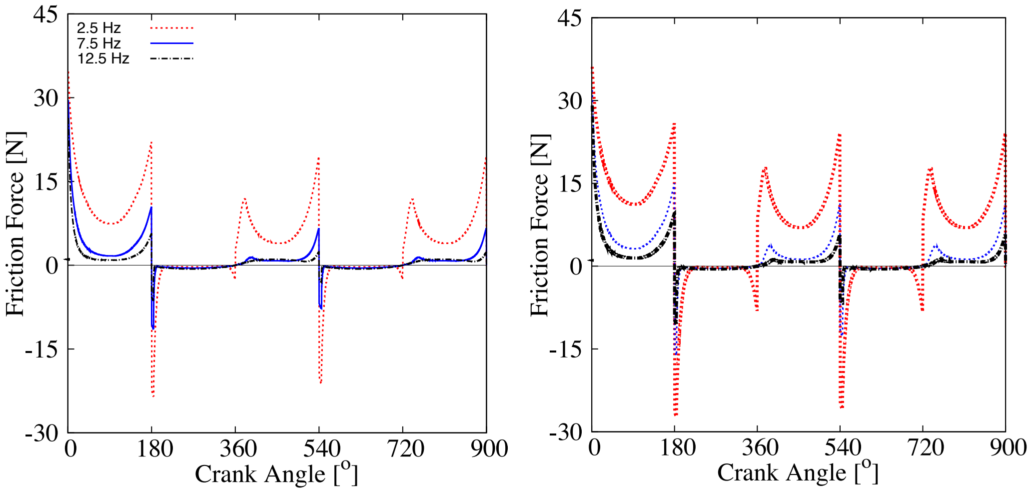

(a) $10W40$ (b) Base

Figure 4.17: Frictional characteristics comparison for *Plint TE77* operating at various frequencies with a constant load of $75N$

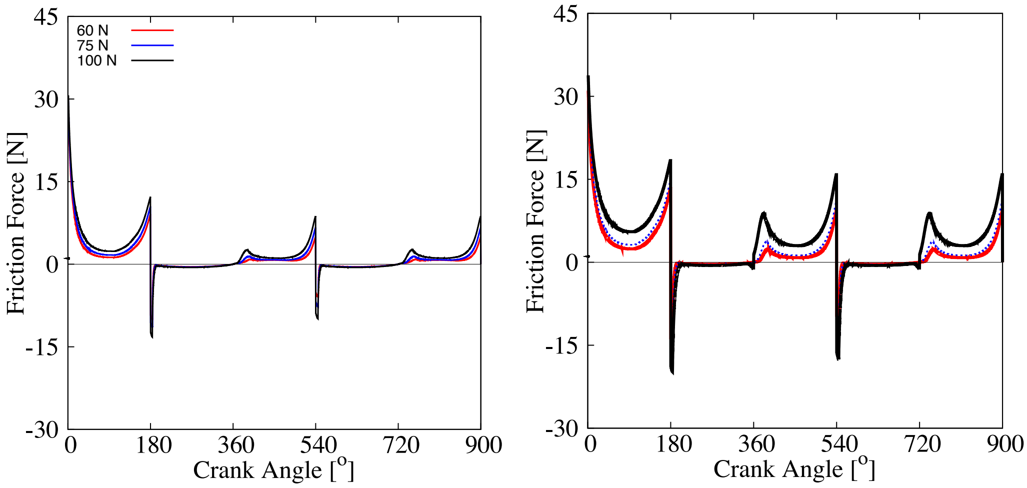

(a) $10W40$ (b) Base

Figure 4.18: Frictional characteristics comparison for *Plint TE77* operating at various loading conditions with a constant operating frequency of $7.5Hz$

4.4 Experimental validation of Modified Elrod's cavitation algorithm

A comparison of numerical and experimental data for the minimum film thickness at 450° (mid-span stroke) is shown in figure 4.19 for different operating conditions. Figure 4.19 shows the minimum film thickness change for different loading conditions at $7.5Hz$ operating frequency for the base oil. It can be seen that at higher loads, the film thickness for both the numerical and experimental analysis show saturation. A further increase in load no longer reduces the film thickness significantly due to the increasing elastohydrodynamic action. Additionally, it can be observed that the numerical model agrees reasonably well with the trend of the experimental data. However, the magnitude of the film thickness does not agree as well. This is because the tilting of the ring occurs in the Plint TE77, which was not considered in the numerical model. Furthermore, the analysis is one-dimensional, with the sense that the contact is assumed to be conformed in its peripheral direction. This means that the one-dimensional analysis of ring-bore contact may be assumed along the ring face-width. In practice, the contact of a segment of the ring to the liner may be only partially conforming in the circumferential direction. Therefore, one would not usually expect very close agreement between the analysis and the experiment.

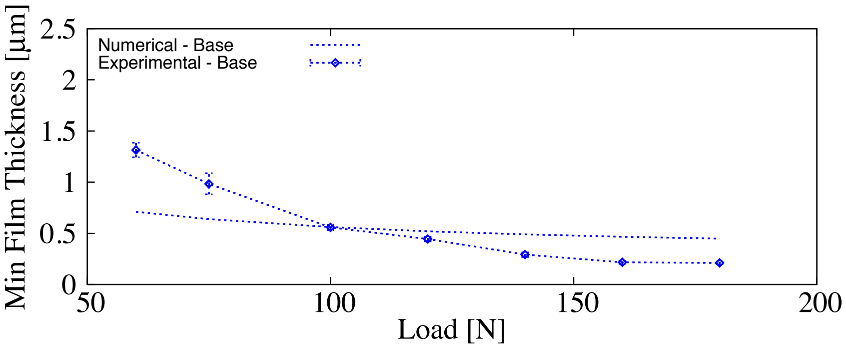

(a) Base oil

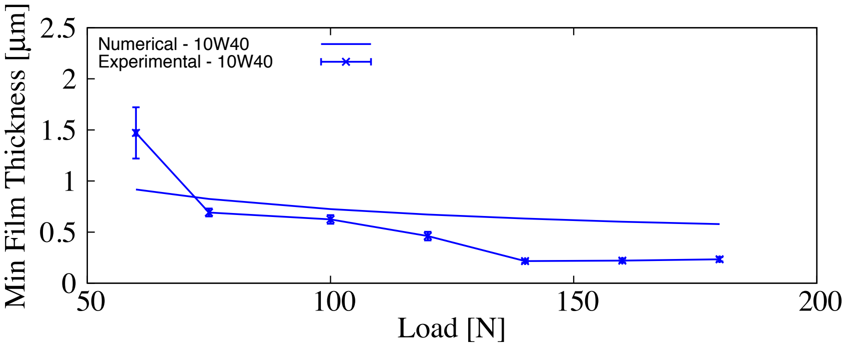

(b) $SAE10W40$

Figure 4.19: Numerical and experimental comparison for minimum film thickness at 450° (mid-span stroke) - Loading variation at constant operating frequency of $7.5Hz$

4.5 Summary

This chapter mainly focuses on the validation of the modified Elrod's cavitation model which is used to predict the minimum film thickness of the ring-liner contact. It should be noted that the main purpose of the experimental validation is to increase the level of confidence towards the modified Elrod's cavitation algorithm in predicting film thickness. The asperity interactions governing the friction between the contact at small separations will be discussed in part 2 of the study. The development of a more detailed friction model, considering asperity adhesion and thin film shearing, will be included in the following chapters.

Part II

Asperity Level Tribology

Chapter 5

Overview of tribology at small scale

5.1 Introduction

The second part of the thesis proposes successive mathematical models for the interaction between rough surfaces during sliding. This will be integrated with the overall ring-liner tribology model described in *Chapter 2*. *Chapter 6* investigates the elastic and elasto-plastic deformation and adhesion of asperities between rough surfaces in contact. *Chapter 7* models the thin film shearing mechanism considering the influence of intermolecular forces (e.g. solvation). *Chapter 8* extends this approach for fluid mixtures considering the effect of molecule adsorption on the surface. *Chapter 9* integrates the asperity interaction mechanisms for rough surfaces during sliding, forming the friction model. Two approaches for rough surface analysis are discussed and compared. The friction model is applied to predict the frictional characteristic along the ring-liner contact.

5.2 Piston ring-liner conjunction near reversals

Chapter 2 proposed a modified Elrod's cavitation algorithm for predicting ring-liner lubrication during engine operation. It was shown that while the piston reciprocates between the top and bottom dead centres, it momentarily stops at both of them. This results in a very low film thickness during reversals and possible ring-liner metal-to-metal interaction. Therefore, the ring-liner friction force is expected to be significantly higher.

The combustion pressure reaches its maximum only once during a single engine cycle, at the power-stroke top dead centre. This applies additional load to the ring-liner conjunction leading to thinner films, significantly increasing the chance of metal-to-metal interaction and higher friction force. In *Chapter 2*, it was shown that the modified Elrod algorithm can predict the extent of the outlet low pressure region during the entire cycle. The film collapses in this region, forming a vapor cavitation pocket at the outlet. Although this bubble is significantly smaller during the reversal than during the mid-span, it was shown (*Chapter 2*) that it could survive through the inlet reversal. The cavitation bubble, generated by the drop in pressure at the outlet before reversal, is located at the inlet after reversal, leading to starvation and depleting the oil film. Consequently, the oil film during the power stroke reversal is often extremely thin.

The minimum film thickness in the ring-liner conjunction during the reversals is often smaller than the height of individual surface features. Therefore, direct interaction cannot be avoided, and it must be taken into consideration when predicting friction along the contact. This boundary friction is determined by two factors: (i) the extent of which the interacting surfaces are covered by a layer of adsorbed film and (ii) material hardness and shear characteristics of the interacting surfaces [63]. Thus, this part of the study focuses on the fundamental understanding of the mechanisms governing the boundary friction on a rough surface contact.

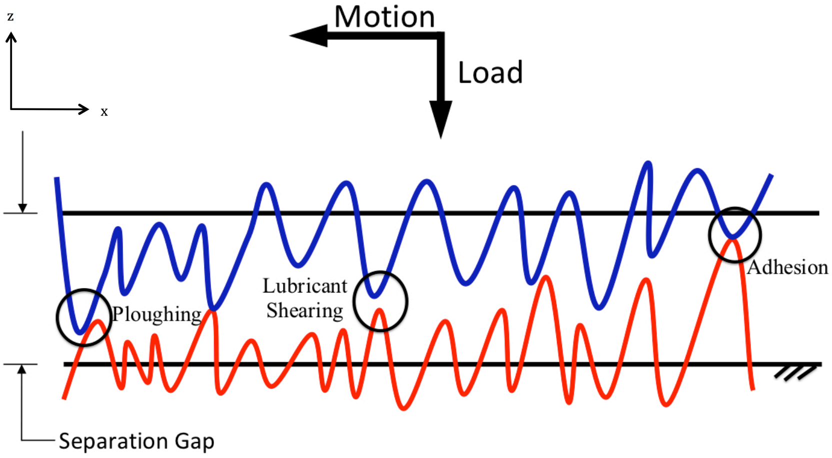

Figure 5.1: Asperity interactions along a rough surface

Without lubrication, asperity adhesion might occur if the asperities come in direct contact. Further loading of the asperity might induce plasticity. However, the asperities are most of the time separated by a thin adsorbed film, which will prevent metal-to-metal contact unless penetrated. Therefore, it is critical to understand the characteristic of the protective film at nano-scale.

5.3 The influence of oil formulation

For very thin lubricant films, the interaction between surface features on opposite sides of the contact represents the main friction mechanism during rolling or sliding. However, in most cases a molecularly thin layer of lubricant adsorbs to both sides of the contact providing a low shear strength film. This represents the underlying principle, which led to the development of friction reducing lubricant additives.

Engine lubricants consist of a base oil (typically $80 - 95\%$, usually mineral oil) and a large number of additives [64, 65, 66], added in very small concentrations. The base oil can be categorized based on various standards introduced by a number of organizations. The simplest forms of base oil types are mineral oils, Very High Viscosity Index (VHVI) base oils and synthetics. The viscosity of mineral oils, refined from crude oil, are determined by the carbon chain length and processing temperature. The mineral oil usually consists of three to four types of hydrocarbons [66]. The VHVI base oils are mineral oils but with a very high viscosity index which are obtained through a two-stage hydrotreating refinement process. The use of these base oils is increasing because of the compatibility with lower emission engine components. Synthetic base oils consist of molecules of simpler substances in order to provide desired oil properties. These oils are more expensive than typical mineral oils due to the more sophisticated chemical process production. A few of the most commonly used synthetic base oil in automotive applications are: Olefin oligomers, dibasic acid esters, polyol esters and alkylated aromatics [66] .

Additives are added to base oils to achieve specific performance-improving characteristics. The most commonly used additives are: detergent, dispersant, oxidation and corrosion inhibitors, extreme-pessure and antiwear agents, friction modifiers, antioxidant and metal deactivators, viscosity index improvers, antirust agents, pour point depressants and etc [64, 66, 67, 68, 69, 70]. Some of the additives should always be dormant and stable during normal lubrication process and only become active when triggered. For example, antioxidants in the base oil become active only when oxidant free radicals are present [66]. In this study, the focus will be to understand the friction along a tribological conjunction. Therefore, it is important to be able to understand the mechanism of friction reduction introduced by the additives (friction modifiers). As an example, one of the common additives which acts as a friction modifier in a typical engine lubricant is molybdenum.

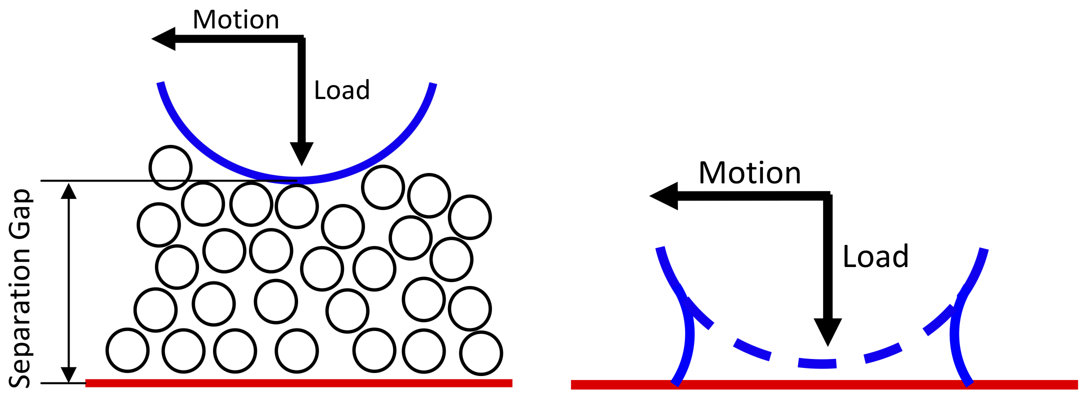

(a) Asperity thin film shearing

(b) Asperity adhesion

Figure 5.2: Asperity contact

Hardy and Doubleday [71] stated that the boundary lubrication at vanishing separations is predominantly influenced by adsorption of additives such as friction modifiers. The adsorption of the thin film on the asperity tips form a low shear strength film which prevents direct metal-to-metal contact, reducing boundary friction. The formation of this protective layer is critical in reducing friction. The characteristics of the friction modifier is dependent on: (i) the type of additive molecules, (ii) asperity deformation, (iii) concentration of additives and (iv) contact temperature.

Short linear hydrocarbons with surface-active end groups are often used as friction modifier in lubricating oil [72, 69]. Studt [69] looked at the influence of adsorbed films on friction considering various types of additives ranging from straight chain to long chain compounds with polar end groups . He showed that shifting the polar end groups of the chain compound to the middle of the chain produces an increase in friction. This is because the chain molecule with polar end groups in the middle of the chain adsorbs parallel to the surface. The existence of other polar compounds in a lubricating system also disrupts the adsorption capability of friction modifiers, which is similar to what Wu and Dacre [73] observed. In their study, Wu and Dacre mentioned that changing the base oil of simple chain hydrocarbon (e.g. hexadecane) to a polar natured synthetic base stock reduced the adsorption rate of the friction modifiers such as zinc di-isopropyl-dithiophosphate (IPZ). This is caused by the competitive adsorption between additives and the polarized base oil, disrupting the formation of a stable protective layer.

The amount of friction modifiers added to the base oil should also be in small quantity. The usual concentration of additives such as ZDDP in a base oil is $\approx 1\%$ to achieve optimum friction reduction [73]. Tung and Gao [74, 75] showed that the base oil (no additives) gives higher friction coefficient before the inclusion of an organic and molybdenum based friction modifier, added in small percentages varying from $0.25 - 1\%$. Podgornik and Vizintin [76] also observed that the friction performance of the friction modifier is dependent on the concentration of the additives (see figure 5.3) and also the contact temperature. Wu and Dacre [73], Choa *et al* [77] and Zhang *et al* [78] observed that the friction reduction introduced by friction modifiers is temperature dependent, where higher temperature induces adsorption, producing a lower friction coefficient. Thermal desorption of this protective layer increases rapidly the friction [79].

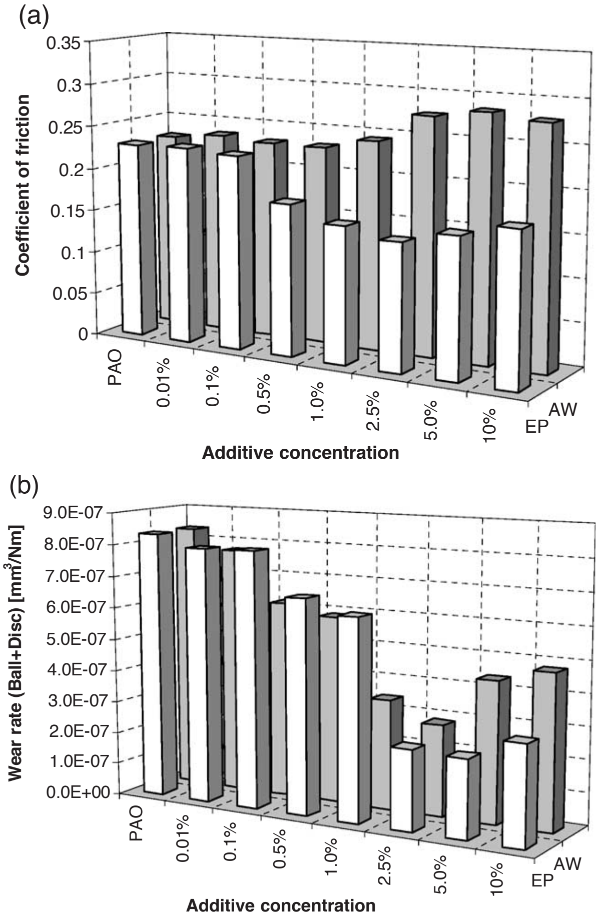

Figure 5.3: Influence of friction modifier concentration on the friction along a contact [76]

Many attempted to model the adsorption of friction modifiers to further understand the extend of friction reduction of this additives. Among them, Jahanmir and Beltzer [80] and So and Lin [81] developed adsorption models to predict friction for an additive component in a lubricant base oil. Jahanmir and Beltzer [80] used as a base Temkin isothermal adsorption model [82] and assumed that friction arises only due to direct surface interaction. They concluded that higher adsorption capability of the additives help reduce friction on contacting surfaces in relative motion.

5.4 The influence of surface texture

A significant amount of research has been conducted to reduce friction especially at the ring-liner conjunction through the control of surface finishing and modifications, leading to the increase of an IC engine's efficiency. Surface characterisation for the cylinder liner is critical as this defines the ring-liner contact especially at the vicinity of power-stroke TDC. It is because at this region, the separation between the ring-liner is small and might inhibit metal-to-metal contact. The probability of asperity interaction depends heavily on the roughness of the liner surface. Tung and Gao [74, 75] observed that the performance of friction modifiers along interacting surfaces vary with coating materials and their deposition methods such as physical vapor deposited diamond-like carbon (DLC) and thermal-sprayed chromium-nitride (CrN). Podgornik and Vizintin [76] also showed that friction modifiers like extreme-pressure (EP) additives had no influence on a certain type of surface coating (e.g. unhydrogenated amorphous carbon coatings). They concluded that the surface topography affects the tribological performance of the friction modifiers. As a result, the specification and control of the liner's surface finishing is very important.

The early liner surfaces have high peaks of asperities which have to be worn down through the "run-in" process. However, with the precision of modern surface finishing techniques, "run-in" liner surfaces can be created through a three-stage honing process: (i) boring (formation of the bore), (ii) base or coarse honing and (iii) plateau honing [83]. The coarse honing of the liner produces a rough surface with high asperity peaks and low valleys as a result of material ploughing. The low valleys on the surface acts as micro-reservoirs to trap lubricants, hence reducing the possibility of lubricant depletion. However, the high asperity peaks increases the friction along the ring-liner contact. Therefore, the plateau honing is used to reduce the asperity peaks but leaves the valleys unaltered. The honing process is considered to be the most familiar and earliest commercial application of surface finishing (see figure 5.4) in an effort to reduce friction [84].

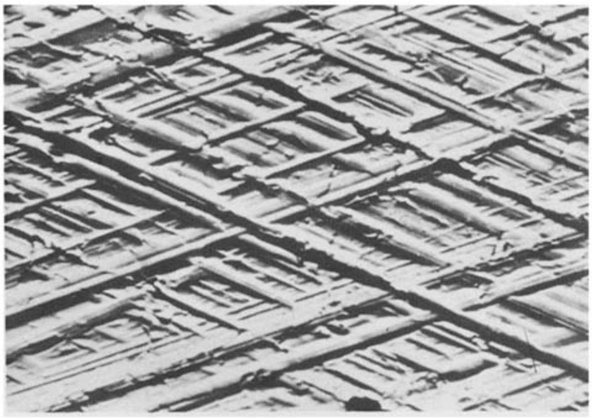

Figure 5.4: Surface after plateau honing [85]

The liner's roughness is heavily dependent on the plateau honing process, which is functionally critical to the tribological conjunction of the ring-liner. The roughness of the plateau-honed surfaces can be characterized using image-processing techniques [86, 87]. However, these techniques provide only qualitative information which cannot be used to understand and control the honing process. As an alternative, the surface finish due to honing can be characterised using various numerical methods which can be useful for tribological studies. The average roughness parameter, R_a is widely used to characterise the liner surface [88]. However, the parameter is not well suited for surfaces generated through a multi-stage process. An alternative method to characterise the liner surface is through linearisation of the bearing area curve [89]. The advantage of this method is that it can take into consideration the effect of multiple processes such as base and plateau honing [90, 91]. An extension to the linearisation of the bearing area curve is the R_k parameters [92] (see figure 5.5). The approach divides the texture into three regions: extreme peaks, core and extreme valleys.

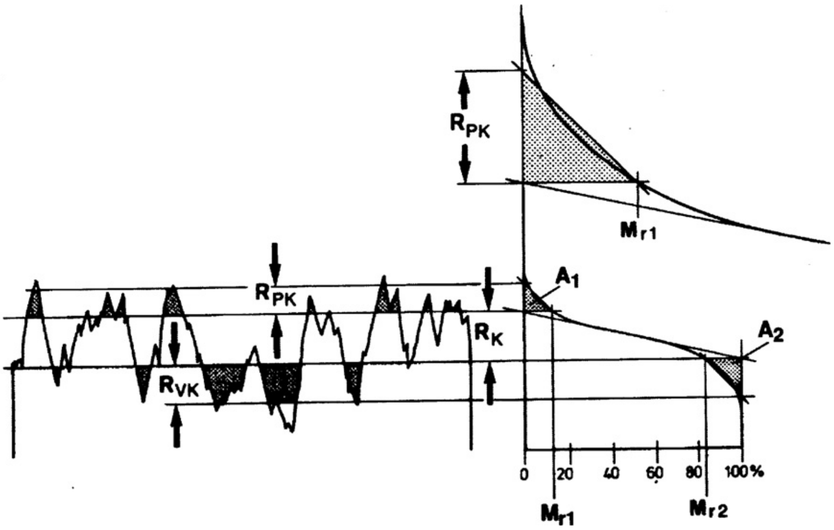

Figure 5.5: Definition of R_k parameters [93]

Surface coatings on the cylinder liner or the ring itself are also meant to improve the tribological performance of the piston ring-liner conjunction. In modern IC engines, numerous types of coatings are used to compensate for the deficiencies of the bulk material used. The surface coatings are meant to improve wear and corrosion resistance. Anti-wear surface coatings are divided into soft and hard coatings. Soft coatings such as molybdenum disulfide are used as sacrificial coatings. Coatings such as diamond-like carbon (DLC), boron nitride, silicon carbide, titanium nitride etc are considered to be hard coatings [94]. The hard coatings have been shown to reduce wear on both the interacting surfaces in quite acidic lubricating oil [74]. For dry steel-to-steel contact, hard coatings such as diamond-like carbon (DLC) reduced the friction by a massive 50% [94]. However, the hard coatings, if not properly deposited, might change the surface topography, hence affecting the adsorption capability of the lubricant additives (e.g. friction modifiers), leading to higher boundary friction [75]. One of the more effective coating method for DLC is through chemical vapor deposition (CVD), which produced a good wear protection [95].

5.5 Surface patterning

Aside from plateau honing and surface coating, well designed surface texturing on either the liner or the ring itself are able to reduce friction. Early studies [96, 97, 98] have shown that having microasperities such as dimples or even grooves impede lubricant flow, hence increasing the film thickness and reducing friction. The concept has been further enhanced for application by [99, 100, 54] on engineering application such as along the ring liner contact.

Recently, Etsion and Burstein [101] introduced microstructures via etching on mechanical seals. The texturing of the seals showed substantial tribological improvements when tested experimentally [102]. The experimental study showed that an optimum friction reduction can be achieved by varying the dimple depth to shape ratio. Ryk *et al* [53], Etsion [99] and Ryk and Etsion [103] later showed that further friction reduction at the piston ring-liner contact can also be achieved by introducing micro-dimples (see figure 5.6) along the surface of the ring itself. The micro-dimples on the ring surface are deposited using Laser Surface Texturing (LST) [53]. These micro-dimples along the ring surface provide micro-reservoirs that will enhance the lubricant retention along the contact. They also experimentally evaluated the effect of partial LST on piston rings and observed at least 25% of friction reduction as compared to a smooth ring on a reciprocating test rig. Recent studies by Tonder [104], Siripuram and Stephens [105] , Dumitru *et al* [106] and Andersson *et al* [107] also showed friction reduction by introducing micro-features on interacting surfaces.

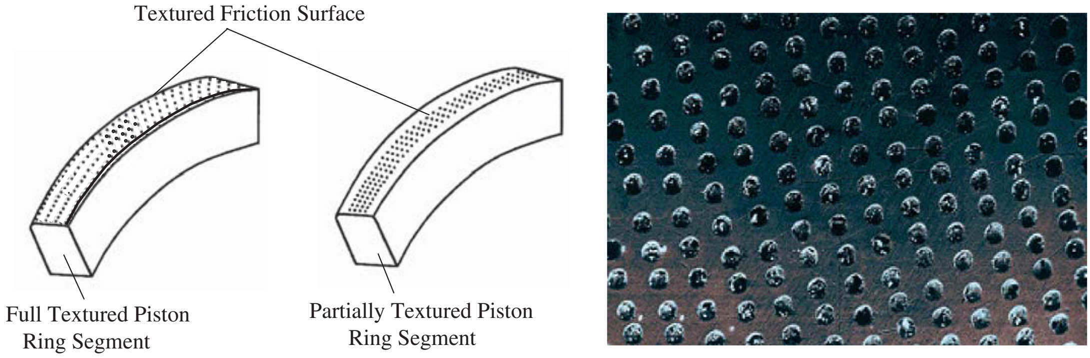

Figure 5.6: Micro-dimples surface texturing on a piston ring [99]

In a later development, Rahnejat *et al* [54] added laser surface textures (see figure 5.7) only along the TDC region of the liner to reduce the friction in the ring-liner contact. This approach is focused solely on the region where friction is highest, which is at the vicinity of the TDC along the liner. Takata *et al* [108] studied the application of dimples and grooves on a ring-liner contact to reduce friction. They observed that friction is reduced as the depths of both dimples and grooves are increased. The same can be noted when the area ratio of the surface textures is increased. However, the groove width and dimple diameter does not influence much the frictional characteristic of the contact

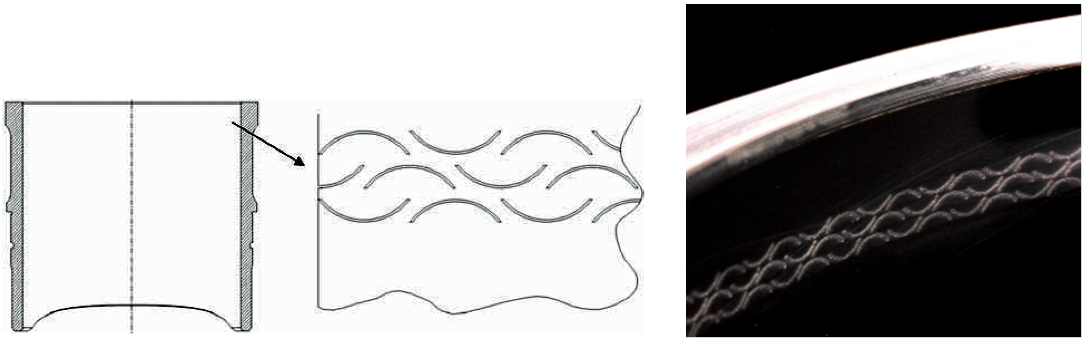

Figure 5.7: Laser etching at the top DC of the cylinder liner [54]

Surface finishing and the introduction of surface textures, either on the ring surface or the cylinder liner, will definitely affect the surface roughness of the contact. Hence, this will influence the probability of asperity interactions between the ring-liner contact especially along the vicinity of the power stroke TDC. For example, in figure 5.8(a), the gap between the ring and liner becomes small as the piston reaches the TDC especially during the power stroke. As a result of this, the surface asperities, due to surface roughnesses, at the ring and liner might interact. To reduce friction, the surface textures at the TDC of the liner is introduced. As the piston ring passes through the laser etched region (see figure 5.8(b)), the ring now interacts with the larger asperities which exist due to the laser etching process.

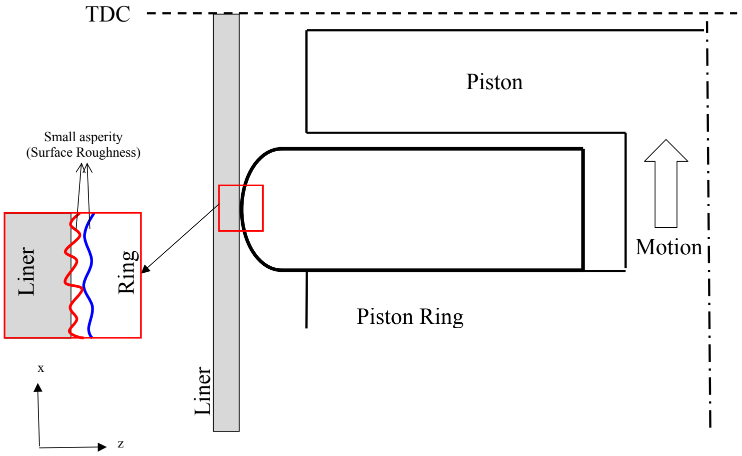

(a) Typical liner

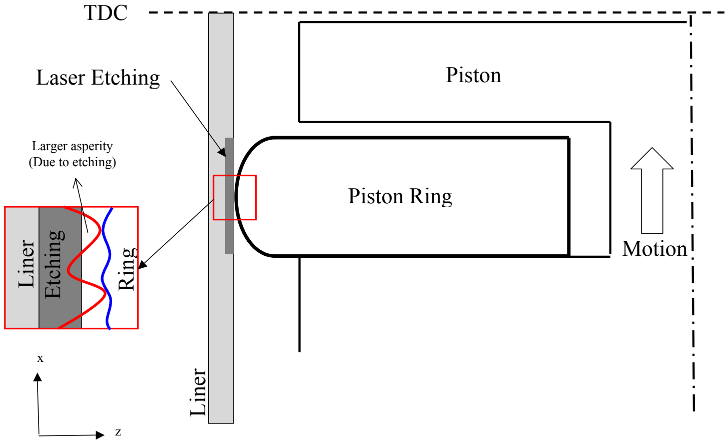

(b) Surface textures at top DC of the liner [54]

Figure 5.8: Asperity interaction along the piston ring-liner conjunction

Therefore, by introducing measures to reduce friction in the piston ring-liner conjunction via control of surface finish, coating and texturing, the piston ring might go through a rougher surface at the vicinity of the power stroke TDC (see figure 5.8). The increased significance of asperity interactions produces different tribological characteristics, which require further understanding, as compared to the conventional tribological approaches. This leads to a different kind of tribology: nano-tribology, which will be subject of interest in the following chapters.

Chapter 6

Review of friction and adhesion at small scale

6.1 Introduction

Engineering surfaces are rarely smooth. They comprise micro-scale surface features, which are either unintentional (a side effect of most manufacturing processes [83, 84, 85]) or intentional to promote specific surface properties (e.g. surface coating [74, 75, 94, 95], micro-dimples and grooves [53, 99, 101, 103, 54]). Cylinder liner surface finishing (e.g. plateau honing (see figure 5.4) in *Chapter 5*) consists of a rough surface with high peaks (asperities) and low valleys, which represent lubricant trapping micro-reservoirs, hence reducing the ring-liner friction. It is also noted that by introducing surface features on the liner or ring surface (see figure 5.6 and 5.7), the frictional losses along the ring-liner contact can be reduced.

In a ring-liner conjunction, a very thin layer of lubricant film usually prevails during the entire engine cycle. This is relatively thick in the mid-stroke and very thin at the reversals, with the thinnest film at the vicinity of the power stroke TDC. Although very thin, this film provides a low shear strength protective film, which is essential for the engine operation. *Chapter 2* proposed a friction model based on Greenwood and Tripp's [51] asperity distribution model. The friction model divides the friction in two: viscous and boundary friction. The viscous friction is caused by shearing the bulk lubricant, while the boundary friction is the result of shearing a very thin film (several layers of molecules), which prevails between interacting asperity tips.

If, the protective layer is penetrated, direct metal-to-metal contact between opposing surface asperities cannot be avoided. It was noted that adding a carefully chosen surface texture to the ring [53, 99, 101, 103] or to the liner surface [54] in the vicinity of the TDC, the film thickness could increase, reducing the chance of metal-to-metal contact and consequently the friction force. One possible drawback of adding surface textures in the vicinity of the TDC (with the intended purpose of carving reservoirs of fluid to be released when the film is excessively thin) is that the manufacturing technique could unintentionally generate micro-scale buildups of material, which for ultra-low films would unavoidably increase the probability of metal-to-metal contact. Therefore, a friction force predictive model should include a fluid film shear component as well as a possible asperity-to-asperity contact. The current chapter investigates the direct contact between idealised spherical asperities. The interaction between asperities separated by thin adhered films will be investigated in *Chapter 7 and 8* while the extension to rough surfaces will be included in *Chapter 9*

These asperities will deform in the vicinity of the initial contact (assumed as single point contact) over an area when being further loaded. One of the first models to describe the deflection and area of an elastic contact was proposed by Hertz [109] in 1881. The contact between a flat plane and a sphere, under a normal load, P results in a contact area described by a contact radius, a (see figure 6.1).

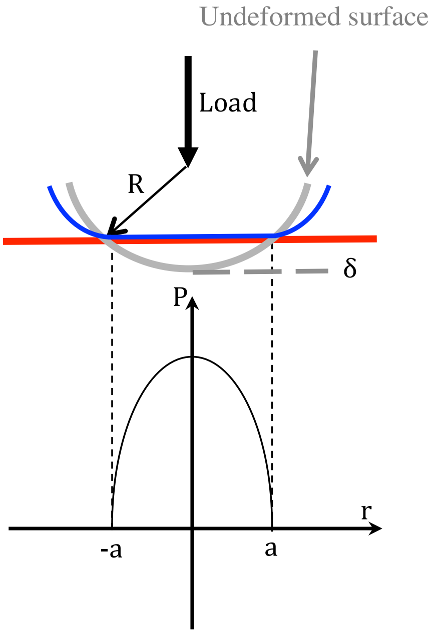

Figure 6.1: Hertzian contact model

The contact load, P and the contact deflection, δ can be expressed as functions of the contact radius, a as:

$$P = \frac{4E^*a^3}{3R} \tag{6.1}$$

$$\delta = \frac{a^2}{R} \tag{6.2}$$

where $1/E^* = \left(1-\nu_1^2\right)/E_1 + \left(1-\nu_2^2\right)/E_2$ and $1/R = 1/R_1 + 1/R_2$

One of the main assumptions of this model is that the material is homogeneous, isotropic, linear elastic and it does not account for surface adhesion [109]. Bradley [110] proposed a contact model between rigid spheres brought in contact based purely on the surface forces (e.g. van der Waals force). Bradley described the *pull-off* force, which refers to the force required to overcome adhesion as:

$$P_{\textit{pull-off}} = 2\pi\Delta\gamma R \tag{6.3}$$

Johnson *et al.* [111] suggested that attractive surface forces, which are significant at low loads, occur within contacting bodies. They observed experimentally that measurements of contact areas were larger than the ones predicted by the Hertzian theory. Therefore, Johnson, Kendall and Roberts proposed an adhesion model commonly known as JKR (see figure 6.2), which assumes that the adhesion force elastically deforms the contact and thus increases the contact area beyond that predicted by Hertz [112].

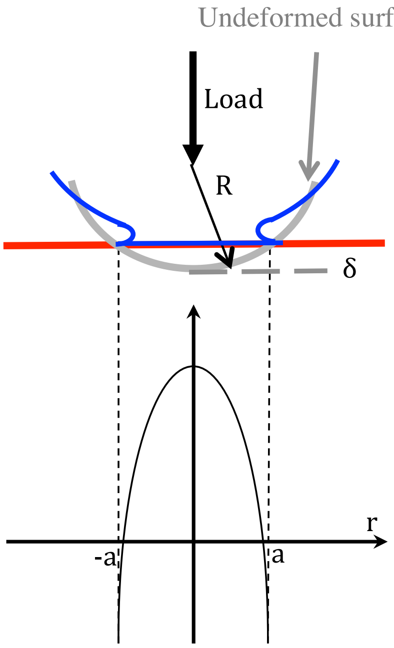

Figure 6.2: JKR adhesion model

The contact load, P and deflection, δ computed using the JKR model are:

$$P = \frac{4E^*a^3}{3R} - \sqrt{8\pi a^3 \Delta\gamma E^*} \tag{6.4}$$

$$\delta = \frac{a^2}{R} - \sqrt{\frac{2\pi a \Delta\gamma}{E^*}} \tag{6.5}$$

The *pull-off* force for the JKR model is expressed as:

$$P_{\textit{pull-off}} = \frac{3}{2}\pi\Delta\gamma R \tag{6.6}$$

Derjaguin, Muller and Toporov [113] proposed a separate set of equations to take into account the effect of adhesion caused by attractive surface forces along the contact of elastic bodies. They assumed that the deformed profile in the contact area follows the Hertzian contact with adhesion occurring only outside the contact area, which leads to the DMT model (see figure 6.3). In the model, the contact area goes to zero when the pull-off force is reached.

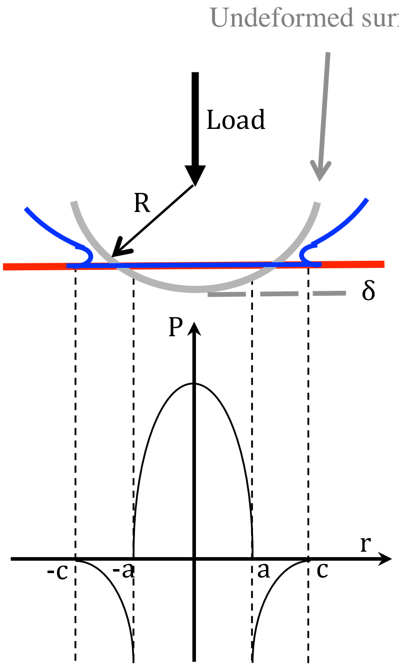

Figure 6.3: DMT contact model

According to the DMT contact model, the contact load, P and deflection, δ can be computed as:

$$P = \frac{4E^*a^3}{3R} - 2\pi\Delta\gamma R \tag{6.7}$$

$$\delta = \frac{a^2}{R} \tag{6.8}$$

The *pull-off* force for the DMT contact model is as follow:

$$P_{\textit{pull-off}} = 2\pi\Delta\gamma R \tag{6.9}$$

Figure 6.4 shows the comparison of the contact forces computed using the Hertz, JKR and DMT models. Due to their conflicting boundary conditions, the validity of both models was initially disputed. It was concluded that JKR model predicts the contact area more accurately when surface forces are short-ranged as compared to the resulting elastic deformation. This model is well suited for larger-radius compliant solids with a less stiff material such as rubber [112]. DMT model predicts more accurately the behaviour of surface forces, which could be considered as long-ranged with respect to the elastic deformation. The DMT model is suitable for stiff spheres with smaller radii.

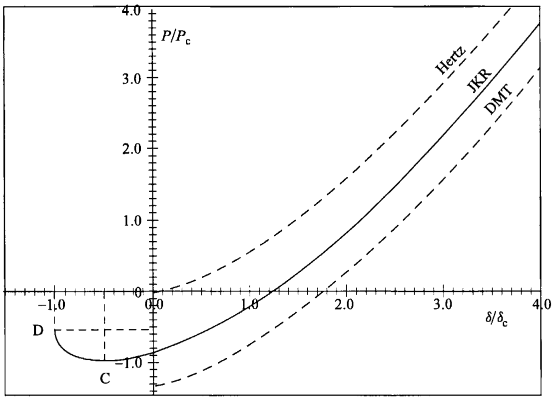

Figure 6.4: Comparison of the normalized adhesion force in the function of normalized deflection for Hertzian, JKR and DMT models [114]

In order to approximate the interaction or contact behaviour using the appropriate model, the Tabor parameter, μ was introduced as a measure for the magnitude of the elastic deformation as compared to the range of surface forces [115]. μ can be expresses as:

$$\mu = \frac{\Delta\gamma^2 R}{(E^*)^2 z_0^3}^{1/3} \tag{6.10}$$

where z_0 is the equilibrium spacing in the Lennard-Jones potential. For $\mu >> 1$, the adhesion contact is reduced to the JKR model. When $\mu << 1$, the DMT model is more appropriate to predict the adhesion characteristics between the contact.

$$\begin{aligned} \mu &>> 1 \rightarrow \text{DMT theory} \\ \mu &<< 1 \rightarrow \text{JKR theory} \end{aligned} \tag{6.11}$$

Hertz's model does not take into account the attractive force and assumes only hard wall repulsion at the contact surfaces. Bradley's model considers adhesion between contact surfaces but neglected the deflection occurring within the contact. The JKR and DMT models include the opposite ends of the short-range and long range adhesion respectively which act within the contact area. However, there were no models which considered the intermediate transition of the contact between the JKR and DMT model. Therefore, Maugis [116] attempted to overcome this deficiency by producing predictions closer to an actual interaction force where the integral of the attractive force corresponds well to the work of adhesion, γ (see figure 6.5). The proposed model is capable of predicting the contact work for the whole range of different material characteristics.

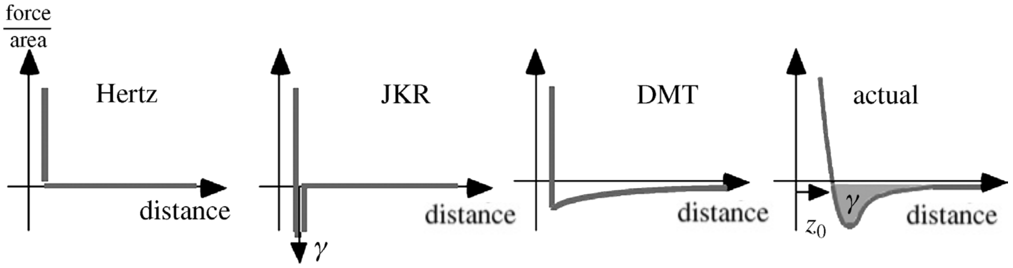

Figure 6.5: Adhesion force potentials for various contact models [117]

Maugis' model uses the Dugdale potential (see figure 6.6 (a)) to describe the attractive forces between contacting surfaces [116]. His model not only predicts the adhesion in a more realistic way (via the Dugdale potential), but also fills the transitional gap between the JKR and DMT contact models (see figure 6.6 (b)). The transitional parameter, λ determines the type of adhesion mode of the contacting solids. If $\lambda > 5$, the model can be reduced to a JKR model. If $\lambda < 0.1$, the model can then be approximated to the DMT contact model. When $0.1 < \lambda < 5$, the model will be able to predict a transitional period, where the adhesion regime is between the JKR and DMT contact models.

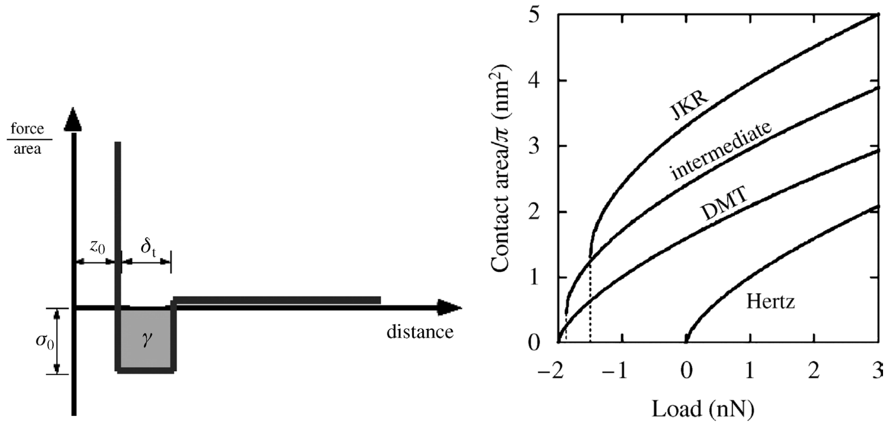

(a) Dugdale potential

(b) Transitional regime between the JKR and DMT contact model

Figure 6.6: Maugis-Dugdale contact [117]

The contact load, P and deflection, δ as described by Maugis are (see figure 6.7):

$$P = \frac{4E^*a^3}{3R} - 2\sigma_0 \left[c^2 cos^{-1}\left(\frac{a}{c}\right) + a\sqrt{c^2 - a^2}\right] \tag{6.12}$$

$$\delta = \frac{a^2}{R} - \left(\frac{2\sigma_0}{E^*}\right)\sqrt{c^2 - a^2} \tag{6.13}$$

where σ_0 is the adhesive force intensity which extends to the contact radius c.

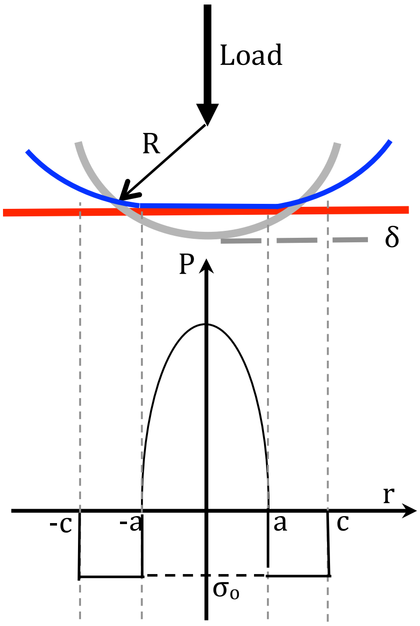

(a) Schematics of contact

Figure 6.7: Maugis-Dugdale model

The adhesive traction for the Dugdale model will fall to zero when the separation between the contacting surfaces exceeds $\Delta\gamma/\sigma_0$. Therefore,

$$h(c) + h_a(c) = \frac{\Delta\gamma}{\sigma_0} \tag{6.14}$$

where

$$h(c) = \frac{c^2}{2R} - \frac{a^2}{R} + \frac{1}{\pi R}\left[\left(2a^2 - c^2\right) sin^{-1}\left(\frac{a}{c}\right) + a\sqrt{c^2 - a^2}\right]$$

$$h_a(c) = \frac{4\sigma_0}{\pi E^*}\left[\sqrt{c^2 - a^2} cos^{-1}\left(\frac{a}{c}\right) + a - c\right]$$

Johnson and Greenwood [118] produced an adhesion map based on all the adhesion contact models discussed above. The map is based on the transitional parameter, λ of Maugis' contact model (see figure 6.8). The purpose of the map is to provide guidance as to which contact model is more appropriate to be used to predict the adhesion characteristics of the desired contact conditions.

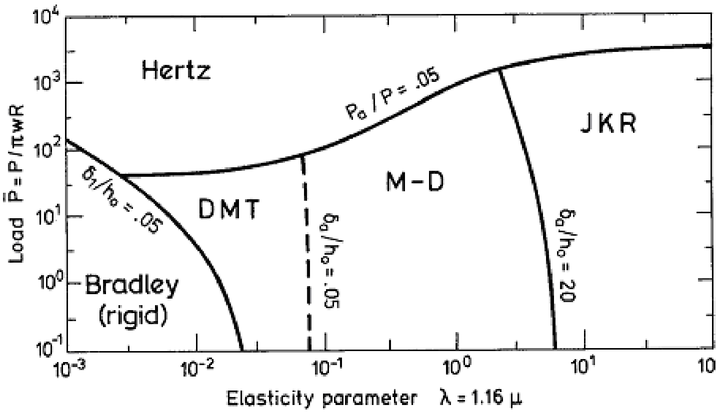

Figure 6.8: Adhesion map [118]

Adhesion within the contacting bodies increases the contact area as compared to the actual contact area predicted using the Hertzian theory. Grierson *et al* [117] and Carpick and Salmeron [119] have shown that the friction force within a single asperity contact is proportional to the actual contact area. Grierson *et al* [117] measured the friction force for a single asperity contact using an Atomic Force Microscopy (AFM) (Figure 6.9). They curved fit the data towards a few contact models such as the JKR and DMT model depending on the contact conditions.

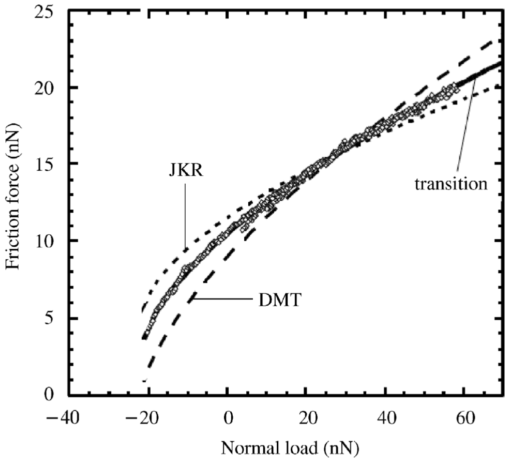

Figure 6.9: Experimental measurements of friction along a single asperity contact using the Atomic Force Microscopy (AFM) [117]

The friction caused by adhesion force for a single asperity, P_f can be obtained by:

$$P_f = \tau_a \times A \tag{6.15}$$

where τ_a is the interfacial shear strength and A is the actual contact area of the asperity contact.

6.2 Elastic point contact

The chapter is aimed at improving the understanding of asperity interactions considering surface adhesion. As the first attempt to build an adhesive contact model, the asperity related parameters in table 6.1 are used to model the Hertz, JKR and Maugis-Dugdale models. The parameters used for the current study are as tabulated unless stated otherwise.

Table 6.1: Single asperity contact model input parameters [120]

Parameters	**Values**
$\Delta\gamma$	0.1 J/m^2
z_o	0.235 nm
R	50 nm [121]
τ_a	$0.8GPa$

Hertzian Contact

To model an asperity contact using the Hertzian assumption, the normalised contact load, $\bar{P}$ and deflection, $\bar{\delta}$ can be expressed as [122]:

$$\begin{aligned} \bar{P} &= \bar{a}^3 \\ \bar{\delta} &= 3^{2/3}\bar{a}^2 \end{aligned} \tag{6.16}$$

where

$$\begin{aligned}\bar{P} &= \frac{P}{3\pi\Delta\gamma R} \\ \bar{a} &= a\left(\frac{4E^*}{9\pi\Delta\gamma R^2}\right)^{\frac{1}{3}} \\ \bar{\delta} &= \delta\left(\frac{16E^{*2}}{9\pi^2\Delta\gamma^2 R}\right)^{\frac{1}{3}}\end{aligned}$$

The change in contact load and radius as the asperity is being loaded are shown in figure 6.10. It can be observed that contact starts to occur at the initial point of contact. An interesting thing to note is that the separation between the approaching surfaces is negative. The negative value represents interference of the contact surface (see figure 6.11). The use of the term separation is to enable a unified y-axis through out the study involving asperity contact.

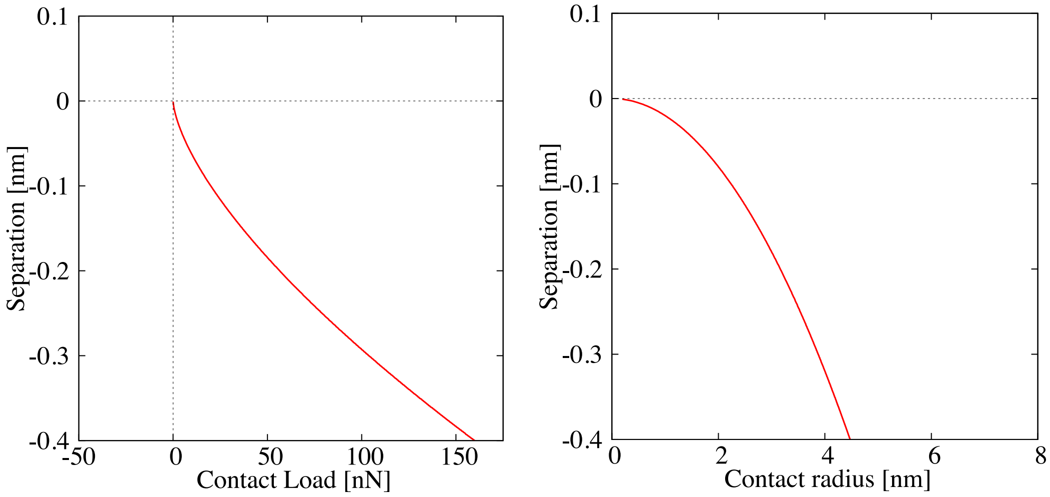

(a) Contact load (b) Contact load

Figure 6.10: Hertzian contact

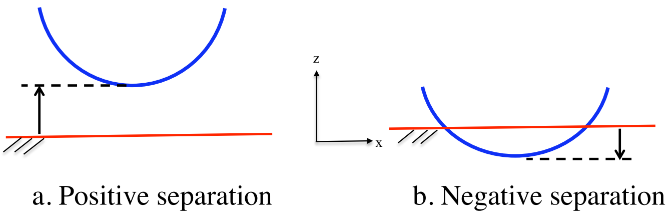

Figure 6.11: Sign convention for the defined term - Separation

JKR Model

As the lubricant layer starts to deplete, asperity adhesion for an elastic contact might occur depending on the critical *pull-off* characteristics of the contact material - the critical asperity stretching, $\delta_{\textit{pull-off}}$. It is assumed that the adhesion is instantaneous as the asperities come close enough to "jump-in" contact. The contact load inclusive of adhesion can be computed using the JKR model. The normalised contact load, $\bar{P}$ and deflection, $\bar{\delta}$ can be expressed in the function of the normalised contact radius, $\bar{a}$ as [123]:

$$\bar{P} = 2(\bar{a}^3 - \sqrt{2\bar{a}^3}) \tag{6.17}$$

$$\bar{\delta} = 2.29.\bar{a}^2\left(1 - \frac{2\sqrt{2}}{3}\bar{a}^{-3/2}\right) \tag{6.18}$$

where

$$\begin{aligned}
\bar{P} &= \frac{P}{2P_{\textit{pull-off}}} \\
\bar{a} &= a\left(\frac{4E^*}{9\pi\Delta\gamma R^2}\right)^{\frac{1}{3}} \\
\bar{\delta} &= \left(\frac{3}{4}\right)^{\frac{1}{3}}\frac{\delta}{\delta_{\textit{pull-off}}} \\
P_{\textit{pull-off}} &= \frac{3\pi R\Delta\gamma}{2} \\
\delta_{\textit{pull-off}} &= \frac{1}{3R}\left(\frac{9RP_{\textit{pull-off}}}{4E^*}\right)^{\frac{2}{3}}
\end{aligned} \tag{6.19}$$

Figure 6.12 illustrates the influence of adhesion on the change in contact load and radius. The initial contact can be observed to occur even before the asperity comes into physical contact with the flat surface. This is due to the work of adhesion pulling the asperity to cause the "jump-in" the contact. A comparison with the Hertzian theory shows that the contact load is more negative due to the work of adhesion. As a result of the adhesion, the contact radius is larger than the one predicted by the Hertzian theory.

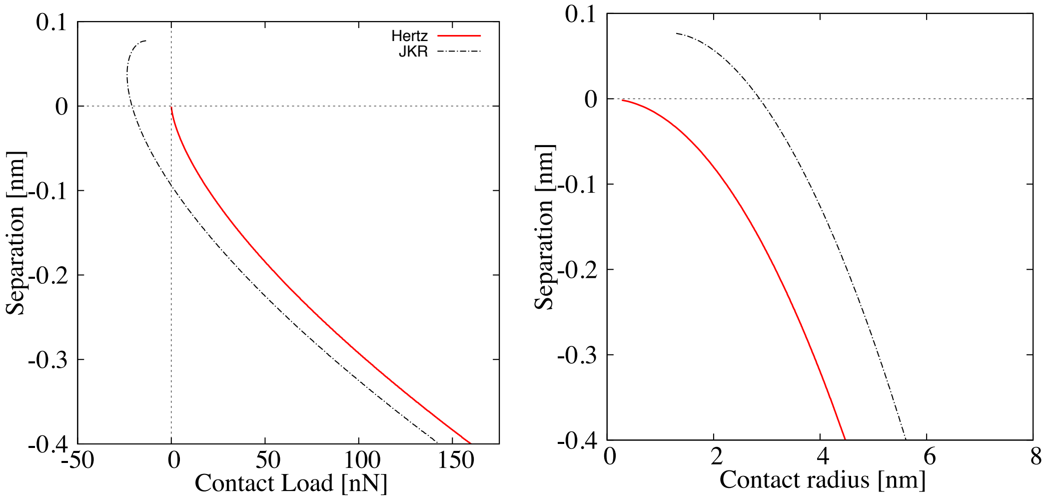

(a) Contact load (b) Contact radius

Figure 6.12: Adhesive contact - JKR

Maugis-Dugdale Model

The selection of appropriate contact model depends on the Tabor parameter, μ. The contact model proposed by Maugis [116] is more flexible as it covers a wider range of contact conditions and material parameters ranging from JKR to DMT contact model and also the transitional region between the JKR and DMT contact model. The normalised contact load, $\bar{P}$ and asperity deflection, $\bar{\delta}$ based on the Maugis-Dugdale model can be described as [122]:

$$\bar{P} = \bar{a}^3 - \lambda\bar{a}^2\left[\sqrt{m^2-1} + m^2 cos^{-1}\left(\frac{1}{m}\right) - m + 1\right] \tag{6.20}$$

$$\bar{\delta} = \bar{a}^2 - \frac{4}{3}\bar{a}\sqrt{m^2-1} \tag{6.21}$$

To be able to apply the Maugis-Dugdale contact model, assuming that $m = c/a$, the solution of $\bar{P}$ and $\bar{\delta}$ must fulfil the condition from equation (6.15) as expressed in non-dimensional terms as follow:

$$\frac{1}{2}\lambda\bar{a}^2\left[(m^2-1)cos^{-1}\left(\frac{1}{m}\right) + \sqrt{m^2-1}\right] + \frac{4}{3}\lambda^2\bar{a}\left[(m^2-1)cos^{-1}\left(\frac{1}{m}\right) - m + 1\right] = 1 \tag{6.22}$$

where

$$
\begin{aligned}
\lambda &= 2\sigma_0 \left(\frac{9R}{16\pi\Delta\gamma E^{*2}} \right)^{\frac{1}{3}} \\
\bar{a} &= a \left(\frac{4E^*}{3\pi\Delta\gamma R^2} \right)^{\frac{1}{3}} \\
\bar{c} &= c \left(\frac{4E^*}{3\pi\Delta\gamma R^2} \right)^{\frac{1}{3}} \\
\bar{\delta} &= \delta \left(\frac{16E^{*2}}{9\pi^2\Delta\gamma^2 R} \right)^{\frac{1}{3}}
\end{aligned}
$$

Assuming the same surface energy, $\Delta\gamma$ (see table 6.1), it can be seen that the contact load and radius predicted using the Maugis-Dugdale (MD) model shows a clear distinction from the ones of the Hertz and JKR model. The Tabor's parameter, μ for the given asperity contact configuration is about 0.2, which is closer to the DMT model. Therefore, care must be taken when choosing the appropriate adhesion model in order to prevent any unnecessary inaccuracy.

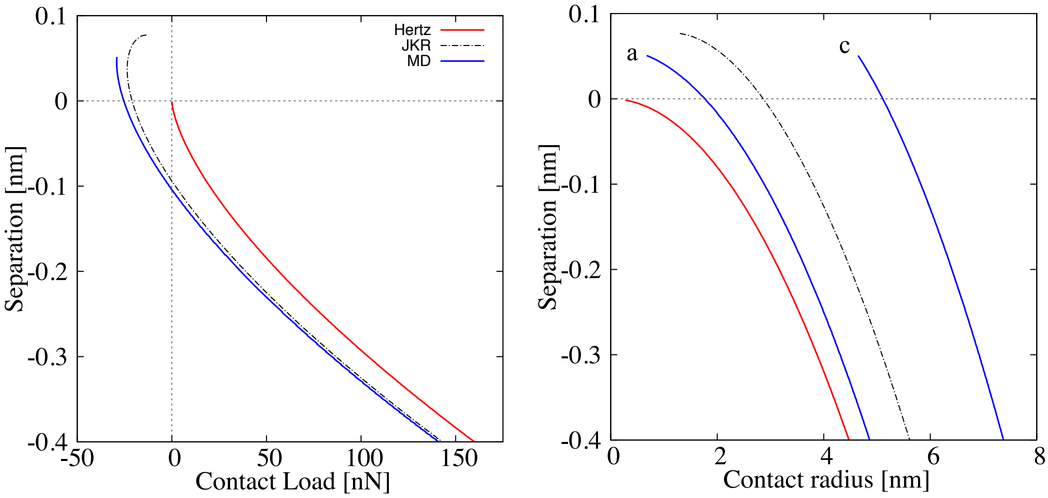

(a) Contact load

(b) Contact load

Figure 6.13: Adhesive contact - Maugis-Dugdale

Figure 6.14 shows the pressure distribution along the asperity contact for different contact models. Hertzian contact assumes zero pressure outside the contact area. The JKR model assumes an infinite adhesion pressure along the contact radius. This can be observed through the sharp spikes along the pressure distribution. The

Maugis-Dugdale model assumes a constant adhesion pressure of intensity σ_0 between contact radius c and a.

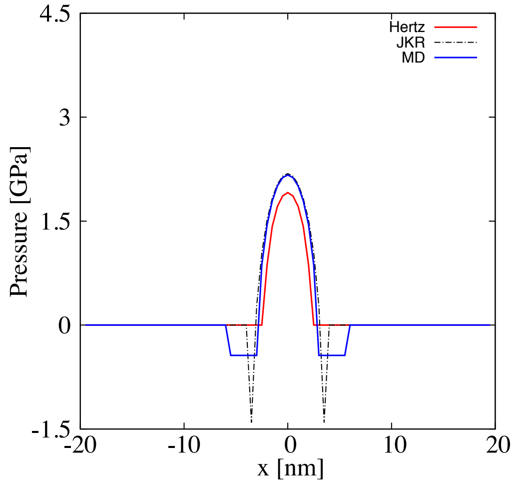

Figure 6.14: Adhesive contact

Friction - Elastic Contact

The friction along the adhered contact is computed assuming the interfacial shear strength, τ_a as $0.8GPa$ (see Table 6.1). Figure 6.15 shows the friction force predicted using the contact area computed based on the Hertz, JKR and Maugis-Dugdale model. The friction force predicted here refers to the resisting force of the contact towards motion. The resisting force that needs to be overcome originates from the work of adhesion for an adhered contact. Due to a larger contact area, the Maugis-Dugdale model predicts a larger friction force. The friction plot below also shows that using the inappropriate contact model might under- or over-estimate the friction between the contact.

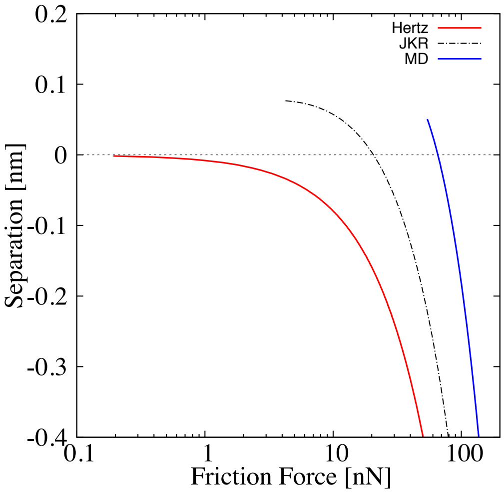

Figure 6.15: Friction due to adhesive contact pressure distribution

6.3 Elastoplastic point contact

Adhesion models for elastic contacts are well understood. However, as the contact is being further loaded, the deformation of the surface will eventually go beyond the yield point, leading to plastic deformation. Therefore, it is very critical to be able to take into consideration the transition of elastic towards elastoplastic or even plastic deformation. A large number of research papers discussed on the adhesion of contacting elastic spheres. However, not many focused on the elastoplastic and fully plastic contact regimes. Pollock [124], Pethica and Tabor [125] and Maugis and Pollock [126] modelled the contacting spheres in the fully plastic region. Chang *et al* [127] used an improved DMT model to study adhesion along the elastoplastic region. Peng and Guo [128] also proposed an adhesion model considering the elastic and fully plastic deformation for asperities. The model was integrated onto a fractal surface. The proposed asperity model considers only either fully elastic or fully plastic asperity deformation.

Lately, Kogut and Etsion [112] proposed an elastoplastic adhesion model based on a similar finite element analysis they applied in an earlier paper for a Hertzian contact [129]. The adhesion model applies the DMT contact model and assumed that the attractive forces act outside the contact area. The assumption limits their model to small curvature radii enough to range from typical asperity summits along a rough surface to AFM tips for stiff materials. Kogut and Etsion considered that the adhesion force might only be significant with respect to the contact load in the elastic regime and early stages of the elastoplastic regime. The adhesion force may then become negligible when the contact becomes fully plastic.

Jackson and Green [130] proposed a separate set of expressions to describe the elastoplastic behaviour of a sphere contact against a rigid flat surface. They derived the model based also on a finite element analysis. The model can be used for macro (e.g. bearings) and micro (e.g. asperity) contacts. The proposed set of expressions can be extended for use in rough surface analysis. The von Mises criterion is used to describe the yielding of the material. Jackson and Green's model considered the geometry and material effects which was not included in Kogut and Etsion's [129] model. They also pointed out that the material hardness changes with the evolving contact geometry and material properties. The hardness that they refer to is biased towards the measure of resistance to dislocation movement in the material, which is related to the yield strength of the material. Their model is set up in the way that the plasticity deformation is embedded in the set of expressions derived.

6.3.1 Hertzian Contact

This section attempts to include the elastoplastic deformation to an asperity contact. As an initial approach, it is assumed that the elastoplastic deformation occurs only within the contact region. The model proposed by Jackson and Green [130] for Hertzian contact is used in the study. Their method assumes that the load-deflection of the contact follows the Hertzian contact during elastic deformation. When yielding starts to occur, the contact characteristics can be described using the expressions derived from Jackson and Green's [130] finite-element-analysis. Therefore, the contact load and deflection for a Hertzian point contact under elastoplastic condition are:

$$\begin{aligned} P_{ep} &= P_c \left\{ e^{-0.25(\delta^*)^{5/12}} (\delta^*)^{3/2} + \frac{4H_G}{CS_y} \left[1 - e^{-0.04(\delta^*)^{5/9}} \right] \delta^* \right\} && (6.23) \\ \delta_{ep} &= \delta_c \left[\left(\frac{a}{a_c} \right)^2 (\delta_t)^B \right]^{\frac{1}{B+1}} && (6.24) \end{aligned}$$

where

$$\begin{aligned}
\delta_t &= 1.9 \\
\delta^* &= \frac{\delta_{ep}}{\delta_c} \\
\delta_c &= \left(\frac{\pi C S_y}{2E^*}\right)^2 R \\
a_c &= \frac{\pi C S_y R}{2E^*} \\
P_c &= \frac{4}{3}\left(\frac{R}{E^*}\right)^2 \left(\frac{\pi C S_y}{2}\right)^3 \\
\frac{H_G}{S_y} &= 2.84\left\{1 - e^{-0.82\left[\frac{\pi C e_y}{2}\sqrt{\delta^*}\left(\frac{\delta^*}{\delta_t}\right)^{B/2}\right]^{-0.7}}\right\} \\
C &= 1.295e^{0.736\nu} \\
B &= 0.14e^{23e_y} \\
e_y &= \frac{S_y}{E^*} \\
S_y &= \frac{\text{Material Hardness}}{2.8}
\end{aligned}$$

The set of expressions above are a combination of finite element analysis and analytical approximations. The critical interference, δ_c refers to the initial point of yielding. Jackson and Green [130] derived the expression for δ_c using the von Mises criterion. The Poisson's ratio used in the model is for the material which has the lower yield strength of the two contacting surfaces. Using the critical interference, the critical load, P_c can be computed. These critical values predict analytically the boundary where initial plasticity starts to occur. The model can also support the fully plastic deformation of the contact. S_y in the model is the von Mises yield criterion while H_G is the limiting average pressure of the material. In the study, the *material hardness* is assumed to be $5.1GPa$. To model the elastoplastic Hertzian contact, the normalised contact load, $\bar{P}$ and asperity deflection, $\bar{\delta}$ can be described as:

$$\bar{P} = \bar{P}_1 \tag{6.25}$$

$$\bar{\delta} = \bar{\delta}_1 \tag{6.26}$$

where

$$\begin{aligned}
\bar{P}_1 &= \begin{cases} \bar{a}^3 & \Rightarrow \quad \text{if } \delta^* < \delta_t \\ \frac{P_{ep}}{\pi \Delta\gamma R} & \Rightarrow \quad \text{if } \delta^* \geq \delta_t \end{cases} \\
\bar{\delta}_1 &= \begin{cases} \bar{a}^2 & \Rightarrow \quad \text{if } \delta^* < \delta_t \\ \delta_{ep} \left(\frac{16E^{*2}}{9\pi^2 \Delta\gamma^2 R} \right)^{\frac{1}{3}} & \Rightarrow \quad \text{if } \delta^* \geq \delta_t \end{cases}
\end{aligned} \tag{6.27}$$

Figure 6.16 differentiates the contact load and radius predicted using the elastic and elastoplastic Hertzian model. It can be seen that by introducing the effect of elastoplastic, the contact load is being decreased when the separation or interference goes beyond the critical interference, δ_c. As part of the contact is now plastically deformed, a slight increase in load will increase the contact area further. This can be observed through the increased contact radius for separations exceeding δ_c as compared to the fully elastic model's prediction of the contact radius.

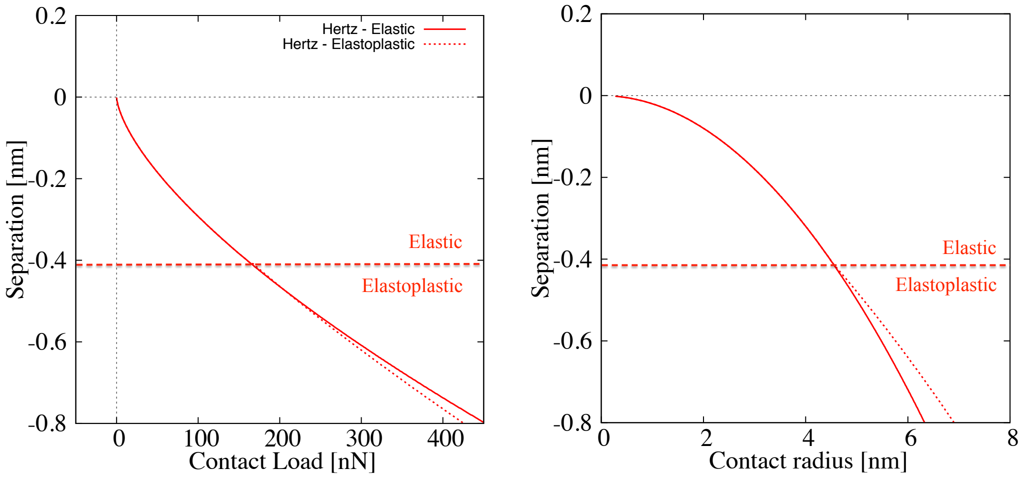

(a) Contact load (b) Contact radius

Figure 6.16: Elastoplastic Hertzian contact

6.3.2 Maugis-Dugdale Adhesion Model

To integrate the elastoplastic model by Jackson and Green [130] onto the Maugis-Dugdale adhesion model, it is assumed that the elastoplastic deformation strictly occurs only within the contact area and the adherence of the contacting surface happens only outside the contact area. This limits the model to adhesion behaving in a similar manner to the DMT model. Therefore, the normalised contact load,

$\bar{P}$ and the normalised asperity deflection, $\bar{\delta}$ for the elastoplasctic contact using the Maugis-Dugdale model can then be described as:

$$\begin{aligned} \bar{P} &= \bar{P}_1 - \lambda \bar{a}^2 \left[\sqrt{m^2 - 1} + m^2 cos^{-1} \left(\frac{1}{m} \right) - m + 1 \right] & (6.28) \\ \bar{\delta} &= \bar{\delta}_1 - \frac{4}{3} \bar{a} \sqrt{m^2 - 1} & (6.29) \end{aligned}$$

where

$$\begin{aligned} \bar{P}_1 &= \begin{cases} \bar{a}^3 & \Rightarrow \quad \text{if } \delta^* < \delta_t \\ \frac{P_{ep}}{\pi \Delta\gamma R} & \Rightarrow \quad \text{if } \delta^* \geq \delta_t \end{cases} \\ \bar{\delta}_1 &= \begin{cases} \bar{a}^2 & \Rightarrow \quad \text{if } \delta^* < \delta_t \\ \delta_{ep} \left(\frac{16E^{*2}}{9\pi^2 \Delta\gamma^2 R} \right)^{\frac{1}{3}} & \Rightarrow \quad \text{if } \delta^* \geq \delta_t \end{cases} \end{aligned} \qquad (6.30)$$

To be able to apply the Maugis-Dugdale contact model, the solution of $\bar{P}$ and $\bar{\delta}$ must fulfil the condition that the Tabor's parameter, μ must be smaller than unity. This means that the adhesion of the contacting surfaces is focused outside of the contact area. For μ larger than unity, adhesion will start to affect the deformation along the actual contact area, which the model might not be able to produce an accurate enough prediction for this kind of contact characteristics.

Using the parameters as in table 6.1, the Tabor's parameter, μ is about 0.2, which fits nicely into the assumed criteria. Figure 6.17 shows the contact load and radius predicted using the fully elastic and elastoplastic adhesion model. As mentioned before, when the contact undergoes elastoplastic deformation, a slight increase in load will easily increase the contact area via a larger deformation. The increase in contact area is reflected in the change in contact radius when the separation or interference of the contact exceeds the critical interference, δ_c as shown in figure 6.17(b).

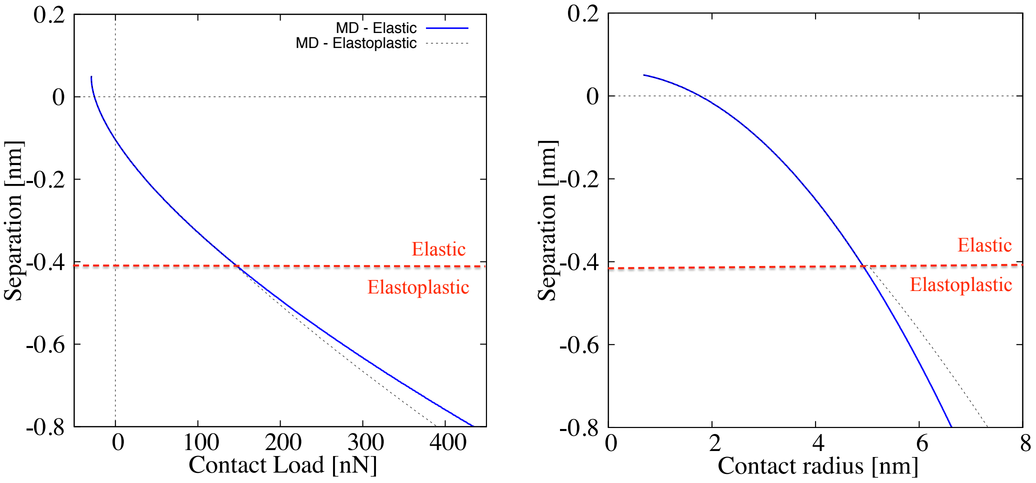

(a) Contact load (b) Contact radius

Figure 6.17: Elastoplastic adhesive contact - Maugis-Dugdale

Friction - Elastoplastic contact

When the asperities on the surfaces interact and goes through elastoplastic deformation, the plastically deformed region of the contact (separation, $\delta > \delta_c$) will then interlock against each other (see figure 6.18). During the elastoplastic deformation, the asperity contact goes through a combination of adhesive and ploughing friction. Therefore, it is very critical to consider the ploughing action of the elastoplastic contact.

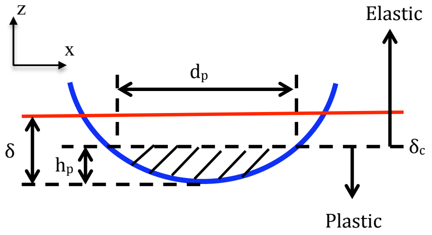

Figure 6.18: Elastoplastic contact

The only way for the interlock section (plastically deformed region) to have relative motion laterally is through local displacement of the opposing asperity [131]. The local displacement of the asperity might occur through ploughing of the asperity. Ploughing of the asperity happens when the harder of the two contacting asperities penetrates the softer asperity (see figure 6.19).

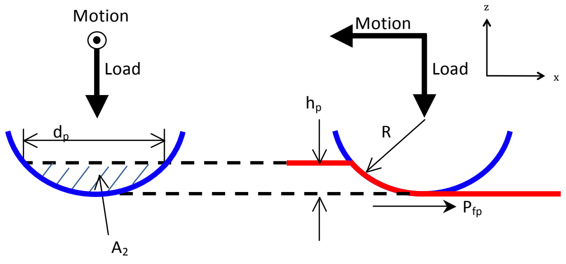

Front View Side View

Figure 6.19: Asperity ploughing model

The resistance to the ploughing motion is known as the ploughing friction, P_{fp}. Tambe and Bhushan [132] proposed an empirical friction model describing the ploughing friction in the function of lateral motion and material hardness for a rough surface contact. Asperity ploughing depends on the penetration followed by the displacement of the asperity contact. It is heavily influenced by the hardness of the contacting material itself. A simple ploughing model by Gohar and Rahnejat [131] is used to predict the friction due to ploughing for a single asperity contact. Therefore, the ploughing friction, P_{fp} can be defined as:

$$P_{fp} = (\text{Material Hardness}) \times A_2 \tag{6.31}$$

where H is the material hardness, $A_2 = 2h_p d_p/3$, $d_p = \sqrt{8h_p R}$ and h_p is the penetration depth. The penetration, h is assumed to have a critical value, h_{crit} where further penetration will no longer be sensible as the material is considered to be fully deformed plastically. In the case of the elastoplastic contact, the total friction can be expressed as:

$$P_{f_{tot}} = \frac{(\text{Material Hardness}) \times 2h_p d_p}{3} + \tau_a . \left[\pi c^2 - \pi d_p^2\right] \tag{6.32}$$

where $h_p = \delta - \delta_c$ and separation, $\delta > \delta_c$. The friction force for a single asperity contact can be obtained as in figure 6.20. It can be observed that the friction force predicted using the elastoplastic deformation considering the ploughing action is higher when the contact separation goes beyond the critical interference, δ_c. The observation shows the importance of considering the influence of plastic deformation which neglected might underestimate the friction force along the contact.

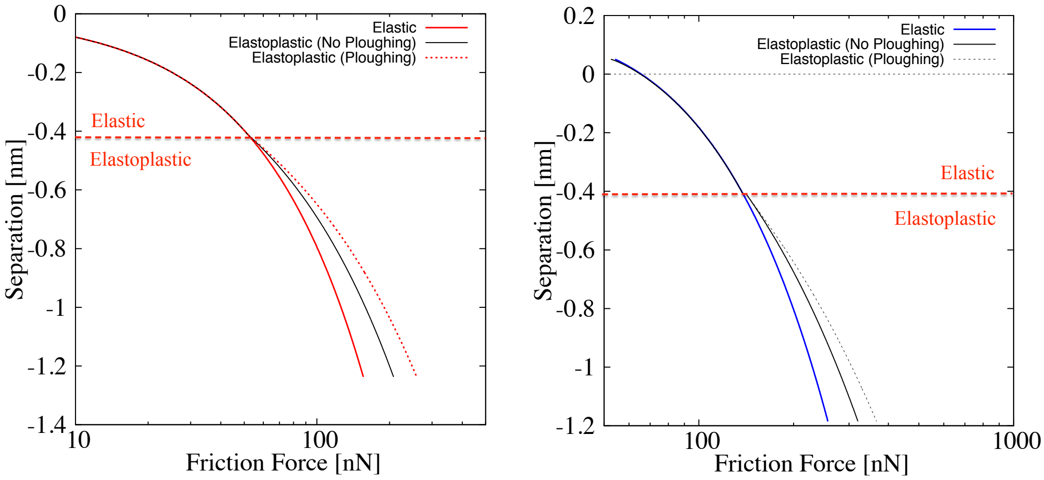

(a) Hertzian (b) Maugis-Dugdale

Figure 6.20: Friction for an elastoplastic point contact

6.4 Summary

This chapter covers the adhesion mechanism for an asperity contact. Different adhesion models for elastic and elastoplatic point contacts are being discussed. The importance of including the effect of the elastoplastic deformation was highlighted in the chapter. The coming chapters will discuss the role played by the thin film adsorbed on the asperity tips.

Chapter 7

Shear of ultra-thin surface films - An Empirical Approach

7.1 Introduction

There is a progressive demand for accurate models to predict boundary friction between *real* (rough) surfaces. The main goal is to reduce frictional losses, and therefore, improve mechanical efficiency. Most frictional losses are as the result of any direct interaction of rough surface asperities. Nevertheless, a significant part of friction is also due to the shear of a thin lubricant film, usually trapped between opposing asperities of the contacting surfaces. In some applications an ultra-thin surface film is only possible, where molecular behaviour of liquid lubricant near surface asperities is of significance. These are usually lightly loaded contacts. However, in the micro-scale conjunctions of light to moderate load intensity, a thin lubricant film adsorbed or entrained in between asperities can also behave in the same manner. This is also true of any lubricated conjunction at start-up or during inlet boundary reversal, where a coherent lubricant film cannot be assured.

This chapter proposes a mathematical model to predict the shearing of ultra-thin surface films along an asperity contact at vanishing gaps. The model takes into account empirically the molecular interactions of the fluid (consisting of only single component hard spheres) confined by two surfaces in relative motion. An extension of this model for fluid mixtures trapped between two sliding surfaces will be explained in *Chapter 8*.

New manufacturing techniques can now provide better control of surface topography (e.g. roughness, texturing). Molecular rheology of lubricant can also be improved by choosing an appropriate composition. This means that additives, having desired molecular interactions with solid bounding surfaces, are added to the base lubricants. It is hoped that the bulk rheology of the mixture would improve the load carrying capacity of the overall conjunction and possess low shear resistance. At the same time molecular behaviour near the smooth solid boundaries or around surface asperities would reduce friction when a coherent film is not formed. Most tribological conjunctions are subject to transient conditions, such as in start-up, inlet boundary reversals or because of application of cyclic loads. Therefore, interactions occur between the various phenomena at different physical scales; between bulk micro-scale lubrication and nano-scale localised interactions (e.g. around asperity tip pair contacts).

At micro-scale, viscous shear is the dominant mechanism underlying friction, as in hydrodynamic and elastohydrodynamic conditions. These mechanisms are better understood. At nano-scale, boundary interactions are affected by other kinetic laws such as intermolecular and surface energy effects. There is, of course, the critical interaction between these phenomena, particularly in the intervening scale. This interaction is between surface topography and lubricant rheology at short range (thin surface films of dimensions of several molecular diameters of the base lubricant or its additives). There is no deterministic model representing the formation of such ultra-thin films, particularly with respect to their interactions with the bulk tribological conditions. This study is an initial attempt to address this shortcoming.

At one end of the interaction range one can consider a single hemisphere. This represents a surface feature (such as an introduced dimple) or an idealised asperity tip, sliding against a perfectly smooth substrate, furnished with a uniform film of a basic lubricant (of a single molecular composition). Such a lubricant may represent a thin protective layer or a sealant, which when subjected to shear forms a thin surface adsorbed film. Octamethycyclotetrasiloxane (OMCTS) is used as a low friction protective layer or a sealant in some applications, for example in siliconised rubber seals. These are often used in inhalation devices. OMCTS is a non-polar fluid with molecular diameter of around $1nm$. Al-Samieh and Rahnejat [133] have shown that near molecularly smooth surfaces the behaviour of such a fluid is dominated by the solvation effect for films of up to several molecular diameters deep. Chan and Horn [134] have shown that there is discretised drainage of OMCTS from such conjunctions, indicating its near surface solvation effect. It is postulated that non-polar small molecular diameter spherical molecules (such as those of OMCTS) reduce localised viscous friction near asperity tips at nano-scale, which one may assume to be ideally smooth at this range. This is because solvation leads to dewetting of contacting surfaces.

At the other limit of this investigation, there are tribological conjunctions in micro-scale, where the load carrying capacity of the contact must be assured. Therefore, dewetting of the contiguous surfaces is not considered as a viable option. Consequently, long chain molecules are used to discourage density perturbation of the lubricant near the bounding contacting solid surfaces. Israelachvili [135] suggests that long chain molecules are best suited for this purpose and indeed are used regularly as additives to base lubricants as boundary friction modifiers. This is another postulate which should be investigated. In the current study the same sliding contact model is used, but with an idealised lubricant film, based on long chain molecules of Hexadecane or Tetradecane. These are used in diesel fuel, where they act as the lubricant in off-road vehicle fuel pumps. They intervene between the sliding teeth surfaces of pump gears.

The mechanism of delivery of the lubricant into the contact in both the examples investigated is assumed to be through hydrodynamics. The method of solution, therefore, combines hydrodynamics of the conjunction with solvation of the lubricant near the smooth surface of an assumed hemispherical feature. The effects of starvation and cavitation beyond the contact exit are also taken into account. Starvation affects the supply of lubricant into the contact, thus the thickness of film which influences solvation. Inclusion of cavitation and lubricant reformation influences the load carrying capacity of the contact, which determines the instantaneous equilibrium load shares of viscous and surface force contributions. Hitherto, such a study has not been reported in open literature. In this chapter, the boundary lubrication on the asperity tip is being modelled for a single species fluidic medium using an empirical approach.

7.2 Mathematical Model

Figure 7.1 is a schematic representation of contact cross-section between a rigid hemispherical feature, sliding relative to a smooth flat semi-infinite elastic half space. Under the usual conditions encountered in lubricated contacts, a number of distinct regions would occur in the conjunction. There is the inlet wedge region, where the lubricant is entrained into the contact (in the opposite direction to the sliding motion), from a curved meniscus. This is followed by a region of parallel film (corresponding to high pressures) with any small strain localised deformation in accord with Hertzian assumptions (elastohydrodynamic region). At the exit region from the Hertzian zone, there is film rupture boundary, beyond which falling pressures below that of lubricant vaporisation leads to streamers: formation of vapour fingers in the lubricant flow. This is the cavitation region. Somewhere downstream of this region, lubricant film is assumed to reform. This rather orderly and now well understood lubricant flow characteristics is based on the principle of continuity of flow, which is fundamental to the bulk lubricant behaviour. Abd Al-Samieh and Rahnejat [136] showed that any near surface effect plays an insignificant role in continuity of flow, until the film thickness is gradually reduced to several molecular diameters of the lubricant. Then, discrete lubricant molecular behaviour pursues, followed by a stepwise drainage from the contact, roughly in accord with the molecular diameter of lubricant, which are assumed to be spherical. This finding conformed to the experimental observations of Chan and Horn [134] and predictions of Matsuoka and Kato [137].

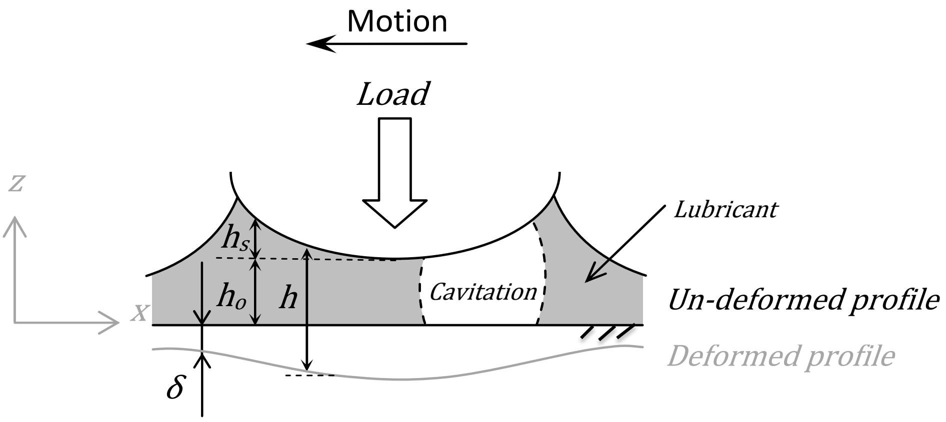

Figure 7.1: Lubricated conjunction

Therefore, for fairly thin films, the pressures generated in the conjunction are due to a number of mechanisms, whose individual contributions vary according to the gap size, $h(x, y)$:

$$h(x, y) = h_0 + h_s(x, y) + \delta(x, y) \tag{7.1}$$

where $h_s(x, y)$ is the local gap at any location within the conjunction and h_0 is the minimum clearance.

For inert surfaces and non-polar lubricants, assuming no direct contact between the surfaces, the total conjunctional pressure is due to hydrodynamics, van der Waals pressure and solvation:

$$p_T = p_h + p_w + p_s \tag{7.2}$$

where: p_h is the hydrodynamic component of the pressure, p_w is the van der Waals component and p_s is the solvation contribution.

It should be noted that the contribution due to van der Waals interaction can become significant at almost vanishing separations.

The load carrying capacity of the contact is obtained as:

$$P = \int p_T dA \tag{7.3}$$

where $p_T > 0$ means that negative (attractive) pressures do not contribute to the load carrying capacity.

7.2.1 Hydrodynamic Pressure

Al-Samieh and Rahnejat [133] and Matsuoka and Kato [137] solved the Reynolds equation to obtain the hydrodynamic contribution. For the point contact geometry, the two dimensional Reynolds equation is:

$$\frac{\partial}{\partial x}\left[\frac{\rho h^3}{\eta}.\frac{\partial p_h}{\partial x}\right] + \frac{\partial}{\partial y}\left[\frac{\rho h^3}{\eta}.\frac{\partial p_h}{\partial y}\right] = 12\left\{U\frac{\partial \rho h}{\partial x} + V\frac{\partial \rho h}{\partial y} + \frac{d}{dt}(\rho h)\right\} \tag{7.4}$$

where, U is the speed of entraining motion of the lubricant into the conjunction, being the average speed of the contacting surfaces (or half the speed of sliding in the case studied here) and V is the speed of any side-leakage of lubricant out of the contact area.

The hydrodynamic load carrying capacity of the contact is confined to the regions of full film, prior to a region of cavitation beyond a film rupture point. Swift-Stieber exit boundary conditions is used: $\bar{P} = \partial\bar{P}/\partial x|_{cavitation} = 0$ [11, 12]. Cavitation, though, plays a very significant role in the disruption of free surface film uniformity as desired for thin protective surface films. Additionally, Reynolds equation is not suited to the prediction of the cavitation region, where the interface between the lubricant and air causes loss of laminar flow. This is an underlying assumption for Reynolds equation.

To overcome this shortcoming the cavitation model proposed by Elrod [32] is used here. This model modifies the Reynolds equation to take into account the boundary between a full film region and that representing a cavitation region. The approach approximates the fully demarcated vaporization cavitation boundary condition proposed by Jakobsson and Floberg [30] and Olsson [31] (now referred to as the JFO boundary condition). In the simplified, but computationally more efficient Elrod method a fractional film content, $0 < \theta \leq 1$ is defined. The hydrodynamic pressure can now be defined as:

$$p_h = g\beta ln\theta + p_c \tag{7.5}$$

where cavitation is assumed to occur at the constant pressure, p_c under the current isothermal analysis, β is the lubricant bulk modulus and g is a switching function:

$$g = \begin{cases} 1 \Rightarrow & \text{Full film, if } \theta \geq 1 \\ 0 \Rightarrow & \text{Cavitation, if } 0 < \theta < 1 \end{cases} \tag{7.6}$$

Now for the full film region, Reynolds equation is modified to:

$$\begin{aligned} \frac{\partial}{\partial x}\left[\frac{\rho_c h^3}{\eta} g\beta \frac{\partial\theta}{\partial x}\right] &+ \frac{\partial}{\partial y}\left[\frac{\rho_c h^3}{\eta} g\beta \frac{\partial\theta}{\partial y}\right] \\ &= 12\left\{U\frac{\partial\theta\rho_c h}{\partial x} + V\frac{\partial\theta\rho_c h}{\partial y} + \frac{d}{dt}\left(\theta\rho_c h\right)\right\} \end{aligned} \tag{7.7}$$

Referring to equation (7.6), it is clear that in the cavitation region the Couette flow only operates, thus:

$$\left\{u\frac{\partial}{\partial x}+v\frac{\partial}{\partial y}+\frac{\partial}{\partial t}\right\}(\theta\rho_c h)=0 \tag{7.8}$$

It is reasonable to assume negligible side leakage from the contact with thin films and at relatively low sliding speeds, thus: $V = 0$. With this assumption taken into account, it is clear that the cavitated region is governed by a balance between the squeeze film effect (the ultimate term in the last equation) and the drainage of the fluid from the contact on the account of hydrodynamics alone. Separation of the surfaces on account of squeeze; $\partial\theta h/\partial t > 0$ increases the chance of cavitation, which is the same as an increase in the speed of entraining motion (Al-Samieh and Rahnejat [138]). One should then expect reduced cavitation at lower sliding speeds as an outcome of the analysis, which would encourage better lubricant distribution on the free surface post film reformation. This is a desired outcome in any reciprocating contact.

Lubricant rheology, therefore, is critical to the maintenance of a continuum. Yet, density alters as a direct result of the different kinetic laws that co-exist in the nano-scale. In bulk it alters with hydrodynamic pressure, and near the solid barrier it has a higher density profile due to the constraining effect of solvation pressure. The bulk density variation with the contact pressure for mineral oils is given by Dowson and Higginson [46]:

$$\rho=\rho_o\left(1+\frac{0.6\times10^{-9}\times p_h}{1+1.7\times10^{-9}\times p_h}\right) \tag{7.9}$$

As a first approximation this is taken to also represent the density-pressure dependency in this analysis. Matsuoka and Kato [137], Abd Al-Samieh and Rahnejat [136] and Al-Samieh and Rahnejat [133, 138] also assumed the same for the bulk hydrodynamic behaviour of the lubricants such as those described above and used in the current analysis. Clearly, for the cavitated region: $\rho = \rho_c$ when $p = p_c$.

Lubricant viscosity-pressure variation can be predicted using the Roelands' equation [45]:

$$\eta = \eta_o e^{\alpha p_h} \tag{7.10}$$

where $\alpha = \frac{1}{p_h}(\ln \eta_o + 9.67)\{[1 + p_h/(1.98 \times 10^8)]^Z - 1\}/p_h$ and $Z = \alpha_o/[5.1 \times 10^{-9}(\ln \eta_o + 9.67)]$.

7.2.2 Solvation Pressure

For very smooth surfaces, the solvation effect dominates in gaps of several molecular diameters of the intervening fluid. The phenomenon is as the result of density variation of liquids near solid boundaries [135]. The effect is significant in nano-scale conjunctions, inducing a structureless conjunctional environment which disrupts the comfort of a hydrodynamic continuum and thus proper wetting of the contiguous solids. Paradoxically, the dewetting action of solvation can guard against the formation of a meniscus, which otherwise would contribute to the work of adhesion.

It is postulated that the effect of solvation is more pronounced for small fluid molecules such as those of perfluoropolyether and Octamethylcyclotetrasiloxane, which have nominally spherical molecules of $1 - 1.5nm$ diameter. This effect is almost negligible for long chain molecules [135]. The contact density variation near the smooth solid surfaces takes the form of (Henderson and Lozada-Cassou [139] and Evans and Perry [140]) :

$$\rho = k_B T \left[\rho(h) - \rho(h \to \infty)\right] \tag{7.11}$$

where $\rho(h \to \infty)$ is the corresponding value for a single surface, implying that $h >> a$. Therefore, it tends to the bulk density of the fluid, whose variation may be assumed to follow equation (7.9).

The density variation near the constraining barriers gives rise to a monotonic exponential pressure variation, which is alternately attractive-repulsive. This variation is explained in some detail by Israelachvili [135], Teodorescu *et al* [141] and, Gohar and Rahnejat [131], resulting in the discrete fluid drainage from the contact conjunction. Israelachvili [135] proposed a solvation pressure of the following form:

$$p_s = -Ce^{-h/a} cos\left(2\pi\frac{h}{a}\right) \tag{7.12}$$

where: $C = k_B T\rho(h \to \infty)$, which for the cases considered here: for OMCTS $C = 172MPa$, Hexadecane $C = 62MPa$ and Tetradecane $C = 49MPa$ (Chan and Horn [134]). Note that the value of C is reduced as the size of the molecule increases. Size is not represented by molecular diameter for long chain molecules, which are rather similar to strings. In fact the diameter of Hexadecane is only $0.4nm$. It is clear that the solvation pressure is only significant for small values of h/a .

7.2.3 van der Waals Pressure

In nano-scale conjunctions other forms of kinetic interaction may also contribute, depending on the molecular structure of the fluid and the atomic structure of the bounding solids. If the fluid is considered as non-polar and the surfaces as inert, then long range van der Waals interactions between the fluid molecules and atoms of the surfaces and between the surfaces themselves play a role. These are weak attractive forces in the nano-scale, but can become very significant at closer range.

The van der Waals forces arising from these interactions can be obtained using Lifshitz theory [142]. For nano-scale conjunctions, the procedure is detailed by Abd Al-Samieh and Rahnejat [136]. The current study addresses the nano-scale range, where some marginal contributions due to van der Waals interactions may be expected. Depending on the contact geometry, Israelachvili [135] provides a simple expression. For flat surfaces (which may be assumed here because of the localized elastic deformation in the central small contact area in figure 7.1):

$$p_w = -\frac{A_h}{6\pi h^3} \tag{7.13}$$

where A_h is the Hamaker constant, its value depends on the atomic structure of contacting bounding solids and the molecular composition of the intervening fluid. Its value is usually in the range: $10^{-21} - 10^{-19}J$, in this case: $A_h = 1.4 \times 10^{-20}J$.

7.2.4 Contact Deflection

Contact deflection, required in equation (7.1) can now be calculated, using the elasticity potential equation (Johnson [143] and Gohar and Rahnejat [131]):

$$\delta(x,y) = \frac{1}{\pi E^*} \int\int \frac{p_T(x',y')}{\sqrt{(x-x')^2 + (y-y')^2}} dx'dy' \tag{7.14}$$

where the deflection at a point (x, y) is determined due to all the generated pressures at points (x', y'). When a computational grid is made with the pressure distribution, $p_{k,l}$, this equation can be stated as:

$$\delta_{i,j} = \sum_k \sum_l D_{i,j}^{k,l} p_{k,l} \tag{7.15}$$

where $D_{i,j}^{k,l}$ are the influence coefficients (Johnson [143]). The reduced elastic modulus is

$$E^* = \left(\frac{1-\nu_1^2}{E_1} + \frac{1-\nu_2^2}{E_2} \right)^{-1} \tag{7.16}$$

7.3 Method of Solution

A solution can now be obtained for $\theta, h, p, \delta, \rho$ and η, by representing equation (7.7) in finite differences and obtaining a solution through low relaxation effective influence Newton-Raphson method with Gauss-Seidel iterations (Al-Samieh and Rahnejat [133], Teodorescu *et al* [141] and Chong *et al* [144]). The procedure places the hemispherical feature at consecutive reducing separations h_0 from the surface of the flat semi-infinite plane. With an assumed speed of entraining motion (U) and time step, this corresponds to the imposition of a rate of rigid body squeeze $(\partial h/\partial t)$. The complete derivation of the point contact model is provided in *Appendix A*. Therefore, the conditions at each quasi-static step at various separations $h_s(x, y)$ may be regarded as rheonomic non-holonomic constraints. The simulation results in section 5 explore contact conditions with different rates of approach.

The convergence criterion used in each quasi-static step is:

$$\frac{\sum_i \sum_j \left|\theta_{i,j}^n - \theta_{i,j}^{n-1}\right|}{\sum_i \sum_j \theta_{i,j}^n} \leq \epsilon_\theta \tag{7.17}$$

where n is the iteration counter. If the above criterion is not satisfied, then:

$$(g\theta)_{i,j}^n = (g\theta)_{i,j}^{n-1} + \Omega\Delta\theta_{i,j}^n \tag{7.18}$$

The process is then repeated at the same separation. When the convergence criterion is met, the separation h_0 is reduced by a molecular diameter of the fluid and the entire iterative procedure is repeated again. In this manner the conjunctional behaviour is noted for different quasi-static steps at progressively reduced separations. The numerical analysis is summarised in figure 7.2.

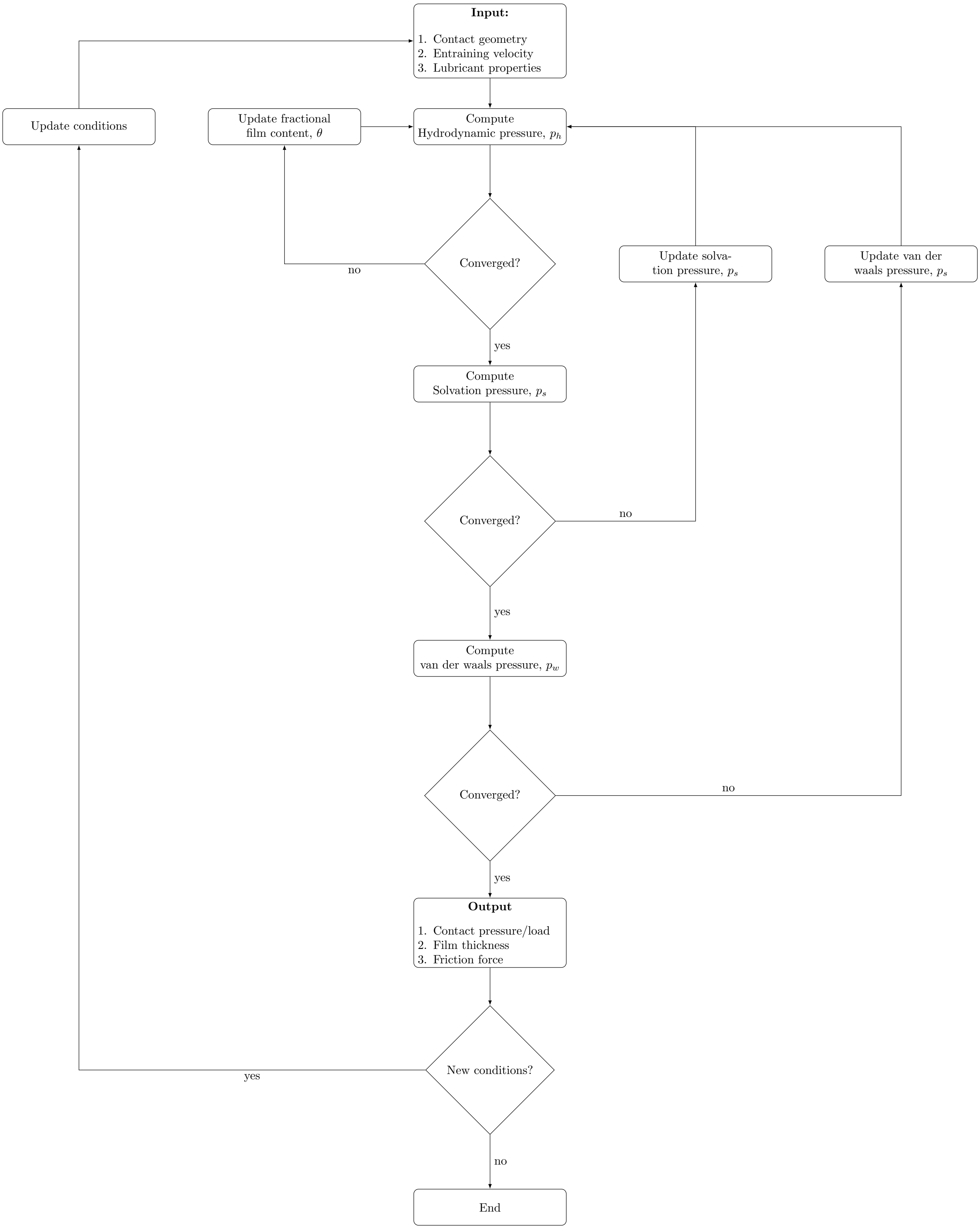

Figure 7.2: Flow chart for the asperity lubricant shearing model

7.4 Conjunctional Friction

Friction generated by the ultra-thin adsorbed films on nominal molecularly smooth surfaces follow non-Newtonian shear due to chemical reactions which are based on thermal activation. Eyring [145] developed a model which described the viscosity of fluids under such circumstances. Eyring's model assumes that the motion of a volume of fluid molecules takes place in the presence of a *cage-like* potential barrier by their mere closely-packed arrangement in the bulk. In order to overcome this potential and escape the *cage*, the fluid molecules have to surmount the activation barrier potential. This is the thermal activation model which Eyring modified to include the effects of prevailing pressure and shear (see figure 7.3) as:

$$E_y = Q + p_T\Omega_y - \tau\phi_y \tag{7.19}$$

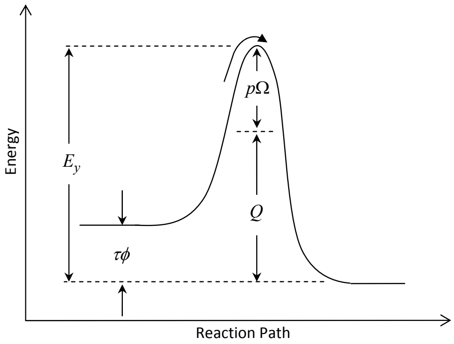

Figure 7.3: The potential barrier in thermal activation

The shear stress acts on a stressed activation volume, ϕ_y , which may be conceived as a *process coherence volume.* This can be interpreted as the size of a moving segment in unit shear, whether it would be a molecule or a dislocation line. Therefore, during sliding motion the potential barrier is repeatedly overcome. The average barrier-hopping time for a single molecule is predicted using the Boltzmann distribution with a regular series of barriers and a high stress limit (i.e. $\tau\phi_y/k_BT > 1$). According to Briscoe and Evans [146], the shear stress is a function of velocity, pressure and temperature. For constant velocity and under isothermal conditions, it can be expressed as:

$$\tau = \tau_0 + \xi p \tag{7.20}$$

where : $\xi = \frac{\Omega_y}{\phi_y}$

The Eyring shear stress is determined as : $\tau_0 = \frac{1}{\phi_y}\left[k_B T ln(\frac{U}{v_0}) + Q_y\right]$.

where v_0 is the characteristic velocity related to the frequency of the process.

The sliding velocity, however, can change according to the operating speed of the contact. To account for this, the value of τ_0 is adjusted at a constant pressure, p_v as:

$$\tau_0 = \frac{k_B T}{\phi_y} lnU + \tau_1 - \xi p_v \tag{7.21}$$

where $\tau_1 = \frac{1}{\phi}\left[Q_y - p_v\Omega_y + k_B T ln v_0\right]$, and for the fluids used in this analysis: $k_B T/\phi_y \approx 3.4/A$, $\tau_1 \approx 11.3/A$, $p_v \approx 100/A$ all in nN/m^2 and $\xi \approx 0.16$ [147]. Note, the contact area is taken as the area of the computational grid: $A = \int\int dxdy$ and thus friction is obtained as:

$$P_f = \int\int \tau dxdy \tag{7.22}$$

Before proceeding to solve the numerical model for the asperity contact with curvature radius of $1.5mm$ sliding at a velocity of $0.2mm/s$, a convergence study was conducted in order to ensure that the grid mesh selected is able to produce a converged solution. The convergence criteria selected for the model is the peak pressure and the minimum fractional film content. When the change of both the parameters are less than 2%, the solution produced by the grid mesh is considered to be well converged. The convergence study is summarised in table 7.1 and 7.2.

Table 7.1: Grid mesh convergence based on peak pressure

No. of Grid Points	**Peak Pressure (MPa)**	**% Deviation**
60×40	0.1130	-
90×60	0.1101	2.56
120×80	**0.1100**	**0.09**

Table 7.2: Grid mesh convergence based on minimum fractional film content

No. of Grid Points	Minimum Fractional Film Content, $\theta(-)$	% Deviation
60×40	1.0015	-
90×60	1.0012	0.03
120×80	**1.0013**	**0.01**

7.5 Results and Discussion

Series of simulations have shown that while the conjunction is separated by a molecularly thin film, the combined effects of solvation and hydrodynamics dominates, while the long range van der Waals interactions play an almost insignificant role.

When the gap is greater than several molecular diameters of the intervening fluid, hydrodynamics dominate. As the gap is reduced the effect of solvation becomes increasingly important. For the fluid used (OMCTS) in the first part of this analysis, with molecular diameter $a \approx 1nm$, an incipient solvation effect begins around gaps of the order of $8nm$ (see figure 7.4). Nevertheless, hydrodynamics always plays the key role of entraining a thin film of lubricant into the conjunction through inlet wedge effect.

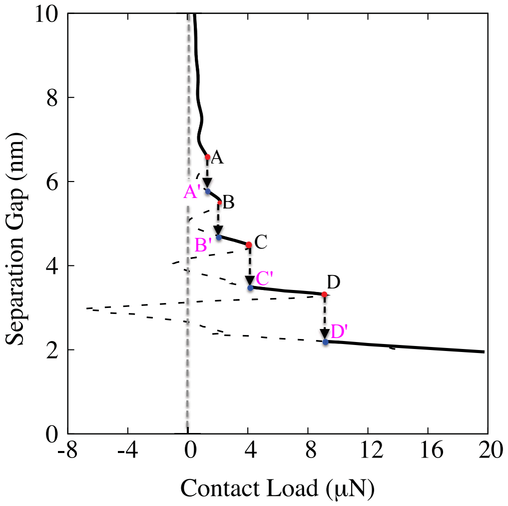

Figure 7.4: Discretized contact characteristics in ultra-thin smooth conjunctions

Figure 7.5(a) shows an isobaric plot of conjunctional pressures. This comprises 4 regions of interest: (1) the inlet meniscus/wedge, (2) the contact proper, (3) a cavitation region and (4) reformation zone (as postulated in description of figure 7.1). Each region plays a key role. The inlet meniscus acts as the reservoir supplying the contact with a film of lubricant. Lubricant ahead of the contact provides the meniscus liquid bridge through wetting action of the lubricant on the contiguous surfaces, and is indicated by the inward curved isobar ahead of the contact. Under these circumstances, for simplicity it is assumed that a meniscus is formed at a pressure close to that of lubricant's vaporization pressure p_c. With entraining motion of the lubricant through the inlet wedge the generated pressures rise. The proper contact comprises a series of almost concentric isobars with increasing pressures towards the rear lubricant exit constriction from the contact. This is a characteristic of hydrodynamic pressures, except that solvation effect in such diminutive gaps causes pressure fluctuations superimposed upon the hydrodynamic pressure profile. Figure 8.11(b) is a cut through the centre line of the isobaric plot, which shows these pressure fluctuations.

The region of high pressures is immediately followed by lubricating film rupture, not unlike the behaviour of any hydrodynamic conjunction. With lubricant pressures falling below its vaporization pressure beyond the lubricant rupture point, cavitation occurs. The depth of cavitation is governed by the speed of entraining motion in the contact, as well as the gap size. The former is contributed by hydrodynamics, whilst the latter determines the extent of solvation. The fluid in the cavitation region is a mix of lubricant and vapour. Beyond this, in the trailing edge of the contact, the pressures are assumed to return to the atmospheric value. This implies the existence of a film reformation region, where the vapour escapes through the liquid. Figure 8.11(b) shows the trend towards reformation. The larger the extent of cavitation and reformation regions become, the greater is the deviation from uniformity of lubricant height upon the free surface of the semi-infinite plane after the exit constriction. It is natural to assume that clumps of lubricant may be formed on any surface beyond the film rupture region if many such hemispherical features or other textures slide along the flat substrate. The analysis here shows that even with assumed steady state condition the transient nature of solvation and its interplay with hydrodynamics can result in non-uniform distribution of lubricant on surfaces.

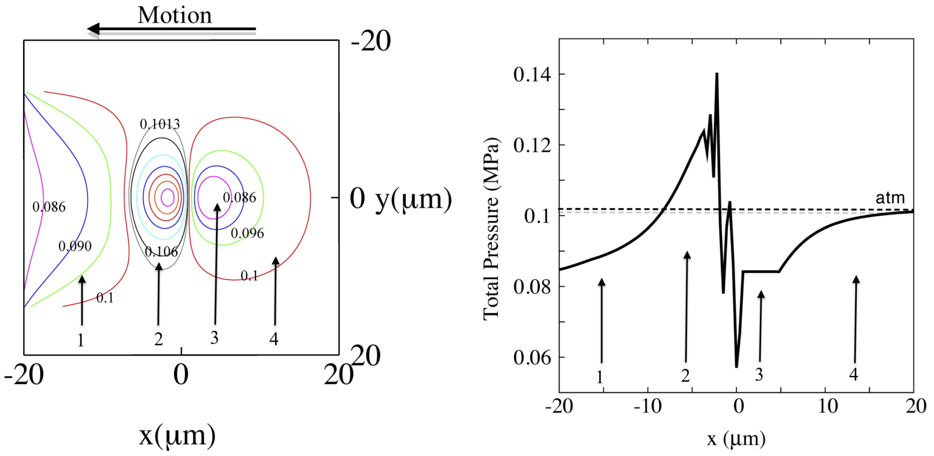

(a) Isobaric pressure plot (MPa) (b) Centre-line conjunctional pressures

Figure 7.5: Pressure variation in an ultra-thin gap of 8 *nm* with (1) the inlet meniscus/wedge, (2) the contact proper, (3) a cavitation region and (4) reformation zone

Now returning to figure 7.4, as the gap is reduced, fluid film discretization occurs (as noted by Matsuoka and Kato [137], and Al-Samieh and Rahnejat [133]). Layers of lubricant molecules are drained in a step-wise fashion from the conjunction, in this case at gap intervals of $1nm$; the diameter of spherical molecules of OMCTS. In each step a further increase in load or a corresponding squeeze action is needed before another layer of lubricant is ejected out of the contact. This means that at a given sliding speed, whilst the hydrodynamic inlet flow follows Newtonian slow viscous action, the drainage from the contact does not conform to the continuity of flow condition.

Solvation in effect accounts increasingly for load carrying capacity of the contact. It disrupts the structured nature of fluid flow and essentially promotes its dewetting. There is, of course, a limit to this height, determined by the meniscus pressure at the inlet (Abd Al-Samieh and Rahnejat [136]). The dotted lines in figure 7.4 indicate the oscillatory behaviour of solvation, in alternate attractive-repulsive action. The loss of load carrying capacity, indicated by the dotted line is purely theoretical as the hydrodynamic pressure at the nib of the contact guards against this effect, unless no entraining motion is to take place (such as in cessation of sliding).

Figure 7.6 shows a series of pressure distributions with the corresponding film shapes and fraction film ratios for steadily decreasing gaps in line with the steps indicated in figure 7.4. As the gap is reduced (e.g. from A to A') at the same sliding speed, the contribution due to solvation pressure is increased. This reorders the molecular content of the conjunction within the contact proper, followed by the drainage of a row of molecules. The film shapes show this discrete molecular drainage. In the intervening intervals (e.g. A' to B) an increase in the contact load (i.e. integrated pressure distribution) is due to molecular disposition to regiment rows of molecules within the conjunction.

With increased pressures and thin films the depth of cavitation is increased directly as the result of the dewetting action of solvation. With larger cavitation and assuming a fairly uniform surface topography, a longer time, hence sliding distance, is required before film reformation is achieved through fluid surface tension. Therefore, under dynamic conditions with varying height of the surface features, it is clear that uneven distribution of film would result on the surfaces. The results indicate that this non-uniformity would be exacerbated at lower gap sizes.

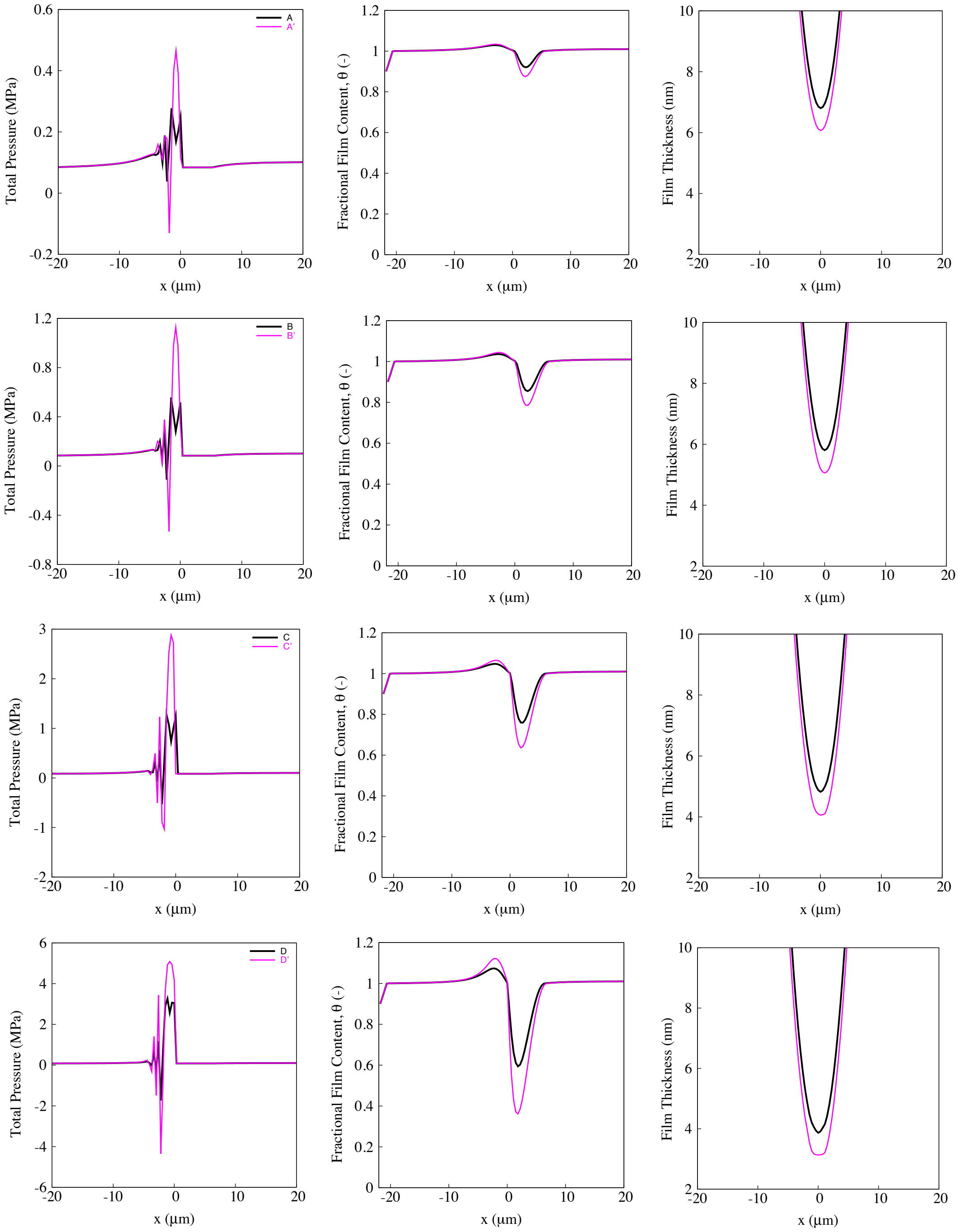

Figure 7.6: Conjunctional conditions at a steadily reduced separation gap (see figure 7.4)

Hydrodynamic entrainment of the lubricant also has its own better known influence upon film rupture and cavitation. The height of lubricant at the meniscus and its distance to the leading edge of contact is critical to its wetting action (Hamrock and Dowson [148], Wedeven *et al* [149]). These are affected by the sliding speed. A faster sliding speed requires a longer inlet distance (i.e. a larger meniscus) in order to avoid starvation of the contact. However, this can also lead to thicker contact films and greater depth of cavitation. These effects lead to conditions that are contrary to the purpose of maintaining a better distribution of liquid lubricant in many applications. It should be noted that the range of sliding speeds chosen is based on the reversal conditions in the ring/liner contact.

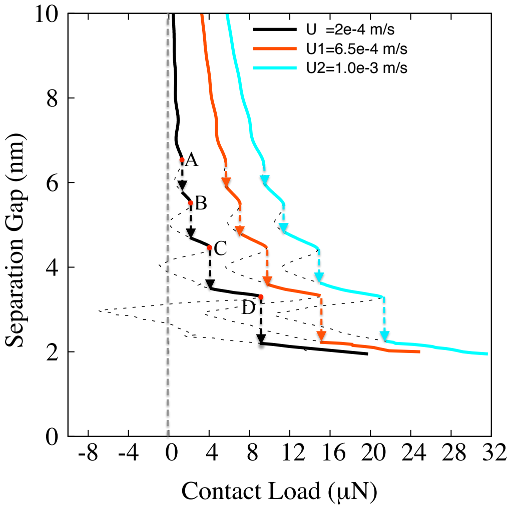

Figure 7.7: Conjunctional characteristics with increasing slider speed

Figure 7.7 shows that the discretisation effect is slightly delayed with increasing speed of entraining motion. This delayed effect is caused by a rise in film thickness, thus more pronounced hydrodynamic action. Figure 7.8 shows a series of pressure distributions with their fraction film ratios, corresponding to different speeds of entraining motion in figure 7.7. Note that the rise in pressures is due to hydrodynamics in the inlet nib to the contact (this diminishes with smaller gaps). The solvation contribution remains the same for all the speeds in the same gap size. Interestingly, the depth of cavitation is increased as normally would with enhanced contact pressures, directly as the result of increased speed at the same effective contact load. Hence, reduced gap and increased sliding speed cause non-uniformity in free surface oil film, the former due to solvation and the latter due to hydrodynamic action.

Another key factor is friction. Assuming very smooth surfaces, at the molecular level separations here, friction is mainly due to viscous action of a lubricant film or introduced by a layer of molecules in drainage in accord with the activation energy required to dislocate them. There is clearly insignificant friction in the cavitation region.

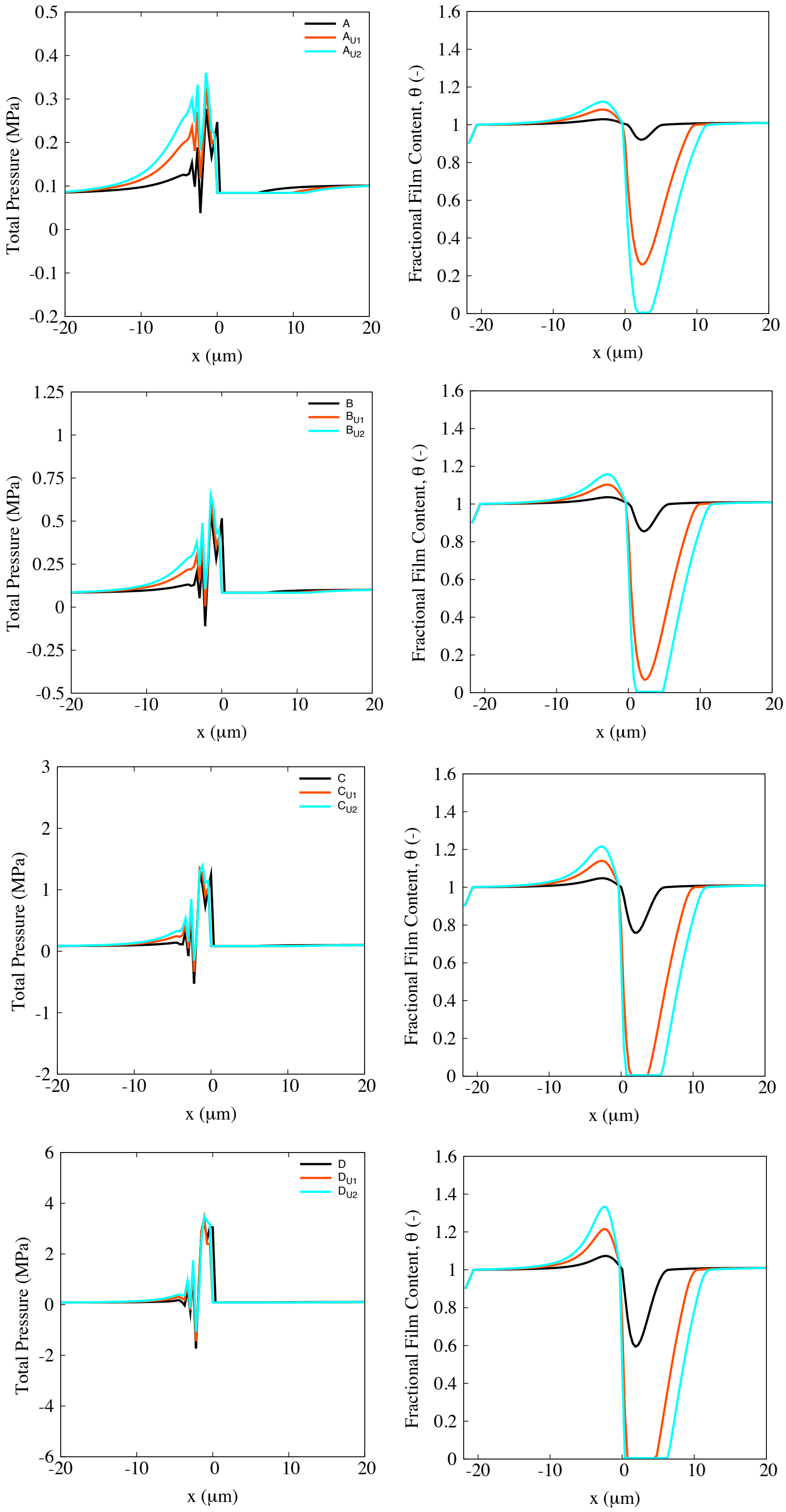

Figure 7.8: Liquid film discretization at increasing speed of entraining motion (sliding speeds based on figure 7.7)

Figure 7.9 shows a plot of friction versus the conjunctional load (at a steadily reducing gap). The quasi-linear relationship between any subsequent instances of drainage is due to shear of a lubricant film, with a slope, which may be interpreted as a coefficient of friction. This alters slightly with both the sliding speed and contact pressures. The linear slope is as the result of changes in lubricant viscosity and film thickness, both affected by increasing load between steps of lubricant discretisation. The slope follows viscous friction. Seth *et al* [150] studied slip of microgel paste particles against a solid boundary in the presence of water molecules. They showed that at each step of separation the slip of microgel particles along the wall follow viscous shear.

Referring back to figure 7.9, the change with pressure is almost insignificant at a given gap size as this is dominated by almost unchanged solvation pressure. However, during drainage a rise in friction occurs with no additional contact load. This is the effort expended to eject a row of molecules. In such instances interpretation of friction based on viscous action (or an effective coefficient of friction) is inappropriate. Here one may regard friction as breaking of cohesive intermolecular bonds during discrete drainage from the contact region or a volume of fluid (i.e. a row of molecules) overcoming an activation barrier to drain from the contact. With increased sliding speed thicker films cause delays in the same characteristics.

Friction characteristics of thin films are quite complex, because they are affected by their actions near solid barriers. This is not only true for OMCTS studied so far, but also for low shear strength films formed by all additives in micro-scale conjunctions in a large variety of engineering applications. One case already mentioned is the action of additive molecules such as Hexadecane in diesel, where the latter also acts as a lubricant, for example in off-road vehicles' fuel pumps. In these cases the surface effects are likely to be concentrated around smooth tips of asperities, which are larger in dimension than the molecular size of the surface active additives. Figure 7.10(a) shows a similar friction characteristic for Hexadecane, if it were to be used instead of OMCTS in the current study under otherwise exact simulation conditions. However, note that in the case of Hexadecane a small rise in friction is only discerned during lubricant drainage. This is because Hexadecane has long and narrow molecular structure which inhibits solvation (see figure 7.10(b)). Thus, the discrete nature of drainage is reduced. This improves friction, at the expense of better wetting of contact. Hence, a quest to reduce wetness of the contact can have significant drawbacks in terms of friction. However, in certain cases this is a desired function, such as in seals of inhalation devices containing volatile mixtures.

The current analysis is isothermal, thus the effect of friction is understated. It is clear that the heat generated as the result of friction would deplete the film thickness, the load carrying capacity of the contact and exacerbate the effect of cavitation.

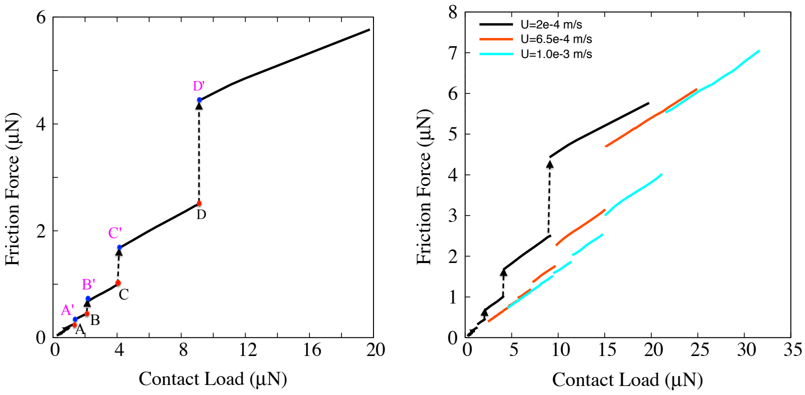

(a) Load-friction characteristics (b) Effect of increased sliding velocity

Figure 7.9: Friction characteristics of OMCTS

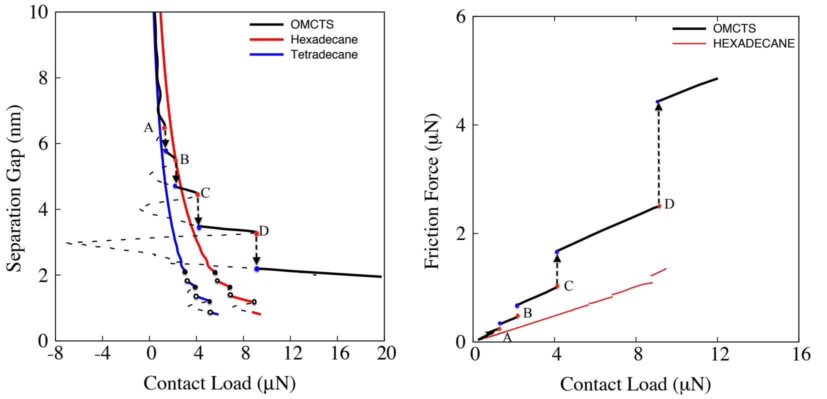

(a) Contact load vs. Separation Gap (b) Friction force vs. Contact Load

Figure 7.10: Friction characteristics of different species of molecules

The analysis shows that for some conjunctions one paradoxically needs the dewetting action of solvation, but uniformity, which is afforded by hydrodynamics. Hence, control of molecular composition of lubricants may be fundamental to future research in ultra-thin film devices.

7.6 Summary

The chapter discussed on thin film shearing considering the influence of intermolecular force (e.g. solvation and van der Waals). The solvation force is based on an empirical equation which limits the analysis to a certain given fluid only. The model also does not consider adsorption of thin films on asperity tips, which plays an important role in boundary lubrication. This will be discussed in the following chapter.

Chapter 8

Shear of ultra-thin surface films - A Statistical Mechanics Approach

8.1 Introduction

Formation of ultra-thin surface adsorbed films is crucial in smooth running of many conjunctions in variety of applications. However, unlike the well-understood lubricant films formed by hydrodynamic viscous action, the knowledge regarding the mechanisms underlying surface or boundary films is still emerging. These thin surface films have low shear strength characteristics and are formed as the result of tribo-chemical interactions between molecules of the lubricant and the surface material. Therefore, the study of lubricant-surface interaction is critical for their understanding and their role in friction. In fact, a recent review by Erdemir [151] shows that lubricant-surface combination must be considered as an integrated system. The review shows that there has been a significant growing volume of research on tribo-films. However, formation of these films is an effect rather than the underlying physio-chemical cause which is because of the intermolecular interactions of a fluid species, as well as with the atoms of the bounding solid surfaces. It is, therefore, essential to understand the plethora of kinetic laws that belie these interactions. The multitude of molecular species and the seemingly abundant kinetic laws in the nano-scale promote a slow progress in understanding.

In the previous chapter, a mathematical model, capable of predicting the shear of ultra-thin films confined by two sliding surfaces, was proposed [152]. The model is limited to a fluid system consisting of only a single species of hard spheres. However, a typical lubricant usually consists of a mixture or blend of molecule species (e.g. base oil and additives). The current chapter extends the model for fluid mixtures considering the effect of molecule adsorption to surface.

Molecules do not move in a straight line path, but in step-wise fashion and in all directions. Einstein and Infeld [153] showed that the mean squared distance moved by assumed hard spherical molecules in Brownian motion is linearly proportional to the elapsed time (or the rate of shear). Thus, surface adsorbed or boundary films may be considered to act as classical fluids with hard particles in a definite volume [153]. Real fluids, though, cannot be considered as idealized classical fluids. The boundary solids are also rough and often anisotropic. Thus, in the diminishing scale, the interaction potential between species of molecules and atoms of surfaces vary.

The complexity of the problem is exacerbated in lightly loaded minute contacts, particularly with very smooth surfaces, such as asperity summits. There are repercussions for emerging technologies such as micro-electromechanical systems and some data storage devices. The same is also true in contacts of low load intensity due to closer contiguity of bounding surfaces. Owing to free surface energy and intermolecular interactions the packing order of the molecules in such conjunctions alter near the solid barriers. Often any film of fluid exhibits a hierarchical nature according to the interaction scale. At diminutive separations the intermolecular interactions comprise long range van der Waal's interactions between the fluid molecular species, as well as with the atoms of the solid barriers [142]. For charged surfaces and/or polar fluids these can also be augmented by electrostatic interactions [131]. Additionally, any formed film of fluid has a different packing of molecules, several molecules deep into its bulk. Due to the free surface energy the fluid molecular density is higher at the solid barriers than in the bulk [135]. With increased loading or convergence of the bounding surfaces an oscillatory monotonic-exponential force results, known as the solvation force [154, 135]. Horn and Israelachvili [155] and Chan and Horn [134] have measured this oscillatory force between very smooth mica surfaces in liquids such as Octamethyltetracyclosiloxane (OMCTS), Hexadecane and Tetradecane, using surface force apparatus (SFA). Lim and O'Shea [156] used an atomic force microscope (AFM) to measure the solvation force for fluid mixtures.

Various theoretical models have been developed, where conjunctional behaviour considers kinetic laws, hydrodynamics, surface energy effects, as well as intermolecular interactions (see section *7.2* in *Chapter 7*). As an alternative approach to describe the solvation force, Mitchel *et al* [157], Henderson and Lozada-Cassou [139] and Attard and Parker [154] have adopted the use of Ornstein-Zernike (OZ) equation. The OZ equation is based on the Percus-Yevick (PY) [158] approximation to predict the pair correlation function; PCF, g^* between hard spherical molecules. The solvation force can then be predicted by applying the Derjaguin approximation for the interaction between usually flat planar surfaces. Alternatively, Monte-Carlo simulation and density function theory can be used to predict the solvation force as in the case of works of Snook and Van Megen [159], Tarazona and Vicente [160], Somers *et al* [161] and Karanikas *et al* [162].

The empirical approach of Chan and Horn [134], however, is rather limited to a few types of basic fluids such as OMCTS. Most lubricants comprise a mix of molecular species, many of which are long hydrocarbon chains, esters and surfactants whose interactions do not conform to those of assumed basic hard impenetrable spheres, which mimic short range characteristics of atoms at close range [153]. Therefore, for real lubricants one is compelled to use molecular dynamics, Monte-Carlo simulations or statistical mechanics. These approaches are computationally time intensive and whilst, they may suit studies of regional colloidal behaviour, they are not suited to predict boundary adsorbed films in contacts of any significant dimensions. Surface adsorbed films act at the assumed smooth summits of surface features which are ubiquitous in any micro-scale contact according to some statistical distribution. If an analytical model for such a typical feature can be derived, then it may be included in an assumed statistical treatment of surface interactions in much the same manner as adhesion of asperities noted by Fuller and Tabor [163] and Johnson and Sridhar [123]. In fact, a combination of kinetic laws may be included in such an analysis as shown for adhesion, meniscus action and hydration by Rahnejat *et al* [164] and Teodorescu *et al* [141] for nano-scale lubricated impact dynamics of a diminutive roller and those of MEMS gear teeth pairs respectively.

When a film of fluid is entrained into a conjunction through hydrodynamic action, the classical OZ theory may be used to account for the intermolecular and surface forces of classical fluids of hard spherical molecules as functions of molecular diameter and intermolecular spacing or distance from a solid barrier. The previous chapter showed that near surface effects dominate in gaps of the order of several molecular diameters. They also showed that spherical molecules tend to solvate near assumed smooth surfaces of asperities at nano-scale. Their discrete drainage at steadily decreasing gaps adds to friction of any bulk lubricant film. However, at the same time this action generates solvation pressures which increase the load carrying capacity. Conversely, long chain molecules of smaller effective diameter tend to inhibit solvation, thus show a decrease in the load carrying capacity whilst through their wetting action reduce friction. The study also included the effect of thin film elastohydrodynamics with inlet lubricant starvation and cavitation and film reformation boundaries.

In the evolutionary process to extend the work in the previous chapter [152], it is necessary to develop a realistic physio-chemical hydrodynamic model, where intermolecular and surface interactions account for a mix of lubricant molecular species. The current contribution supplements the solution of OZ equation with an attractive narrow well potential to describe the characteristics of a simplified real physical fluid system through PY approximation. The solid planar boundary is also considered as a species in the analysis, where the interactions of hard spheres with its atoms are also taken into account. In the solution of OZ equation with PY approximation, adhesion energy of hard spherical molecular species with the solid planar boundaries are allowed. Thus, the work of the previous chapter is not only extended from an idealized fluid to a physical one, but also includes the adsorption/adhesion of molecules to the solid boundary. This is the prelude to the formation of tribo-films of interest in boundary lubrication. A basic lubricant is assumed with spherical molecules. This is supplemented with different concentrations of an additive, represented by a smaller diameter spherical molecule with different levels of adsorption energy. In reality the additive molecules are long chain structures, but with a slender cross-section. These often adsorb to the surfaces through their small diameter terminus with their backbone comprising a long chain tentacle.

8.2 Mathematical Modelling

The fluid between two surfaces can be modelled as a large number of interacting molecules, which in the first approximation can be viewed as hard spheres [154, 165, 166]. These are defined as impenetrable particles of diameter, σ_α and σ_β at a core to core distance of r^* (see figure 8.1). The solvation pressure between approaching surfaces arises as a result of the fluid particles being constricted in a narrow gap with the same order of magnitude as their molecular size.

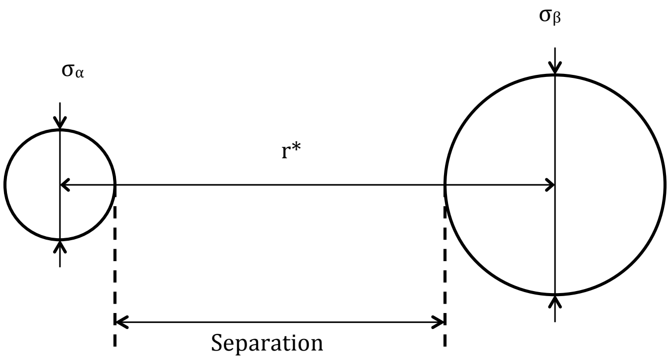

Figure 8.1: Interaction between a pair of particles

The interaction of the hard spheres between macroscopic bodies is of great interest in this study. The hard spheres' interaction between macroscopic curved bodies can be commonly described using the interaction energy, W^{s-s} [135, 167]. Derjaguin approximated the interaction energy between two curved surfaces as [167]:

$$W^{s-s}(r^*) \approx -k_B T[g^*(r^*) - 1] \tag{8.1}$$

where $s-s$ is the interaction between the curved surfaces confining the hard spheres, k_B is the Boltzmann constant and T is the temperature of the fluid system. The net interaction force between the curved surfaces, F^{s-s} can be obtained by differentiating equation (8.1) towards the distance of the curved surfaces, r,

$$F^{s-s} = -\frac{dW^{s-s}(r^*)}{dr^*} \tag{8.2}$$

The Derjaguin approximation can be applied to convert the net force between particles confined by macroscopic curved surfaces into force per unit area or pressure between planar walls. The approximation can be written as:

$$F^{p-p} = p_s = -\frac{dW^{p-p}(r^*)}{dr^*} \tag{8.3}$$

where p–p indicates the interaction between planar walls, $W^{p-p}(r) = F^{s-s}(r)/2\pi R_{eff}$ and $R_{eff} = \sigma_\alpha \sigma_\beta / 2(\sigma_\alpha + \sigma_\beta)$. The function g^* in equation (8.1) is the pair correlation function. The function describes the probability of finding a particle (species β) at a core to core distance, r^* from a referenced particle (species α).

The pair correlation function ($g^*_{\alpha\beta}$ in equation (8.1)) describes the probability of finding a particle (species β) at a core to core distance, r^* from a referenced particle (species α). For a uniform fluid consisting of particles interacting through central forces, the pair correlation function, $g^*_{\alpha\beta}$ is expressed as:

$$g^*_{\alpha\beta}(r^*) = h^*_{\alpha\beta}(r^*) + 1, \alpha, \beta \in \{1, 2, 3...(M+1)\} \tag{8.4}$$

where $h^*_{\alpha\beta}$ is the indirect correlation function, which describes the indirect influence of a particle of species α towards another particle of species β through an intermediate particle trapped in between them, which can be either of species α or β.

Ornstein and Zernike [168] proposed the following equation (OZ equation) for the the indirect correlation function ($h^*_{\alpha\beta}$):

$$h^*_{\alpha\beta}(r^*) \quad = \quad c^*_{\alpha\beta} + \sum_{\gamma=1}^{M+1} \rho^*_\gamma \int c^*_{\alpha\gamma}(|s|) h^*_{\gamma\beta}(|r^* - s|) ds \tag{8.5}$$

where $(M+1)$ is the total number of hard sphere species and s is the core to core distance of the surrounding spherical particles in a fluid system towards a reference particle, either of species α or β. The direct correlation function, $c^*_{\alpha\beta}$ determines the direct interaction between the spherical particles of species α and β. The parameter ρ^*_γ refers to the number density or particle density for the hard spheres of species γ.

Solving the OZ equation requires a suitable expression for the direct correlation function. The most effective ones are:

1) Percus-Yevick (PY) approximation

$$c^*_{\alpha\beta}(r^*) = g^*_{\alpha\beta}.(r^*)[1 - e^{\phi_{\alpha\beta}(r^*)/k_B T}] \tag{8.6}$$

2) Convolution-Hypernetted Chain (CHNC)

$$c^*_{\alpha\beta}(r^*) = h^*_{\alpha\beta}(r^*) - \log g^*_{\alpha\beta}(r^*) - \phi_{\alpha\beta}(r^*)/(k_B T) \tag{8.7}$$

such that particles of type α and β interact through an attraction potential, $\phi_{\alpha\beta}$, which is used to describe the adsorption of molecules [169].

The attractive potential $\phi_{\alpha\beta}$ describes the adsorption between molecules α and β [169]. The adsorption refers to the adhesion of particles, which form a molecularly-thin layer adhered to the surface. The PY approximation is preferred in this study because CHNC often causes divergence in numerical solutions of multi-molecule fluids [170]. Additionally, PY approximation is easier to apply and for strongly repulsive interactions (e.g. solvation) leads to accurate results [171].

Low concentrations of friction modifiers are often added to the base oil to decrease the boundary friction. These adhere to the surfaces, providing a protective layer with minimal shear resistance [69]. Friction modifiers are long chain molecules, typically alkane molecules with ten or more carbon atoms and a complex surface-active group at the end [172].

Jahanmir and Beltzer [80] provide an empirical model for the boundary friction coefficient using a two-component lubricant. They used as a base Temkin isothermal adsorption model [82] and assumed that friction arises only due direct surface interaction. This approach accounts for inhomogeneity in the contacting surfaces, but it is limited to weakly adsorbed base oil. The conclusion was that increasing lubricant adsorption energy reduces the friction coefficient.

Baxter [166] describes the adsorption of molecules to surfaces based on infinitesimally short range potentials and solves the Ornstein-Zernike equation analytically using the Percus-Yevick approximation (OZ-PY). The adsorbent-adsorbate attraction is characterised by a single energy parameter. Therefore, the spheres coming in direct contact with the adsorbate planar surface are deemed to be adsorbed. Dickinson [173] extended the multicomponent sticky hard spheres model to a qualitative model, which could explain the competitive adsorption of protein molecules.

Figure 8.2 shows the most commonly used attractive potentials. These are the square-well attraction (a) and the Yukawa potential (b). Due to its simplicity and versatility, the square-well attraction potential is usually used (see figure 8.2(a)) [174].

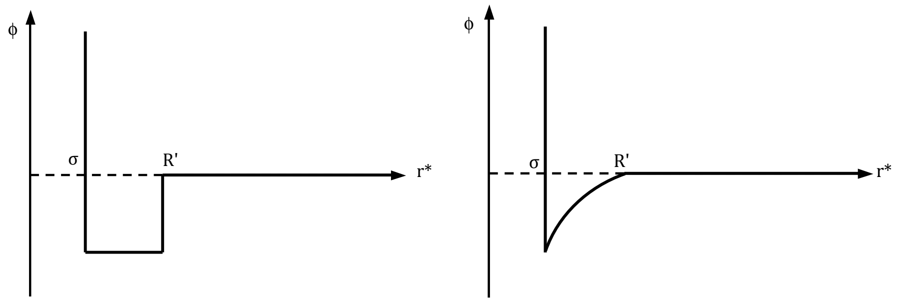

(a) Square-well potential

(b) Yukawa potential (Not used in the current model)

Figure 8.2: Particle interaction potentials

Baxter [166], in his sticky-spheres model, used an infinitely narrow attractive potential, ϕ for a single component fluid. Initially, he described the potential as:

$$\phi(r^*)/k_BT = \begin{cases} \infty & 0 < r^* < \sigma \\ log[12\bar{T}(R' - \sigma)/R'] & \sigma < r^* < R' \\ 0 & r^* > R' \end{cases}$$

where $\bar{T}$ is the dimensionless temperature of the fluid system and σ is the diameter of the hard sphere. He then assumed that $R' \approx \sigma$ and solved the Ornstein-Zernike equation via the Percus-Yevick approximation (OZ-PY) analytically [166]. This infinitely narrow well can be physically interpreted as surface adhesion. The disadvantage of Baxter's method is that it only accounts for a single species of hard spheres. Perram and Smith extended the work of Baxter to a fluid mixture [175]. They redefined the infinitely narrow potential, $\phi_{\alpha\beta}$ for a fluid mixture by first defining the potential as:

$$\phi_{\alpha\beta}(r)/k_BT = \begin{cases} \infty & r^* < R_{\alpha\beta} \\ log[12\bar{T}_{\alpha\beta}(R'_{\alpha\beta} - R_{\alpha\beta})/R'_{\alpha\beta}] & R_{\alpha\beta} < r^* < R'_{\alpha\beta} \\ 0 & r^* > R'_{\alpha\beta} \end{cases}$$

where $R_{\alpha\beta} = (\sigma_\alpha + \sigma_\beta)/2$. Perram and Smith then assumed that $R_{\alpha\beta} \approx R'_{\alpha\beta}$ to convert the potential above to the infinitely narrow well potential, $\phi_{\alpha\beta}$:

$$\phi_{\alpha\beta}(r)/K_BT = \begin{cases} log[12\delta\bar{T}_{\alpha\beta}/R'_{\alpha\beta}] & r^* \leq R_{\alpha\beta} \\ 0 & r^* > R'_{\alpha\beta} \end{cases}$$

where δ is the dirac delta function, which is used to define a limit to the infinitely narrow well potential. The potential, $\phi_{\alpha\beta}$ can be used to obtain the dimensionless temperature parameter, $\bar{T}$, which is used to solve the OZ-PY equation.

To obtain an analytical solution of the OZ equation for fluid mixtures, Baxter [169] took the three-dimensional Fourier transform of equation (8.5) as:

$$[I - \bar{C}_{\alpha\beta}(k)][I + \bar{H}_{\alpha\beta}(k)] = I \tag{8.8}$$

where

$$\begin{aligned} I &= \text{Identitiy matrix of } (M+1) \times (M+1) \text{ matrix} \\ \bar{C}_{\alpha\beta}(k) &= 4\pi\sqrt{(\rho^*_\alpha\rho^*_\beta)}\int_0^\infty\int_{r^*}^\infty s.c^*_{\alpha\beta}(s).cos(kr)dsdr \\ \bar{H}_{\alpha\beta}(k) &= 4\pi\sqrt{(\rho^*_\alpha\rho^*_\beta)}\int_0^\infty\int_{r^*}^\infty s.h^*_{\alpha\beta}(s).cos(kr)dsdr \end{aligned}$$

Rearranging equation (8.8) into:

$$I - \bar{C}_{\alpha\beta}(k) = \bar{Q}^{tr}_{\alpha\beta}(-k)\bar{Q}_{\alpha\beta}(k) \tag{8.9}$$

where

$$\begin{aligned} \bar{Q}_{\alpha\beta} &= \delta_{\alpha\beta} - 2\pi\sqrt{(\rho^*_\alpha\rho^*_\beta)}\int_{S_{\alpha\beta}}^{R_{\alpha\beta}} e^{ikr}q_{\alpha\beta}(r)dr \\ S_{\alpha\beta} &= (\sigma_\alpha - \sigma_\beta)/2 \\ R_{\alpha\beta} &= (\sigma_\alpha + \sigma_\beta)/2 \end{aligned}$$

Equation (8.9) is the Winer-Hopf factorisation [176] of equation (8.5). Therefore, combining equation (8.8) and (8.9) gives

$$\bar{Q}_{\alpha\beta}(k)[I + \bar{H}_{\alpha\beta}(k)] = [\bar{Q}^{tr}(-k)]^{-1} \tag{8.10}$$

By carrying out the inverse one dimensional fourier transform of equation (8.10) using equation (8.9) and then differentiating the product against r^*,

$$\begin{aligned} r^* h^*_{\alpha\beta}(|r^*|) &= -\frac{d}{dr^*} q_{\alpha\beta}(r^*) \\ &\quad + 2\pi \sum_{\gamma=1}^{M+1} \rho^*_\gamma \int_{S_{\alpha\gamma}}^{R_{\alpha\gamma}} q_{\alpha\gamma}(s)(r^* - s) h^*_{\gamma\beta}(|r^* - s|) ds \end{aligned} \tag{8.11}$$

The transformed equation (8.11) can be solved using the method proposed by Perram [177]. Perram and Smith pointed out that the early terms in the virial expansion's coefficient for the indirect correlation function, $h^*_{\alpha\beta}$ when $S_{\alpha\beta} < r < R_{\alpha\beta}$ suggests the form of [175]:

$$h^*_{\alpha\beta}(r^*) = -1 + \frac{1}{12}\lambda_{\alpha\beta} R_{\alpha\beta} \delta(r^* - R_{\alpha\beta}) \tag{8.12}$$

where $\lambda_{\alpha\beta}$ are a set of unknown values to be determined later. The virial expansion is used to express the pressure of a system in equilibrium as a power series in the function of density. Perram and Smith [175] pointed out that $q_{\alpha\beta}(r^*)$ is quadratic in nature by evaluating equation (8.11) and (8.12) for $S_{\alpha\beta} < r < R_{\alpha\beta}$.

Therefore, for $S_{\alpha\beta} < r^* < R_{\alpha\beta}$ [175],

$$q_{\alpha\beta}(r^*) = a_\alpha (r^{*2} - R^2_{\alpha\beta})/2 + b_\alpha (r^* - R_{\alpha\beta}) + \lambda_{\alpha\beta} R^2_{\alpha\beta}/12 \tag{8.13}$$

where

$$\begin{aligned} a_\alpha &= (1 - \zeta_3 + 3R_\alpha \zeta_2)/(1 - \zeta_3)^2 - X_\alpha/(1 - \zeta_3) \\ b_\alpha &= (-3R^2_\alpha \zeta_2)/2(1 - \zeta_3)^2 - R_\alpha X_\alpha / 2(1 - \zeta_3) \\ X_\alpha &= \frac{\pi}{6} \sum_{\gamma=1}^{M+1} \rho^*_\gamma \lambda_{\alpha\gamma} R^2_{\alpha\gamma} \sigma_\gamma \\ \zeta_j &= \frac{\pi}{6} \sum_{\gamma=1}^{M+1} \rho^*_\gamma \sigma^j_\gamma, j = 1, 2, 3 \end{aligned}$$

As for $r^* > R_{\alpha\beta}$,

$$q_{\alpha\beta}(r^*) = \frac{d}{dr^*}q_{\alpha\beta}(r^*) = 0 \tag{8.14}$$

Assuming the planar or flat surface is species $(M+1)$, particle diameter $\sigma_{M+1} \rightarrow \infty$ and the number density or particle density $\rho^*_{M+1} \rightarrow 0$, equation (8.11) can be rewritten as:

$$\begin{aligned} r^* h^*_{\alpha\beta}(|r^*|) &= -\frac{d}{dr^*}q_{\alpha\beta}(r^*) \\ &\quad +2\pi \sum_{\gamma=1}^{M} \rho^*_{\gamma} \int_{S_{\alpha\gamma}}^{R_{\alpha\gamma}} q_{\alpha\gamma}(s)(r^*-s)h^*_{\gamma\beta}(|r^*-s|)ds \end{aligned} \tag{8.15}$$

The $\lambda_{\alpha\beta}$ parameter can be related to the dimensionless temperature of the system $\bar{T}$ using the approximation proposed by Perram and Smith [178]. The relationship can be written as follow:

$$\lambda_{\alpha\beta}\bar{T}_{\alpha\beta} = a_{\alpha} + b_{\alpha}/R_{\alpha\beta} + \frac{\pi}{6}\sum_{\gamma=1}^{M+1} \rho_{\gamma}\frac{\lambda_{\beta\gamma}R^2_{\beta\gamma}}{R_{\alpha\beta}}q_{\alpha\gamma}(S_{\alpha\gamma}) \tag{8.16}$$

In this study, the hard spheres are considered not to adhere/adsorb to each other but only to the wall ($\lambda_{\alpha\beta} \approx 0$, $\alpha, \beta \neq M+1$) [171, 178, 179]. Hence, this limits sphere-sphere interaction solely to the repulsive hard core potential. If needed, this assumption can be easily removed to account for inter-molecular adsorption. With the wall species diameter, $\sigma_{M+1} \rightarrow \infty$, the adsorption parameter, d_{α} can be defined as [171]:

$$d_{\alpha}(T) = \int_0^{\infty} [e^{-\phi_{\alpha}(r^*)/k_B T} - 1]dr^* \tag{8.17}$$

The corresponding infinitely narrow well potential, ϕ_{α} for hard spheres adsorbing to the planar wall in equation (8.17) is [171]:

$$\phi_{\alpha}(r^*) = \begin{cases} -\epsilon(\sigma_{\alpha} - r^*)/\sigma_{\alpha} & 0 < r^* < \sigma_{\alpha} \\ 0 & r^* > \sigma_{\alpha} \end{cases}$$

where ϵ is the adsorption energy per unit k_BT. Substituting a_α, b_α and S_α into equation (8.16), $\lambda_{\alpha,M+1}$ can be determined using the following expression [171]:

$$\frac{\lambda_{\alpha,M+1}R_{\alpha,M+1}}{12d_\alpha(T)} = \frac{1-\zeta_3+3\sigma_\alpha\zeta_2}{(1-\zeta_3)^2} - \frac{\pi\sigma_\alpha}{12(1-\zeta_3)}\sum_{\gamma=1}^{M}\rho_\gamma^*\sigma_\gamma\lambda_{\gamma,M+1}R_{\gamma,M+1} \quad (8.18)$$

Therefore, for $r^* > R_{\alpha\beta}$ and a multicomponent fluid equation (8.15) becomes [178, 177]:

$$\begin{aligned} & h^*_{\alpha\beta}[R_{\alpha\beta}+(m+1)\Delta] = \\ = & \frac{\pi\Delta\sum_{\gamma=1}^{M}\sum_{\eta=0}^{N_\gamma}\rho^*_\gamma\left\{\begin{array}{l} q_{\alpha\gamma}(S_{\alpha\gamma}+\eta\Delta)\times \\ (R_{\gamma\beta}+(m+1-\eta)\Delta)\times \\ h^*_{\gamma\beta}[|R_{\gamma\beta}+(m+1-\eta)\Delta|] \end{array}\right\}}{(R_{\alpha\beta}+(m+1)\Delta)} \end{aligned} \quad (8.19)$$

where m $(= 1, 2, 3......)$ is the grid point along hard sphere separation axis, N_γ $(= \sigma_\gamma/\Delta)$ is the limit to the integral term in equation (8.11) and Δ is the grid step size.

The pair correlation function, $g^*_{\alpha\beta}$ can be calculated once the indirect correlation function, $h^*_{\alpha\beta}$ is obtained from equation (8.19). The solvation pressure p_s generated by hard spheres confined by flat bodies is computed from equation (**??**) using a forward finite difference scheme [165]:

$$p_s[m\Delta] = -\frac{k_BT}{2\pi R_{eff}\Delta^2}\left\{\begin{array}{l} g^*_{M+1,M+1}[(m+1)\Delta] - 2g^*_{M+1,M+1}[m\Delta] \\ +g^*_{M+1,M+1}[(m-1)\Delta] \end{array}\right\} \quad (8.20)$$

The asperity contact load is:

$$P = \int p_s dxdy \quad (8.21)$$

8.3 Frictional conjuction

Friction generated by the ultra-thin adsorbed films on nominal molecularly smooth surfaces follow a non-Newtonian shear due to chemical reactions which are based on thermal activation. It was discussed in the previous chapter that Eyring [145] developed a model which described the viscosity of fluids under such circumstances. Eyring's model assumes that the motion of a volume of fluid molecules takes place in the presence of a cage-like potential barrier by their mere closely-packed arrangement in the bulk. In order to overcome this potential and escape the cage, the fluid molecules have to surmount the activation barrier potential. This is the thermal activation model which Eyring modified to include the effects of prevailing pressure, p and shear, τ_y as:

$$E_y = Q_y + p\Omega_y - \tau_y \phi_y^* \tag{8.22}$$

where E_y is the barrier height for Eyring model, Q is the process activation energy, Ω_y is the pressure activation volume where pressure, p_s is acting on and ϕ_y^* is the shear activation volume. The shear activation volume, ϕ_y^* is interpreted as the size of segment that moves during the shear stress process. This volume can be a part of a molecule or a dislocation line. The pressure activation volume, Ω_y is associated with the local increase in volume to permit the molecular motion to occur.

For a wall-wall interaction, the pressure, p_s acting on the wall can be assumed to consist of only the solvation pressure, which can be computed using equation (8.20). Therefore, the barrier height, E_y is equivalent to the solvation energy produced by the hard sphere particles. From equation (8.3), the barrier height, E_y can be expressed as:

$$\begin{aligned} E_y &= W^{p-p}(r) \\ &= \frac{F^{s-s}}{2\pi R_{eff}} \\ &= -\frac{1}{2\pi R_{eff}} \cdot \frac{dW^{s-s}(r^*)}{dr^*} \\ &= \frac{k_B T}{2\pi R_{eff}} \cdot \frac{d}{dr^*}[g^*_{M+1,M+1}(r^*) - 1] \end{aligned} \tag{8.23}$$

Using the backward finite differencing scheme, E_y can be solved as follow in J/m^2:

$$E_y[m\Delta] = \frac{k_B T}{2\pi R_{eff}\Delta}\left\{g^*_{M+1,M+1}[m\Delta] - g^*_{M+1,M+1}[(m-1)\Delta]\right\} \tag{8.24}$$

where m is the grid points $(1, 2, 3......)$ and Δ is the grid step size

By rearranging equation (8.22), the shear stress, τ_y can be defined as:

$$\tau_y = \frac{Q_y + p\Omega_y - E_y}{\phi^*_y} \tag{8.25}$$

Therefore, the friction force is:

$$P_f = \int \tau_y dxdy \tag{8.26}$$

The parameters Q_y, Ω_y and ϕ^*_y must be obtained experimentally. As a first approximation in predicting the shear stress, the values of these parameters are taken from the experimental measurements of He *et al* [147]. The values are: $Q_y = 1.33 \times 10^{-20} J$, $\Omega = 1.93 \times 10^{-13} m^3/m^2$ and $\phi^*_y = 1.21 \times 10^{-12} m^3/m^2$. Therefore, the shear stress between planar walls can be predicted using equation (8.25).

8.4 Results and Discussions

The study attempts to understand the inter-molecular interactions of fluid mixtures considering adsorption. The proposed model predicts solvation pressure (using equation (8.20)) and shear stress (using equation (8.25)) generated by the confinement of hard spheres within flat walls. The approach is first used to understand the role of molecular concentration and adsorption in a single component fluid confined by flat walls. The study also simulates the inter-molecular characteristics of a dual component fluid between flat walls with each hard sphere species having different molecular sizes, concentration ratios, r_w and adsorption capabilities.

8.4.1 Single component fluid confined by planar walls

The idealised fluid comprises a single species of assumed hard spherical molecules, confined by planar walls (figure 8.3). The molecular diameter is assumed to be $1nm$.

An example of such an idealised fluid is OMCTS.

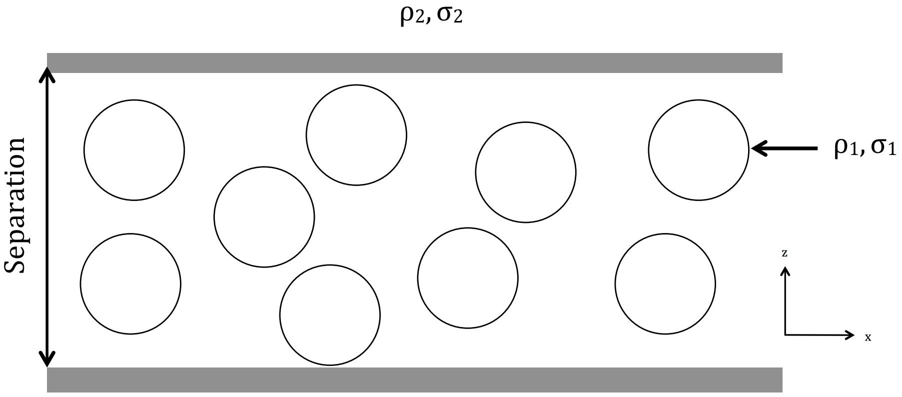

Figure 8.3: Single component fluid confined by planar walls

The pair correlation function between the hard spheres, g_{11}^* can be obtained as shown in figures 8.4 (a) and (b) through solution of the OZ-PY equation. The packing fraction, η_α^* denotes the occupied volume fraction by the molecular disposition and can be expressed as:

$$\eta_\alpha^* = \pi\rho_\alpha^*\sigma_\alpha^3/6 \tag{8.27}$$

A smaller packing fraction, η_1^* represents a smaller number density, ρ_1^*. Thus, the amplitude of oscillations reduces significantly for a smaller packing fraction, η_1^*, attenuating the effect of solvation. It can be observed that g_{11}^* behaves in an oscillatory manner as the separation gap is reduced. However, due to the increased packing fraction, the interaction between particles g_{11}^* for $\eta_1^* = 0.4$ promotes a larger amplitude.

Figure 8.4 also shows the pair correlation function for hard sphere-wall g_{21}^* and wall-wall g_{22}^* interactions. It is noted that the g_{21}^* is negative at small separations which reflects a strong exclusion of the hard spheres from the confined region (figure 8.4(c) and (d)). It can be observed that with increasing adsorption energy, ϵ_1, a sharp peak becomes apparent at the separation height of $1nm$ (the molecular diameter of the species). This peak is caused by the packing of the hard spheres onto the already adsorbed mono-layer on the planar wall surface. The increment ϵ_1 encourages adsorption of hard spheres to form a denser layer on the planar wall. The adsorption of an increasing number of hard spheres, packing on an already formed monolayer instead of the bare planar wall reduces the oscillatory behaviour there. This is true for both g^*_{21} and g^*_{22}. For smaller values of η^*_1 (figure 8.4 (a) and (c)), the packing of the hard spheres onto the monolayer at the planar surface resembles the observations made by Perram and Smith [178].

Figure 8.5 illustrates the solvation pressure computed using different adsorption energy values, ϵ_1. Higher values of ϵ_1 encourage the formation of a denser monolayer. Hence, this increases the solvation pressure at separations near the monolayer. A smaller η^*_1 value (see figure 8.5 (a)) reduces the solvation pressure due to the dilution of the fluid. An interesting point is to note that solvation pressure is noticeable only beyond $2nm$. This is because the separation of the walls is limited by the adsorbed monolayers on the contiguous approaching walls.

The packing fraction, $\eta^*_1 = 0.4$ is used by Henderson and Lozada-Cassou [139] and Matsuoka and Kato [165] to compute the solvation pressure for OMCTS. Therefore, a comparison can be made between the solvation pressure computed based on this packing fraction and that obtained by Chan and Horn empirically (see figure 8.5 (b)) for OMCTS [134]. It can be observed that both methods show good agreement in terms of oscillatory characteristics but at a slightly varying amplitudes.

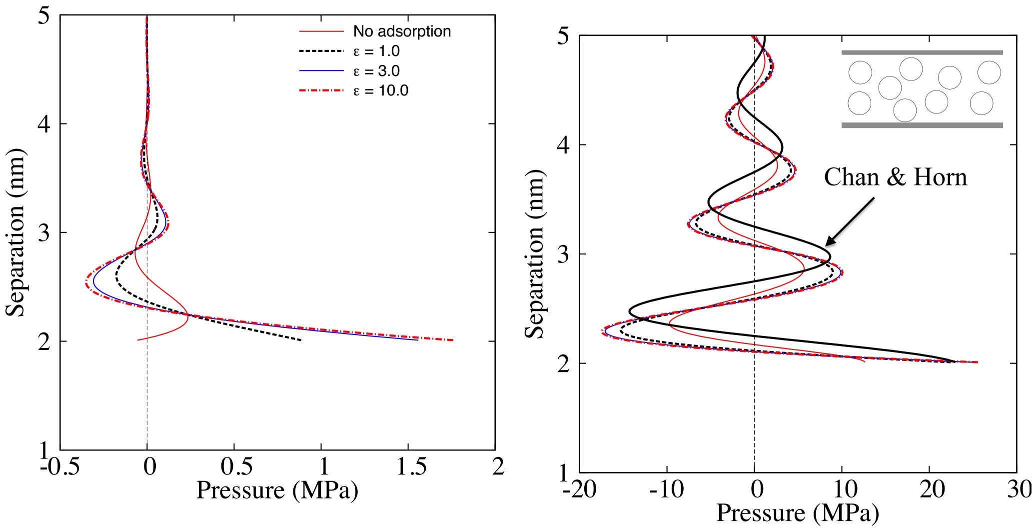

(a) $\eta^*_1 = 0.2$ (b) $\eta^*_1 = 0.4$

Figure 8.5: Solvation pressure for a single component fluid

The solvation energy required to compute the shear stress using the Eyring model [145] is plotted in figure 8.6 for different adsorption energy levels of hard spheres. The solvation energy has a larger amplitude for $\eta^*_1 = 0.4$ due to increased solvation. Using

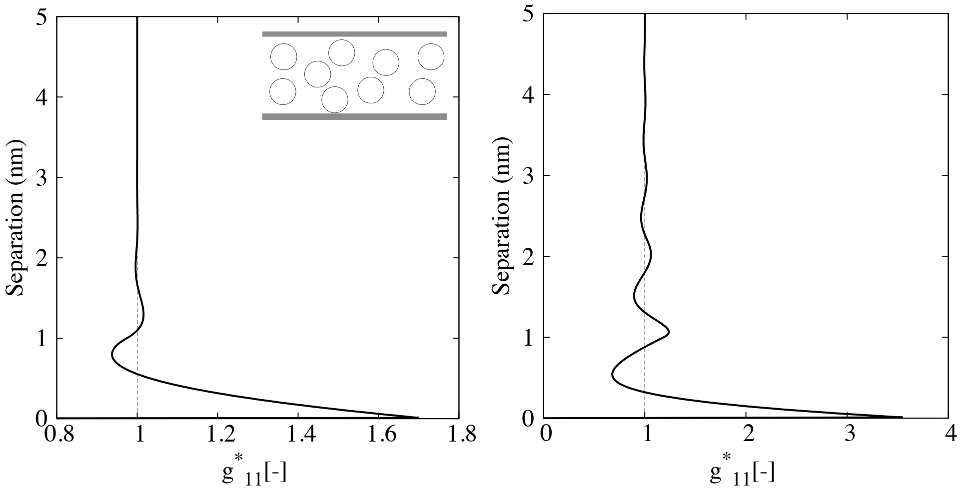

(a) $\eta_1^* = 0.2$

(b) $\eta_1^* = 0.4$

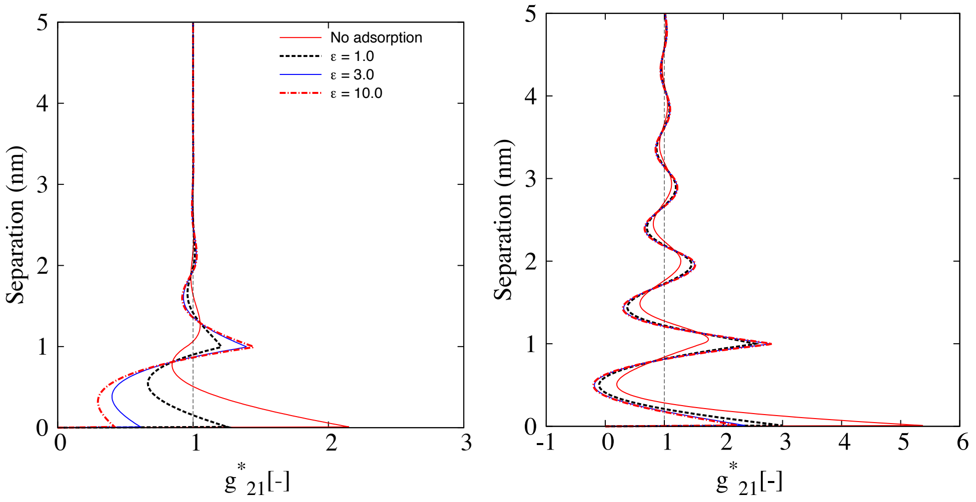

(c) $\eta_1^* = 0.2$

(d) $\eta_1^* = 0.4$

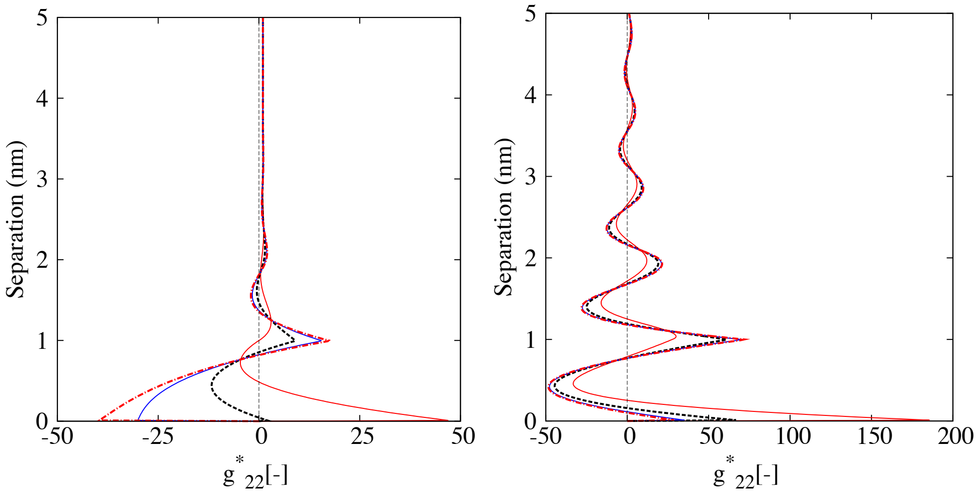

(e) $\eta_1^* = 0.2$

(f) $\eta_1^* = 0.4$

Figure 8.4: Pair correlation functions for a single component fluid

equation (8.25), the shear stress can be obtained for a wall-wall (g_{22}^*) interaction as shown in figure 8.7. Negative shear stress in the figure is discussed later.

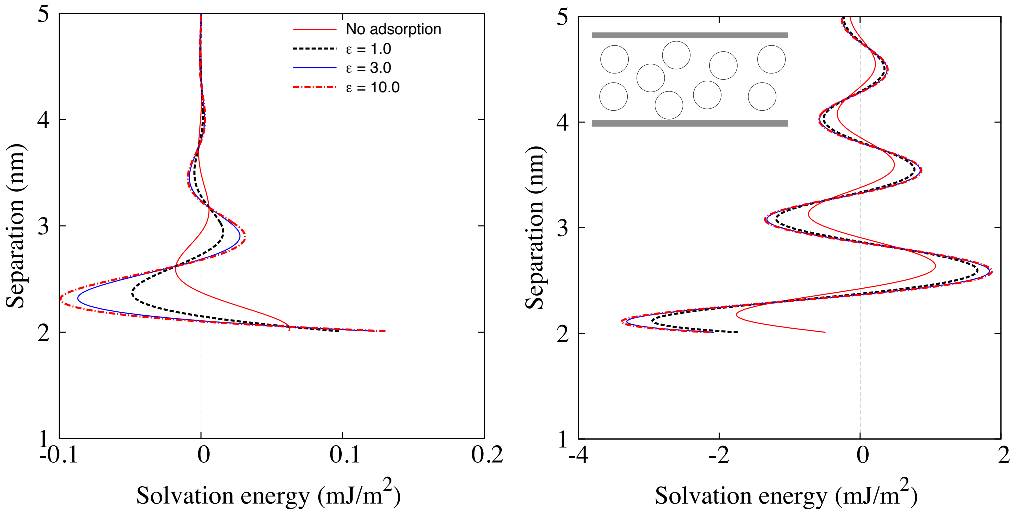

(a) $\eta_1^* = 0.2$ (b) $\eta_1^* = 0.4$

Figure 8.6: Solvation energy for a single component fluid

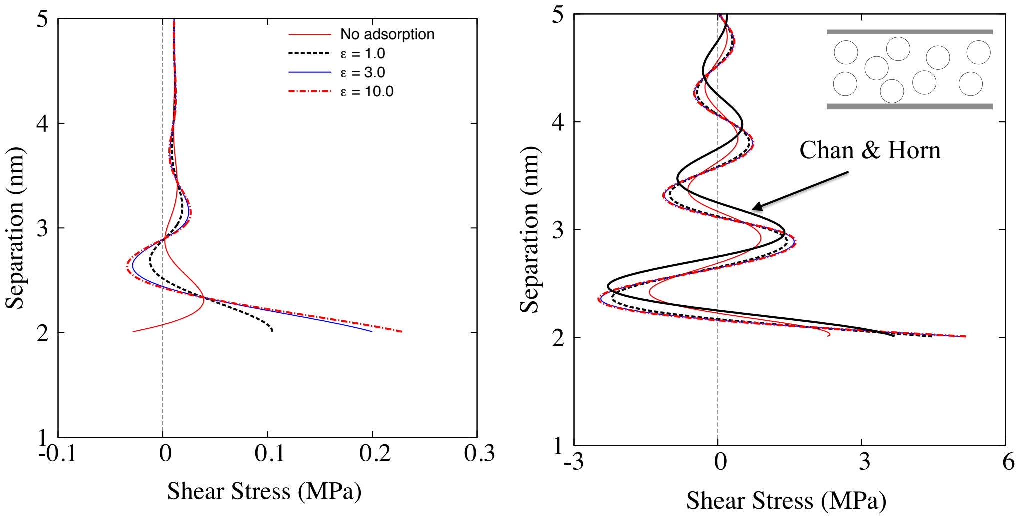

(a) $\eta_1^* = 0.2$ (b) $\eta_1^* = 0.4$

Figure 8.7: Shear stress for a single component fluid

8.4.2 Dual component fluid mixture confined by planar walls

Real physical fluids comprise a multitude of molecular species. The model described thus far can be extended to a simple physical fluid containing two molecular components (figure 8.8). The empirical method derived by Chan and Horn [134] only limited to a single component fluid system. The same limitation does not apply to the model developed here. In the model of figure 8.8, the two molecular species are represented by hard spheres, one of nominal average diameter $0.5nm$ (species 1) and the other of nominal average diameter $1nm$ (species 2). It is assumed that the species 1 has significantly higher adsorption energy than species 2. This choice is purely arbitrary.

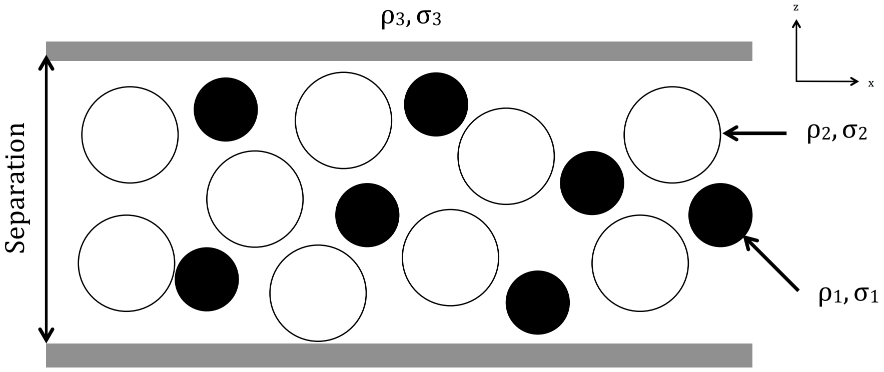

Figure 8.8: Dual component fluid confined by planar walls

The overall packing fraction for the fluid mixture is assumed to remain constant at $\eta^*_{tot} = 0.4$. Therefore, for a given concentration ratio, r_w of the species, their packing fractions are obtained as:

$$\eta^*_1 = r_w \eta^*_{tot}, \qquad \eta^*_2 = (1 - r_w)\eta^*_{tot} \tag{8.28}$$

Figure 8.9 shows pressure perturbations and discontinuous shear stress variations caused by the local minima in the intermolecular pair correlation functions (local potentials between individual molecules of the same or different species). The effect of molecular adsorption energy to the solid barrier as well as the molecular concentrations are investigated. There is an ideal concentration of each component, which leads to the optimal (minimum or maximum) load carrying capacity and shear. The figure shows that for a higher molecular packing fraction, both the solvation pressure and shear stress levels increase. The increase in pressure is due to a higher density of the molecules in the fluidic medium. Therefore, the density fluctuation near the solid barriers due to solvation effect would be higher. Similarly, a higher shear stress would be expected with the greater packing fraction because friction caused by the layering effect (i.e. ejection of rows of molecules out of the conjunction) would be subjected to the presence of a larger number of molecules. The lower packing fraction would be representative of a medium tending to a vapour or gaseous environment. On the other hand, the higher packing faction of $\eta^*_{tot} = 0.4$ is more representative of a liquid medium. Therefore, the conclusions arrived at with regard to figure 8.9 are only natural. Figure 8.9 also shows results for different concentrations of the species with greater adsorption energy.

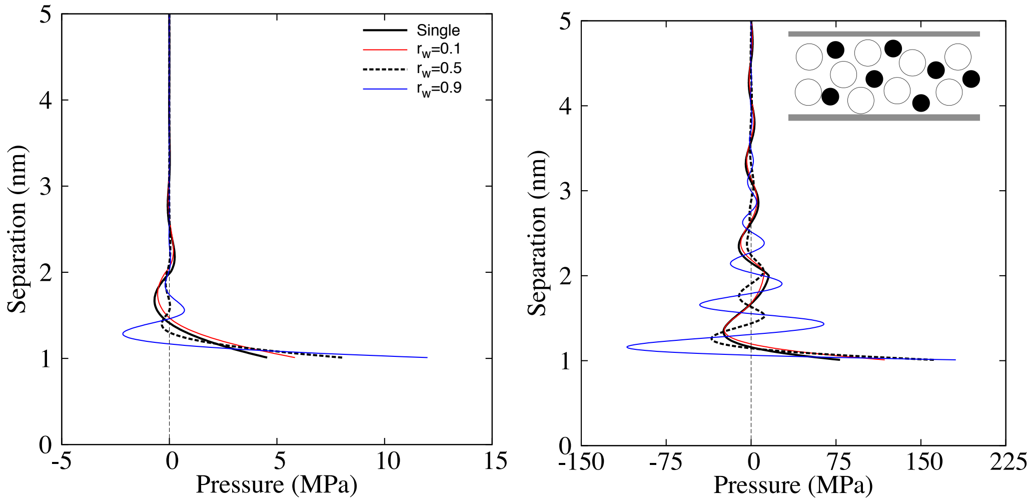

(a) $\eta^*_{tot} = 0.2$ (b) $\eta^*_{tot} = 0.4$

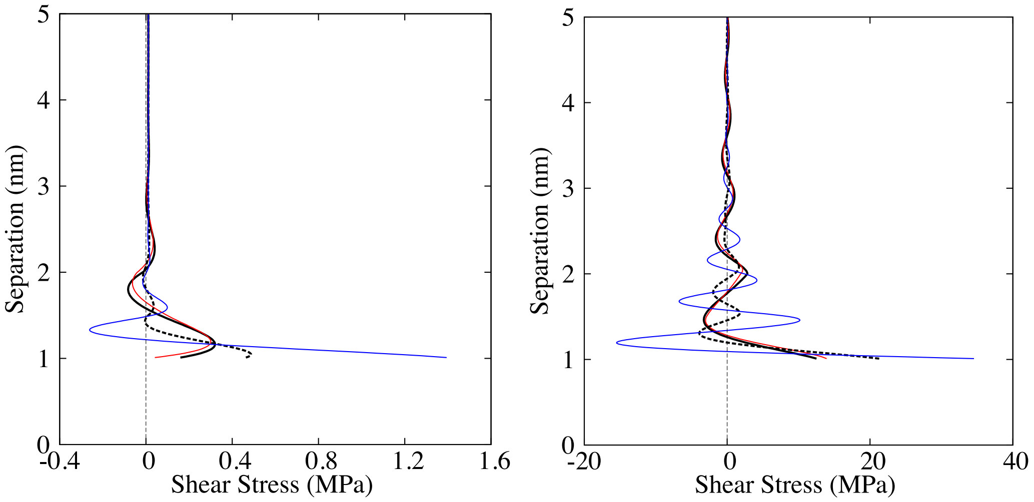

(c) $\eta^*_{tot} = 0.2$ (d) $\eta^*_{tot} = 0.4$

Figure 8.9: Pressure and shear stress for a dual component fluid system considering different concentration ratio, r_w for species 1 ($\epsilon_1 = 10, \epsilon_2 = 0.1$)

Differences are noted between generated pressures and shear with different concentration levels. This is more evident in figure 8.10 where for a given packing fraction, larger concentrations of the species with higher adsorption energy lead to formation of a thicker adsorbed layer. This tends to create a lower shear strength film, thus reducing shear. However, it is clear in figure 8.10 (c) and (d) that after a minimum shear stress level is achieved, any further accumulation of adsorbed molecules increases the shear stress. It can surmised that thicker adsorbed films result in an effective increase in viscosity of the film, thus a greater shear stress. This maybe the underline explanation for the observed micro scale phenomena of shear stress variation in direct proportion to fluid viscosity. Figures 8.10 (a) and (b) show that for any packing fraction generated pressures increase with the greater concentration of the species with higher adsorption energy. With sufficient concentration, a plateau effect is observed which infers that the adsorbed layer inhibits solvation. However, as a further increase in concentration takes place, the density variation near the surfaces reaches a saturation point where the solvation effect seems to exacerbate. With the solvation phenomenon, rows of molecules are ejected at discrete energy levels as shown by Chong *et al* [152]. It is therefore natural that with increasing concentration, there would be a limit where the advantages gained through reduced shear strength of a layer is lost by the energy required to eject a larger number of molecules out of a conjunction of a mutually approaching solid barriers. Referring to the micro scale behavior of fluidic films in conjunctions subject to pure squeeze, shear stress is governed by $\tau = \pm(h/2)(\partial p_s/\partial x)$, where x is the direction normal to the line of approach. The pressure gradient here is a function of number of layers and molecules in each layer which are subject to solvation pressure (discretisation and ejection of rows of molecules). Therefore, the larger number of molecules and thicker adsorbed films constitute a higher shear stress. In an allusion to the micro scale behaviour, the underlined nano scale phenomena observed here indicates that changes in oscillatory behaviour of solvation pressure (attraction-repulsion) alters the shearing characteristics of surface adsorbed films. Since the changes in pressure gradient results in layering of the adsorbed film, the layers of molecule rearrange, thus alter the sense of shear. Negative shear occurs in transition between discrete layers of the adsorbed film. This explains the negative shear stress noted in figure 8.7.

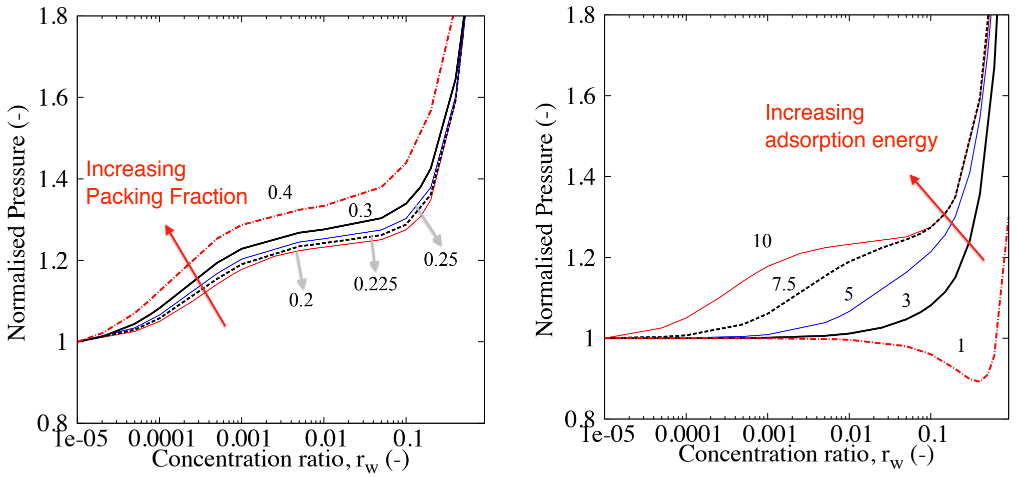

(a) Packing fraction, η^*_{tot} variation ($\epsilon_1 = 10, \epsilon_2 = 0.1$)

(b) Adsorption energy, ϵ_1 variation ($\eta^*_{tot} = 2, \epsilon_2 = 0.1$)

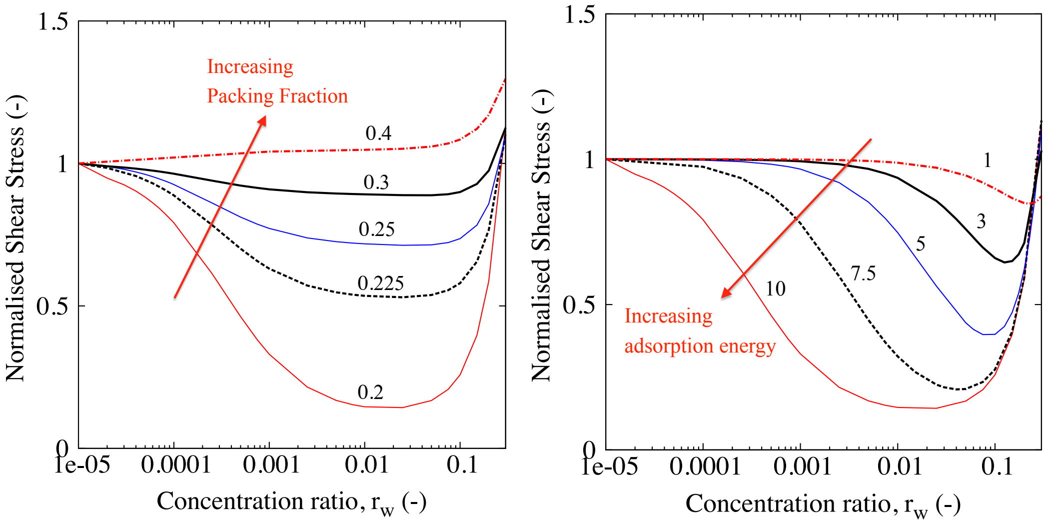

(c) Packing fraction, η^*_{tot} variation ($\epsilon_1 = 10, \epsilon_2 = 0.1$)

(d) Adsorption energy, ϵ_1 variation ($\eta^*_{tot} = 2, \epsilon_2 = 0.1$)

Figure 8.10: Normalised pressure and shear stress at $1nm$ for a dual component fluid system considering different concentration ratio, r_w for species 1

8.4.3 Asperity Contact

The model proposed in section *8.4.2* predicts the load carrying capacity and the shear force of a dual component lubricant confined between parallel walls. However, the final goal of the study is to predict the frictional losses between rough surfaces. The current section extends the two-component fluid model to predict the shear between two approaching asperities separated by a thin film, while *Chapter 9* will propose several models for the friction between rough surfaces (with statistical and fractal asperity distributions). The core of the numerical algorithm and the convergence criteria described in *Chapter 7* (see figure 7.2) are maintained. To predict the behaviour of the two component fluid, the empirical expression of the solvation pressure component (equation (7.12)) is replaced by equation (8.20). The new code predicts the tribological characteristic of a single spherical asperity approaching a flat surface.

Figure 8.11 shows the contact pressure distribution and film profile between a typical asperity ($0.1mm$ radius) and a horizontal plane at $8nm$ separation gap and $0.6mm/s$ entrainment velocity. The three-dimensional contact pressure of the contact is shown in figure 8.11(a). Similarly with figure 7.5 for a single component lubricant, the pressure distribution shows four distinct regions: 1) inlet meniscus/wedge, 2) pressurised region, 3) cavitation region and 4) lubricant reformation zone.

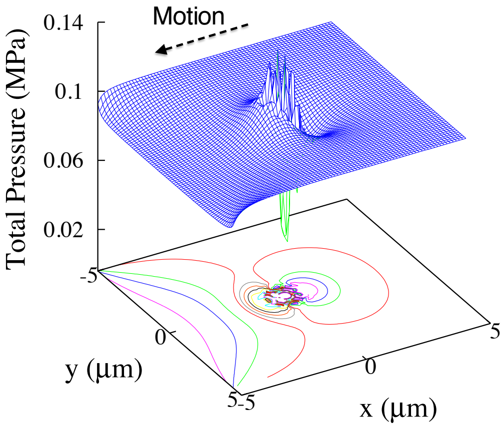

(a) Point-contact pressure distribution

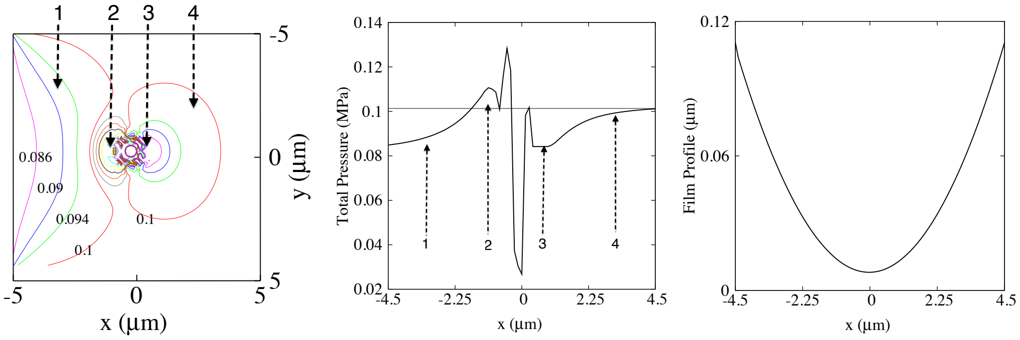

(b) Isobaric plot for contact pressure

(c) Contact Pressure

(d) Film profile

Figure 8.11: Contact characteristics

Figure 8.12(a) shows the the total load variation with the reduction of the separation gap for one asperity. The predictions of the proposed method (PS) are shown with dotted line and the predictions of Chan and Horn's (CH) with full line. The two load curves are in good agreement in terms of the oscillating behaviour. Figure 8.12(b) shows the friction force for the asperity point contact. The friction force predicted using PS's method is smaller than CH's prediction. This is mainly due to the smaller load computed for the asperity contact using PS's method. Except for the slightly smaller magnitude, both predictions show similar trends.

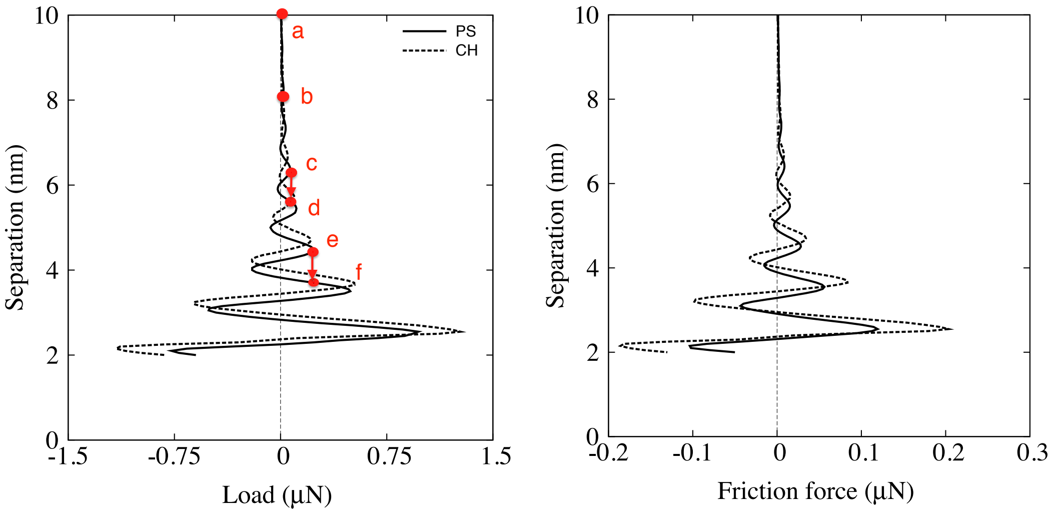

(a) (b)

Figure 8.12: Load comparison between Chan and Horn (CH) and Perram and Smith's (PS) method for a single component fluid

Figure 8.13 illustrates the contact pressure distribution from points a to f (see figure 8.12(a)). At $10nm$, the oscillatory characteristics of the pressure distribution predicted using PS's method is more significant. However, as the separation gap between the contact is being further reduced, CH's method seems to predicting a much more severe oscillation as compared to PS's approach.

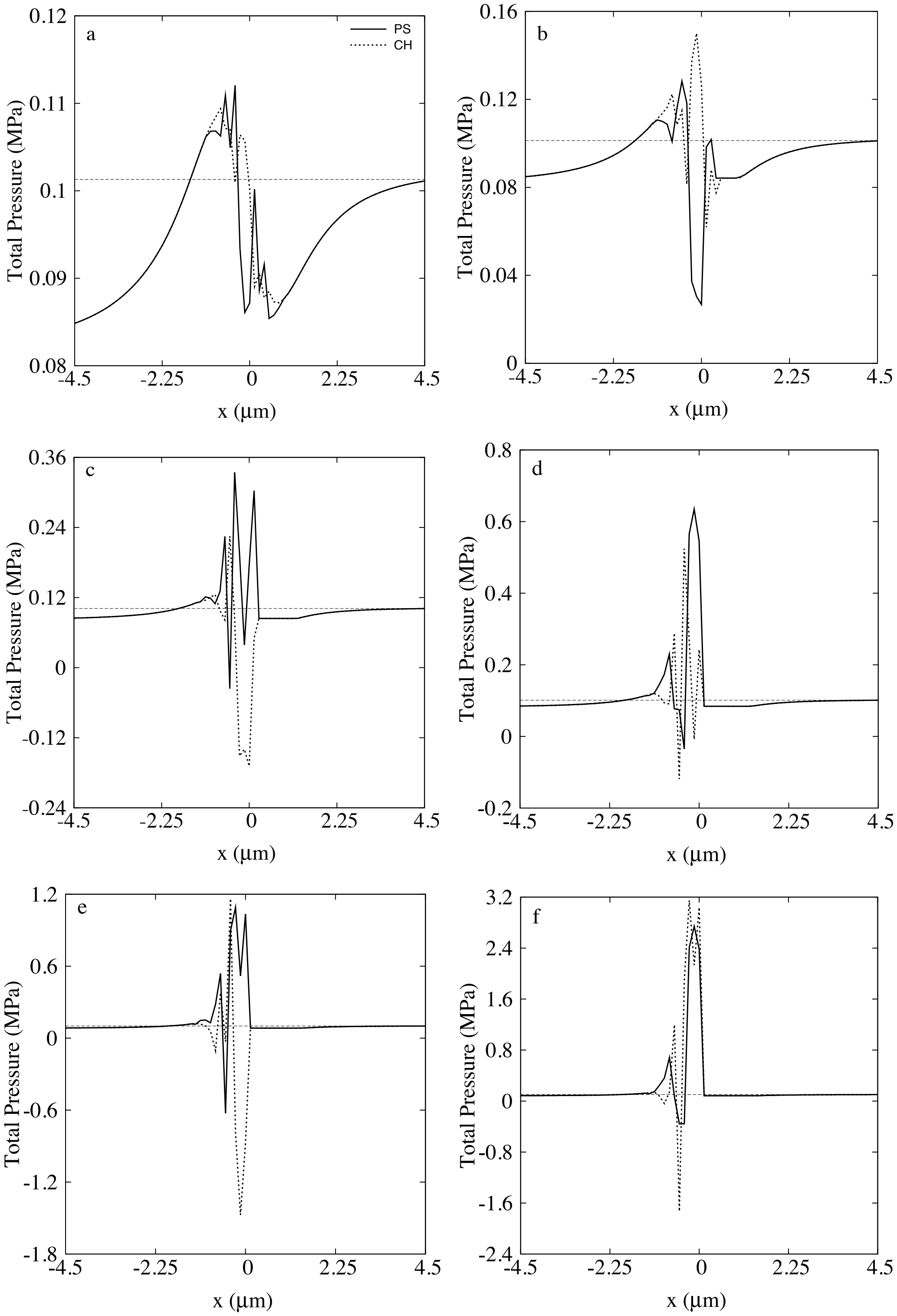

Figure 8.13: Contact pressure distribution for a single component fluid - No adsorption

Figure 8.14 shows the load and friction force predicted for an asperity contact considering a bi-component fluid mixture. The molecular concentration of the highly adsorbed species (species 1) is increased to observe the change in load carrying capacity and friction force. It can be observed from figure 8.14(a) that larger concentration of the highly adsorbed species inhibits a more significant oscillatory characteristics. It can also be seen that the load carrying capacity at the adsorbed monolayer (at $1nm$) increases with the larger molecular concentration of species 1. However, for the friction force, there is an optimum molecular concentration of species 1 which gives a minimal frictional characteristic (see figure 8.14). The same was observed in figure 8.10 for planar walls.

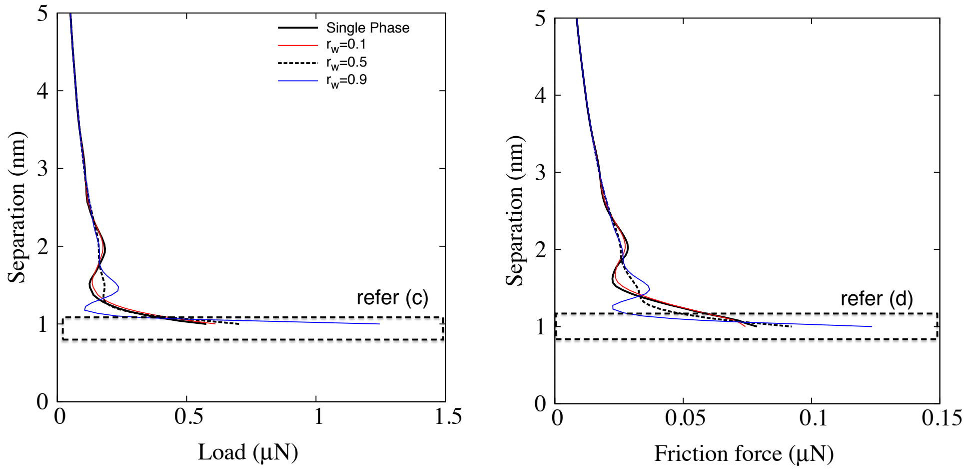

(a) Load (b) Friction

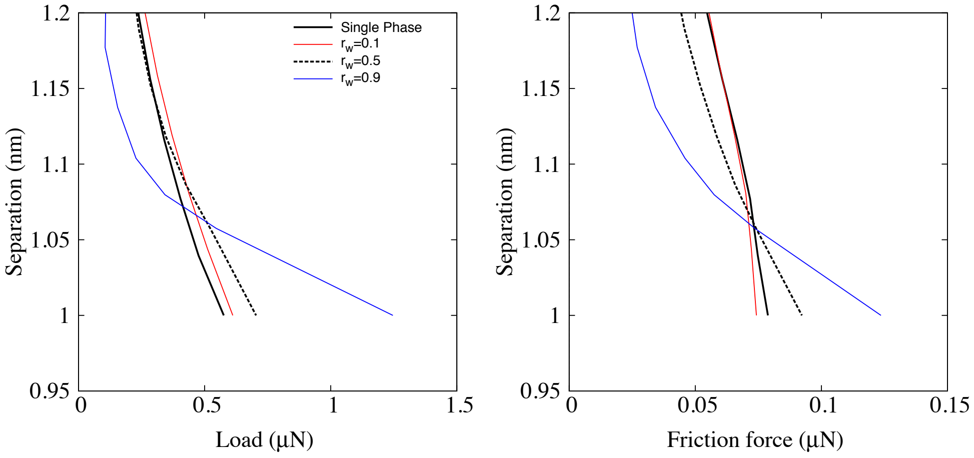

(c) Load (d) Friction

Figure 8.14: Dual component lubricant at $\eta^*_{tot} = 0.2$ with variation in concentration ratio for species 1, r_W ($\epsilon_1 = 10$, $\epsilon_2 = 0.1$)

8.5 Summary

This chapter develops a statistical mechanics model to predict the solvation force between planar walls. The wall-wall model is applied to the asperity contact model in the previous chapter. The current model accounts for bi-species fluidic medium and if required, can be extended for multi-species medium. The adsorption factor influencing the boundary lubrication is also included in the statistical model. The next chapter attempts to combine the asperity models discussed thus far to predict friction force for a rough surface.

Chapter 9

Rough Surface Contact

9.1 Introduction

The contact models developed by Hertz [109], Johnson *et al* [111], Derjaguin *et al* [113] and Maugis [114] assumed contacts between a sphere loaded purely in the normal direction and a plane. They all assumed that the contacting solids have a smooth surface. However, all contacting surfaces are rough. A highly polished surface under a profilometer or microscope, shows a succession of peaks and valleys [180]. The peaks are known as asperities, which are responsible for the contact between two surfaces. Therefore, regardless of the geometrical size of the contact, the actual size of the contact (the summation of all contacting asperities) is significantly smaller inducing a high compressive stress in each asperity. Hence, this could induce localised (asperity level) yielding and plastic deformation. Therefore, it is critical to have an effective surface characterisation model which will help in accurately predicting and understanding the frictional behaviour of contacting surfaces. In this chapter, various rough surface characterisation method will be explored. It should be noted that the rough surface analysis included in this chapter is strictly limited to the isotropic surfaces only.

The chapter proposes a generic multi-scale friction model to predict the friction between rough surfaces, which are applied for a piston ring-liner conjunction. At micro-scale, the friction between surfaces in relative motion is dominated by the bulk surface and oil properties. However, interaction between individual asperities is at nano-scale. At such vanishing gaps, the friction no longer follow bulk properties of the material and lubricant. The nano-scale friction is affected by the kinetics discussed in *Chapters 6-8*. The friction at asperity level is governed by shearing of thin adsorbed film. At high loads the low shear strength thin film is penetrated and depending on the conditions, asperities adhere elastically or plastically. Each of the mechanisms underlying friction at asperity level can be expanded to predict friction of a flat rough surface. The last section of this chapter attempts to use the rough surface model to predict the friction force for the ring-liner conjunction in *Chapter 2*. The concept of the multi-scale friction model is summarised in figure 9.1.

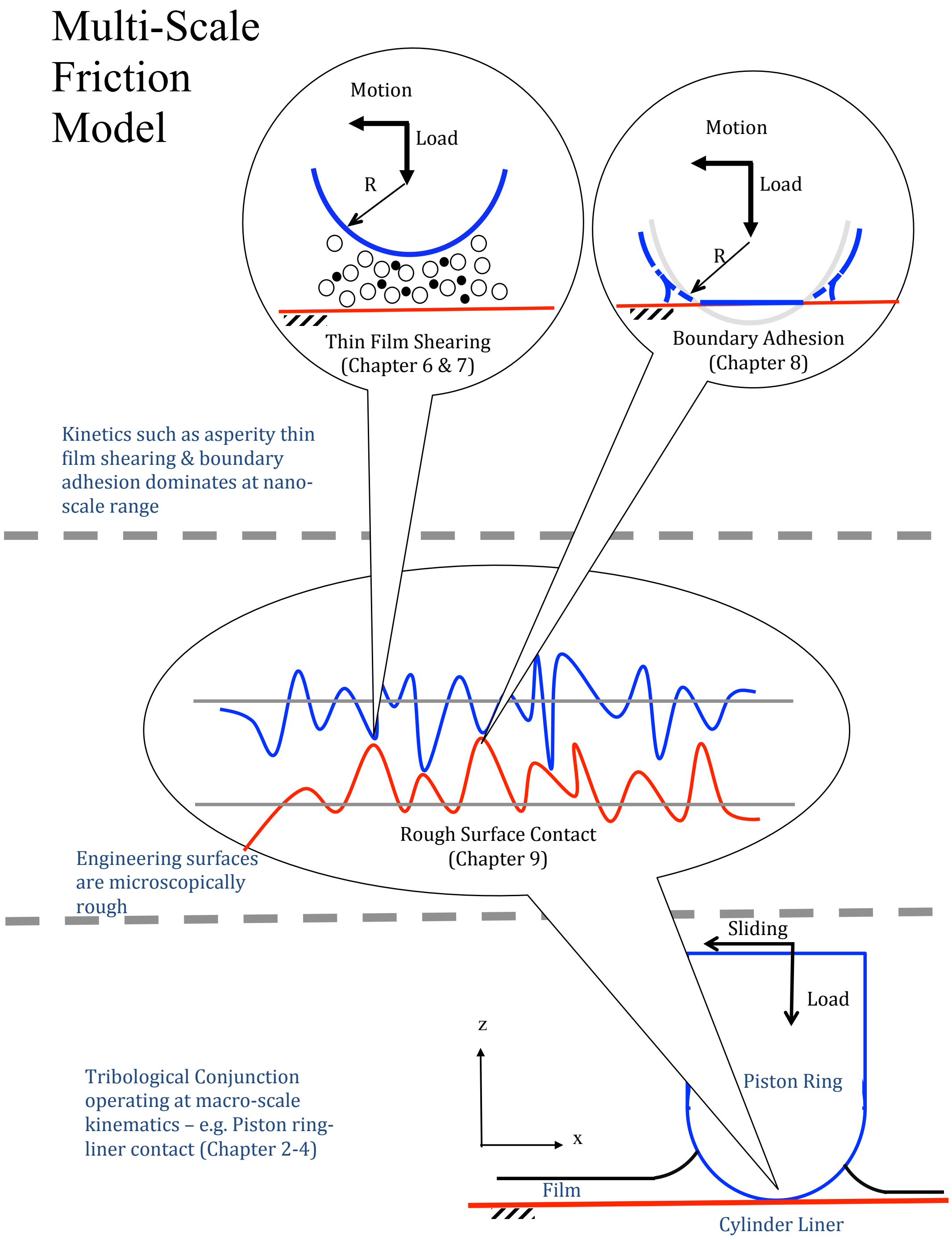

Figure 9.1: The concept of multi-scale friction model

9.2 Statistical Approach

The most commonly applied approach to characterise a rough surface is the Greenwood and Williamson model [181]. Greenwood and Williamson observed that the asperities on the surface of a bead-blasted aluminium are Gaussian distributed. Therefore, they proposed a statistical distribution for the asperities, which can be characterised by the root-mean-square (rms), σ, slope, σ' and also the curvature, σ'' of the asperities. Greenwood and Williamson [181] assumed that a rough surface comprises of spherical asperities with a constant curvature radius distributed throughout the whole surface. The model considers Hertzian contact between approaching asperities and predicts the friction force as a function of the nominal distance between surfaces [181]. Fuller and Tabor [163] proposed an alternative the model to account for adhesive contact between asperities (using JKR contact model) and Kogut and Etsion [182] extended this approach for elastoplastic asperity contacts. Shi and Polycarpou [183] combined the Maugis-Dugdale adhesion model for elastic region with the elasto-plastic adhesion model proposed by Kogut and Etsion [112]. The model also considers the existence of a thin layer of lubrication film through the application of the Lennard-Jones potential.

Using the notation proposed by Fuller and Tabor [163], the statistical distribution of the asperities, $\phi(z)$ along the rough surface is defined as [163]:

$$\phi(z) = \frac{1}{\sigma\sqrt{2\pi}} e^{-R^2/(2\sigma^2)} \tag{9.1}$$

To account for the effect of adhesion between rough surfaces, Fuller and Tabor [163] relates the asperity interference, δ_{int} (Figure 9.2) to the *pull-off* characteristics of the rough surface itself ($\delta_{\textit{pull-off}}$ and $P_{\textit{pull-off}}$). Therefore, the contact force is:

$$F = \frac{nP_{\textit{pull-off}}}{\sqrt{2\pi}} \int_0^\infty fn\left(\frac{\Delta}{\Delta_{\textit{pull-off}}}\right) e^{-(h+\Delta)^2/2} d\Delta \tag{9.2}$$

where $\Delta = \delta/\sigma$, $\Delta_{\textit{pull-off}} = \delta_c/\sigma$, $h = d/\sigma$ and σ is the r.m.s. roughness.

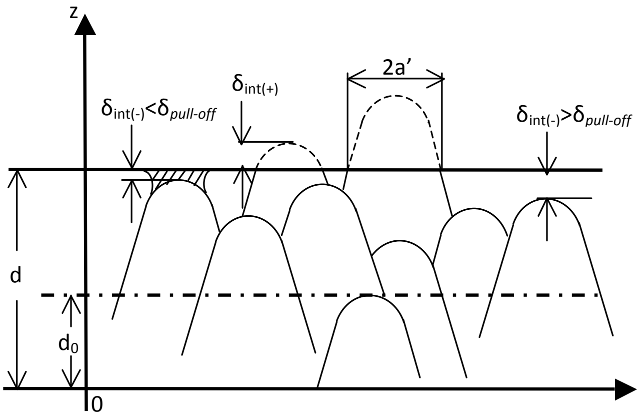

Figure 9.2: Gaussian distributed asperities

The function fn can be expressed as:

$$fn\left(\frac{\Delta}{\Delta_{pull\text{-}off}}\right) = \bar{P}(\bar{\delta}) \tag{9.3}$$

where $\bar{P}$ is the adhesion force for a single asperity contact. The total contact force, F, considering adhesion, computed above assumes that the asperities in contact are in compression or being loaded. However, this might not be the case all the time, where the rough surface contact might be separated or being unloaded. Due to the separation, some of the asperities might be stretched up to the limit of $\delta_{pull\text{-}off}$. Therefore, to consider for the rough surface unloading and the asperity stretching, Fuller and Tabor [163] defined the total force acting on the rough surface as:

$$F = \frac{nP_{pull\text{-}off}}{\sqrt{2\pi}} \int_{-L}^{\infty} fn\left(\frac{\Delta}{\Delta_{pull\text{-}off}}\right) e^{-(h+\Delta)^2/2} d\Delta \tag{9.4}$$

where $L = \Delta_{pull\text{-}off}$ or $= h - h_o$, whichever is smaller.

9.3 Fractal Approach

Roughness measurements of a variety of engineering surfaces have shown that their topographies are multi scale and random [184]. Nayak [185] applied the Greenwood and Williamson approach to consider the contact characteristics of a rough surface contact. He found out that the assumption of Gaussian asperity distribution is not applicable to all rough surface contacts. Sayles and Thomas [186] found that surface topography has a multi-scale nature.

It was often concluded that the surface topography of a rough surface depends strongly on the resolution of the roughness-measuring instrument [186, 187, 188]. Therefore, the need of scale independent contact models becomes more apparent. A fractal geometry (see figure 9.3) refers to a fragmented geometrical shape which can be divided into parts, each of which is a reduced-sized version of the full sized geometry [189].

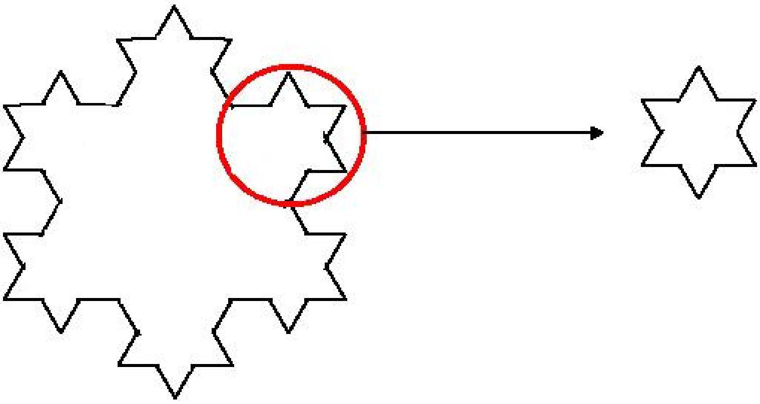

Figure 9.3: An example of a fractal geometry - Koch snowflake

Majumdar and Bhushan [190] used the Weierstrass and Mandelbrot (WM) fractal function to develop a fractal contact model. Their model is based on a 2-dimensional multi-scale surface profile generated by the WM function. Yan and Komvopoulos [187] proposed an algorithm based on the WM fractal function to generate a 3-dimensional fractal surface. They used the model to investigate the elastic-fully-plastic contact of rough surfaces. Bora *et al* [191], Morrow and Lovell [192] and Moraq and Etsion [188] used Yan and Komvopoulos's [187] fractal geometry approach in their work to analyse rough surface contacts.

Komvopoulos [193] used the fractal geometry to analyse the contact between rough surfaces considering surface forces such as van der Waals, meniscus, electrostatic and deformation forces. Komvopoulos and Ye [194] used a 3-dimensional fractal geometry to study the rough surface contact based on the Hertzian contact. The contact model considered the elastic and fully plastic deformation of the asperities along the rough surface. Yan and Komvopoulos [187] characterised a three dimensional rough surface topography as:

$$\begin{aligned} z(x,y) &= L\left(\frac{G}{L}\right)^{(D-2)}\left(\frac{ln\gamma}{M}\right)^{1/2}\sum_{m=1}^{M}\sum_{n=0}^{n_{max}}\gamma^{n(D-3)} \\ &\times\left\{\begin{array}{l} cos(\phi_{m,n})- \\ \\ cos\left[\frac{2\pi\gamma^n(x^2+y^2)^{1/2}}{L}cos\left(tan^{-1}(\frac{y}{x})-\frac{\pi m}{M}\right)+\phi_{m,n}\right] \end{array}\right\} \end{aligned} \tag{9.5}$$

where n is the frequency index, $n_{max} = [log(L/L_s)/log\gamma]$, D is known as the fractal dimension of the profile, G is the height scaling parameter or the fractal roughness of the profile, γ determines the density of frequencies in the profile, M denotes the number of ridges required to construct the profile and ϕ_n is a random phase.

D refers to the slope while G refers to the intersection of the power spectrum of the fractal surface at 0 frequency. The parameters D and G can be obtained experimentally by plotting the power spectrum of the fractal surface against the frequency of the AFM measurement in logarithmic scales. Assuming that the microcontact force is mainly due to the deformation of asperity with the base length, corresponding to the frequency index, n_o,

$$n_o = \frac{ln(L/2a')}{ln\gamma} \tag{9.6}$$

where a' is the truncated contact radius (see figure 9.4), equation (9.5) then reduces to

$$\begin{aligned} z(x,y) &= L\left(\frac{G}{L}\right)^{(D-2)}\left(\frac{ln\gamma}{M}\right)^{1/2}\sum_{m=1}^{M}\gamma^{n_o(D-3)} \\ &\times\left\{\begin{array}{l} cos(\phi_{m,n_o})- \\ \\ cos\left[\frac{2\pi\gamma^n(x^2+y^2)^{1/2}}{L}cos\left(tan^{-1}(\frac{y}{x})-\frac{\pi m}{M}\right)+\phi_{m,n_o}\right] \end{array}\right\} \end{aligned} \tag{9.7}$$

The asperity interference, δ is the peak to valley amplitude of equation (9.7). Therefore,

$$\delta = L\left(\frac{G}{L}\right)^{(D-2)}\left(\frac{ln\gamma}{M}\right)^{1/2}\sum_{m=1}^{M}\gamma^{n_o(D-3)} \tag{9.8}$$

The equivalent curvature radius, R of the asperity can then be computed as:

$$R = \frac{(a')^2}{2\delta} \tag{9.9}$$

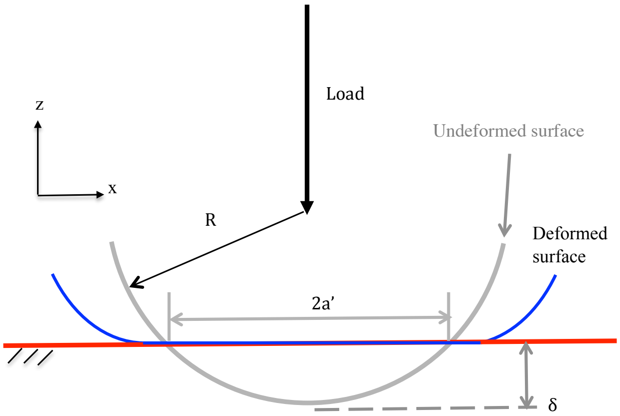

Figure 9.4: Truncated microcontact

To compute the total load and friction force acting on the rough surface,

$$\begin{aligned} F &= \int dP.n(A').dA \\ F_{frict} &= \int dP_f.n(A').dA \end{aligned} \tag{9.10}$$

where the asperity truncated area, A' is $\pi(a')^2$, dP (asperity contact load) and dP_f (asperity friction force) is due to adhesion (*Chapter 6*) and solvation (*Chapter 7 & 8*), and the truncated asperity size distribution function, $n(A')$ can be expressed as:

$$n(A') = \frac{D-1}{2A'_L}\left(\frac{A'_L}{A'}\right)^{(D+1)/2} \tag{9.11}$$

The largest truncated area, A'_L can be computed using the total truncated area, A'_{tot} as:

$$A'_L = \left(\frac{3-D}{D-1}\right) A'_{tot} \tag{9.12}$$

By using the expressions above, contact models such as JKR, DMT and Maugis-Dugdale models can be applied to analyse the contact behaviour of a rough surface contact, characterised based on the fractal geometry approach. Morrow and Lovell [192] applied the approach by Yan and Komvopoulos [187] to the Maugis-Dugdale model to predict the effect of adhesion on a rough surface contact. However, the fractal model proposed by Yan and Komvopoulos only considers rough surface contact as being loaded, neglecting the unloading characteristics of the rough surface contact.

As a first attempt to build the fractal contact model, the fractal dimension, D and fractal roughness, G of 2.4 and $1.36 \times 10^{-11} m$ is used to generate a fractal geometry [187]. The generated fractal geometry is shown in figure 9.5.

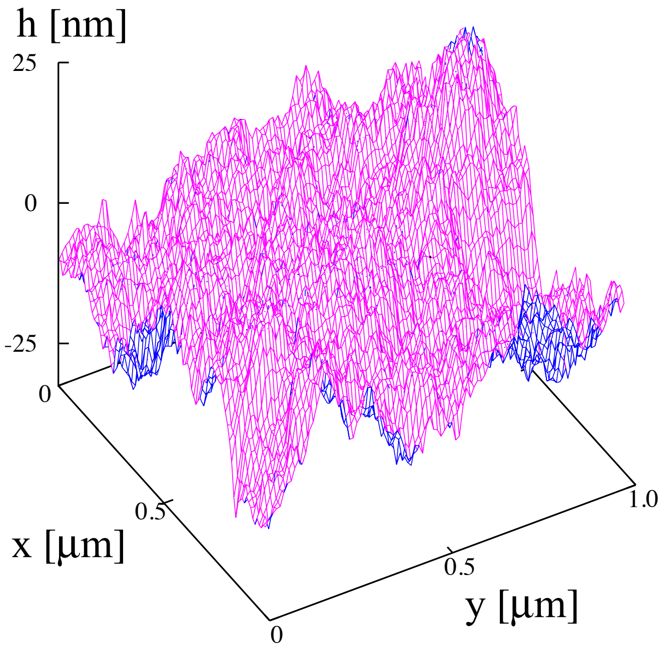

Figure 9.5: Fractal surface

The contact load for the fractal geometry based on the Hertzian contact are shown in figure 9.6. A comparison is made with the results from Yan and Komvopoulos [187]. The comparison is used as a sanity check for the fractal contact model before proceeding to integrating the elastoplastic Maugis-Dugdale adhesion model. It can be seen that by introducing the elastoplastic model for the Hertzian contact, the load predicted behaves in a very similar way as in Yan and Komvopoulos's work, which considers elastic and fully plastic deformations of the asperities.

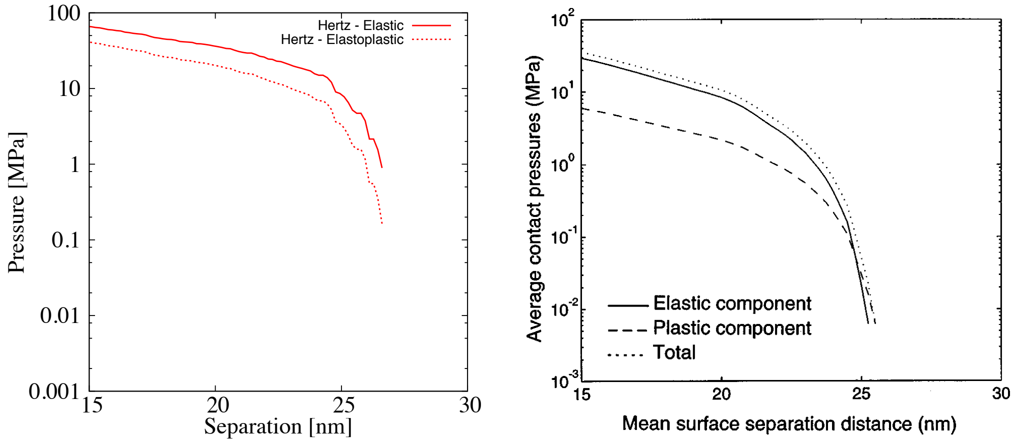

(a) Current (b) Yan and Komvopoulos [187]

Figure 9.6: Contact pressure

Even though the predicted load for the elastoplastic Hertzian model shows a good comparison, the contact area predicted shows otherwise (see figure 9.7). This might be due to the fact that Yan and Komvopoulos considers only elastic and fully plastic deformations only. This shows the importance of including the transitional elastoplastic deformation in predicting the contact behaviour of rough surfaces, which help prevents the underestimation of the actual contact area.

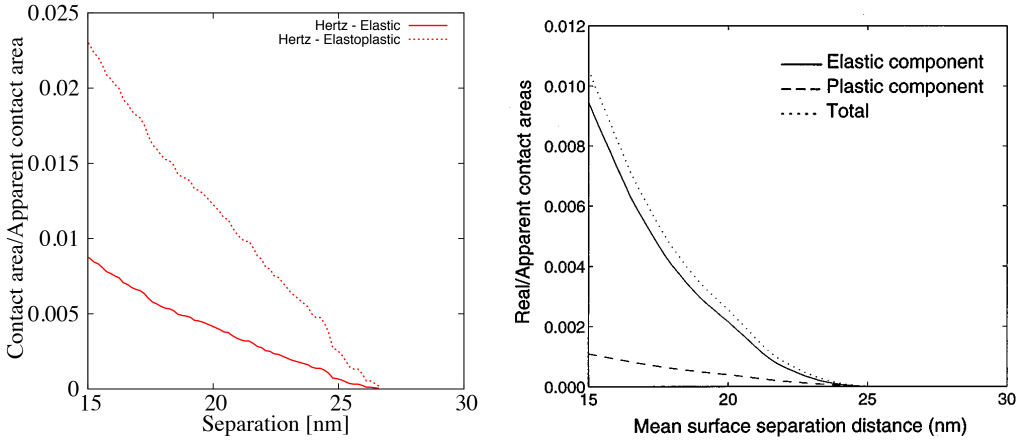

(a) Current (b) Yan and Komvopoulos

Figure 9.7: Contact area

Figure 9.8 shows (a) the contact pressure and (b) the contact area/apparent contact area between two parallel rough surfaces considering fully elastic deformation models of Hertzian contact and Maugis-Dugdale. The models do not show a significant difference between the load and actual area of contact. This might be due to the small surface energy, $\Delta\gamma$ used ($= 0.1 J/m^2$), which results in a minimal work of adhesion.

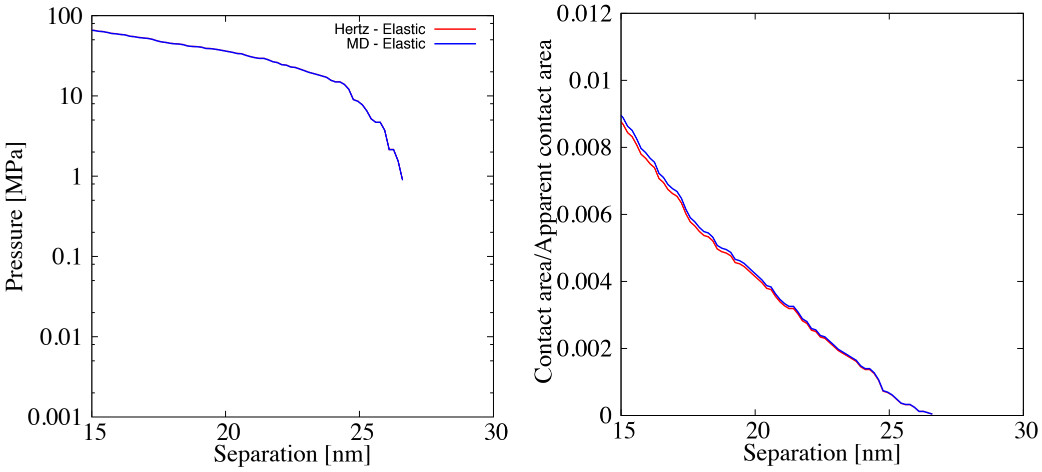

(a) Contact load

(b) Contact area

Figure 9.8: Contact characteristics

Figure 9.9 shows the contact pressure (a) and the contact area/apparent contact area (b) between two parallel rough surfaces using the elastoplastic models based on Hertzian and Maugis-Dugdale models. It can be seen that the contact area predicted by the elastoplastic Maugis-Dugdale model is larger than the one predicted by the Hertzian model. Figure 9.10 shows the friction predicted using both models. It should be noted that the friction force accounting for elastoplastic deformation is significantly larger than the one which does not account for the elastoplastic deformation.

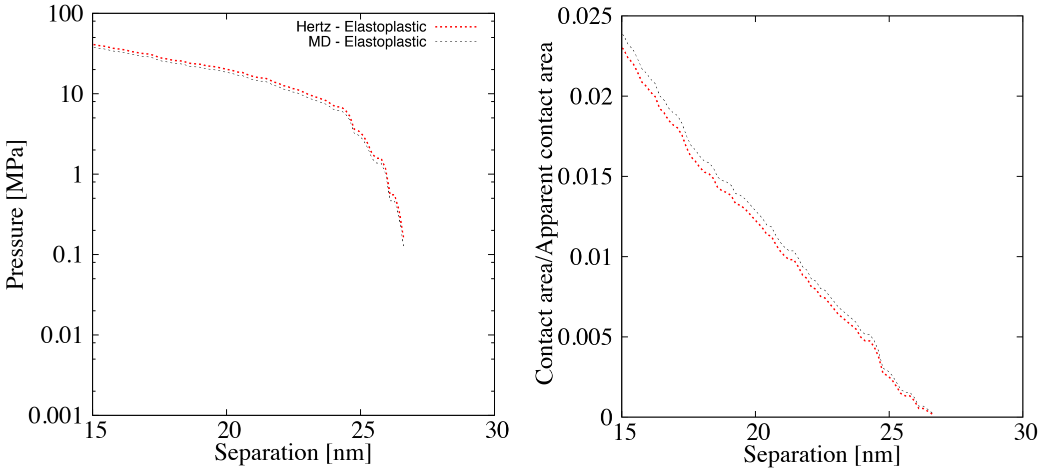

(a) Contact load (b) Contact area

Figure 9.9: Contact characteristics of a fractal geometry

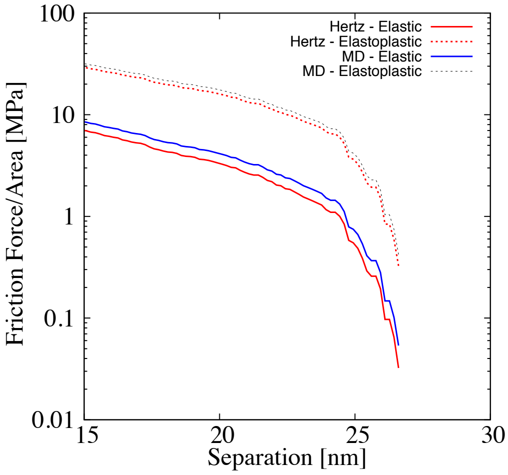

Figure 9.10: Friction force of a fractal geometry

The validation study conducted in this section proved to be useful in elevating the confidence of the rough surface contact model based on a fractal analysis. The next section will include a comparison study between the statistical and fractal analysis.

9.4 Statistical and fractal analysis comparison

Kogut and Jackson [121] and Jackson and Streator [195] compared the contact modelling based on both the statistical and fractal approaches for rough surfaces coming into contact. The statistical approach by Greenwood and Williamson might be a straight forward solution. However, it has been shown that the spectral moments, which gives the classical parameters required by the Greenwood and Williamson model, depend heavily on the resolution of the surface measuring apparatus and the selected sample length. This dependency will influence the prediction of the actual contact area and contact load. Therefore, fractal geometries are often preferred to the statistical approach.

Kogut and Jackson [121] showed that by using the fractal analysis, the Greenwood and Williamson parameters can be extracted from the fractal dimension, D and the fractal roughness, G using McCool's method [196]. Assuming different sampling resolutions for the same surface, they compared the contact load and contact area predicted using the fractal contact analysis and the Greenwood and Williamson's contact analysis for rough surface. From their results, it can be observed that a good comparison can be obtained if the correct sampling resolution is used to extract the Greenwood and Williamson's parameter.

The current study attempts to integrate the effect of adhesion and elastoplastic deformation onto the rough surface contact. The statistical parameters extracted from the fractal geometry using McCool's method [196] for different normalised sampling resolutions are as in table 9.1 [121]. The corresponding fractal dimension, D and fractal roughness, G are 2.44 and $9.46 \times 10^{-12} m$ (see table 9.2). These data will be used for the first case study conducted comparing the statistical and fractal analysis.

Table 9.1: Rough surface input parameters for statistical analysis [121]

Normalised Sampling Resolution, SR	**r.m.s. Roughness,** $\sigma(nm)$	**Asperity Radius,** $R(m)$	**Asperity Areal Density,** $n(m^{-2})$
0.001	6.49	3.27×10^{-10}	1.10×10^{17}
0.01	4.61	5.01×10^{-8}	1.18×10^{15}
0.1	4.59	8.65×10^{-6}	1.31×10^{13}

Table 9.2: Rough surface input parameters for fractal analysis [121]

Parameters	**Values**
Fractal dimension, D	2.44
Fractal roughness, G	$9.46 \times 10^{-12} m$

Figure 9.11 shows the contact load predicted using the elastic and elastoplastic Maugis-Dugdale model coupled with the statistical rough surface contact model. The difference between the elastic and elastoplastic analysis for the statistical rough surface contact becomes increasingly distinct with the decreasing sampling resolution. This is because with the reduction of sampling resolution, smaller asperities exists. The smaller the asperity size, the smaller the critical interference, δ_c will be. This means that the asperities are easier to be plastically deformed. This behaviour can be observed especially for $SR = 0.001$. The elastic model predicted a totally different trend as compared to the elastoplastic model due to the increasing significance of the elastoplastically deformed asperities.

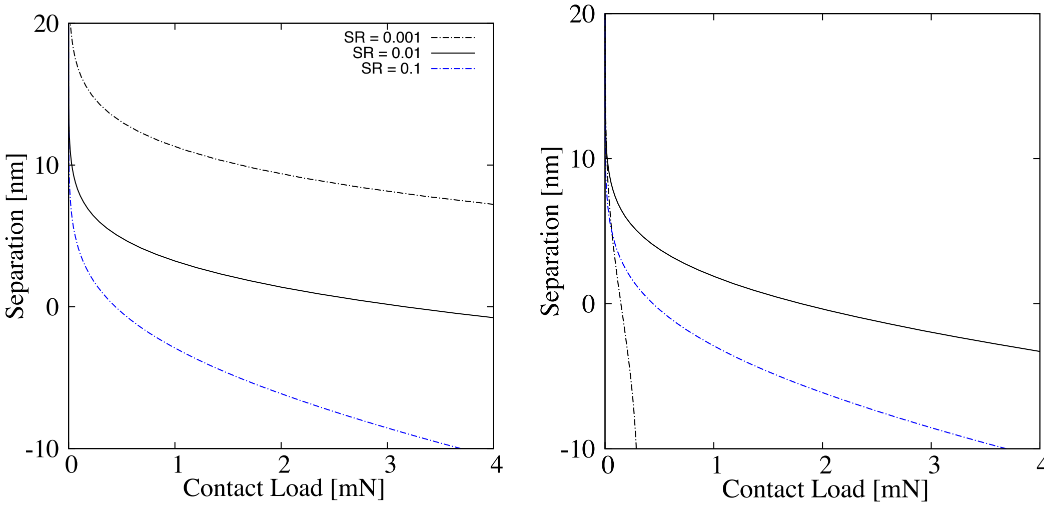

(a) Elastic deformation

(b) Elastoplastic deformation

Figure 9.11: Contact load for the statistical approach

The actual contact area for the rough surface contact based on the statistical approach is shown in figure 9.12. As plasticity starts to exist, a slight increase in load will easily extend the contact area further. It can be seen that especially for $SR = 0.001$, even at a much smaller load, the contact area predicted based on the elastoplastic model is still comparable to the fully elastic model's predicted contact area.

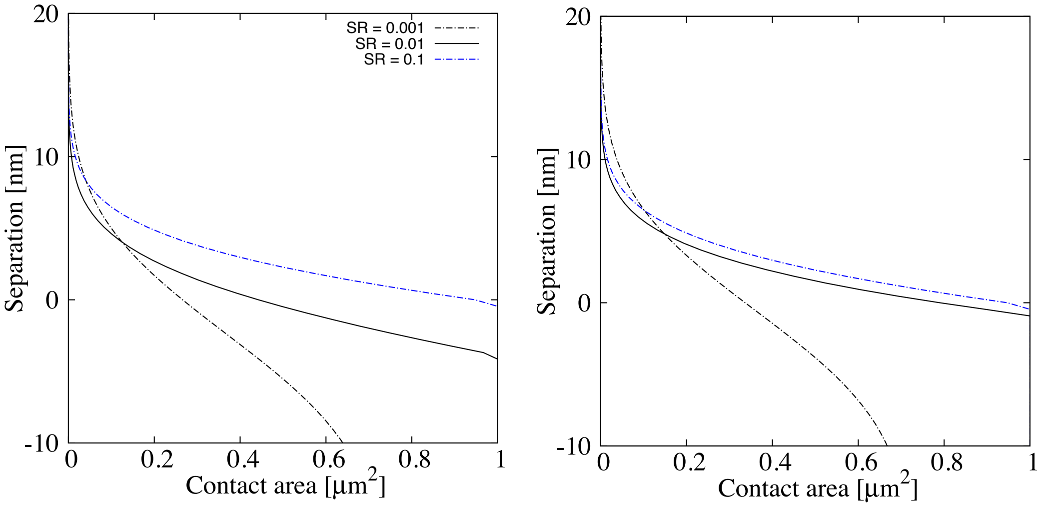

(a) Elastic deformation

(b) Elastoplastic deformation

Figure 9.12: Contact area for the statistical approach

Based on the actual contact area predicted along the rough surface, the friction force can be computed as in figure 9.13. The interfacial shear strength, τ_a is assumed to be $0.8GPa$. As it can be seen, the friction force depends significantly on the contact area of the approaching rough surface.

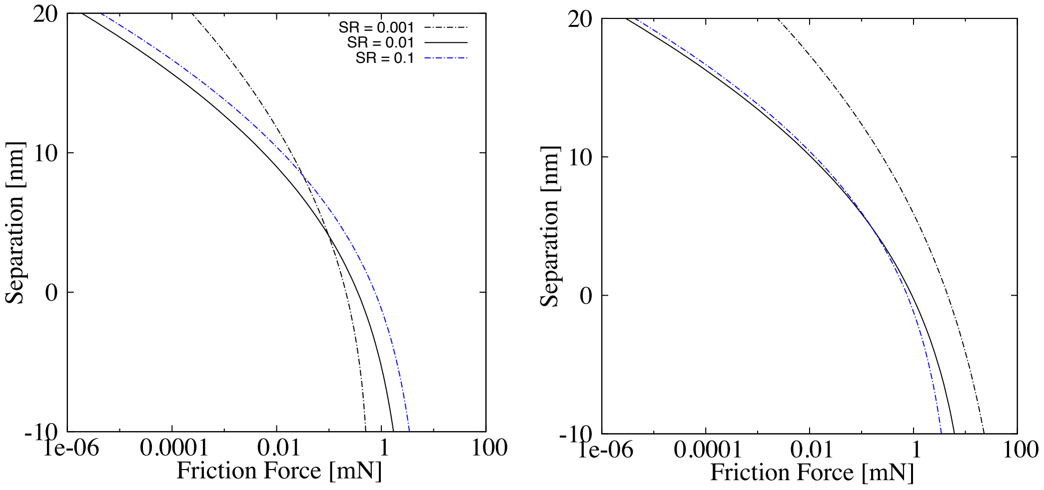

(a) Elastic deformation

(b) Elastoplastic deformation

Figure 9.13: Friction force for the statistical approach

Using the fractal parameters as in table 9.2, the fractal geometry of interest is generated in figure 9.14.

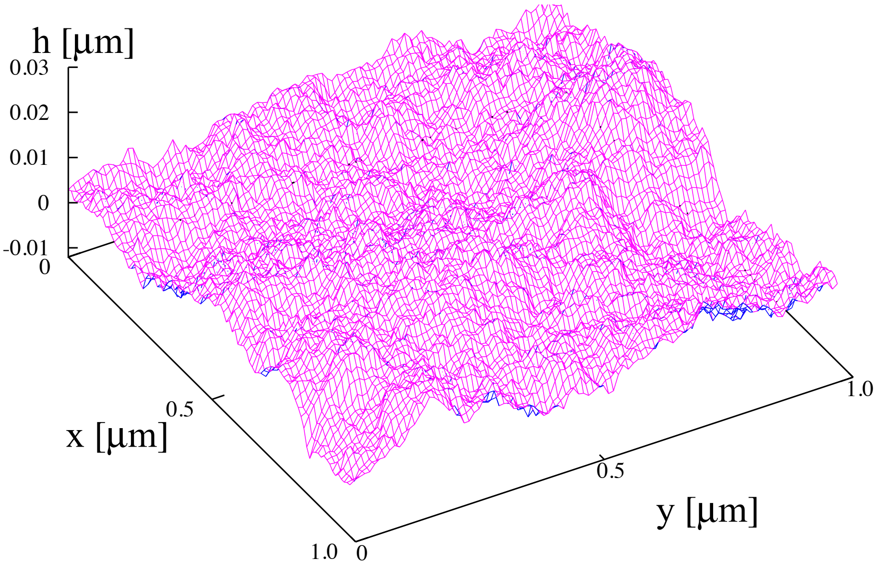

Figure 9.14: Fractal surface for Case Study 1

Figure 9.15 shows the increasing truncated contact area as the rough surface is being further loaded. The inset in the figure reflects the contact *"islands"* at different separations or interferences. The total truncated area, A'_{tot} computed based on the inset figures is used to predict the largest truncated contact area, A'_L, which in turn is required to compute the truncated contact area's distribution, $n(A')$.

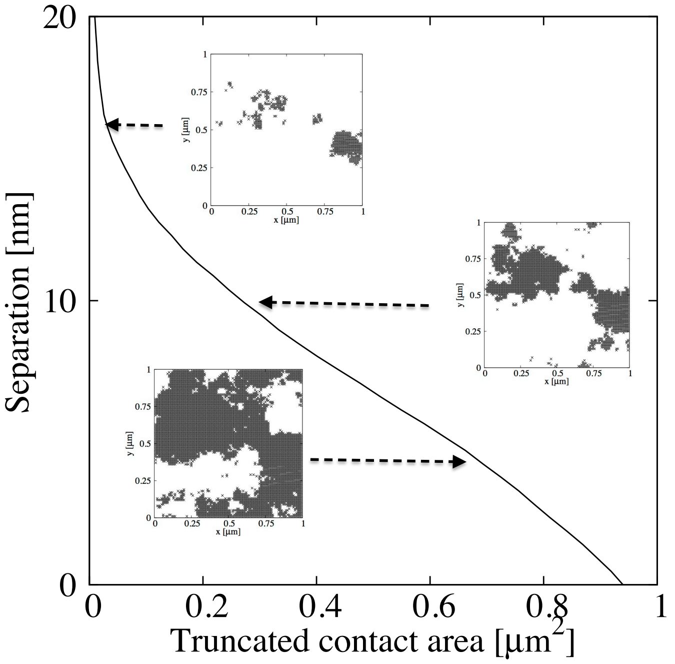

Figure 9.15: Truncated contact area

The contact load variation for the elastic and elastoplastic model (Hertzian and Maugis-Dugdale) is being illustrated in figure 9.16. As shown in earlier discussions, including the elastoplastic deformation decreases the contact load. However, a lower contact load in the elastoplastic region predicts a larger contact area than the fully elastic consideration. This can be observed in figure 9.16. The elastoplastic deformation of the asperities also show a decrease in load carrying capacity of the rough surface.

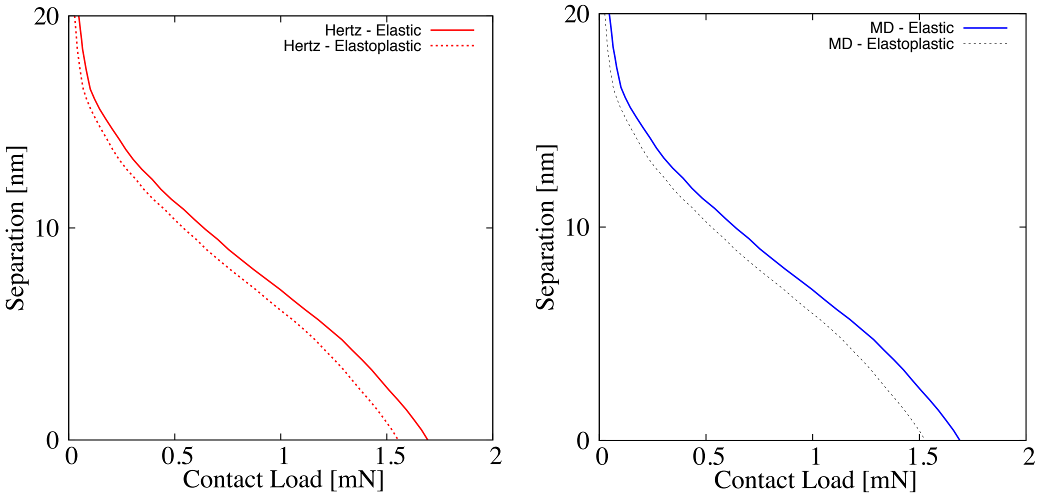

(a) Hertzian Contact (b) Maugis-Dugdale Contact

Figure 9.16: Contact load for the fractal analysis

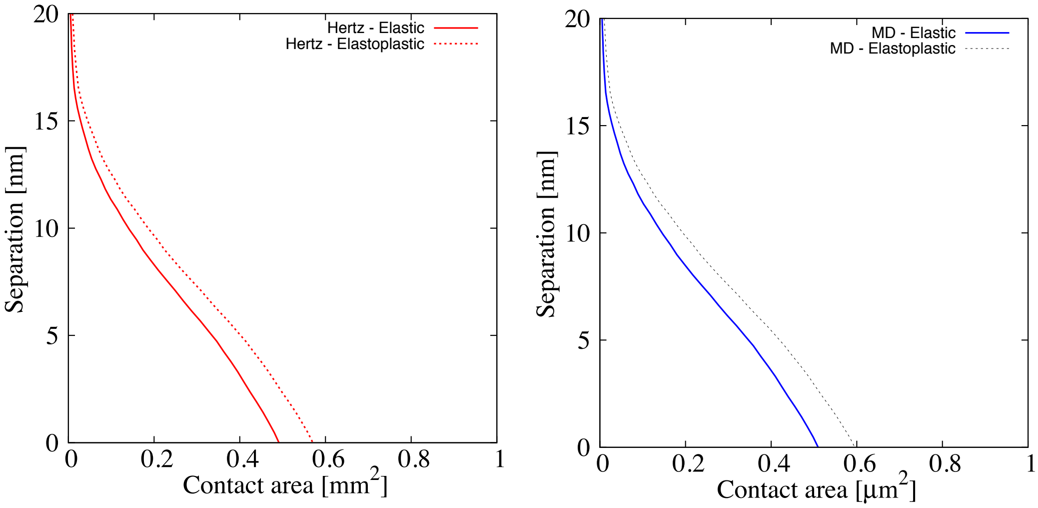

(a) Hertzian Contact (b) Maugis-Dugdale Contact

Figure 9.17: Contact area for a fractal analysis

The change in actual contact area over the truncated contact area is plotted in figure 9.18. The plot shows that the actual contact area is just a portion of the truncated contact area. This shows that neglecting the asperity microcontacts might produce an inaccurate prediction of friction force along the approaching rough surfaces.

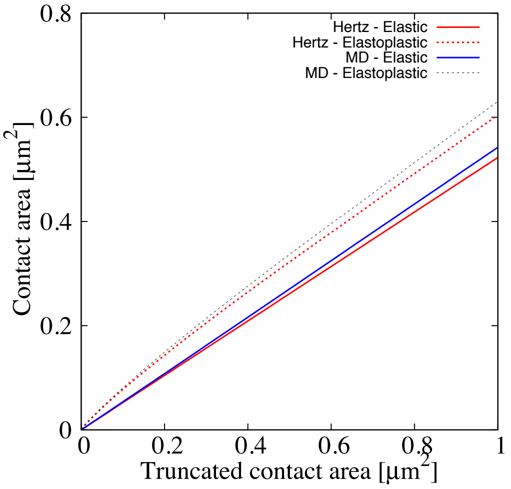

Figure 9.18: Actual contact area vs apparent contact area

The friction force for the generated rough surface is shown in figure 9.19. It can be observed that the friction force is a lot larger considering elastoplastic deformation especially at larger separations. This is due to asperity progressive deformation, the computed asperity curvature radius will increase. A larger contact area of the asperity will increase the resistance towards plastic deformation, which can be described based on the critical interference, δ_c parameter.

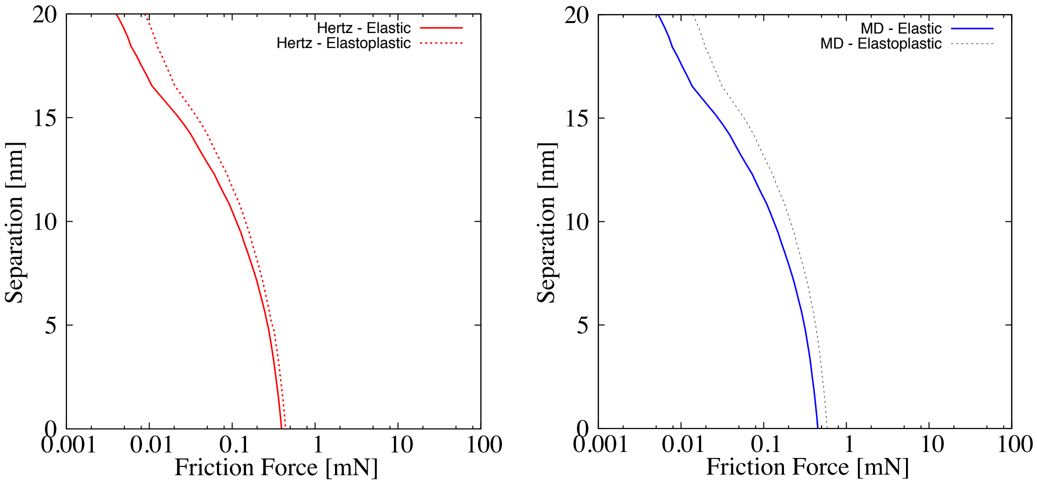

(a) Hertzian Contact (b) Maugis-Dugdale Contact

Figure 9.19: Friction force for a fractal analysis

The contact load comparison between the statistical and fractal analysis is provided in figure 9.20. The fractal contact load shows a similar trend to the statistical model ($SR = 0.001$) at larger separations (A in figure 9.20 (a)) especially for the fully elastic models. However as the separation gap is being decreased, it shows that the fractal contact load differs from the statistical model's prediction. This is due to the multi scale characteristics of the fractal geometry which can predict engineering surfaces more accurately. When the elastoplastic deformation is included, the drop in contact load is more obvious for the statistical models than the fractal model.

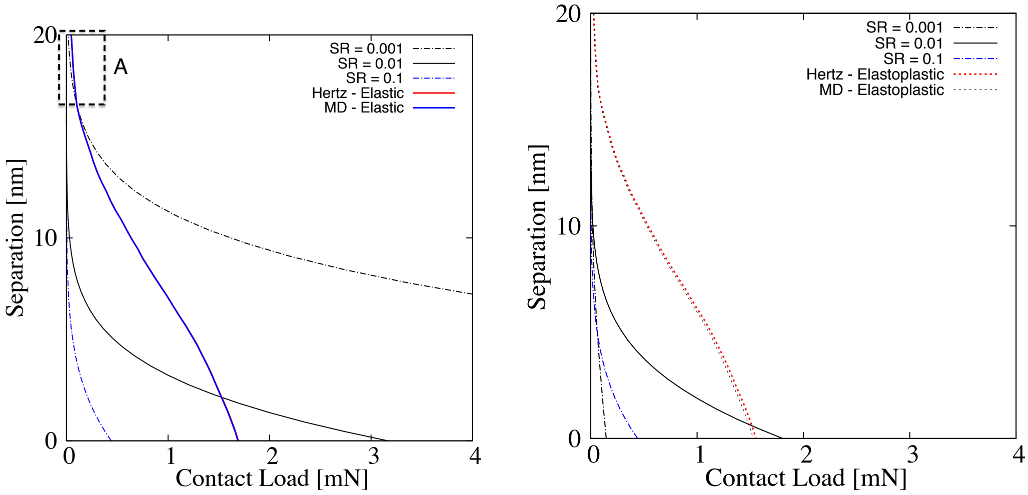

(a) Elastic deformation (b) Elastoplastic deformation

Figure 9.20: Contact load comparison between a statistical and fractal approach

Figure 9.21 illustrates the contact area change with the decrease of separation gap. The contact area predicted based on the fractal geometry tends to be larger at higher separations but saturates as the separation get smaller. The same can be observed for the elastoplastic models. This is mainly due to the fact that the contact area of rough surface eventually reaches the apparent contact area.

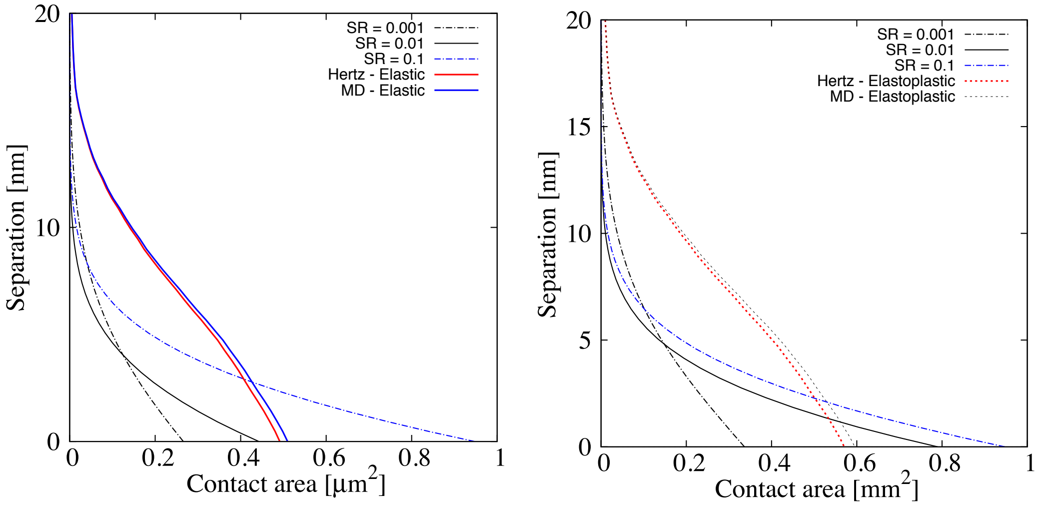

(a) Elastic deformation (b) Elastoplastic deformation

Figure 9.21: Contact area comparison between a statistical and fractal approach

The friction force computed using the actual contact area for the rough surface contact is shown in figure 9.22. The fractal model predicts a higher friction at large separations than the statistical model. At larger separations, smaller asperities exist on the tip of larger asperities along the fractal surface. Smaller asperities tend to deform plastically with the increase in load, leading to the higher friction predicted by the fractal model. However, the trend goes the opposite direction when smaller separations are reached.

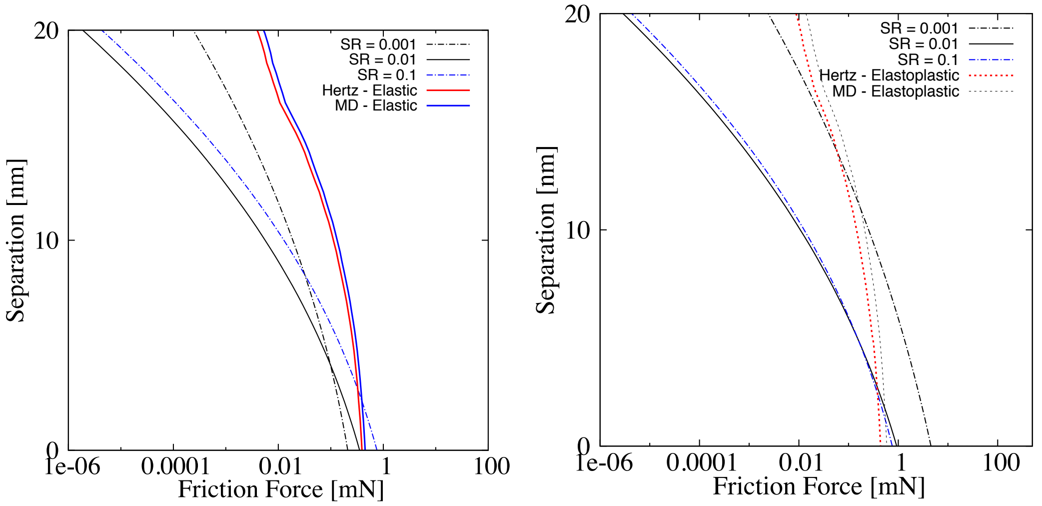

(a) Elastic deformation (b) Elastoplastic deformation

Figure 9.22: Friction force comparison between a statistical and fractal approach

9.5 Lubricated rough surface

In the previous sections the rough surface contact is assumed dry. In an attempt to include the effect of a dual component lubricating film towards the rough surface contact, a single asperity friction map is obtained combining the influence of intermolecular forces as described in *Chapters 6 to 8* (e.g. solvation and van der Waals forces). The contact load variation for the asperity curvature radius predicted using different sampling resolutions, SR is provided in figure 9.23. It can be observed that the magnitude of surface and intermolecular forces for bigger sampling resolutions are larger in magnitude. The forces decrease with the reduction in sampling resolution. As the curvature radius predicted for $SR = 0.001$ is too small, it is assumed that the intermolecular forces do not have a significant influence on the contact behaviour.

The oscillatory characteristic of the contact load at separations larger than $1nm$ is due to the solvation forces induced by the fluid molecules trapped in between the approaching contact. The limit of $1nm$ is set as a lubricating film can only be formed with two layers of molecules, which in this case study is limited by the diameter of the smaller molecule of the dual component fluid used in this section ($0.5nm$). The load holding the contact together after $1nm$ is the van der Waals force. The van der Waals force will then be overruled by adhesion of the contact when the "jump-in" to the contact occurs. From this point onwards, the contact load is dominated by the surface-to-surface interaction.

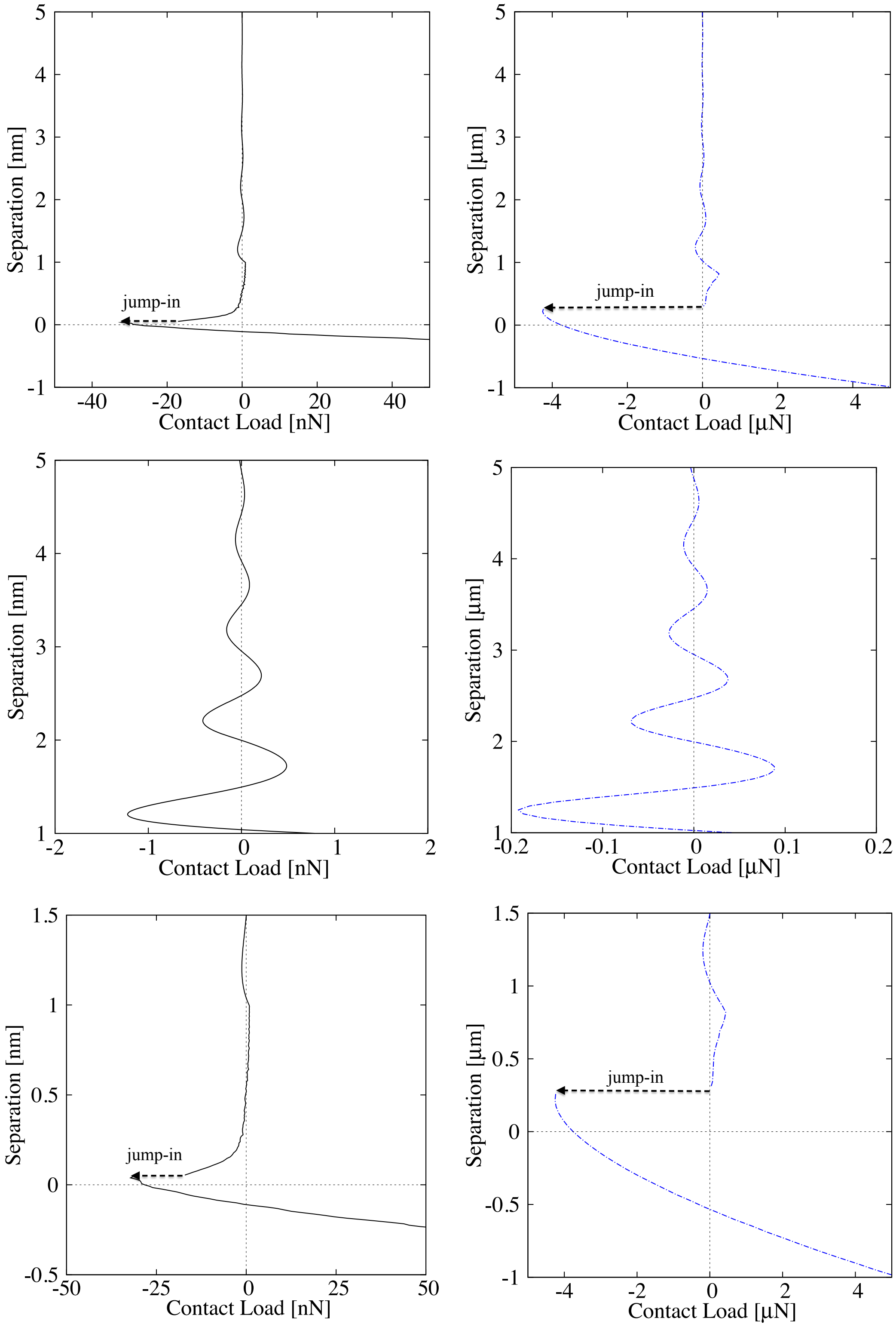

(a) $SR = 0.01$ (b) $SR = 0.1$

Figure 9.23: Load for a single asperity contact

The friction map for the single asperity contact is shown in figure 9.24 for $SR = 0.01$ and 0.1. The friction force for a larger sampling resolution is higher due to the larger features of the asperity. The friction map (see figure 9.24) is intended for a specific asperity curvature radius, which is suitable for the statistical contact model. For the fractal model, the single asperity model considering surface and intermolecular forces is embedded directly into the fractal contact model due to the varying asperity curvature radii. The change in curvature radii are as a result of the multi scale nature of the fractal surface itself.

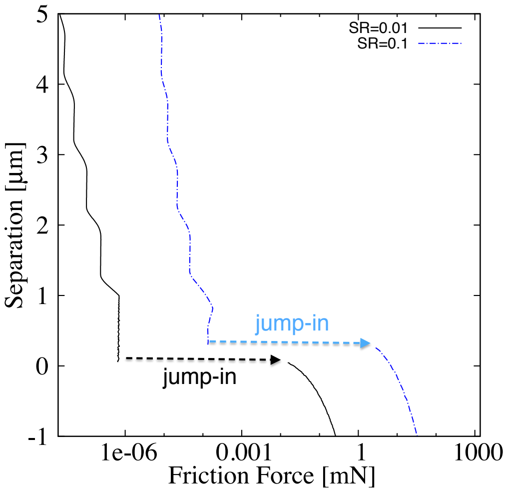

Figure 9.24: Friction map for a single asperity contact

Figure 9.25 shows the friction of the rough surface contact for both the statistical and fractal model due to intermolecular forces only. Even though similar in trend, the fractal friction force shows significant variance as compared to the statistical model. The higher friction force predicted using the fractal analysis is because of the interactions with smaller features on the fractal surface which cannot be captured based on a statistical analysis.

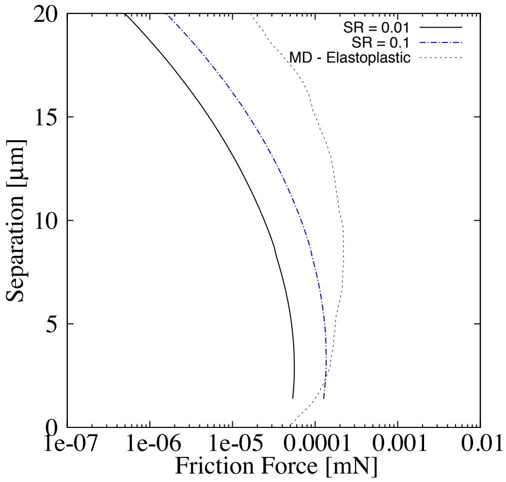

Figure 9.25: Friction force for a lubricated rough surface contact - Thin film shearing

The friction force due to the intermolecular forces and direct surface-to-surface interaction using the fractal analysis is shown in figure 9.26. Based on the elastoplastic Maugis-Dugdale model, it can be seen that the surface-surface interaction dominates over the influence of the intermolecular forces at the separation gaps chosen.

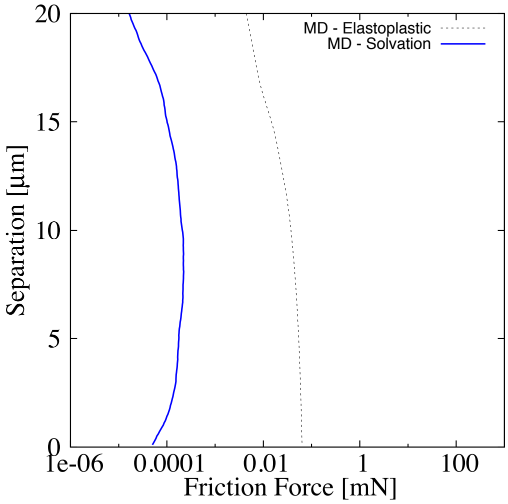

Figure 9.26: Friction force components for a lubricated rough surface contact - fractal analysis

The chapter discussed on the various approaches to consider a rough surface contact. Comparisons of the statistical and fractal approach in modelling a rough surface contact were conducted. The importance of being able to use the appropriate approach is repeatedly being highlighted throughout the case studies conducted.

9.6 Total Friction Model - A multi-scale approach

The concept of the multi-scale friction model is depicted in figure 9.1. As been highlighted throughout the study, friction of interacting surfaces is a multi-scale phenomenon. Therefore, the understanding of various kinetic mechanisms underlying friction at asperity level is investigated in the previous chapters. Initially, the mechanisms are each examined as a separate entity. The asperity interactions are integrated on the fractal rough surface model to predict friction (see *Chapter 10*). This might not be sufficient for practical application such as the ring-liner conjunction as the contacting surfaces are not planar.

Assuming the friction force and area of the fractal planar rough surface predicted based on the previous chapter to be dP_f and dA, the friction force for a given contacting profile can be predicted as:

$$F_f = \int dF_{frict}.dA \tag{9.13}$$

The friction force, dP_f in the previous chapter consists of only the thin film shearing and the boundary adhesion component. To consider the micro-scale contact, a third friction component- viscous shear must be considered. Therefore, the friction force, dF_{frict} for the multi-scale model is:

$$dF_{frict} = (dF_{frict})_v + [(dF_{frict})_s + (dF_{frict})_{adh}] \tag{9.14}$$

where h is the separation, $(dF_{frict})_v = (\eta u e^{\alpha p}/h).dA$ is the viscous shear component, u is the sliding velocity, p is the total contact pressure, α is the lubricant viscosity coefficient, $(dF_{frict})_s$ is the friction due to solvation (computed based on equation (8.26)) and $(dF_{frict})_{adh}$ is the friction due to adhesion and direct surface-to-surface contact (computed based on equation (6.32)). As the first approximation, the solvation component, $(dF_{frict})_s$ is assumed to only exist when $h \leq 10nm$.

The proposed model has a similar approach to the simplified friction model used in *Chapter 2*. The simplified friction model is based on the Greenwood and Tripp asperity interaction model [51], which assumes a statistical distribution of asperities under Hertzian contact loadings. However, the boundary component of the simplified friction model is now being replaced by the thin film shearing and boundary adhesion models, which forms the new boundary friction. The new boundary component has an advantage over the simplified model as it considers the influence of thin adsorbed film shearing and asperity adhesion at nano-scale. The thin film shearing model considers the influence to intermolecular interaction for fluidic mixtures which is not the case in the simplified model. Aside from this, the elasto-plastic deformation of the asperities distributed on the rough surface is also being taken into account. The rough surface characterization method (fractal approach) used in this model is independent of any equipment's measurement resolution (e.g. profilometer). The asperity radii used in the fractal analysis depends on the asperity interference, leading to non-consistent curvature radii. This is otherwise for the simplified friction model where a constant curvature radius is used throughout the analysis. The method currently included in this study considers only isotropic surfaces, which if required, can be modified accordingly to accommodate anisotropic surfaces. This is an aspect which the simplified friction model will not be able to include in predicting friction for the ring-liner conjunction.

9.7 Results and Discussions

The proposed multi-scale model is used to predict friction on the ring-liner contact as discussed in *Chapter 2*. To be able to have a reasonable comparison, the fractal geometry is generated using the parameters in table 9.3. The corresponding r.m.s surface roughness required for the simplified friction model is $0.115\mu m$ [121] (representative of the ring/liner conjunction [27]) which is a decent value for a ring-liner contact. The generated fractal geometry is shown in figure 9.27. It should be noted that the fractal geometry used is an isotropic surface, which might not be true for an actual ring-liner contact. However, this assumption is made as a first attempt to put the proposed multi-scale friction model to action.

Table 9.3: Rough surface input parameters [121]

Parameters	**Values**
Fractal dimension, D	2.597
Fractal scaling parameter for profile height, G	2.86×10^{-10}

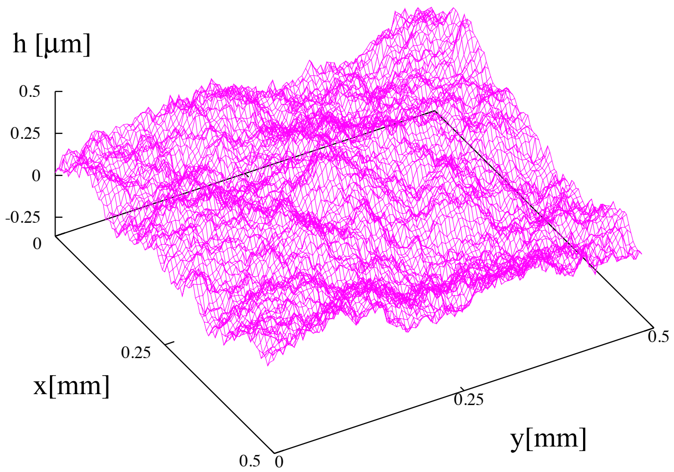

Figure 9.27: Fractal surface representative of the ring-liner conjunction

First, the frictional characteristics of the planar fractal surface is investigated using the multi-scale model. At micro-scale separations, the friction is dominated by the viscous component (see figure 9.28). The viscous friction is observed to increase with sliding speed. The surface-to-surface interaction of the asperities is predicted using the Hertzian and Maugis-Dugdale elastoplactic model discussed in *Chapter 8*. Figure 9.28(b) shows that the Maugis-Dugdale model predicts a higher friction than the Hertzian contact. This is true due to the larger contact area induced by adhesion in the Maugis-Dugdale model, leading to a larger friction force.

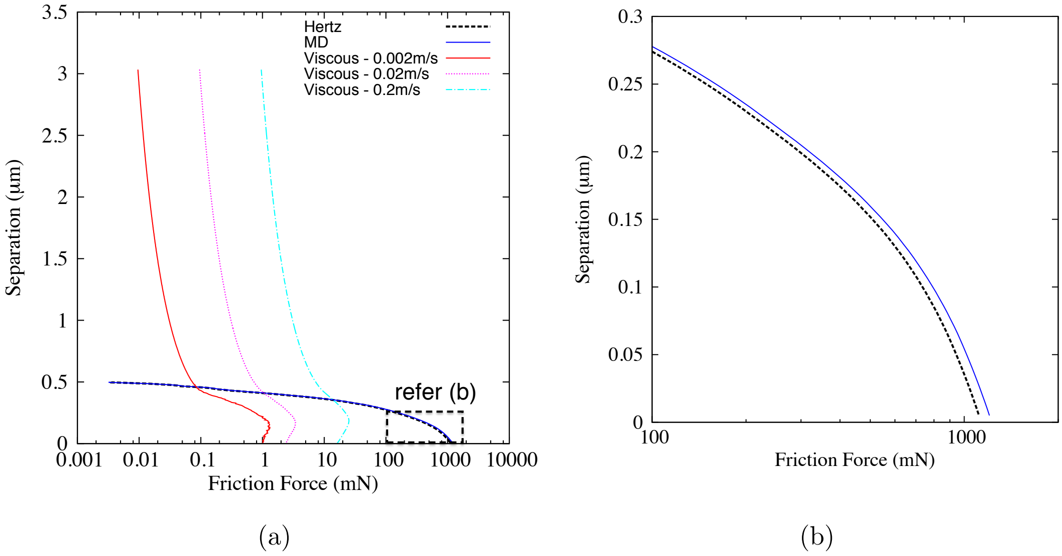

(a) (b)

Figure 9.28: Friction force for the planar fractal geometry

The friction force for the ring-liner contact (*Chapter 2*) is first predicted using the simplified friction model (known as “initial”) for the r.m.s. surface roughness of $0.115\mu m$. Then the multi-length scale friction model is applied to predict the friction for the same conjunction using the Hertzian and Maugis-Dugdale models. Figure 9.29(a) shows the total friction force comparison. It should be noted that during the mid-span stroke of the ring-liner contact, the friction is dominated by the viscous friction due to the macro-scale kinematics of the piston sliding. However, at the dead centers, especially at the power-stroke TDC, the viscous friction is presided by the boundary friction. It can be observed through the magnitude difference of both the viscous and boundary components in figures 9.29 (b) and (c).

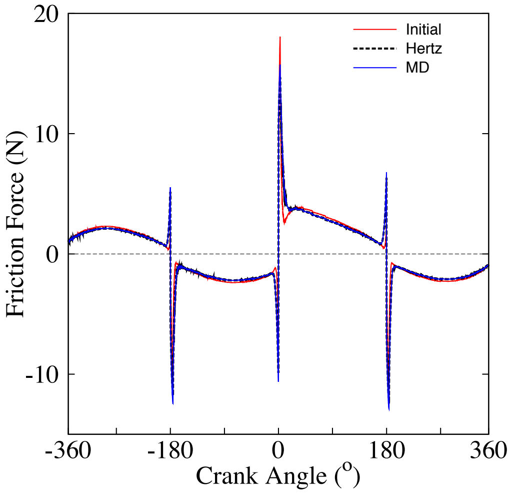

(a) Total Friction

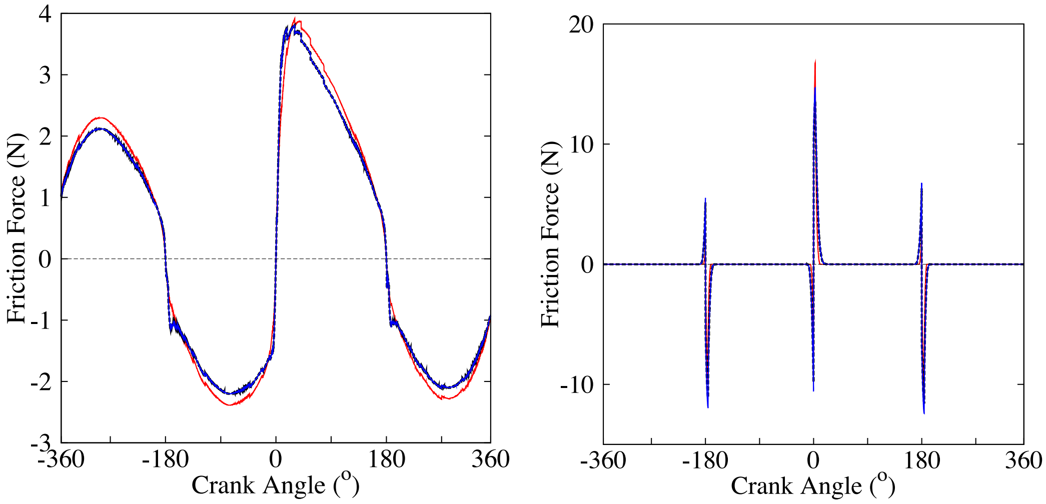

(b) Viscous Friction

(c) Boundary Friction

Figure 9.29: Friction force comparison for a ring-liner contact (2000 rev/min)

It is mentioned in *Chapters 2, 3 and 4* that the high friction region along the ring-liner conjunction is at the vicinity of the power-stroke TDC. Figure 9.30 shows the friction force predicted using the simplified friction model (initial) and the multi-scale model (Hertz and Maugis-Dugdale(MD)). Both the methods show similar trend. The simplified friction model predicted a higher friction than the other two estimates after piston motion reversal. However, as the piston sliding speed increases, it should be noted that the proposed friction models predicted higher friction forces.

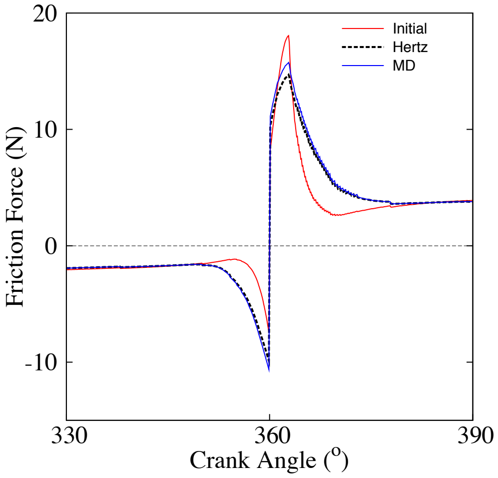

Figure 9.30: Friction force comparison for a ring-liner contact at the vicinity of power stroke TDC (2000 rev/min)

Figure 9.31 shows the viscous and boundary shear at 362.8° where the film is at its minimum (figure 2.9 in *Chapter 2*). The viscous shear predicted using the simplified model (*Chapter 2*) and the proposed model (*Chapter 7 and 8*) shows a significant variation. The new model proposed considers the intermolecular forces and adsorption at vanishing gaps, which forms a low shear strength thin film, leading to a lower shear stress. The boundary shear shown in figure 9.31(b) reflected a higher peak predicted by the simplified friction model. The variation here is because of the different rough surface contact analysis used to consider asperity interaction.

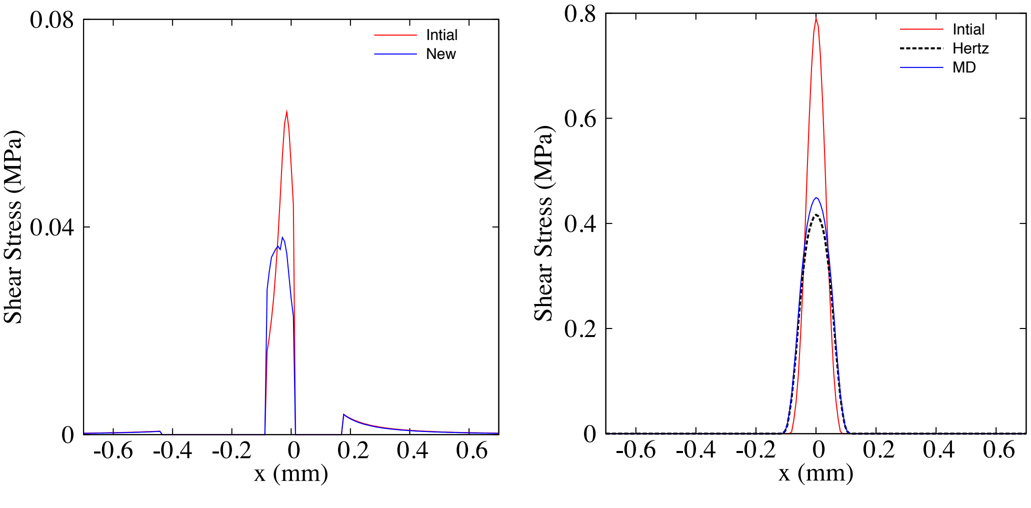

(a) Viscous Shear

(b) Boundary Shear

Figure 9.31: Shear stress components at 362.8°

Another advantage of the new multi-length scale friction model is that the surface or material characteristics can be manipulated. For example, the surface energy of the contacting surfaces show a higher friction when being increased (see figure 9.32). The surface energy affects the adherence of the interacting asperities on the rough surface contact. Higher surface energy increases the contact area, leading to larger friction. Another material characteristic that can be varied is the material hardness. Increasing the material hardness results in lower friction force as in figure 9.32. This is because softer materials deflects more than the harder material under the same loading conditions, increasing the possibility of plastic deformation.

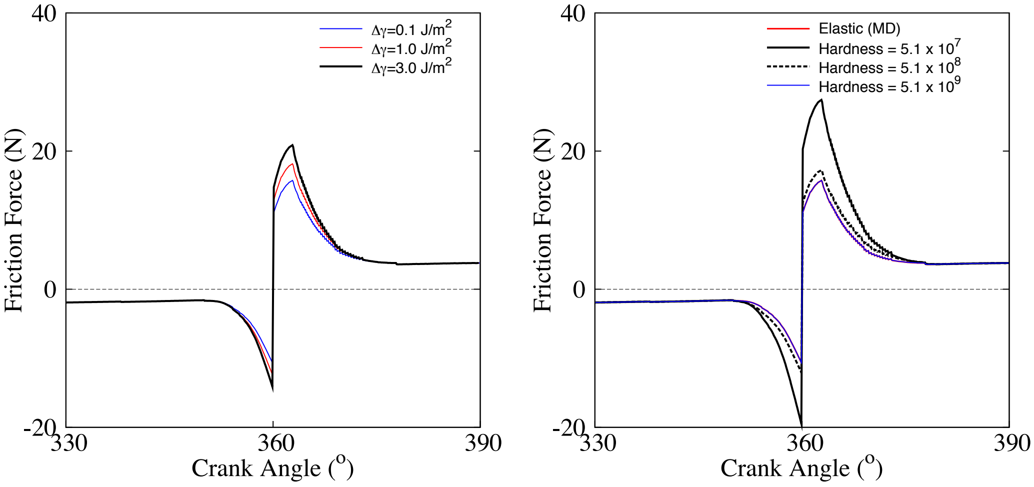

(a) Surface Energy (b) Material Hardness

Figure 9.32: Influence of material surface energy and hardness on friction force at the vicinity of the power stroke TDC

9.8 Summary

This chapter introduces a new multi-scale friction model. The capabilities of the model are discussed by comparing the model to the simplified friction model used in *Chapter 2*. The initial predictions based on the new model showed promising results.

Chapter 10

Conclusion and Future Work

10.1 Overall Conclusion

The current study has established an integrated friction model considering micro- and nano-scale kinetics for piston ring-liner contact. A numerical model is used to determine the microscopic tribological characteristics of the piston ring-liner contact. This provided details to the critical regions along the liner with high friction force. The modified Elrod's cavitation algorithm predicts the pressure distribution and film profile. The model has at its basis the approach proposed by Vijayaraghavan and Keith [29] for Elrod's cavitation algorithm. To account for localised contact deflection, which may have significant consequences for the cavitation development, the finite difference scheme suggested by Jalali *et al* [28] for an elastohydrodynamic contact was carefully adopted for the studied conditions.

The cavitation region predicted using the modified Elrod's algorithm, contracts considerably in the vicinity of the dead centres. However, it partly survives beyond the dead centre reversal as a confined bubble at the leading edge of the contact. Although this bubble quickly diminishes and is absorbed by the lubricant film, it can deplete the available lubricant supply, causing starvation. Immediately beyond the dead centre, a new cavitation region forms at the trailing edge of the contact. Although these two cavitation regions only coexist for a brief period of time, low entrainment velocity and high contact loads can lead to thinner films and thus higher friction forces. The friction force predicted is based on a simple friction model, combining viscous and boundary friction components.

The piston ring-liner lubrication analysis is also considered with blow-by effects, using measured new and worn top ring profiles. The inter-ring pressure, influenced by the blow-by effect and also the combustion chamber, affects the cavity formation along the ring-liner conjunction during the engine cycle. The new and worn ring profiles also play a significant role in affecting the frictional behaviour along the ring-liner contact. Worn rings, which show a flatter profile produce lower friction under most of contact conditions, except after the power stroke TDC. This is because of the increased viscous friction incurred by the worn ring itself. The observation shows that the friction force of the ring-liner contact depends not only on the lubricant itself, but also on the profile of the ring.

A numerical analysis is conducted to simulate the ring-liner contact on the Plint TE77. A tapered ring profile is used on the rig. The validation is performed on two different types of lubricant - a base oil and the $SAE10W40$. Due to the tapered ring profile, the tribological characteristics can be observed to be different from the top compression ring, especially the transient nature of the cavitation formation. The trend of the film thickness predicted numerically shows good agreement with the experimental data.

The vanishing gaps between the ring-liner contact at power stroke TDC inhibits asperity interaction. In the absence of a protective lubricant layer, direct surface-to-surface contact may occur. This means that there is a need to consider asperity contact adhesion. Various adhesion models are studied. It is concluded that appropriate contact models must be used to prevent inaccuracy in the prediction of friction. A simple elastoplastic adhesion model is developed, based on Jackson and Green's [130] method using the Maugis-Dugdale adhesion model. The method assumes that the elastoplastic deformation is strictly confined within the actual contact area. By considering the elastoplastic deformation, the model shows that when elastoplasticity is initiated, the asperity contact starts to lose its load carrying capacity. This leads to an increased contact area which produces a higher adhesive friction. The downside of the model is that it is restricted to materials which fulfil the conditions set by the Tabor's parameter with $\mu < 1$.

The load carrying asperities are wet due to boundary lubrication because of an adsorbed thin film on their tips. The kinetic laws involved in nano-scale separations of the thin adsorbed films are understood through asperity models. There is a strong correlation between lubricant molecular structure and tribological behaviour of a conjunction. It is even more obvious in diminutive conjunctions at asperity level. The study investigates the interaction between local asperity or small feature deflection and molecular-level lubricant drainage as well as their impact on friction and local load carrying capacity of the lubricant.

It is found that while long chain molecules inhibit discrete drainage of the lubricant from the contact leading to lower friction, they also lower asperity level load carrying capacity because of the absence of any significant solvation pressure. This can potentially lead to increased metal-to-metal interactions. This is a major finding of the current investigation.

A typical lubricating film usually includes a small proportion of additives. A small percentage of additives adsorbed to surfaces and help improve the lubricant performance of the lubricant in reducing friction. The initial asperity thin film shearing model uses a simplified empirical method which considers only a single component fluid. To consider a more realistic fluid, a statistical mechanics approach is proposed for a fluid mixture which includes adsorption of the fluid particles to the boundary surface. The method by Perram and Smith [178], based on Baxter's *sticky hard sphere* model, gives a good idea of the influence of lubricant additives and the adsorption of particles onto the surface. The different configurations of additives' concentration and adsorption capability are studied.

Another important finding, confirming general belief is that a highly adsorbing additives in a weakly adsorbing base oil helps keep the friction force low. The concentration of additives must be added with care as higher concentration might increase friction.

10.2 Contributions to knowledge

There are several key contributions to knowledge. These may be viewed across the physics of scale. At the macro/micro scale, the study has established a new numerical model for piston ring-liner pressure distribution and film profile. It is found that cavitation region located at the trailing edge of the contact pre-reversal is briefly sustained after reversal as a confined bubble at the leading edge of contact. This can result in starvation. The phenomenon has only been hitherto observed experimentally by Arcoumanis *et al* [24].

Another contribution to knowledge is the development of a multi-scale friction model using a friction map considering nano-scale kinetic laws governing the asperity interactions. The rough surface contact is first being investigated by understanding the pros and cons of the statistical (Greenwood-Williamson) and fractal approach. The comparison shows that the friction predicted by the statistical and fractal analysis differ significantly at larger separations due to the multi-scale nature of the rough surface. The study also shows that the statistical approach is heavily dependent on the type of measurement equipment and sample length selected. Care must be taken when using the statistical approach in order to avoid a huge error in friction calculation. A fractal approach towards analysing a rough surface contact is more favourable as the method reflects more closely the actual physical contact profile. The friction model can be applied onto a micro-scale tribological conjunction such as the piston ring-liner contact. This is an alternative and computationally more effective method than the alternative molecular dynamics.

The study also includes a new friction model based on the fractal analysis for rough surface contact considering the effect of asperity interaction due to adhesion, elastoplastic deformation and thin adsorbed film formation.

10.3 Future Work

A multi-length scale approach based on asperity models (e.g. thin film shearing and boundary adhesion) are used to predict friction for a rough surface which can be extended for use in a tribological conjunction such as the piston ring-liner contact. Rough surface characterisation parameters must be measured accordingly for the desired interacting surfaces in relative motion. The model requires experimental validations before it can be further extended for practical applications. The validation should also be achieved by conducting experiments at both micro- and nano-scale levels. The fractal analysis currently considers only isotropic surfaces, which might not be true for all engineering applications. Therefore, the fractal analysis can also be extended to take into account anisotropic surfaces such as the honing marks on cylinder liners.

The asperity thin film shearing model considers only spherical molecules, which is not the case for real lubricants. The model can be extended by introducing chain molecules - hard chains. The chain molecule consideration might require significant understanding of molecular dynamics and physical chemistry of lubricant rheology.

An elastoplastic adhesion model is proposed in the study. The model may not be able to accommodate all range of materials, based on the Tabor's parameter. A detailed study should be conducted in order to consider the influence of adhesion upon elastoplastic deformation in the contact. Further work can be undertaken by developing a non-linear finite element model to consider the coupling effect of adhesion and elastoplasticity.

The elastoplastic adhesion model considers only homogeneous material, which might not be true for all modern engineering surface. Therefore, another extension to the elastoplastic adhesion model is to include layered solids for a graded elastic coating, representing a typical coated engineering surface.

References

[1] Lubrication (tribology) education and research. *Jost Report*, Department of Education and Science, HMSO, 1966.

[2] Amontons G. De la resistance causee dans les machines. *Memoires de LAcadmie Royale, A*, pages 275–282, 1699.

[3] Coulomb C. A. Recherches sur la meilleure maniere de fabriquer les aigulles aimantes. *Memoires Mathematical Physic IX*, pages 166–342, 1780.

[4] Reynolds O. On the theory of lubrication and its application to mr beauchamp tower's experiments, including an experimental determination of the viscosity of olive oil. *Philosophical Transactions of the Royal Society*, 177:157–234, 1886.

[5] Dowson D. Thin films in tribology. In *Proceedings of the 19th Leeds-Lyon Symposium on Tribology*, volume 25, pages 3–12, 1993.

[6] B. S. Anderson. Vehicle tribology. *17th Leeds-Lyon Symposium on Tribology, Elsevier Tribology Series*, 18:503–506, 1991.

[7] C.M. Taylor. Automobile engine tribology - design considerations for efficiency and durability. *Wear*, 221:1–8, 1998.

[8] Taylor C. M. *Engine tribology - Leeds-Lyon Symposium on Tribology 9th 1982 University of Leeds.*, volume 26. Elsevier, Amsterdam ; New York, c1993.

[9] Tung S. C. and McMillan M. L. Automotive tribology overview of current advances and challenges for the future. *Tribology International*, 37(7):517–536, 2004.

[10] Akalin O. and Newaz G. M. Piston ring-cylinder bore friction modeling in mixed lubrication regime: Part 1: Analytical results. *Journal of tribology*, 123:211, 2001.

[11] Swift W. The stability of lubricating in journal bearings. *Proc. of the Institute Civil Engineers*, 233:267–288, 1932.

[12] Steiber W. Hydrodynamische theorie des gleitlagers. *Das Schwimmlager, V.D.I Verlag, Berlin*, 1933.

[13] Priest M., Dowson D., and Taylor C. M. Theoretical modelling of cavitation in piston ring lubrication. *Proceedings of the Institution of Mechanical Engineers, Part C: Journal of Mechanical Engineering Science*, 214(3):435–447, 2000.

[14] Brewe D. E. Theoretical modeling of the vapor cavitation in dynamically loaded journal bearings. *Journal of Tribology*, 108(4):628–638, 1986.

[15] Dowson D. Laboratory experiments and demonstration in tribology. the principles of hydrodynamic lubrication and cavitation in lubricating films. *Tribology*, 1(2):104–108, 1968.

[16] Dowson D. and Taylor C. M. Fundamental aspects of cavitation in bearings. In *Cavitation and related phenomena in lubrication: proceedings of the 1st Leeds-Lyon Symposium on Tribology*, page 15. Institution of Mechanical Engineers, 1975.

[17] Bara R. J. *Rupture point movement in journal bearings*, 2004.

[18] Young F. R. *Cavitation.* Imperial College Press, 1999.

[19] Sahlin F., Almqvist A., Larsson R., and Glavatskih S. A cavitation algorithm for arbitrary lubricant compressibility. *Tribology International*, 40(8):1294–1300, 2007.

[20] Etsion I. and Ludwig L. P. Observation of pressure variation in the cavitation region of submerged journal bearings. *Journal of Lubrication Technology*, 104(2):157–163, 1982.

[21] Stadler K., Izumi N., Morita T., Sugimura J., and Piccigallo B. Estimation of cavity length in ehl rolling point contact. *Journal of Tribology*, 130(3):315021–315029, 2008.

[22] Floberg L. Lubrication of two rotating cylinders at variable lubricant supply with reference to the tensile strength of the liquid lubricant. *Journal of Lubrication Technology*, 95:155–165, 1972.

[23] Floberg L. Cavitation boundary conditions with regard to the number of streamers and tensile strength of the liquid. In *Proceedings of 1st Leeds-Lyon Symposium on Tribology: Cavitation and Related Phenomena in Lubrication*, pages 31–35, New York, 1976. Mechanical Engineering Publications.

[24] Arcoumanis C., Duszynski M., Flora H., and Ostovar P. Development of a piston-ring lubrication test-rig and investigation of boundary conditions for modelling lubricant film properties. *SAE transactions*, 104:1433–1451, 1995.

[25] Dhunput A., Teodorescu M., and Arcoumanis C. Investigation of cavitation development in the lubricant film of piston-ring assemblies. *Journal of Physics: Conference Series*, 85(1), 2007.

[26] ASTM Standard D341-2009. Standard practice for viscosity-temperature charts for liquid petroleum products. *ASTM International, West Conshohocken, PA*, 2009, DOI : 10.1520/D0341-09, www.astm.org.

[27] Jeng Y. R. Theoretical analysis of piston-ring lubrication: Part 1 : Fully flooded lubrication. *Tribology Transactions*, 35(4):696–706, 1992.

[28] Jalali-Vahid D., Rahnejat H., and Jin Z. M. Elastohydrodynamic solution for concentrated elliptical point contact of machine elements under combined entraining and squeeze-film motion. *Proceedings of the Institution of Mechanical Engineers, Part J: Journal of Engineering Tribology*, 212(6):401–411, 1998.

[29] Vijayaraghavan D. and Keith Jr. T. G. Development and evaluation of a cavitation algorithm. *Tribology Transactions*, 32(2):225–233, 1989.

[30] Jakobsson B. and Floberg L. The finite journal bearing considering vaporization. *Transactions of Chalmers University of Technology*, 1957.

[31] Olsson K. O. Cavitation in dynamically loaded bearings. *Transactions of Chalmers University of Technology*, 1965.

[32] Elrod H. G. A cavitation algorithm. *Journal of Lubrication Technology*, 103:350–354, 1981.

[33] Elrod H. G. and Adams M. L. Computer program for cavitation and starvation problems. In *Proceedings of 1st Leeds-Lyon Symposium on Tribology: Cavitation and Related Phenomena in Lubrication*, pages 37–41, New York, 1976. Mechanical Engineering Publications.

[34] Coyne J. C. and Elrod H. G. Conditions for the rupture of a lubricating film - part 2. *Journal of Lubrication Technology*, 93(1):156–167, 1971.

[35] Yang Q. and Keith T. G. An elastohydrodynamic cavitation algorithm for piston ring lubrication. *Tribology Transactions*, 38(1):97–107, 1995.

[36] Cioc S. and Keith Jr. T. G. Application of the ce/se method to two-dimensional flow in fluid film bearings. *International Journal of Numerical Methods for Heat and Fluid Flow*, 13(2-3):216–243, 2003.

[37] Sawicki J. T. and Yu B. Analytical solution of piston ring lubrication using mass conserving cavitation algorithm. *Tribology Transactions*, 43(3):419–426, 2000.

[38] Bayada G., Chambat M., and El Alaoui M. Variational formulations and finite element algorithms for cavitation problems. *Journal of Tribology*, 112(2):398–403, 1990.

[39] Damiens B., Venner C. H., Cann P. M. E., and Lubrecht A. A. Starved lubrication of elliptical ehd contacts. *Journal of Tribology*, 126(1):105–111, 2004.

[40] Venner C. H., Berger G., and Lugt P. M. Waviness deformation in starved ehl circular contacts. *Journal of Tribology*, 126(2):248–257, 2004.

[41] Heywood J. B. *Internal combustion engine fundamentals.* McGraw-Hill Science Engineering, 1988.

[42] Namazian M. and Heywood J. B. Flow in the piston-cylinder-ring crevices of a spark-ignition engine: effect on hydrocarbon emissions, efficiency and power. *SAE transactions*, 91(1):261–288, 1982.

[43] Aghdam E. A. and Kabir M. M. Validation of a blowby model using experimental results in motoring condition with the change of compression ratio and engine speed. *Experimental Thermal and Fluid Science*, 2010.

[44] Yang L. Friction modelling for internal combustion engines. *PhD Thesis, University of Leeds, UK*, 1992.

[45] Roelands C. J. A. Correlational aspects of the viscosity-temperature-pressure relationships of lubricating oils. *PhD Thesis, Technische Hogeschool te Delft., Netherlands*, 1966.

[46] Dowson D. and Higginson G. R. *Elastohydrodynamic Lubrication: The Fundamentals of Roller and Gear Lubrication.* Pergamon, Oxford, 1966.

[47] Mishra P. C., Balakrishnan S., and Rahnejat H. Tribology of compression ring-to-cylinder contact at reversal. *Proceedings of the Institution of Mechanical Engineers, Part J: Journal of Engineering Tribology*, 222(7):815–826, 2008.

[48] Houpert L. G. and Hamrock B. J. Fast approach for calculating film thicknesses and pressures in elastohydrodynamically lubricated contacts at high loads. *Journal of Tribology*, 108(3):411–419, 1986.

[49] Teodorescu M., Kushwaha M., Rahnejat H., and Rothberg S. J. Multi-physics analysis of valve train systems: From system level to microscale interactions. *Proceedings of the Institution of Mechanical Engineers, Part K: Journal of Multi-body Dynamics*, 221(3):349–361, 2007.

[50] Evans C. R. and Johnson K. L. Rheological properties of elastohydrodynamic lubricants. *Proceedings of the Institution of Mechanical Engineers, Part.C : Mechanical Engineering Science*, 200:303–312, 1986.

[51] Greenwood J. A. and Tripp J. H. The contact of two nominally flat rough surfaces. *Proceedings of the Institute of Mechanical Engineering*, 185(48):625–633, 1971.

[52] Teodorescu M., Taraza D., Henein N. A., and Bryzik W. Simplified elasto-hydrodynamic friction model of the cam-tappet contact. *SAE transactions*, 112:1271–1282, 2003.

[53] Ryk G., Kligerman Y., and Etsion I. Experimental investigation of laser surface texturing for reciprocating automotive components. *Tribology Transactions*, 45(4):444–449, 2002.

[54] Rahnejat H., Balakrishnan S., King P. D., and Howell-Smith S. In-cylinder friction reduction using a surface finish optimization technique. *Proceedings of the Institution of Mechanical Engineers, Part D: Journal of Automobile Engineering*, 220(9):1309–1318, 2006.

[55] Rabute R. and Tian T. Challenges involved in piston top ring designs for modern si engines. *Journal of Engineering for Gas Turbines and Power*, 123:448, 2001.

[56] Eweis M. Reibungs-und undichtigkeitsverluste an kolbenringen. 1935.

[57] Ting L. L. and Mayer J. E. Piston ring lubrication and cylinder bore wear analysis, part i - theory. *Transactions of ASME, Series F*, 96(3), 1974.

[58] Ting L. L. and Mayer J. E. Piston ring lubrication and cylinder bore wear analysis, part ii - theory verification. *Transactions of ASME, Series F*, 96(3), 1974.

[59] Ruddy B. L., Dowson D., and Economou P. N. The prediction of gas pressures within the ring packs of large bore diesel engines. *Proceedings of the Institute of Mechanical Engineers, Part C: Journal of Mechanical Engineering Sciences*, 23:295C304, 1981.

[60] Kuo T. W., Sellnau M. C., Theobald M. A., and Jones J. D. Calculation of flow in the piston-cylinder-ring crevices of a homogeneous-charge engine and comparison with experiment. In *Society of Automotive Engineers international congress and exposition*, volume 27, 1989.

[61] Mufti R. A., Priest M., and Chittenden R. J. Analysis of piston assembly friction using the indicated mean effective pressure experimental method to validate mathematical models. *Proceedings of the Institution of Mechanical Engineers, Part D: Journal of Automobile Engineering*, 222(8):1441–1457, 2008.

[62] Avan E. Y., Mills R., and Dwyer-Joyce R. S. Simultaneous film thickness and friction measurement for a piston ring-cylinder contact. *ASME International Joint Tribology Conference 2010, San Francisco, California*, 2010.

[63] Bowden F. P. and Tabor D. *The friction and lubrication of solids.* Clarendon Press, Oxford, 1950.

[64] Klamann D. *Lubricants and related products.* Verlag Chemie, Weinheim, 1984.

[65] Bartz W. J. *Engine Oils and Automotive Lubrication.* Dekker, New York, 1993.

[66] van Rensselar J. How base stokcs and additives are improving energy efficiency. *Tribology and Lubrication Technology*, pages 34–46, 2011.

[67] Mortier R. M. and Orszulik S. T. *Chemistry and technology of lubricants.* Kluwer, Dordrecht, 1997.

[68] Taylor R. I., Mainwaring R., and Mortier R. M. Engine lubricant trends since 1990. *Proceedings of the Institution of Mechanical Engineers, Part J: Journal of Engineering Tribology*, 219:331–346, 2005.

[69] Studt P. Boundary lubrication : adsorption of oil additives on steel and ceramic surfaces and its influence on friction and wear. *Tribology International*, 22(2):111–119, 1989.

[70] Murase A. and Ohmori T. Tof-sims analysis of friction surfaces tested with mixtures of a phosphite and a friction modifier. *Surface and Interface Analysis*, 31:232–241, 2001.

[71] Hardy W. B. and Doubleday I. Boundary lubrication - the paraffin series. *Proceedings of the Royal Society London, Series A*, 100:550–574, 1921.

[72] Greenfield M. L. and Ohtani H. Molecular dynamics simulation study of model friction modifier additives confined between two surfaces. *Tribology Letters*, 7:137–145, 1999.

[73] Wu Y. L. and Dacre B. Effects of lubricant-additives on the kinetics and mechanisms of zddp adsorption on steel surfaces. *Tribology International*, 30:445–453, 1997.

[74] Tung S. C. and Gao H. Tribological investigation of piston ring coatings operating in an alternative fuel and engine oil blend. *Tribology Transactions*, 45(3):381–389, 2002.

[75] Tung S. C. and Gao H. Tribological characteristics and surface interaction between piston ring coatings and a blend of energy conserving oils and ethanol fuels. *Wear*, 255:1276–1285, 2003.

[76] Podgornik B. and Vizintin J. Tribological reactions between oil additives and dlc coatings for automotive applications. *Surface and Coatings Technology*, 200:1982–1989, 2005.

[77] Choa S. H., Ludema K. C., Potter G. E., Dekoven B. M., Morgant T. A., and Kar K. K. A model of the dynamics of boundary film formation. *Wear*, 177:33–45, 1994.

[78] Zhang H., Chang L., Webster M. N., and Jackson A. A micro-contact model for boundary lubrication with lubricant/surface physiochemistry. *Journal of Tribology*, 125:8–15, 2003.

[79] Frewing J. J. The heat adsorption of long-chain compounds ad their effect on boundary lubrication. *Proceedings of the Royal Society London, Series A*, 182:270–285, 1944.

[80] Jahanmir S. and Beltzer M. An adsorption model for friction in boundary lubrication. *Tribology Transactions*, 29(3):423–430, 1985.

[81] So H. and Lin Y. C. The theory of antiwear for zddp at elevated temperature in boundary lubrication condition. *Wear*, 177:105–115, 1994.

[82] Temkin M. I. Adsorption equilibrium and the kinetics of processes on nonhomogeneous surfaces and in the interaction between adsorbed molecules. *Journal of Physical Chemistry (USSR)*, 15:296–332, 1941.

[83] Anderberg C., Pawlus P., Rosen B. G., and Thomas T. R. Alternative descriptions of roughness for cylinder liner production. *Journal of Materials Processing Technology*, 209:1936–1942, 2009.

[84] Jeng Y. R. Impact of plateaued surfaces on tribological performances. *Tribology Transactions*, 39:354–361, 1996.

[85] Willis E. Surface finish in relation to cylinder liners. *Wear*, 109:351–366, 1986.

[86] Mainsah E., Greenwood J. A., and Chetwynd D. G. *Metrology and Properties of Engineering Surfaces.* Springer-Verlag, Berlin, 2001.

[87] Puente Leon F. Evaluation of honed cylinder bores. *Ann. CIRP*, 51:503506, 2002.

[88] Stout K. J. and Spedding T. A. The characterisation of internal combustion engine bores. *Wear*, 83:311–326, 1983.

[89] Trautwein R. Characteristic values for determining and evaluating the surface of cylinder bores. *Mercury Marine Company*, 1978.

[90] Torrance A. A. A simple datum for measurement of the abbott of a profile and its first derivatives. *Tribology International*, 30:239–244, 1997.

[91] Kumar R., Kumar S., Prakash B., and Sethuramiah A. Assessment of engine liner wear from bearing area curves. *Wear*, 239:282–286, 2000.

[92] DIN4776. Measurement of surface roughness : parameters $r_k, r_{pk}, r_{vk}, m_{r1}, m_{r2}$ for the description of the material portion (profile bearing length ratio) in the roughness profile. *Measuring conditions and evaluation procedures*, 1990.

[93] Schneider U., Steckroth A., Rau N., and Hubner G. An approach to the evaluation of surface profiles by separating them into functionally different parts. *Surface Topography*, 1:343–355, 1988.

[94] Zhmud B. Developing energy-efficient lubricants and coatings for automotive applications. *Feature article in Tribology and Lubrication Technology*, pages 42–49, 2011.

[95] Tung S. C. and Cheng Y. T. Tribological characteristics and microstructures of pvd thin film coatings on steel substrates. In *Proceedings of the International Wear Conference*, San Francisco, California, 12-17 April 1993.

[96] Hamilton D. B., Walowit J. A., and Allen C. M. A theory of lubrication by microirregularities. *Journal of Basic Engineering*, 88:177–185, 1966.

[97] Anno J. N., Walowit J. A., and Allen C. M. Microasperity lubrication. *Journal of Lubrication Technology*, 90:351–355, 1968.

[98] Anno J. N., Walowit J. A., and Allen C. M. Load support and leakage from microasperity-lubricated face seals. *Journal of Lubrication Technology*, 91:726–731, 1969.

[99] Etsion I. Improving tribological performance of mechanical components by laser surface texturing. *Tribology Letters*, 17(4):733–737, 2004.

[100] Etsion I. State of the art in laser surface texturing. *Journal of Tribology*, 127:248–253, 2005.

[101] Etsion I. and Burstein L. A model for mechanical seals with regular microsurface structure. *Tribology Transactions*, 39:677–683, 1996.

[102] Etsion I., Halperin G., and Greenberg Y. Increasing mechanical seal life with laser-textured seal faces. In *15th International Conference On Fluid Sealing, BHR Group*, pages 3–11, Maastricht, 1997.

[103] Ryk G. and Etsion I. Testing piston rings with partial laser surface texturing for friction reduction. *Wear*, 261:792–796, 2006.

[104] Tonder K. Hydrodynamic effects of tailored inlet roughness: Extended theory. *Tribology International*, 37:137–142, 2004.

[105] Siripuram R. B. and Stephens L. S. Effect of deterministic asperity geometry on hydrodynamic lubrication. *Journal of Tribology*, 126:527–534, 2004.

[106] Dumitru G., Romano V., Weber H. P., Gerbig Y., Haefke H., Bruneau S., Hermann J., and Sentis M. Femtosecond laser ablation of cemented carbides: Properties and tribological applications. *Applied Physics A: Material Science Process*, 79:629–632, 2004.

[107] Andersson P., Koskinen J., Varjus S., Gerbig Y., Haefke H., Georgiou S., Zhmud B., and Buss W. Microlubrication effect by laser-textured steel surfaces. *Wear*, 262:369–379, 2006.

[108] Takata R., Li Y., and Wong V. W. Effects of liner surface texturing on ring/liner friction in large-bore ic engines. In *Proceedings of the Internal Combustion Engine Division*, pages 5–8 November 2006, Sacramento, California, 2006.

[109] Hertz H. On the contact of elastic solids. *J.reine angew.Math*, 92:156171, 1881.

[110] Bradley R. S. The cohesive force between solid surfaces and the surface energy of solids. *Philosophical Magazine*, 13:853, 1932.

[111] Johnson K. L., Kendall K., and Roberts A. D. Surface energy and the contact of elastic solids. *Proceedings of the Royal Society of London.Series A, Mathematical and Physical Sciences*, pages 301–313, 1971.

[112] Kogut L. and Etsion I. Adhesion in elastic-plastic microcontact. *Journal of Colloid and Inteface Science*, 261:372–378, 2003.

[113] Derjaguin B. V., Muller V. M., and Toporov Y. P. Effect of contact deformation on the adhesion of elastic solids. *Journal of Colloid and Interface Sciences*, 53:31426, 1975.

[114] Maugis D. On the contact and adhesion of rough surfaces. *Journal of Adhesion Science Technology*, 10(2):161–175, 1996.

[115] Greenwood J. A. Adhesion of elastic spheres. *Proceedings of the Royal Society of London : Mathematical, Physical and Engineering Sciences*, 453:1277–1297, 1997.

[116] Maugis D. Adhesion of spheres: the jkr-dmt transition using a dugdale model. *Journal of Colloid and Interface Sciences*, 150(1):243–269, 1992.

[117] Grierson D. S., Flater E. E., and Carpick R. W. Accounting for the jkr-dmt transition in adhesion and friction measurements with atomic force microscopy. *Journal of Adhesion Science and Technology*, 19(3-5):291–312, 2005.

[118] Johnson K. L. and Greenwood J. A. An adhesion map for the contact of elastic spheres. *Journal of Colloid and Interface Science*, 192:326–333, 1997.

[119] Carpick R. W. and Salmeron M. Scratching the surface : Fundamental investigations of tribology with atomic force microscopy. *Chemical Reviews*, 97(4):1163–1194, 1997.

[120] Thoreson E. J., Martin J., and Burnham N. A. The role of few-asperity contacts in adhesion. *Journal of Colloid and Interface Science*, 298:94–101, 2006.

[121] Kogut L. and Jackson R. L. A comparison of contact modelling utilising statistical and fractal approaches. *Journal of Tribology*, 128:213–217, 2006.

[122] Johnson K. L. Adhesion and friction between a smooth elastic spherical asperity and a place surface. *Proceedings of the Royal Society of London.Series A, Mathematical and Physical Sciences*, 453:163–179, 1997.

[123] Johnson K. L. and Sridhar I. Adhesion between a spherical indenter and an elastic solid with a compliant elastic coating. *Journal of Physics D : Applied Physics*, 34:683–689, 2001.

[124] Pollock H. M. Contact adhesion between solids in vacuum. ii. deformation and interfacial energy. *Journal of Physics D*, 11(1):39, 1978.

[125] Pethica J. B. and Tabor D. Contact of characterised metal surfaces at very low loads: Deformation and adhesion. *Surface Science*, 89:182–190, 1979.

[126] Maugis D. and Pollock H. M. Surface forces, deformation and adherence at metal microcontacts. *Acta Metallurgica*, 32(9):1323–1334, 1984.

[127] Chang W. R., Etsion I., and Bogy D. B. Adhesion model for metallic rough surfaces. *Journal of Tribology*, 110(1):50, 1988.

[128] Peng Y. F. and Guo Y. B. An adhesion model for elastic-plastic fractal surfaces. *Journal of Applied Physics*, 102:053510, 2007.

[129] Kogut L. and Etsion I. Elastic-plastic contact analysis of a sphere and a rigid flat. *Journal of Applied Mechanics*, 69:657–662, 2002.

[130] Jackson R. L. and Green I. A finite element study of elasto-plastic hemispherical contact against a rigid flat. *Journal of Tribology*, 127:343–354, 2005.

[131] Gohar R. and Rahnejat H. *Fundamentals of tribology.* Imperial College Press, London, 2008.

[132] Tambe N. S. and Bhushan B. Friction model for the velocity dependence of nanoscale friction. *Nanotechnology*, 16:2309–2324, 2005.

[133] Al-Samieh M. and Rahnejat H. Ultra-thin lubricating films under transient conditions. *Journal of Physics D: Applied Physics*, 34:2610–2621, 2001.

[134] Chan D. Y. C. and Horn R. G. The drainage of thin liquid films between solid surfaces. *Journal of Chemical Physics*, 83(10):5311–5324, 1985.

[135] Israelachvili J. N. *Intermolecular and surface forces*. Academic press London, 1992.

[136] Abd. Al-Samieh M. F. and Rahnejat H. Nano-lubricant film formation due to combined elastohydrodynamics and surface force action under isothermal conditions. *Proceedings of Institute of Mechanical Engineers, Part C : Journal of Mechanical Engineering Science*, 215:1019–1029, 2001.

[137] Matsuoka H. and Kato T. Discrete nature of ultrathin lubrication film between mica surfaces. *Journal of Tribology*, 118:832, 1996.

[138] Al-Samieh M. and Rahnejat H. Physics of lubricated impact of a sphere in a plate in a narrow continuum to gaps of molecular dimensions. *Journal of Physics D: Applied Physics*, 35:2311–2326, 2002.

[139] Henderson D. and Lozada-Cassou M. A simple theory for the force between spheres immersed in a fluid. *Journal of Colloid and Interface Science*, 114(1):180–183, 1986.

[140] Evans R. and Parry A. O. Liquids at interfaces : What can a theorist contribute? *Journal of Physics : Condensed Matters*, 2, 1990.

[141] Teodorescu M., Balakrishnan S., and Rahnejat H. Physics of ultra-thin surface films on molecularly smooth surfaces. *Proceedings of the Institution of Mechanical Engineers, Part N: Journal of Nanoengineering and Nanosystems*, 220(1):7–19, 2006.

[142] Lifshitz E. M. The theory of molecular attractive forces between solids. *Soviet Physics JETP*, 2:94–110, 1956.

[143] Johnson K. L. *Contact mechanics*. Cambridge University Press, Cambridge, 1985. K. L. Johnson.

[144] Chong W. W. F., Teodorescu M., and Vaughan N. D. Cavitation induced starvation for piston ring/liner tribological conjunction. *Tribology International*, 44(4):483–497, 2011.

[145] Eyring H. Viscosity, plasticity, and diffusion as examples of absolute reaction rates. *The Journal of chemical physics*, 4:283, 1936.

[146] Briscoe B. J. and Evans D. C. B. The shear properties of langmuir-blodgett layers. *Proceedings of the Royal Society of London.Series A, Mathematical and Physical Sciences*, pages 389–407, 1982.

[147] He M., Szuchmacher Blum A., Overney G., and Overney R. M. Effect of interfacial liquid structuring on the coherence length in nanolubrication. *Physical Review Letters*, 88(15):154302, 2002.

[148] Hamrock B. J. and Dowson D. Elastohydrodynamic lubrication of elliptical contacts for materials of low elastic modulus: Part 1- fully flooded conjunction. *Journal of Tribology*, 100:236–245, 1978.

[149] Wedeven L. D., Evans D., and Cameron A. Optical analysis of abll bearing. *Journal of Tribology*, 93:349–363, 1971.

[150] Seth J. R., Cloitre M., and Bonnecaze R. T. Influence of short range forces on wall-slip in microgel pastes. *Journal of Rheology*, 52(5):1241–1268, 2008.

[151] Erdemir A. Review of engineered tribological interfaces for improved boundary lubrication. *Tribology International*, 38(3):249–256, 2005.

[152] Chong W. W. F., Teodorescu M., and Rahnejat H. Effect of lubricant molecular rheology on formation and shear of ultra-thin surface films. *Journal of Physics D : Applied Physics*, 44(16):165302, 2011.

[153] Einstein A. and Infeld L. *The evolution of physics: the growth of ideas from early concepts to relativity and quanta*. Simon and Schuster, New York, 1938.

[154] Attard P. and Parker J. L. Oscillatory solvation forces: A comparison of theory and experiment. *Journal of Physical Chemistry*, 96(12):5086–5093, 1992.

[155] Horn R. G. and Israelachvili J. N. Direct measurement of structural forces between two surfaces in a nonpolar liquid. *Journal of Chemical Physics*, 75(3):1400–1412, 1981.

[156] Lim R. Y. H. and O'Shea S. J. Discrete solvation layering in confined binary liquids. *Langmuir*, 20(12):4916–4919, 2004.

[157] Mitchell D. J., Ninham B. W., and Pailthorpe B. A. Hard sphere structural effects in colloid systems. *Chemical Physics Letters*, 51(2):257–260, 1977.

[158] Percus J. K. and Yevick G. J. Analysis of classical statistical mechanics by means of collective coordinates. *Physical Review*, 110:1–13, 1958.

[159] Snook L. and van Megen W. Structure of dense liquids at solid interfaces. *Journal of Chemical Physics*, 70:3099–3105, 1979.

[160] Tarazona P. and Vicente L. A model for density oscillations in liquids between solid walls. *Molecular Physics*, 56:557–572, 1985.

[161] Somers S. A., McCormick A. V., and Davis H. T. Superselectivity and solvation forces of a two component fluid adsorbed in slit micropores. *Journal of Chemical Physics*, 99:9890, 1993.

[162] Karanikas S., Dzubiella J., Moncho-Jord A., and Louis A. A. Density profiles and solvation forces for a yukawa fluid in a slit pore. *Journal of Chemical Physics*, 128:204704, 2008.

[163] Fuller K. N. G. and Tabor D. The effect of surface roughness on the adhesion of elastic solids. *Proceedings of the Royal Society of London.Series A, Mathematical and Physical Sciences*, pages 327–342, 1975.

[164] Rahnejat H., Johns-Rahnejat P. M., Teodorescu M., Votsios V., and Kushwaha M. A review of some tribo-dynamics phenomena from micro- to nano-scale conjunctions. *Tribology International*, 42(11-12):1531–1541, 2009.

[165] Matsuoka H. and Kato T. An ultrathin liquid film lubrication theory - calculation method of solvation pressure and its application to the ehl problem. *Journal of Tribology*, 119:217–226, 1997.

[166] Baxter R. J. Percus-yevick equation for hard spheres with surface adhesion. *Journal of Chemical Physics*, 49(6):2770–2774, 1968.

[167] Derjaguin B. V. Adhesion of small particles. *Kolloid-Zeit.*, 69:155–164, 1935.

[168] Ornstein L. S. and Zernike F. Accidental deviations of density and opalescence at the critical point of a single substance. *Proceedings of the Royal Academy, Amsterdam*, 17:793–806, 1914.

[169] Baxter R. J. Ornstein-zernike relation and percus-yevick approximation for fluid mixtures. *Journal of Chemical Physics*, 52(9):4559–4562, 1970.

[170] Hirata F. *Molecular Theory of Solvation.* Kluwer Academic Publishers, Dordrecht, 2003.

[171] Perram J. W. and Smith E. R. Percus-yevick theory of adsorption. *Chemical Physics Letter*, 39(2):328–332, 1976.

[172] Ruths M., Ohtani H., Greenfield M. L., and Granick S. Exploring the "friction modifier" phenomenon : nanorheology of n-alkane chains with polar terminus dissolved in n-alkane solvent. *Tribology Letters*, 6:207–214, 1999.

[173] Dickinson E. Adsorption of sticky hard spheres : Relevance to protein competitive adsorption. *Journal of Chemical Society - Faraday Transactions*, 88(24):3561–3565, 1992.

[174] Hansen J. P. and McDonald I. R. *Theory of Simple Liquids.* Academic press London, 2006.

[175] Perram J. W. and Smith E. R. A model for the examination of phase behaviour in multicomponent systems. *Chemical Physics Letter*, 35(1):138–140, 1975.

[176] Wertheim M. S. Analytic solution of the percus-yevick equation. *Journal of Mathematical Physics*, 5:643–651, 1964.

[177] Perram J. W. Hard sphere correlation functions in the percus-yevick approximation. *Molecular Physics*, 30(5):1505–1509, 1975.

[178] Perram J. W. and Smith E. R. Competitive adsorption via percus-yevick approximation. *Proceedings of Royal Society A*, 353:193–220, 1977.

[179] Cummings P. T., Perram J. W., and Smith E. R. Percus-yevick theory of correlation functions and nucleation effects in the sticky hard-sphere model. *Molecular Physics*, 31(2):535–548, 1976.

[180] Hamrock B. J., Schmid S. R., and Jacobson B. O. *Fundamentals of fluid film lubrication.* Dekker, New York, 2004.

[181] Greenwood J. A. and Williamson J. B. P. Contact of nominally flat surfaces. *Proceedings of the Royal Society of London : Mathematical and Physical Sciences*, 295:300–319, 1966.

[182] Kogut L. and Etsion I. A static friction model for elastic-plastic contacting rough surfaces. *Journal of Tribology*, 126:34–40, 2004.

[183] Shi X. and Polycarpou A. An elastic-plastic hybrid adhesion model for contacting rough surfaces in the presence of molecularly thin lubricant. *Journal of Colloid and Interface Science*, 290:514–525, 2005.

[184] Majumdar A. and Tien C. L. Fractal characterisation and simulation of rough surfaces. *Wear*, 136:313–327, 1990.

[185] Nayak P. R. Random pressure model of rough surfaces. *Journal of Lubrication Technology*, 93(3):398–407, 1971.

[186] Sayles R. S. and Thomas T. R. Surface topography as a nonstationary random process. *Nature*, 271:431–434, 1978.

[187] Yan W. and Komvopoulos K. Contact analysis of elastic-plastic fractal surfaces. *Journal of Applied Physics*, 84(7):3617–3624, 1998.

[188] Morag Y. and Etsion I. Resolving the contradiction of asperities plastic to elastic mode transition in current contact models of fractal rough surfaces. *Wear*, 262(5-6):624–629, 2006.

[189] Mandelbrot B. B. *The fractal geometry of nature.* W. H. Freeman and Company, 1982.

[190] Majumdar A. and Bhushan B. Fractal model of elastic-plastic contact between rough surfaces. *Journal of Tribology*, 113(1), 1991.

[191] Bora C. K., Flater E. E., Street M. D., Redmond J. M., Starr M. J., Carpick R. W., and Plesha M. E. Multiscale roughness and modeling of mems interface. *Tribology Letters*, 19(1):37–48, 2005.

[192] Morrow C. A. and Lovell M. R. A solution for lightly loaded adhesive rough surfaces with application to mems. *Journal of Tribology*, 127:206–212, 2005.

[193] Komvopoulos K. Surface engineering and microtribology for microelectromechanical systems. *Wear*, 200:305–327, 1996.

[194] Komvopoulos K. and Ye N. Three-dimensional contact analysis of elastic-plastic layered media with fractal surface topographies. *Journal of Tribology*, 123:632–640, 2001.

[195] Jackson R. L. and Streator J. L. A multi-scale model for contact between rough surfaces. *Wear*, 261:1337–1347, 2006.

[196] McCool J. L. Comparison of models for the contact of rough surfaces. *Wear*, 107:37–60, 1985.

Appendix A

Derivation of Modified Elrod Algorithm

A.1 Introduction

The chapter will cover the derivation of a numerical model based on Elrod's Cavitation Algorithm. The assumptions and conditions as described by Elrod [32] are applied onto the Reynolds' Equation as shown in Eqn. A.1.

$$\frac{\partial}{\partial x}\left[\frac{\rho h^3}{\eta}.\frac{\partial p}{\partial x}\right]=12\left\{\frac{\partial}{\partial x}\left[\rho h\left(u_{av}\right)\right]+\frac{d}{dt}\left(\rho h\right)\right\} \tag{A.1}$$

A.2 Finite Difference Scheme Derivation: Line Contact Solution

There are two main components of the Elrod Cavitation Algorithm that need to be incorporated into the Reynolds' Equation as shown in Eqn. A.1. They are:

- The pressure equation relating the contact pressure, p to the fractional film content, θ
- The density equation relating the lubricant density at full film region, ρ to the density at cavitation region, ρ_c

Pressure Equation:-

The pressure equation as derived by Elrod [32] is as shown in Eqn. A.2.

$$p = g\beta \ln \theta + p_c \tag{A.2}$$

Where $\theta \neq 0$

Eqn. A.3 can be derived by computing the derivative of pressure, p towards the fractional film content, θ,

$$\begin{aligned} \frac{dp}{d\theta} &= \frac{g\beta}{\theta} \\ dp &= \frac{g\beta}{\theta}.d\theta \end{aligned} \tag{A.3}$$

Density Equation:-

Elrod [32] relates the fractional film content, θ to the ratio of the density at full film region and cavitation region. The relationship can be expressed as Eqn. A.4.

$$\begin{aligned} \theta &= \frac{\rho}{\rho_c} \\ \rho_c &= \frac{\rho}{\theta} \end{aligned} \tag{A.4}$$

Elrod Cavitation Algorithm:-

The Elrod Cavitation Algorithm can be derived by substituting Eqn. A.3 and Eqn. A.4 into Eqn. A.1, The derived equation which also reflects the solution for a full film region is shown as Eqn. A.5.

$$\begin{aligned}\frac{\partial}{\partial x}\left[\frac{\theta\rho_c h^3}{\eta}.\frac{\frac{g\beta}{\theta}.d\theta}{\partial x}\right] &= 12\left\{\frac{\partial}{\partial x}\left[\theta\rho_c h\left(u_{av}\right)\right]+\frac{d}{dt}\left(\theta\rho_c h\right)\right\}\\ \frac{\partial}{\partial x}\left[\frac{\rho_c h^3}{\eta}.g\beta.\frac{d\theta}{\partial x}\right] &= 12\left\{\frac{\partial}{\partial x}\left[\theta\rho_c h\left(u_{av}\right)\right]+\frac{d}{dt}\left(\theta\rho_c h\right)\right\}\end{aligned} \tag{A.5}$$

Cavitation Region:-

Based on Elrod, the Coutte term plays a major role in the cavitation region in comparison to the Poiseuille term. Hence, the Poiseuille term can be neglected at the cavitation region. Therefore, Eqn. A.5 can be rewritten as Eqn. A.6 for the cavitation region.

$$\frac{\partial}{\partial x}\left[\theta\rho_c h\left(u_{av}\right)\right]+\frac{d}{dt}\left(\theta\rho_c h\right)=0 \tag{A.6}$$

A.3 Dimensionless Parameters

Table A.1: Non-Dimensional Parameters

Parameters	**Dimensionless**	**Relation**
$x\,(m)$	X	$X = \frac{x}{b}$
$y\,(m)$	Y	$Y = \frac{y}{a}$
$\rho\left(\frac{kg}{m^3}\right)$	$\bar{\rho}$	$\bar{\rho} = \frac{\rho}{\rho_o}$
$\eta\left(\frac{N.s}{m^2}\right)$	$\bar{\eta}$	$\bar{\eta} = \frac{\eta}{\eta_o}$
$h\,(m)$	H	$H = \frac{h.R_x}{b^2}$
$p\,(Pa)$	P	$P = \frac{p}{p_H}$
$t\,(s)$	$\bar{t}$	$\bar{t} = \frac{u_{av}.t}{R_x}$
$W\,(s)$	W^*	$W^* = \frac{W}{E^*.R_x.L}$
$u_{av}\left(\frac{m}{s}\right)$	U^*	For 1-Dimensional:
		$U^* = \frac{u_{av}.\eta_o}{E^*.R_x}$
		For 2-Dimensional:
		$U^* = \frac{u}{u_{av}}$
$v_{av}\left(\frac{m}{s}\right)$	V^*	$V^* = \frac{u}{u_{av}}$
$\beta\left(\frac{N}{m^2}\right)$	$\bar{\beta}$	$\bar{\beta} = \frac{\beta.R_x}{\eta_o.u_{av}}$

A.4 Governing Equation Derivation

A.4.1 Non-Dimensional Term

Eqn. A.5 must first be non-dimensionalized before being finite-differenced based on Jalali *et al*'s approach [28]. The non-dimensional parameters as shown in Table A.1 are substituted into Eqn. A.5 as being described using Eqn. A.7.

$$\begin{aligned}
\frac{\partial}{\partial x}\left[\frac{\rho_c h^3}{\eta}.\frac{g\beta.\partial\theta}{\partial x}\right] &= 12\left\{\frac{\partial}{\partial x}\left[\theta\rho_c h\left(u_{av}\right)\right]+\frac{d}{dt}\left(\theta\rho_c h\right)\right\}\\
\frac{\partial}{(b\partial X)}\left[\frac{\left(\bar{\rho}_c\rho_o\right)\left(\frac{Hb^2}{R_x}\right)^3}{\left(\bar{\eta}\eta_o\right)}.\frac{g\left(\frac{\bar{\beta}\eta_o u_{av}}{R_x}\right).\partial\theta}{(b\partial X)}\right] &= 12\left\{\frac{\partial}{(b\partial X)}\left[\theta\left(\bar{\rho}_c\rho_o\right).\left(\frac{Hb^2}{R_x}\right).\left(u_{av}\right)\right]+\frac{d}{dt}\left(\theta\left(\bar{\rho}_c\rho_o\right)h\right)\right\}\\
\left(\frac{\bar{\beta}\rho_o b^4 u_{av}}{{R_x}^4}\right)\frac{\partial}{\partial X}\left[g\frac{\bar{\rho}_c H^3}{\bar{\eta}}\frac{\partial\theta}{\partial X}\right] &= \left(\frac{12\rho_o u_{av} b}{R_x}\right)\left\{\frac{\partial}{\partial X}\left[\theta\bar{\rho}_c H\right]+\frac{R_x}{b}\frac{{dh}/{dt}}{u_{av}}\left(\theta\bar{\rho}_c\right)\right\}\\
\frac{\partial}{\partial X}\left[g\frac{\bar{\rho}_c H^3}{\bar{\eta}}\frac{\partial\theta}{\partial X}\right] &= \frac{12}{\bar{\beta}}\left(\frac{R_x}{b}\right)^3\left\{\frac{\partial}{\partial X}\left[\theta\bar{\rho}_c H\right]+\frac{R_x}{b}\frac{{dh}/{dt}}{u_{av}}\left(\theta\bar{\rho}_c\right)\right\}
\end{aligned}\tag{A.7}$$

By assuming that,

$$\psi = \frac{12}{\bar{\beta}}\left(\frac{R_x}{b}\right)^3 \tag{A.8}$$

$$S = \frac{{dh}/{dt}}{u_{av}} \tag{A.9}$$

Eqn. A.7 can be rewritten by substituting Eqn. A.8 and Eqn. A.9, as shown in Eqn. A.10.

$$\frac{\partial}{\partial X}\left[g\frac{\bar{\rho}_c H^3}{\bar{\eta}}\frac{\partial\theta}{\partial X}\right]=\psi\left\{\frac{\partial}{\partial X}\left[\theta\bar{\rho}_c H\right]+\frac{R_x}{b}S\left(\theta\bar{\rho}_c\right)\right\} \tag{A.10}$$

Vijayaraghavan and Keith [29] stated that the finite-differencing of the switch function, g should be done based on Eqn. A.11 to be able to fully represent the physical meaning of the algorithm.

$$g\frac{d\theta}{dX} = \frac{dg(\theta-1)}{dX} \tag{A.11}$$

As a result of the assumption above, Eqn. A.10 can be rewritten as:

$$\frac{\partial}{\partial X}\left[\frac{\bar{\rho}_c H^3}{\bar{\eta}}\frac{\partial g(\theta-1)}{\partial X}\right] = \psi\left\{\frac{\partial}{\partial X}\left[\theta\bar{\rho}_c H\right] + \frac{R_x}{b}S\left(\theta\bar{\rho}_c\right)\right\} \tag{A.12}$$

A.4.2 Finite Differencing

The finite difference scheme is based on Eqn. A.12. As mentioned by Vijayaraghavan and Keith [29], Eqn. A.12 when used in full film region is an elliptic partial differential equation. This means that the central finite differencing method should be used to reflect the physical representation of the equation.

At cavitation region, the Coutte term of Eqn. A.12 predominates over the Poiseuille term. The remainder of Eqn. A.12 reflects a hyperbolic type of partial differential equation. Therefore, the most suitable finite differencing scheme for this region is the backward finite differencing method.

For the LHS of Eqn. A.12

$$
\begin{aligned}
&\frac{\partial}{\partial X}\left(\frac{\bar{\rho}_c H^3}{\bar{\eta}}.\frac{\partial\left[g\left(\theta-1\right)\right]}{\partial X}\right)\\
=\;&\frac{\left(\frac{\bar{\rho}_c H^3}{\bar{\eta}}.\frac{\partial[g(\theta-1)]}{\partial X}\right)_{i+\frac{1}{2}}-\left(\frac{\bar{\rho}_c H^3}{\bar{\eta}}.\frac{\partial[g(\theta-1)]}{\partial X}\right)_{i-\frac{1}{2}}}{\Delta X}\\
=\;&\left(\frac{\bar{\rho}_c H^3}{\bar{\eta}}\right)_{i+\frac{1}{2}}\left(\frac{\left[g\left(\theta-1\right)\right]_{i+1}-\left[g\left(\theta-1\right)\right]_{i}}{\Delta X^2}\right)-\left(\frac{\bar{\rho}_c H^3}{\bar{\eta}}\right)_{i-\frac{1}{2}}\left(\frac{\left[g\left(\theta-1\right)\right]_{i}-\left[g\left(\theta-1\right)\right]_{i-1}}{\Delta X^2}\right)\\
=\;&\frac{1}{2\Delta X^2}\left\{\begin{array}{l}
\left[\left(\frac{\bar{\rho}_c H^3}{\bar{\eta}}\right)_{i+1}+\left(\frac{\bar{\rho}_c H^3}{\bar{\eta}}\right)_{i}\right]\left(\left[g\left(\theta-1\right)\right]_{i+1}-\left[g\left(\theta-1\right)\right]_{i}\right)\\
-\left[\left(\frac{\bar{\rho}_c H^3}{\bar{\eta}}\right)_{i}+\left(\frac{\bar{\rho}_c H^3}{\bar{\eta}}\right)_{i-1}\right]\left(\left[g\left(\theta-1\right)\right]_{i}-\left[g\left(\theta-1\right)\right]_{i-1}\right)
\end{array}\right\}\\
=\;&\frac{1}{2\Delta X^2}\left\{\begin{array}{l}
\left[\left(\frac{\bar{\rho}_c H^3}{\bar{\eta}}\right)_{i+1}+\left(\frac{\bar{\rho}_c H^3}{\bar{\eta}}\right)_{i}\right]\left[g\left(\theta-1\right)\right]_{i+1}\\
-\left[\left(\frac{\bar{\rho}_c H^3}{\bar{\eta}}\right)_{i+1}+2\left(\frac{\bar{\rho}_c H^3}{\bar{\eta}}\right)_{i}+\left(\frac{\bar{\rho}_c H^3}{\bar{\eta}}\right)_{i-1}\right]\left[g\left(\theta-1\right)\right]_{i}\\
+\left[\left(\frac{\bar{\rho}_c H^3}{\bar{\eta}}\right)_{i}+\left(\frac{\bar{\rho}_c H^3}{\bar{\eta}}\right)_{i-1}\right]\left[g\left(\theta-1\right)\right]_{i-1}
\end{array}\right\} \qquad \text{(A.13)}
\end{aligned}
$$

As mentioned above, the Coutte term should be able to reflect different types of behavior in the full film region and cavitation region. Therefore, a term, Φ is introduced as a switching term between the central and backward finite differencing scheme.

For the RHS of Eqn. A.12:-

$$
\begin{aligned}
&\psi\left[\frac{\partial\left(\theta\bar{\rho}_c H\right)}{\partial X}+\frac{R_x\theta\bar{\rho}_c}{b}S^*\right]\\
=\;&\psi\left\{\left(1-\Phi\right)\frac{\left[\left(\theta\bar{\rho}_c H\right)_{i+1}-\left(\theta\bar{\rho}_c H\right)_{i}\right]}{\Delta X}+\left(\Phi\right)\frac{\left[\left(\theta\bar{\rho}_c H\right)_{i}-\left(\theta\bar{\rho}_c H\right)_{i-1}\right]}{\Delta X}+\frac{R_x(\theta\bar{\rho}_c)_i}{b}.S^*\right\}\\
=\;&\frac{\psi}{\Delta X}\left\{\left(1-\Phi\right)\left[\left(\theta\bar{\rho}_c H\right)_{i+1}-\left(\theta\bar{\rho}_c H\right)_{i}\right]+\left(\Phi\right)\left[\left(\theta\bar{\rho}_c H\right)_{i}-\left(\theta\bar{\rho}_c H\right)_{i-1}\right]\right\}\\
&+\psi\frac{R_x(\theta\bar{\rho}_c)_i}{b}S^* \qquad \text{(A.14)}
\end{aligned}
$$

If $\Phi = 1.0$, Eqn. A.14 can be rewritten as a backward differencing equation.

$$\frac{\psi}{\Delta X}\left[(\theta\bar{\rho}_c H)_i - (\theta\bar{\rho}_c H)_{i-1}\right] + \psi\frac{R_x(\theta\bar{\rho}_c)_i}{b}S^* \tag{A.15}$$

If $\Phi = 0.5$, Eqn A.14 can be rewritten as a central differencing equation.

$$\frac{\psi}{2\Delta X}\left[(\theta\bar{\rho}_c H)_{i+1} - (\theta\bar{\rho}_c H)_{i-1}\right] + \psi\frac{R_x(\theta\bar{\rho}_c)_i}{b}S^* \tag{A.16}$$

A.4.3 Modified Newton-Raphson method

The modified Newton-Raphson method is used to solve the finite difference scheme derived above for the modified Elrod's algorithm. Eqn. A.13 and Eqn. A.14 are rearranged as shown in Eqn. A.17.

$$\begin{aligned}
F_i = \quad & \frac{1}{2\Delta X^2}\left\{\begin{array}{l}
\left[\left(\frac{\bar{\rho}_c H^3}{\bar{\eta}}\right)_{i+1} + \left(\frac{\bar{\rho}_c H^3}{\bar{\eta}}\right)_i\right][g(\theta-1)]_{i+1} \\
-\left[\left(\frac{\bar{\rho}_c H^3}{\bar{\eta}}\right)_{i+1} + 2\left(\frac{\bar{\rho}_c H^3}{\bar{\eta}}\right)_i + \left(\frac{\bar{\rho}_c H^3}{\bar{\eta}}\right)_{i-1}\right][g(\theta-1)]_i \\
+\left[\left(\frac{\bar{\rho}_c H^3}{\bar{\eta}}\right)_i + \left(\frac{\bar{\rho}_c H^3}{\bar{\eta}}\right)_{i-1}\right][g(\theta-1)]_{i-1}
\end{array}\right\} \\
& -\frac{\psi}{\Delta X}\left\{(1-\Phi)\left[(\theta\bar{\rho}_c H)_{i+1} - (\theta\bar{\rho}_c H)_i\right] + (\Phi)\left[(\theta\bar{\rho}_c H)_i - (\theta\bar{\rho}_c H)_{i-1}\right]\right\} \\
& -\psi\frac{R_x(\theta\bar{\rho}_c)_i}{b}S^*
\end{aligned} \tag{A.17}$$

By using the Taylor's series expansion,

$$\begin{aligned}\bar{F_i} &= F_i + \frac{\partial F_i}{\partial[g\theta]_{i+1}}\left\{[g\bar{\theta}]_{i+1} - [g\theta]_{i+1}\right\} + \frac{\partial F_i}{\partial[g\theta]_i}\left\{[g\bar{\theta}]_i - [g(\theta)]_i\right\} \\ &\quad + \frac{\partial F_i}{\partial[g\theta]_{i-1}}\left\{[g\bar{\theta}]_{i-1} - [g\theta]_{i-1}\right\} \\ &= F_i + \frac{\partial F_i}{\partial[g\theta]_{i+1}}[g_{i+1}\left(\bar{\theta}_{i+1} - \theta_{i+1}\right)] + \frac{\partial F_i}{\partial[g\theta]_i}[g_i\left(\bar{\theta}_i - \theta_i\right)] \\ &\quad + \frac{\partial F_i}{\partial[g\theta]_{i-1}}[g_{i-1}\left(\bar{\theta}_{i-1} - \theta_{i-1}\right)] \end{aligned} \tag{A.18}$$

Assuming that

$$\Delta\theta_n = g_n\left(\bar{\theta}_n - \theta_n\right)$$

$$\bar{F_i} = F_i + \frac{\partial F_i}{\partial[g\theta]_{i+1}}\Delta\theta_{i+1} + \frac{\partial F_i}{\partial[g\theta]_i}\Delta\theta_i + \frac{\partial F_i}{\partial[g\theta]_{i-1}}\Delta\theta_{i-1} \tag{A.19}$$

With the assumption that the Jacobian, J terms can be expressed as:

$$J_{m,n} = \frac{\partial F_m}{\partial[g\theta]_n} \tag{A.20}$$

By substituting Eqn. A.20, Eqn. A.19 can be written as Eqn. A.21

$$\bar{F_i} = F_i + J_{i,i+1}\Delta\theta_{i+1} + J_{i,i}\Delta\theta_i + J_{i,i-1}\Delta\theta_{i-1} \tag{A.21}$$

The Gauss-Seidel iteration method is used to solve Eqn. A.21. The iteration equation is shown in Eqn. A.22.

$$\begin{aligned}\Delta\theta_i^k &= \frac{-F_i - J_{i,i-1}\Delta\theta_{i-1}^k - J_{i,i+1}\Delta\theta_{i+1}^k}{J_{i,i}} \\ \Delta\theta_i^k &= \frac{-J[3] - J[0]\Delta\theta_{i-1}^k - J[2]\Delta\theta_{i+1}^k}{J[1]}\end{aligned} \tag{A.22}$$

Where k is the interation step.

To calculate the new fractional film content, θ_i^k,

$$g_k\theta_i^k = g_k\theta_i^{k-1} + \omega\Delta\theta_i^k \tag{A.23}$$

Where ω is the relaxation factor.

Eqn. A.2 states that $\theta \neq 0$. For Eqn. A.23 to be valid, the switch function, g must be unity. Therefore, Eqn. A.23 can be simplified as

$$\theta_i^k = \theta_i^{k-1} + \omega\Delta\theta_i^k \tag{A.24}$$

A.4.4 Jacobian, J terms

Based on Eqn. A.17, the first Jacobian term, $J[0]$ of Eqn. A.22 is computed as follow:-

$$
\begin{aligned}
J[0] &= J_{i,i-1} \\
&= \frac{\partial}{\partial[g\theta]_{i-1}} \left[\frac{1}{2(\Delta X^2)} \left\{ \begin{array}{l} \left[\left(\frac{\bar{\rho}_c H^3}{\bar{\eta}}\right)_{i+1} + \left(\frac{\bar{\rho}_c H^3}{\bar{\eta}}\right)_i \right] [g(\theta-1)]_{i+1} \\ - \left[\left(\frac{\bar{\rho}_c H^3}{\bar{\eta}}\right)_{i+1} + 2\left(\frac{\bar{\rho}_c H^3}{\bar{\eta}}\right)_i + \left(\frac{\bar{\rho}_c H^3}{\bar{\eta}}\right)_{i-1} \right] [g(\theta-1)]_i \\ + \left[\left(\frac{\bar{\rho}_c H^3}{\bar{\eta}}\right)_i + \left(\frac{\bar{\rho}_c H^3}{\bar{\eta}}\right)_{i-1} \right] [g(\theta-1)]_{i-1} \end{array} \right\} \right] \\
&\quad - \frac{\partial}{\partial[g\theta]_{i-1}} \left[\begin{array}{l} \frac{\psi}{\Delta X} \left\{ (1-\Phi) \left[(\theta\bar{\rho}_c H)_{i+1} - (\theta\bar{\rho}_c H)_i \right] + (\Phi) \left[(\theta\bar{\rho}_c H)_i - (\theta\bar{\rho}_c H)_{i-1} \right] \right\} \\ \\ + \psi \frac{R_x(\theta\bar{\rho}_c)_i}{b} S^* \end{array} \right] \\
&= \frac{1}{2(\Delta X)^2} . \left\{ \begin{array}{l} \left[\frac{\partial\left(\frac{\bar{\rho}_c H^3}{\bar{\eta}}\right)_{i+1}}{\partial[g\theta]_{i-1}} + \frac{\partial\left(\frac{\bar{\rho}_c H^3}{\bar{\eta}}\right)_i}{\partial[g\theta]_{i-1}} \right] \left[g\left(\theta-1\right)\right]_{i+1} \\ \\ \left[\frac{\partial\left(\frac{\bar{\rho}_c H^3}{\bar{\eta}}\right)_{i+1}}{\partial[g\theta]_{i-1}} + \frac{\partial\left(\frac{\bar{\rho}_c H^3}{\bar{\eta}}\right)_i}{\partial[g\theta]_{i-1}} + \frac{\partial\left(\frac{\bar{\rho}_c H^3}{\bar{\eta}}\right)_{i-1}}{\partial[g\theta]_{i-1}} \right] \left[g\left(\theta-1\right)\right]_i \\ \\ + \left[\frac{\partial\left(\frac{\bar{\rho}_c H^3}{\bar{\eta}}\right)_i}{\partial[g\theta]_{i-1}} + \frac{\partial\left(\frac{\bar{\rho}_c H^3}{\bar{\eta}}\right)_{i-1}}{\partial[g\theta]_{i-1}} \right] \left[\left([g\theta]\right)\right]_{i-1} \\ \\ + \left[\left(\frac{\bar{\rho}_c H^3}{\bar{\eta}}\right)_i + \left(\frac{\bar{\rho}_c H^3}{\bar{\eta}}\right)_{i-1} \right] \end{array} \right\} \\
&\quad - \frac{\psi}{\Delta X} \left\{ \begin{array}{l} (1-\Phi) \left[\frac{\partial(\theta\bar{\rho}_c H)_{i+1}}{\partial[g\theta]_{i-1}} - \frac{\partial(\theta\bar{\rho}_c H)_i}{\partial[g\theta]_{i-1}} \right] \\ \\ + (\Phi) \left[\frac{\partial(\theta\bar{\rho}_c H)_i}{\partial[g\theta]_{i-1}} - \frac{\partial(\theta\bar{\rho}_c H)_{i-1}}{\partial[g\theta]_{i-1}} \right] \end{array} \right\} \\
&\quad - \psi . \frac{R_x}{b} . \frac{\partial(\theta\bar{\rho}_c)_i}{\partial[g\theta]_{i-1}} . S^* \qquad \text{(A.25)}
\end{aligned}
$$

Therefore,

$$\begin{aligned} M_l^k &= \frac{\partial\left(\bar{\rho}_c H^3/\bar{\eta}\right)_k}{\partial[g\theta]_l} \\ M_l^k &= \left(\frac{H^3}{\bar{\eta}}\right)_k \frac{\partial(\bar{\rho}_c)_k}{\partial[g\theta]_l} - \left(\frac{\bar{\rho}_c H^3}{\bar{\eta}^2}\right)_k \frac{\partial\bar{\eta}_k}{\partial[g\theta]_l} + 3\left(\frac{\bar{\rho}_c H^2}{\bar{\eta}}\right)_k \frac{\partial H_k}{\partial[g\theta]_l} \qquad \text{(A.26)} \end{aligned}$$

$$\begin{aligned} N_l^k &= \frac{\partial(\theta\bar{\rho}_c H)_k}{\partial[g\theta]_l} \\ N_l^k &= (\theta H)_k \frac{\partial(\bar{\rho}_c)_k}{\partial[g\theta]_l} + (\theta\bar{\rho}_c)_k \frac{\partial H_k}{\partial[g\theta]_l} + (\bar{\rho}_c H)_k \frac{\partial\theta_k}{\partial[g\theta]_l} \qquad \text{(A.27)} \end{aligned}$$

$$\begin{aligned} LL_l^k &= \frac{\partial(\theta\bar{\rho}_c)_k}{\partial[g\theta]_l} \\ LL_l^k &= (\theta)_k \frac{\partial(\bar{\rho}_c)_k}{\partial[g\theta]_l} + (\bar{\rho}_c)_k \frac{\partial\theta_k}{\partial[g\theta]_l} \qquad \text{(A.28)} \end{aligned}$$

As

$$\frac{\partial\theta_k}{\partial[g\theta]_l} = 0.0$$

Therefore,

$$N_l^k = (\theta H)_k \frac{\partial(\bar{\rho}_c)_k}{\partial[g\theta]_l} + (\theta\bar{\rho}_c)_k \frac{\partial H_k}{\partial[g\theta]_l} \qquad \text{(A.29)}$$

$$LL_l^k = (\theta)_k \frac{\partial(\bar{\rho}_c)_k}{\partial[g\theta]_l} \qquad \text{(A.30)}$$

By substituting Eqn A.26, Eqn A.29 and Eqn A.30 into Eqn A.25,

$$
\begin{aligned}
J[0] = \quad & \frac{1}{2(\Delta X)^2}.\left\{\begin{array}{l}
\left[M_{i-1}^{i+1} + M_{i-1}^{i}\right]\left[g\left(\theta-1\right)\right]_{i+1} \\[2ex]
-\left[M_{i-1}^{i+1} + M_{i-1}^{i} + M_{i-1}^{i-1}\right]\left[g\left(\theta-1\right)\right]_{i} \\[2ex]
+\left[M_{i-1}^{i} + M_{i-1}^{i-1}\right]\left[g\left(\theta-1\right)\right]_{i-1} \\[2ex]
+\left[\left(\frac{\bar{\rho}_c H^3}{\overline{\eta}}\right)_i + \left(\frac{\bar{\rho}_c H^3}{\overline{\eta}}\right)_{i-1}\right]
\end{array}\right\} \\
& -\frac{\psi}{\Delta X}\left\{(1-\Phi)\left[N_{i-1}^{i+1} - N_{i-1}^{i}\right] + (\Phi)\left[N_{i-1}^{i} - N_{i-1}^{i-1}\right]\right\} \\
& -\psi.\frac{R_x}{b}.LL_{i-1}^{i}.S^{*}
\end{aligned} \tag{A.31}
$$

The same procedure is to be repeated for the remaining Jacobian components of Eqn A.22.

$$
\begin{aligned}
J[1] = \quad & \frac{1}{2(\Delta X)^2}.\left\{\begin{array}{l}
\left[M_{i}^{i+1} + M_{i}^{i}\right]\left[g\left(\theta-1\right)\right]_{i+1} \\[2ex]
-\left[M_{i}^{i+1} + 2M_{i}^{i} + M_{i}^{i-1}\right]\left[g\left(\theta-1\right)\right]_{i} \\[2ex]
+\left[M_{i}^{i} + M_{i}^{i-1}\right]\left[g\left(\theta-1\right)\right]_{i-1} \\[2ex]
-\left[\left(\frac{\bar{\rho}_c H^3}{\overline{\eta}}\right)_{i+1} + 2\left(\frac{\bar{\rho}_c H^3}{\overline{\eta}}\right)_i + \left(\frac{\bar{\rho}_c H^3}{\overline{\eta}}\right)_{i-1}\right]
\end{array}\right\} \\
& -\frac{\psi}{\Delta X}\left\{(1-\Phi)\left[N_{i}^{i+1} - N_{i}^{i}\right] + (\Phi)\left[N_{i}^{i} - N_{i}^{i-1}\right]\right\} \\
& -\psi.\frac{R_x}{b}.LL_{i}^{i}.S^{*}
\end{aligned} \tag{A.32}
$$

$$
\begin{aligned}
J[2] = \quad & \frac{1}{2(\Delta X)^2} \cdot \left\{ \begin{array}{l}
\left[M_{i+1}^{i+1} + M_{i+1}^{i}\right] \left[g\left(\theta - 1\right)\right]_{i+1} \\[2ex]
- \left[M_{i+1}^{i+1} + 2M_{i+1}^{i} + M_{i+1}^{i-1}\right] \left[g\left(\theta - 1\right)\right]_{i} \\[2ex]
+ \left[M_{i+1}^{i} + M_{i+1}^{i-1}\right] \left[g\left(\theta - 1\right)\right]_{i-1} \\[2ex]
+ \left[\left(\frac{\bar{\rho}_c H^3}{\bar{\eta}}\right)_{i+1} + \left(\frac{\bar{\rho}_c H^3}{\bar{\eta}}\right)_{i}\right]
\end{array} \right\} \\
& - \frac{\psi}{\Delta X} \left\{(1 - \Phi) \left[N_{i+1}^{i+1} - N_{i+1}^{i}\right] + (\Phi) \left[N_{i+1}^{i} - N_{i+1}^{i-1}\right]\right\} \\
& - \psi . \frac{R_x}{b} . LL_{i+1}^{i} . S^* \qquad \text{(A.33)}
\end{aligned}
$$

$$
\begin{aligned}
J[3] = \quad & \frac{1}{2\Delta X^2} \left\{ \begin{array}{l}
\left[\left(\frac{\bar{\rho}_c H^3}{\bar{\eta}}\right)_{i+1} + \left(\frac{\bar{\rho}_c H^3}{\bar{\eta}}\right)_{i}\right] \left[g\left(\theta - 1\right)\right]_{i+1} \\[2ex]
- \left[\left(\frac{\bar{\rho}_c H^3}{\bar{\eta}}\right)_{i+1} + 2\left(\frac{\bar{\rho}_c H^3}{\bar{\eta}}\right)_{i} + \left(\frac{\bar{\rho}_c H^3}{\bar{\eta}}\right)_{i-1}\right] \left[g\left(\theta - 1\right)\right]_{i} \\[2ex]
+ \left[\left(\frac{\bar{\rho}_c H^3}{\bar{\eta}}\right)_{i} + \left(\frac{\bar{\rho}_c H^3}{\bar{\eta}}\right)_{i-1}\right] \left[g\left(\theta - 1\right)\right]_{i-1}
\end{array} \right\} \\
& - \frac{\psi}{\Delta X} \left\{(1 - \Phi) \left[(\theta \bar{\rho}_c H)_{i+1} - (\theta \bar{\rho}_c H)_{i}\right] + (\Phi) \left[(\theta \bar{\rho}_c H)_{i} - (\theta \bar{\rho}_c H)_{i-1}\right]\right\} \\
& - \psi \frac{R_x (\theta \bar{\rho}_c)_i}{b} S^* \qquad \text{(A.34)}
\end{aligned}
$$

A.4.5 Density

In EHL, the density of the lubricant can no longer be a constant matter. Therefore, Eqn. A.35 as mentioned in Chapter 2 is used.

$$
\bar{\rho}_k = 1 + \frac{0.6 \times 10^{-9} \times p_k}{1 + 1.7 \times 10^{-9} \times p_k} \qquad \text{(A.35)}
$$

By simplifying Eqn. A.2 as

$$
p_k = g_k \beta (\theta_k - 1) + p_c \qquad \text{(A.36)}
$$

Eqn. A.36 is substituted into A.35

$$\bar{\rho}_k = 1 + \frac{0.6 \times 10^{-9} \times (g_k\beta(\theta_k - 1) + p_c)}{1 + 1.7 \times 10^{-9} \times (g_k\beta(\theta_k - 1) + p_c)} \tag{A.37}$$

To compute the derivative of ρ_c towards $g\theta$, Eqn. A.4 is substituted into Eqn. A.37.

$$\begin{aligned}
\frac{\partial(\bar{\rho})_k}{\partial[g\theta]_l} &= \frac{\partial}{\partial[g\theta]_l}\left\{1 + \frac{0.6 \times 10^{-9} \times (g_k\beta(\theta_k - 1) + p_c)}{1 + 1.7 \times 10^{-9} \times (g_k\beta(\theta_k - 1) + p_c)}\right\} \\
\frac{\partial(\bar{\rho})_k}{\partial[g\theta]_l} &= \frac{\partial}{\partial[g\theta]_l}\left\{\frac{0.6 \times 10^{-9} \times (g_k\beta(\theta_k - 1) + p_c)}{1 + 1.7 \times 10^{-9} \times (g_k\beta(\theta_k - 1) + p_c)}\right\} \\
\frac{\partial(\theta\bar{\rho}_c)_k}{\partial[g\theta]_l} &= \frac{\partial}{\partial[g\theta]_l}\left\{\frac{0.6 \times 10^{-9} \times (g_k\beta(\theta_k - 1) + p_c)}{1 + 1.7 \times 10^{-9} \times (g_k\beta(\theta_k - 1) + p_c)}\right\} \\
\frac{\partial(\bar{\rho}_c)_k}{\partial[g\theta]_l} &= \frac{\partial}{\partial[g\theta]_l}\left\{\frac{1}{\theta_k}.\frac{0.6 \times 10^{-9} \times (g_k\beta(\theta_k - 1) + p_c)}{1 + 1.7 \times 10^{-9} \times (g_k\beta(\theta_k - 1) + p_c)}\right\}
\end{aligned} \tag{A.38}$$

Eqn. A.38 can be simplified as

$$\begin{aligned}
&\frac{\partial(\bar{\rho}_c)_k}{\partial[g\theta]_l} \\
=\ & \frac{0.6 \times 10^{-9}}{\theta_k\left(1 + 1.7 \times 10^{-9} \times [g_k\beta(\theta_k - 1) + p_c]\right)^2}\begin{bmatrix} \frac{\partial[g\theta]_k}{\partial[g\theta]_l}.\beta\left(1 + 1.7 \times 10^{-9} \times [g_k\beta(\theta_k - 1) + p_c]\right) \\ \\ -\frac{\partial[g\theta]_k}{\partial[g\theta]_l}.\beta(1.7 \times 10^{-9} \times [g_k\beta(\theta_k - 1) + p_c]) \end{bmatrix} \\
=\ & \frac{0.6 \times 10^{-9} \times \beta}{\theta_k\left(1 + 1.7 \times 10^{-9} \times [g_k\beta(\theta_k - 1) + p_c]\right)^2}.\frac{\partial[g\theta]_k}{\partial[g\theta]_l}
\end{aligned}$$

where

$$\begin{aligned}
ifk \neq l; \frac{\partial[g\theta_k]}{\partial[g\theta]_l} &= 0; \\
ifk = l; \frac{\partial[g\theta]_k}{\partial[g\theta]_l} &= 1;
\end{aligned}$$

A.4.6 Viscosity

To be able to accommodate the EHL, piezoviscous property of the lubricant should be taken into consideration. Eqn. A.39 as discussed in Chapter 2 is used.

$$\bar{\eta}_k = e^{(\ln \eta_o + 9.67)\left[-1+\left(1+\frac{p}{p_o}\right)^z\right]} \tag{A.39}$$

By replacing the pressure term, p described in Eqn. A.36 into Eqn. A.39,

$$\bar{\eta}_k = e^{(\ln \eta_o + 9.67)\left[-1+\left(1+\frac{g_k\beta(\theta_k-1)+p_c}{p_o}\right)^z\right]} \tag{A.40}$$

Computing the derivative of Eqn. A.40 towards $g\theta$,

$$\begin{aligned}
\frac{\partial\bar{\eta}_k}{\partial[g\theta]_l} &= \frac{\partial\left[e^{(\ln \eta_o + 9.67)\left[-1+\left(1+\frac{[g_k\beta(\theta_k-1)+p_c]}{p_o}\right)^z\right]}\right]}{\partial[g\theta]_l} \\
&= \bar{\eta}_k\frac{\partial\left\{(\ln \eta_o + 9.67)\left[-1+\left(1+\frac{[g_k\beta(\theta_k-1)+p_c]}{p_o}\right)^z\right]\right\}}{\partial[g\theta]_l} \\
&= \bar{\eta}_k\,(\ln \eta_o + 9.67)\,\frac{\partial\left\{\left[\left(1+\frac{[g_k\beta(\theta_k-1)+p_c]}{p_o}\right)^z\right]\right\}}{\partial[g\theta]_l} \\
&= (\ln \eta_o + 9.67)\,(\beta)\left(\frac{z\bar{\eta}_k}{p_o}\right)\left(1+\frac{[g_k\beta(\theta_k-1)+p_c]}{p_o}\right)^{z-1}\frac{\partial[g\theta]_k}{\partial[g\theta]_l}
\end{aligned} \tag{A.41}$$

From A.41, the conditions for this equation to be applicable are:

$$if k \neq l; \frac{\partial\theta_k}{\partial\theta_l} = 0; \frac{\partial\bar{\eta}_k}{\partial\theta_l} = 0$$

$$if k = l;; \frac{\partial\theta_k}{\partial\theta_l} = 1; \frac{\partial\bar{\eta}_k}{\partial\theta_l} = (\ln \eta_o + 9.67)\,(\beta)\left(\frac{z\bar{\eta}_k}{p_o}\right)\left(1+\frac{[g_k\beta(\theta_k-1)+p_c]}{p_o}\right)^{z-1}$$

A.4.7 Film Profile

The equation used to represent the lubricant film profile is:

$$H_i = H_o + H_s + D_m \frac{p}{P_H} \tag{A.42}$$

By Eqn. substituting A.36 into Eqn. A.42,

$$H_k = H_o + H_s + D_{m(k,l)} \frac{g_k \beta(\theta_k - 1) + p_c}{P_H} \tag{A.43}$$

The derivative of A.43 towards the fractional film content, θ is obtained as follow:

$$\frac{\partial H_k}{\partial [g\theta]_l} = D_{m(k,l)} \left(\frac{\beta}{P_H} \right) \tag{A.44}$$

A.5 Finite Difference Scheme Derivation: Point Contact Solution

The finite difference scheme for Elrod Cavitation Algorithm's 2-dimensional solution is derived based on the 1-dimensional solution discussed above.

A.5.1 Jacobian, J terms

$$\begin{aligned} \Delta\theta^n_{k,l} &= \frac{-F_{k,l} - J^{k,l}_{k-1,l}\Delta\theta^n_{k-1,l} - J^{k,l}_{k+1,l}\Delta\theta^{n-1}_{k+1,l} - J^{k,l}_{k,l-1}\Delta\theta^n_{k,l-1} - J^{k,l}_{k,l+1}\Delta\theta^{n-1}_{k,l+1}}{J^{k,l}_{k,l}} \\ \Delta\theta^n_{k,l} &= \frac{-J[5] - J[1]\Delta\theta^n_{k-1,l} - J[0]\Delta\theta^n_{k+1,l} - J[3]\Delta\theta^n_{k,l-1} - J[2]\Delta\theta^n_{k,l+1}}{J[4]} \end{aligned} \tag{A.45}$$

$$J[0] = A_0 + k^2 B_0 - C_0 - kD_0 - \psi \left[\frac{R_x}{b} S^* \frac{\partial(\theta\bar{\rho}_c)_{i,j}}{\partial\theta_{i+1,j}} \right] \tag{A.46}$$

where

$$A_0 = \frac{1}{2(\Delta X)^2}\cdot\left\{\begin{array}{l} \left[M^{i+1,j}_{i+1,j} + M^{i,j}_{i+1,j}\right]\left[g\left(\theta-1\right)\right]_{i+1,j} \\ -\left[M^{i+1,j}_{i+1,j} + 2M^{i,j}_{i+1,j} + M^{i-1,j}_{i+1,j}\right]\left[g\left(\theta-1\right)\right]_{i,j} \\ +\left[M^{i,j}_{i+1,j} + M^{i-1,j}_{i+1,j}\right]\left[g\left(\theta-1\right)\right]_{i-1,j} \\ +\left[\left(\frac{\bar{\rho}_c H^3}{\bar{\eta}}\right)_{i+1,j} + \left(\frac{\bar{\rho}_c H^3}{\bar{\eta}}\right)_{i,j}\right] \end{array}\right\} \tag{A.47}$$

$$B_0 = \frac{1}{2(\Delta \mathrm{Y})^2}\cdot\left\{\begin{array}{l} \left[M^{i,j+1}_{i+1,j} + M^{i,j}_{i+1,j}\right]\left[g\left(\theta-1\right)\right]_{i,j+1} \\ -\left[M^{i,j+1}_{i+1,j} + 2M^{i,j}_{i+1,j} + M^{i,j-1}_{i+1,j}\right]\left[g\left(\theta-1\right)\right]_{i,j} \\ +\left[M^{i,j}_{i+1,j} + M^{i,j-1}_{i+1,j}\right]\left[g\left(\theta-1\right)\right]_{i,j-1} \end{array}\right\} \tag{A.48}$$

$$C_0 = \frac{\psi}{\Delta X}\left\{(1-\Phi)\left[N^{i+1,j}_{i+1,j} - N^{i,j}_{i+1,j}\right] + (\Phi)\left[N^{i,j}_{i+1,j} - N^{i-1,j}_{i+1,j}\right]\right\} \tag{A.49}$$

$$D_0 = \frac{\psi}{\Delta \mathrm{Y}}\left\{(1-\Phi)\left[N^{i,j+1}_{i+1,j} - N^{i,j}_{i+1,j}\right] + (\Phi)\left[N^{i,j}_{i+1,j} - N^{i,j-1}_{i+1,j}\right]\right\} \tag{A.50}$$

$$J[1] = A_1 + k^2 B_1 - C_1 - kD_1 - \psi\left[\frac{R_x}{b}S^*\frac{\partial(\theta\bar{\rho}_c)_{i,j}}{\partial\theta_{i-1,j}}\right] \tag{A.51}$$

where

$$A_1 = \frac{1}{2(\Delta X)^2} \cdot \left\{ \begin{array}{l} \left[M_{i-1,j}^{i+1,j} + M_{i-1,j}^{i,j}\right] \left[g\left(\theta-1\right)\right]_{i+1,j} \\ \\ -\left[M_{i-1,j}^{i+1,j} + 2M_{i-1,j}^{i,j} + M_{i-1,j}^{i-1,j}\right] \left[g\left(\theta-1\right)\right]_{i,j} \\ \\ +\left[M_{i-1,j}^{i,j} + M_{i-1,j}^{i-1,j}\right] \left[g\left(\theta-1\right)\right]_{i-1,j} \\ +\left[\left(\frac{\bar{\rho}_c H^3}{\bar{\eta}}\right)_{i,j} + \left(\frac{\bar{\rho}_c H^3}{\bar{\eta}}\right)_{i-1,j}\right] \end{array} \right\} \tag{A.52}$$

$$B_1 = \frac{1}{2(\Delta \mathrm{Y})^2} \cdot \left\{ \begin{array}{l} \left[M_{i-1,j}^{i,j+1} + M_{i-1,j}^{i,j}\right] \left[g\left(\theta-1\right)\right]_{i,j+1} \\ \\ -\left[M_{i-1,j}^{i,j+1} + 2M_{i-1,j}^{i,j} + M_{i-1,j}^{i,j-1}\right] \left[g\left(\theta-1\right)\right]_{i,j} \\ \\ +\left[M_{i-1,j}^{i,j} + M_{i-1,j}^{i,j-1}\right] \left[g\left(\theta-1\right)\right]_{i,j-1} \end{array} \right\} \tag{A.53}$$

$$C_1 = \frac{\psi}{\Delta X} \left\{(1-\Phi)\left[N_{i-1,j}^{i+1,j} - N_{i-1,j}^{i,j}\right] + (\Phi)\left[N_{i-1,j}^{i,j} - N_{i-1,j}^{i-1,j}\right]\right\} \tag{A.54}$$

$$D_1 = \frac{\psi}{\Delta \mathrm{Y}} \left\{(1-\Phi)\left[N_{i-1,j}^{i,j+1} - N_{i-1,j}^{i,j}\right] + (\Phi)\left[N_{i-1,j}^{i,j} - N_{i-1,j}^{i,j-1}\right]\right\} \tag{A.55}$$

$$J[2] = A_2 + k^2 B_2 - C_2 - k D_2 - \psi \left[\frac{R_x}{b} S^* LL_{i,j+1}^{i,j} \frac{\partial(\theta\bar{\rho}_c)_{i,j}}{\partial\theta_{i,j+1}}\right] \tag{A.56}$$

where

$$A_2 = \frac{1}{2(\Delta X)^2}.\left\{\begin{array}{l} \left[M^{i+1,j}_{i,j+1} + M^{i,j}_{i,j+1}\right]\left[g\left(\theta-1\right)\right]_{i+1,j} \\ \\ -\left[M^{i+1,j}_{i,j+1} + 2M^{i,j}_{i,j+1} + M^{i-1,j}_{i,j+1}\right]\left[g\left(\theta-1\right)\right]_{i,j} \\ \\ +\left[M^{i,j}_{i,j+1} + M^{i-1,j}_{i,j+1}\right]\left[g\left(\theta-1\right)\right]_{i-1,j} \end{array}\right\} \tag{A.57}$$

$$B_2 = \frac{1}{2(\Delta \mathrm{Y})^2}.\left\{\begin{array}{l} \left[M^{i,j+1}_{i,j+1} + M^{i,j}_{i,j+1}\right]\left[g\left(\theta-1\right)\right]_{i,j+1} \\ \\ -\left[M^{i,j+1}_{i,j+1} + 2M^{i,j}_{i,j+1} + M^{i,j-1}_{i,j+1}\right]\left[g\left(\theta-1\right)\right]_{i,j} \\ \\ +\left[M^{i,j}_{i,j+1} + M^{i,j-1}_{i,j+1}\right]\left[g\left(\theta-1\right)\right]_{i,j-1} \\ \\ +\left[\left(\frac{\bar{\rho}_c H^3}{\bar{\eta}}\right)_{i,j+1} + \left(\frac{\bar{\rho}_c H^3}{\bar{\eta}}\right)_{i,j}\right] \end{array}\right\} \tag{A.58}$$

$$C_2 = \frac{\psi}{\Delta X}\left\{(1-\Phi)\left[N^{i+1,j}_{i,j+1} - N^{i,j}_{i,j+1}\right] + (\Phi)\left[N^{i,j}_{i,j+1} - N^{i-1,j}_{i,j+1}\right]\right\} \tag{A.59}$$

$$D_2 = \frac{\psi}{\Delta \mathrm{Y}}\left\{(1-\Phi)\left[N^{i,j+1}_{i,j+1} - N^{i,j}_{i,j+1}\right] + (\Phi)\left[N^{i,j}_{i,j+1} - N^{i,j-1}_{i,j+1}\right]\right\} \tag{A.60}$$

$$J[3] = A_3 + k^2 B_3 - C_3 - kD_3 - \psi\left[\frac{R_x}{b} S^* LL^{i,j}_{i,j-1}\right] \tag{A.61}$$

where

$$A_3 = \frac{1}{2(\Delta X)^2}.\left\{\begin{array}{l} \left[M^{i+1,j}_{i,j-1} + M^{i,j}_{i,j-1}\right]\left[g\left(\theta-1\right)\right]_{i+1,j} \\ -\left[M^{i+1,j}_{i,j-1} + 2M^{i,j}_{i,j-1} + M^{i-1,j}_{i,j-1}\right]\left[g\left(\theta-1\right)\right]_{i,j} \\ +\left[M^{i,j}_{i,j-1} + M^{i-1,j}_{i,j-1}\right]\left[g\left(\theta-1\right)\right]_{i-1,j} \end{array}\right\} \tag{A.62}$$

$$B_3 = \frac{1}{2(\Delta \mathrm{Y})^2}.\left\{\begin{array}{l} \left[M^{i,j+1}_{i,j-1} + M^{i,j}_{i,j-1}\right]\left[g\left(\theta-1\right)\right]_{i,j+1} \\ -\left[M^{i,j+1}_{i,j-1} + 2M^{i,j}_{i,j-1} + M^{i,j-1}_{i,j-1}\right]\left[g\left(\theta-1\right)\right]_{i,j} \\ +\left[M^{i,j}_{i,j-1} + M^{i,j-1}_{i,j-1}\right]\left[g\left(\theta-1\right)\right]_{i,j-1} \\ +\left[\left(\frac{\bar{\rho}_c H^3}{\bar{\eta}}\right)_{i,j} + \left(\frac{\bar{\rho}_c H^3}{\bar{\eta}}\right)_{i,j-1}\right] \end{array}\right\} \tag{A.63}$$

$$C_3 = \frac{\psi}{\Delta X}\left\{(1-\Phi)\left[N^{i+1,j}_{i,j-1} - N^{i,j}_{i,j-1}\right] + (\Phi)\left[N^{i,j}_{i,j-1} - N^{i-1,j}_{i,j-1}\right]\right\} \tag{A.64}$$

$$D_3 = \frac{\psi}{\Delta \mathrm{Y}}\left\{(1-\Phi)\left[N^{i,j+1}_{i,j-1} - N^{i,j}_{i,j-1}\right] + (\Phi)\left[N^{i,j}_{i,j-1} - N^{i,j-1}_{i,j-1}\right]\right\} \tag{A.65}$$

$$J[4] = A_4 + k^2 B_4 - C_4 - kD_4 - \psi\left[\frac{R_x}{b} S^* LL^{i,j}_{i,j}\right] \tag{A.66}$$

where

$$A_4 = \frac{1}{2(\Delta X)^2}\cdot\left\{\begin{array}{l} \left[M^{i+1,j}_{i,j-1} + M^{i,j}_{i,j-1}\right]\left[g\left(\theta-1\right)\right]_{i+1,j} \\ -\left[M^{i+1,j}_{i,j} + 2M^{i,j}_{i,j} + M^{i-1,j}_{i,j}\right]\left[g\left(\theta-1\right)\right]_{i,j} \\ +\left[M^{i,j}_{i,j} + M^{i-1,j}_{i,j}\right]\left[g\left(\theta-1\right)\right]_{i-1,j} \\ -\left[\left(\frac{\bar{\rho}_c H^3}{\bar{\eta}}\right)_{i+1,j} + 2\left(\frac{\bar{\rho}_c H^3}{\bar{\eta}}\right)_{i,j} + \left(\frac{\bar{\rho}_c H^3}{\bar{\eta}}\right)_{i-1,j}\right] \end{array}\right\} \tag{A.67}$$

$$B_4 = \frac{1}{2(\Delta \mathrm{Y})^2}\cdot\left\{\begin{array}{l} \left[M^{i,j+1}_{i,j} + M^{i,j}_{i,j}\right]\theta_{i,j+1} \\ -\left[M^{i,j+1}_{i,j} + 2M^{i,j}_{i,j} + M^{i,j-1}_{i,j}\right]\left[g\left(\theta-1\right)\right]_{i,j} \\ +\left[M^{i,j}_{i,j} + M^{i,j-1}_{i,j}\right]\left[g\left(\theta-1\right)\right]_{i,j-1} \\ -\left[\left(\frac{\bar{\rho}_c H^3}{\bar{\eta}}\right)_{i,j+1} + 2\left(\frac{\bar{\rho}_c H^3}{\bar{\eta}}\right)_{i,j} + \left(\frac{\bar{\rho}_c H^3}{\bar{\eta}}\right)_{i,j-1}\right] \end{array}\right\} \tag{A.68}$$

$$C_4 = \frac{\psi}{\Delta X}\left\{(1-\Phi)\left[N^{i+1,j}_{i,j} - N^{i,j}_{i,j}\right] + (\Phi)\left[N^{i,j}_{i,j} - N^{i-1,j}_{i,j}\right]\right\} \tag{A.69}$$

$$D_4 = \frac{\psi}{\Delta \mathrm{Y}}\left\{(1-\Phi)\left[N^{i,j+1}_{i,j} - N^{i,j}_{i,j}\right] + (\Phi)\left[N^{i,j}_{i,j} - N^{i,j-1}_{i,j}\right]\right\} \tag{A.70}$$

The parameters M,N, and L used in the Jacobian, J terms can be expressed as follow:

$$\begin{aligned} M^{i,j}_{k,l} &= \frac{\partial\left(\bar{\rho}_c H^3/\bar{\eta}\right)_{i,j}}{\partial[g\theta]_{k,l}} \\ M^{i,j}_{k,l} &= \left(\frac{H^3}{\bar{\eta}}\right)_{i,j}\frac{\partial(\bar{\rho}_c)_{i,j}}{\partial[g\theta]_{k,l}} - \left(\frac{\bar{\rho}_c H^3}{\bar{\eta}^2}\right)_{i,j}\frac{\partial\bar{\eta}_{i,j}}{\partial[g\theta]_{k,l}} + 3\left(\frac{\bar{\rho}_c H^2}{\bar{\eta}}\right)_{i,j}\frac{\partial H_{i,j}}{\partial[g\theta]_{k,l}} \qquad \text{(A.71)} \\ N^{i,j}_{k,l} &= \frac{\partial(\theta\bar{\rho}_c H)_{i,j}}{\partial[g\theta]_{k,l}} \\ N^{i,j}_{k,l} &= (\theta H)_{i,j}\frac{\partial(\bar{\rho}_c)_{i,j}}{\partial[g\theta]_{k,l}} + (\theta\bar{\rho}_c)_{i,j}\frac{\partial H_{i,j}}{\partial[g\theta]_{k,l}} \qquad \text{(A.72)} \\ LL^{i,j}_{k,l} &= \frac{\partial(\theta]\bar{\rho}_c)_{i,j}}{\partial[g\theta]_{k,l}} \\ LL^{i,j}_{k,l} &= (\theta)_{i,j}\frac{\partial(\bar{\rho}_c)_{i,j}}{\partial[g\theta]_{k,l}} \qquad \text{(A.73)} \end{aligned}$$

Appendix B

List of Publications

Journal Papers

J5. **Chong W.W.F.**, Teodorescu M. and Rahnejat H. *Physio-chemical hydrodynamic mechanism underlying the formation of thin adsorbed boundary films,* Royal Society of Chemistry: Faraday Discussion 156 (Accepted for conference/under-review for journal publication)

J4. **Chong W.W.F.**, Teodorescu M. and Rahnejat H. *Formation of ultra-thin bi-molecular boundary adsorbed films,* Journal of Physics D: Applied Physics (Accepted)

J3. De la Cruz M., **Chong W.W.F.**, Teodorescu M., Theodossiades S. and Rahnejat H. *Transient mixed thermo-elastohydrodynamic lubrication in multi-speed transmissions,* Tribology International (In-press)

J2. **Chong W.W.F.**, Teodorescu M. and Rahnejat H. *Effect of lubricant molecular rheology on formation and shear of ultra-thin surface films*, Journal of Physics D: Applied Physics, 44(16):165302, **2011**.

J1. **Chong W.W.F.** , Teodorescu M. and Vaughan N.D. *Cavitation induced starvation for piston ring/liner tribological onjunctions*, Tribology International, 44(4): 483-497, **2011**.

Journal Papers under preparation/review

U3. Chidlow S., **Chong W.W.F.** and Teodorescu M. On the two-dimesional solution of a contact problem involving functionally graded materials

U2. **Chong W.W.F.**, Chidlow S. and Teodorescu M. Adhesive contact on graded elastic coating.

U1. **Chong W.W.F.**, Teodorescu M. and Rahnejat H. Transient dynamics of valve train system with mixed thermo-elastohydrodynamic cam-tappet contact.

Refereed Conference Proceedings

C5. Chidlow S., **Chong W.W.F.**, Teodorescu M., Vaughan N. D. *Adhesive contacts for graded-elastic coatings using Fourier series decomposition*, Proc. STLE/ASME International Joint Tribology Conference, **October 24-26 2011**, Los Angelas, California, US, organised by STLE/ASME.

C4. Avan E.Y., **Chong W.W.F.**, Mills R., Dwyer-Joyce R.S. and Teodorescu M. *Experimental and numerical investigations on a simulated piston ring-liner contact*, 38th Leeds-Lyon Symposium on Tribology, **September 6-9 2011**, Lyon, France, organised by the Laboratoire de Mcanique des Contacts et des Structures (LaMCoS).

C3. **Chong W.W.F.**, Teodorescu M. and Rahnejat H. *Influence of ultra-thin film tribology on hard disk areal storage*, Proc. STLE/ASME International Joint Tribology Conference, **October 17-20 2010**, San Francisco, California, US, organised by STLE/ASME.

C2. **Chong W.W.F.**, Teodorescu M. and Vaughan N.D. *Piston ring cavitation and starvation during entrainment motion reversal*, Proc. STLE/ASME International Joint Tribology Conference, **October 17-20 2010**, San Francisco, California, US, organised by STLE/ASME

C1. **Chong W.W.F.**, Teodorescu M. and Rahnejat H. *Rupture and reformation of ultra-thin surface films*, Proc. ASME International Design Engineering Technical Conferences & Computers and Information in Engineering Conference, **August 15-18 2010**, Montreal, Quebec, Canada, organised by ASME.

Poster Presentation

P2. *Effect of lubricant rheology on ultra-thin surface films* during the Poster Conference **2011** organised by the Doctoral Training Center (DTC), School of Engineering, Cranfield University

P1. *Effect of near surface film friction on asperity contact* at the 4th International Conference on Micro and Nanosystems (MNS) during the Proceedings of the ASME **2010** International Design Engineering Technical Conferences & Computers and Information in Engineering Conference